THEORY, DEVELOPMENT, AND APPLICATION OF QUANTITATIVE PHASE IMAGING MODALITIES ON STANDARD MICROSCOPE PLATFORMS

A Dissertation
Presented to
The Academic Faculty

by

Yijun Bao

In Partial Fulfillment
of the Requirements for the Degree
Doctor of Philosophy in the
School of Electrical and Computer Engineering

Georgia Institute of Technology
May 2019

THEORY, DEVELOPMENT, AND APPLICATION OF QUANTITATIVE PHASE IMAGING MODALITIES ON STANDARD MICROSCOPE PLATFORMS

Approved by:

Prof. Thomas K. Gaylord, Advisor
School of Electrical and Computer Engineering
Georgia Institute of Technology

Dr. Christopher R. Valenta
Georgia Tech Research Institute
Georgia Institute of Technology

Prof. Gee-Kung Chang
School of Electrical and Computer Engineering
Georgia Institute of Technology

Prof. Martin Short
School of Mathematics
Georgia Institute of Technology

Prof. Wenshan Cai
School of Electrical and Computer Engineering
Georgia Institute of Technology

Dr. Sorin Tibuleac
ADVA Optical Networking

Date Approved: March 27, 2019

ACKNOWLEDGEMENTS

I would like to thank my thesis advisor, Professor Thomas K. Gaylord, who has given me tremendous help in both research and everyday life. I am also grateful to the members of my committee for their attention and advice for my proposal.

I would like to thank Dr. Micah H. Jenkins, who did a great pioneer work on this research and gave me significant help in my starting stage. I am also grateful to my previous and current fellow students, Pengfei Wang, Ben Popko, Grayson Noah, George Dong, Ji Chun, Ashton Hattori, Bradley Zarek, Jacob Bruhn, David Goldfarb, and Nazli Gollar, for their participation and assistant in various projects.

I would like to thank my roommates and friends for sharing happiness and pains during my PhD career. Last but not the least, I would like to thank my parents for supporting me financially and spiritually throughout my life.

TABLE OF CONTENTS

LIST OF TABLES

LIST OF FIGURES

LIST OF ABBREVIATIONS

1D	One-Dimensional
2D	Two-Dimensional
3D	Three-Dimensional
AOTF	Absorption Optical Transfer Function
BC	Boundary Condition
CTF	Contrast Transfer Function
DHM	Digital Holographic Microscopy
DIC	Differential Interference Contrast
DICM	Differential Interference Contrast Microscopy
DT	Diffraction Tomography
ePIE	Extended Ptychographic Iterative Engine
FBG	Fiber Bragg Grating
FPM	Fourier Ptychographic Microscopy
FWHM	Full Width at Half Maxima
HMC	Hoffmann Modulation Contrast
HPM	Hilbert Phase Microscopy
ITDPM	Iterative Tomographic Deconvolution Phase Microscopy
IWFR	Iterative Wave Function Reconstruction
LPFG	Long-Period Fiber Grating
LS-MFPI-PC	Least-Squares MFPI-PC
MCF	Multi-Core Fiber
MEMS	Microelectromechanical Systems

MFPI-PC	Multifilter Phase Imaging with Partially Coherent Light
MFT	Multifocus Tomography
MTF	Modulation transfer function
NA	Numerical Aperture
NAc	Numerical Aperture of Condensor Lens
NAci	Numerical Aperture of the Inner Aperture of Condensor Lens
NAo	Numerical Aperture of Objective Lens
nP-MFPI-PC	Nonparaxial MFPI-PC without OF Modification
nP-MFPI-PC-OF	Nonparaxial MFPI-PC with OF Modification
nP-POTF	Nonparaxial POTF without OF Modification
nP-POTF-OF	Nonparaxial POTF with OF Modification
nP-WD-PCTF	Nonparaxial WD-PCTF without OF Modification
nP-WD-PCTF-OF	Nonparaxial WD-PCTF with OF Modification
NRMSE	Normalized Root-Mean-Aquare Error
NTDPM	Non-Tomographic Deconvolution Phase Microscopy
OA-DHM	Off-Axis Digital Holographic Microscopy
OAH	Off-Axis Holography
ODT	Optical Diffraction Tomography
OF	Obliquity Factor
OFS	Optimal Frequency Selection
OQM	Optical Quadrature Microscopy
OTF	Optical Transfer Function
PCF	Photonic Crystal Fiber
PCM	Phase Contrast Microscopy
PCTF	Phase Contrast Transfer Function

PMF	Polarization-Maintaining Fiber
P-MFPI-PC	Paraxial MFPI-PC
POTF	Phase Optical Transfer Function
POTFR	Phase Optical Transfer Function Recovery
P-POTF	Paraxial POTF
PS-DHM	Phase-Shifting Digital Holographic Microscopy
PSF	Point Spread Function
PSH	Phase-Shifting Holography
PT	Projection Tomography
P-WD-PCTF	Paraxial WD-PCTF
QPI	Quantitative Phase Imaging
QPM	Quantitative Phase Microscopy
QPT	Quantitative Phase Tomography
QWLSI	Quadri-Wave Lateral Shearing Interferometry
RI	Refractive Index
RMSE	Root-Mean-Square Error
SCOT	Scanning Color Optical Tomography
SGDF	Savitzky–Golay Differentiation Filters
SI-DPM	Structured Illumination Microscopy
SII-QPM	Spatially Incoherent Illumination Quantitative Phase Microscopy
SLIM	Spatial Light Interference Microscopy
SLM	Spatial Light Modulator
SMF	Single Mode Fiber
SNR	Signal-to-Noise Ratio
SP	Scattering Potential

TDPM	Tomographic Deconvolution Phase Microscopy
TE	Transverse electric
TIE	Transport-of-Intensity Equation
TIE-PCTF	PCTF with TIE approximation
TM	Transverse magnetic
TPM	Tomographic Phase Microscopy
USAF	US Air Force
WD-PCTF	Weakly-Defocused PCTF
wDPM	White Light Diffraction Phase Microscopy
WDT	White-Light Diffraction Tomography
WLS-MFPI-PC	Weighted Least-Squares MFPI-PC
WOTF	Weak Optical Transfer Function

LIST OF SYMBOLS

$\boldsymbol{x} = (x, y)$	Lateral 2D spatial coordinate (μm)
z	Longitudinal spatial coordinate (μm)
$\boldsymbol{r} = (\boldsymbol{x}, z)$	3D spatial coordinate (μm)
$\boldsymbol{\rho} = (\rho_x, \rho_y)$	Lateral 2D spatial frequency (μm^{-1})
η	Longitudinal spatial frequency (μm^{-1})
$\boldsymbol{f} = (\boldsymbol{\rho}, \eta)$	3D spatial frequency (μm^{-1})
λ	Wavelength (μm)
k_0	Wavevector magnitude (μm^{-1})
n_0	Background refractive index (dimensionless)
$n(\boldsymbol{r})$	Refractive index (dimensionless)
Δn	Refractive index difference between object to environment (dimensionless)
i	Imaginary unit $\sqrt{-1}$ (dimensionless)
$v(\boldsymbol{r})$	Scattering potential (μm^{-2})
$v_P(\boldsymbol{r})$	Real/Phase part of scattering potential (μm^{-2})
$v_A(\boldsymbol{r})$	Imaginary/Absorption part of scattering potential (μm^{-2})
$V(\boldsymbol{f})$	Spatial spectrum of scattering potential (μm)
$V_P(\boldsymbol{f})$	Spatial spectrum of real/phase part of scattering potential (μm)
$V_A(\boldsymbol{f})$	Spatial spectrum of imaginary/absorption part of scattering potential (μm)
$h(\boldsymbol{r})$	3D (phase) point spread function (μm^{-3})
$h_A(\boldsymbol{r})$	3D absorption point spread function (μm^{-3})
$H(\boldsymbol{f})$	3D (phase) optical transfer function (dimensionless)
$H_A(\boldsymbol{f})$	3D absorption optical transfer function (dimensionless)

$I(\boldsymbol{r})$	3D intensity (μm^{-2})
$\tilde{I}(\boldsymbol{f})$	3D intensity spatial spectrum (μm)
B	Background intensity (μm^{-2})
$*$	Convolution
$(\cdot)^*$	Complex conjugate
$\delta(\cdot)$	Delta function
$\tilde{p}(\boldsymbol{\rho})$	Pupil function (dimensionless)
$\tilde{S}(\boldsymbol{\rho})$	Source function (dimensionless)
$\mathrm{NA_o}$	Numerical aperture of objective lens (dimensionless)
$\mathrm{NA_c}$	(Outer) Numerical aperture of condenser lens (dimensionless)
$\mathrm{NA_{ci}}$	Inner numerical aperture of condenser lens (dimensionless)
ρ_p	Boundary of nonzero pupil function (μm^{-1})
ρ_s	(Outer) Boundary of nonzero source function (μm^{-1})
ρ_{si}	Inner boundary of nonzero source function (μm^{-1})
$\partial_z I(\boldsymbol{x}, z)$	Longitudinal intensity derivative (μm^{-3})
$\partial_z I(\boldsymbol{x}, 0)$	Longitudinal intensity derivative at focal plane (μm^{-3})
$\partial_z I(\boldsymbol{\rho})$	Spatial spectrum of longitudinal intensity derivative at focal plane (μm^{-1})
$\phi(\boldsymbol{x})$	Phase of the object (radians = dimensionless)
$\Phi(\boldsymbol{\rho})$	Spatial spectrum of phase (μm^2)
$\nabla_\perp$	Lateral gradient operator
$T(\boldsymbol{\rho})$	Phase contrast transfer function (μm^{-3})
$T_{\mathrm{TIE}}(\boldsymbol{\rho})$	Phase contrast transfer function in TIE approximation (μm^{-3})
$T_{\mathrm{W}}(\boldsymbol{\rho})$	Weakly-defocused phase contrast transfer function (μm^{-3})
$T_k(\boldsymbol{\rho})$	Phase contrast transfer function of (2k-1)th order SGDF (μm^{-3})

$a_i^{(k)}$	Coefficient of (2k-1)th order SGDF(dimensionless)
Δz	Distance between neighboring intensity planes (μm)
$H_{SG,k}\left(e^{2\pi i\eta\Delta z}\right)$	Transfer function of (2k-1)th order SGDF (μm^{-1})
$\xi^{(k)}(\rho)$	Weighting filter of the phase from (2k-1)th order SGDF in MFPI-PC (dimensionless)
$\xi_{LS}^{(k)}(\rho)$	Weighting filter of the phase from (2k-1)th order SGDF in LS-MFPI-PC (dimensionless)
$\xi_{WLS}^{(k)}(\rho)$	Weighting filter of the phase from (2k-1)th order SGDF in WLS-MFPI-PC (dimensionless)
ϵ	Threshold (dimensionless)
$\mathrm{PTF_k}(\rho)$	PTF of (2k-1)th order SGDF (dimensionless)
$t(\boldsymbol{x})$	Planar transmittance function (dimensionless)
$a(\boldsymbol{x})$	Absorption of the object (dimensionless)
$A(\boldsymbol{\rho})$	Spatial spectrum of object aborption (μm^2)
$I_z(\boldsymbol{x})$	Intensity at plane z (μm^{-2})
$\tilde{I}_z(\boldsymbol{\rho})$	Spatial spectrum of intensity at plane z (dimensionless)
$\Delta\tilde{I}_z(\boldsymbol{\rho})$	Spatial spectrum of intensity difference between planes at z and -z (dimensionless)
$h_z(\boldsymbol{x})$	2D (phase) point spread function at plane z (μm^{-4})
$h_{A,z}(\boldsymbol{x})$	2D absorption point spread function at plane z (μm^{-4})
$H_z(\boldsymbol{\rho})$	2D (phase) optical transfer function (μm^{-2})
$H_{A,z}(\boldsymbol{\rho})$	2D absorption optical transfer function (μm^{-2})
$\Phi_z(\boldsymbol{\rho})$	Spatial spectrum of phase recovered from planes ±z (μm^2)
$\xi_z(\rho)$	Weighting filter for results from planes ±z (dimensionless)
$\tilde{J}_{OBJ}(\boldsymbol{\rho}_1;\boldsymbol{\rho}_2)$	Spatial spectrum of mutual intensity (μm^2)
$G(\boldsymbol{r};\boldsymbol{r}')$	Green's function (μm^{-1})

$\tilde{G}(\boldsymbol{\rho}, z)$	Annular spectrum of Green's function (μm)
$G'(\boldsymbol{r}; \boldsymbol{r}')$	Modified Green's function after Type-2 OF modification (μm^{-1})
$G'(\boldsymbol{\rho}, z)$	Annular spectrum of modified Green's function after Type-2 OF modification (μm)
$K(\boldsymbol{r}; \boldsymbol{r}')$	Obliquity factor (dimensionless)
$K(\theta, \theta')$	Obliquity factor in terms of angles (dimensionless)
$K(\boldsymbol{\rho})$	Spatial spectrum of obliquity factor (μm^2)
$u(\boldsymbol{r})$	Amplitude of light field (dimensionless)
$u_{IN}(\boldsymbol{r})$	Incident amplitude of light field (dimensionless)
$h^{(2)}(\boldsymbol{r}; \boldsymbol{r}')$	Point spread function in 2D diffraction theory (μm^{-1})
$\mathrm{d}\phi$	Incremental phase induced by a slice of object (radians = dimensionless)
$\mathrm{d}\phi'$	Incremental phase induced by a slice of object after Type-1 OF modification (radians = dimensionless)
β	Threshold (dimensionless)
$H(\boldsymbol{\rho}, \eta; \rho_{si}, \rho_s)$	3D (phase) optical transfer function for annular source with inner and outer annulus determined by μ_{si} and μ_s (dimensionless)
$H(\boldsymbol{\rho}, \eta; 0, \rho_s)$	3D (phase) optical transfer function for disk source determined by μ_s (dimensionless)
$\widetilde{H}$	3D (phase) optical transfer function normalized by background intensity. (μm^2)
$\phi_0(x, y)$	Ideal phase of a test object (radians = dimensionless)
$\phi_r(x, y)$	Recovered phase of a test object (radians = dimensionless)
P	Positivity indicator (dimensionless)
D	Relative difference (dimensionless)
β	Absorption coefficient (dimensionless)
ζ	Spatial frequency ratio (dimensionless)
$\lvert\lvert\cdot\rvert\rvert$	L^2 norm

A	Imaging operator representing a convolution with PSF (dimensionless)
F	Fourier transform operator (μm^3)
F^{-1}	Inverse Fourier transform operator (μm^{-3})
$J(v)$	Regularization function (dimensionless)
$\lvert\nabla v\rvert$	Gradient magnitude of $v(\boldsymbol{r})$ (μm^{-3})
ε	A small number (unit depends on application)
$\Psi(v, I)$	Cost function (μm^{-1})
$\Psi_o(v, I)$	Cost function in object rotation representation (μm^{-1})
$\Psi_i(v, I)$	Cost function in image rotation representation (μm^{-1})
N	Total number of angles (dimensionless)
α	Regularization parameter (unit depends on application)
I_m	3D intensity at the m-th angle (μm^{-2})
A_m	Imaging operator at the m-th angle (dimensionless)
v_m	Scattering potential at the m-th angle (μm^{-2})
Θ_m	Rotation operator, which rotates the object or image by the m-th angle (dimensionless)
A_{-m}	Imaging operator in the opposite direction of m-th angle (dimensionless)
Θ_{-m}	Rotation operator, which rotates the object or image by the m-th angle in the opposite direction (dimensionless)
$\nabla\Psi(v, I)$	Gradient of cost function (μm^{-2})
$A^\dagger$	Adjoint operator of A (dimensionless)
$\nabla J(v)$	Gradient of regularization function (μm^{-1})
$\Theta_m^\dagger$	Adjoint operator of Θ_m (dimensionless)
$v^{(0)}$	Initial scattering potential in ITDPM (μm^{-2})
n_i	Ideal refractive index of the object (dimensionless)

n_r	Recovered refractive index of the object (dimensionless)
$(\cdot,\cdot)$	Inner product
$\hat{I}(\rho_x, \rho_y)$	Pixel-integrated intensity spectrum (dimensionless)
$\Pi(x, y)$	Window function (μm^{-2})
$\tilde{\Pi}(\rho_x, \rho_y)$	Spatial spectrum of window function (dimensionless)
Λ_0	Period of fiber Bragg grating (μm)
$\Lambda(x)$	Local period of fiber Bragg grating (μm)
f_c	Spatial frequency corresponding to grating period (μm^{-1})
$\gamma(\rho_x)$	Modulation transfer function (dimensionless)
γ_0	Modulation transfer function at grating period (dimensionless)
n_D	DC part of refractive index (dimensionless)
n_A	Envelope/Apodization of AC part of refractive index (dimensionless)
δx	Pixel size for digital image processing (μm)
Δx	Camera resolution (μm)
$\Delta x'$	Camera sensor size (μm)
FF	Fill factor (dimensionless)
u	Upsampling factor (dimensionless)
$\mathrm{round}(x)$	Nearest integer (dimensionless)
f_s	Sampling spatial frequency (μm^{-1})
$f_c{}'$	Measured/Aliased center spatial frequency (μm^{-1})
$HT(\cdot)$	Hilbert transform
$n_h(x)$	AC part of refractive index distribution (dimensionless)
$\tilde{n}_h(x)$	Complex analytic function related to n_h (dimensionless)
$\mathrm{sgn}(\rho_x)$	Sign function (dimensionless)

$\tilde{\psi}(x)$	Phase of $\tilde{n}_h(x)$ (radians)
$\psi(x)$	Phase of envelope/apodization of AC part of refractive index (radians)
$D(\psi(x))$	Differentiation of $\psi(x)$ (μm^{-1})
σ	Standard deviation of Additive white Gaussian noise (unit depends on application)

SUMMARY

The object of this thesis is to develop and generalize quantitative phase imaging (QPI) methods to enable their more widespread use and their application to new classes of objects. Microscopic qualitative phase imaging has already produced impressive progress in biological and medical research. QPI is now being used even more widely in these existing fields as well as in industrial applications such as optical fiber characterization. QPI is not only quantitative in nature, but also label-free and thus able to image live cells in their natural, unperturbed environment. However, the conventional approach for QPI typically involves expensive custom stand-alone systems. To meet the growing QPI need and to reduce the cost, the Optics Laboratory has developed several new QPI methods that can be implemented on existing standard commercial microscope platforms. These methods include 1) 2D QPI method multifilter phase imaging with partially coherent light (MFPI-PC), 2) 2D QPI method phase optical transfer function recovery (POTFR), and 3) 3D QPI method tomographic deconvolution phase microscopy (TDPM). Since these methods have some limitations, the present thesis focuses on improving these methods.

First, an analytical nonparaxial partially coherent 3D phase optical transfer function (POTF) was derived to describe the 3D image formation theory. Using this analytical nonparaxial 3D POTF, MFPI-PC was generalized to the nonparaxial condition without increasing computational time. In order to make MFPI-PC more suitable for annular illumination, weighted-least-squares MFPI-PC (WLS-MFPI-PC) was developed, in which a set of filters derived from least-squares fitting, further multiplied by an extra

weight inversely proportional to the noise magnification factor, is used to replace the original binary filters. The analytical 3D POTF also greatly reduces the computation time needed in POTFR by making the transfer function semi-analytical. The improved MFPI-PC and POTFR have been compared through simulations. In addition, a unified, complete, and consistent description of the use of obliquity factor (OF) and OF modifications in 2D and 3D imaging of thin and thick objects was developed. In 3D QPI, an iterative regularization algorithm has been developed for TDPM, so that the refractive index can be reconstructed with high accuracy and with fewer rotation angles required, which enables faster measurements. An application of 3D QPI to fiber Bragg grating characterization was proposed by combining digital image processing techniques to overcome the short-period difficulty. Finally, specific future work is proposed, which includes further development of QPI methods as well as more applications.

CHAPTER 1. INTRODUCTION

1.1 Concept and Application

Most of our knowledge about cell biology can be attributed to advances in optical microscopy, where cells are imaged through some contrast, either intrinsic or extrinsic. A common modality utilizing extrinsic contrast is fluorescence microscopy, in which a specimen is labeled with a fluorescent molecule to provide targeted morphological information [1]. The importance of fluorescence microscopy has been made evident by the 2014 Nobel Prize in chemistry. Despite its success, however, there are a growing number of applications in biology, where methods employing intrinsic contrast are required, because label-free methods are not subject to phototoxicity and/or photobleaching and therefore permit the observation of living cells in their natural environment with little or no sample preparation.

The primary challenge associated with intrinsic contrast is that cells are transparent objects and produce very little contrast under conventional illumination conditions. Historically, this problem has been solved optically using methods such as phase contrast microscopy (PCM) [2], differential interference contrast (DIC) [3], and Hoffmann modulation contrast (HMC) [4] microscopy. Although useful, these methods all suffer from an important drawback, which is that the measured intensity has a nonlinear, and thus non-invertible, relationship with the phase of the specimen. Thus, extracting morphologically quantities and refractive index (RI) is difficult.

In order to overcome this limitation, a burgeoning field of quantitative phase imaging (QPI) has been developed, which combines innovations in optics, imaging theory, and computational methods to produce quantitative phase images [5]. Two-dimensional (2D) QPI resolves the optical path thickness of a specimen, which is proportional to the RI integrated along its optical axis and also proportional to the phase. Three-dimensional (3D) QPI resolves the RI of a specimen in the full 3D space. Figure 1.1 illustrates the information typically available from 2D and 3D QPI experiments in the literature. QPI has two major advantages, quantitative and non-invasive. Since it is quantitative, morphologically quantities such as size, volume, and dry mass [6] can be quantitatively determined, which provide much more information than that can be obtained by qualitative methods. Since it is non-invasive, cells can be imaged in their natural and unperturbed environment, so that biological processes lasting for hours or days can be characterized, and the obtained information is close to reality.

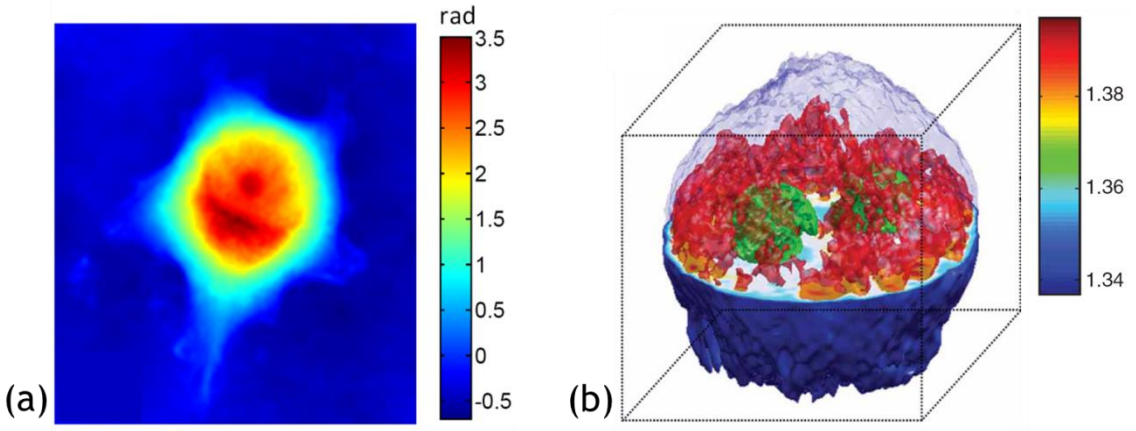

Figure 1.1. (a) 2D quantitative phase image of the total optical path delay through a breast cancer cell (MCF-7, Figure 7 in Ref. [7], copyright granted by the publisher). The unit is radians. (b) 3D refractive index image of a HeLa cell (Figure 2 in Ref. [8], copyright granted by the publisher). The unit is absolute refractive index.

QPI has been used in a wide variety of biological investigations [9-28]. For example, QPI has recently been applied to measure cell cycle-dependent growth patterns by exploiting the fact that phase images are proportional to dry mass density [9]. Likewise, QPI has been used to quantify intracellular mass transport [10], monitor the effects of ATP on red blood cell membrane dynamics [11], and measure chromosomal mass in living cells [12]. QPI has enabled the monitoring of cytoskeletal/organelle interactions on short timescales because of its ability to image these structures simultaneously [13], since it does not need multiple fluorescent labels. QPI has been used to record dynamically the morphology of red blood cells with nanoscale accuracy during a six-second period [24], measuring the cell volume variation and shape transformation with an acquisition time of 10.3 milliseconds per image. High-speed QPI method is also used to investigate contractile activity in individual cardiomyocytes [17].

In addition to biology, QPI is having an impact in the realm of clinical diagnostics [29-38], where it has recently manifested itself as a powerful tool for low-cost, high-

throughput, and high-sensitivity red blood cell screening [29]. Also in cancer diagnostics, QPI is being used to differentiate cancerous cells in isolation [30], to identify tissue self-affinity as a potential biomarker for precancers [31], to detect calcium oxalate as a breast cancer screening tool [32], and to correlate cancerous regions in prostate biopsies with high variance regions in the phase image [32].

Furthermore, QPI has many other applications in the areas outside of optical microscopy, such as semiconductor research, development, and manufacturing using electron microscopy [39-41], as well as X-ray radiology [42-53]. QPI could dramatically increase signal-to-noise ratio in soft tissue tomography [42]. Three-dimensional QPI methods have even been applied toward characterizing RI variations in commercial [54, 55] and developmental [56, 57] optical fibers.

Overall, it is clear that QPI has evolved and sustained enormous impact across a wide variety of disciplines. In the following section, an overview of state-of-the-art QPI methodologies is provided, and they are categorized according to their inherent properties and performance characteristics. From this overview, research directions will be proposed which addresses key issues facing QPI as a whole. The remainder of the thesis will focus on describing solutions to these key issues.

1.2 State-of-the-art Methods

1.2.1 2D QPI Methods

Two-dimensional QPI methods image the optical path thickness of a phase object integrated along the optical axis of the system. There are many state-of-the-art 2D QPI methods [5]. They can be divided into three broad categories: interference-based QPI, scanning-based QPI, and defocus-based QPI.

Interference-based QPI is the most widely used method in literature, and holography is the most important interferometry technique. In digital holography, an incident plane wave splits into two beams, a sample beam passing the object and a reference beam essentially unchanged. The two beams then recombine and create a hologram in the camera plane [5]. Conventional digital holographic microscopy (DHM) usually separates the two interfering beams by an angle, and use numerical Fresnel propagation to reconstruct the object phase from the hologram, so it is also called off-axis holography (OAH) [58-60]. Alternatively, a hologram can be taken when the two beams are collinear, but in this case, the reference arm has to be designed to allow phase shift, since a quantitative phase recovery requires four images with equal increments in the reference phase shifts. The phase image is obtained from the four holograms using trigonometric relationships. This technique is called phase-shifting holography (PSH) [61-63]. Phase shift can be achieved by a liquid crystal phase modulator [62], piezoelectric transducer [63], or an acousto-optic modulator [64]. OAH is fast, and the speed is only limited by the camera readout speed, since the phase can be retrieved by a single hologram, but the spatial resolution is limited by the angle between the beams. On

the other hand, PSH can achieve diffraction-limited spatial resolution, but it is slower since four phase-shifted images are required for a phase reconstruction. In addition, both of them require laser as the coherent light source, which causes coherent noise such as ringing artifact and speckle defect [65]. Some new designs have been created to overcome the shortcomings. Some of them use common path geometries, which improves spatial stability, or polychromatic light illumination, which improves temporal stability [5]. Hilbert phase microscopy (HPM) [66] uses a similar configuration as OAH, but the hologram is captured at the focal plane, so Hilbert transform is used to recover the phase instead of numerical Fresnel propagation, and the diffraction-limited spatial resolution can be achieved. Optical quadrature microscopy (OQM) [67] uses a similar concept as PSH, but the four phase-shifted images are taken simultaneously by making use of the polarization states and polarizing beam splitters, so the measurement speed can be as fast as OAH. White light diffraction phase microscopy (wDPM) [60] is another variant of OAH. It generates two beams by a diffraction grating and spatially filters the zeroth order beam by a pinhole, so the zeroth order beam acts as the reference beam, and the first order beam acts as the sample beam. It enables common-path configuration and the use of polychromatic light, which enhance spatial and temporal stabilities [5]. However, all of the above methods require phase unwrapping [68].

In addition to holography, there are other interference-based QPI methods. Spatial light interference microscopy (SLIM) [62] is a quantitative version of PCM. It incorporates phase shifting in the reference beam by a liquid crystal phase modulator, and four phase-shifted interferograms are combined to produce a quantitative phase of the object, similar to PSH. It is a common-path configuration compatible with polychromatic

light. Differential interference contrast microscopy (DICM) [69] is a quantitative version of DIC. It also uses four phase-shifted interferograms to reconstruct the phase gradient quantitatively. The phase gradients along two orthogonal directions are measured separately by rotating the shear. Then the phase is calculated by numerical integration or Fourier-space integration of the phase gradients along two orthogonal directions. Quadri-wave lateral shearing interferometry (QWLSI) [70] is another method similar to DIC. It used a specific 2D diffraction grating, modified Hartmann mask, instead of a birefringent prism to extract the phase gradients along two orthogonal directions simultaneously. It enables the phase recovery from a single interferogram, and polychromatic can be used.

The major scanning-based QPI technique is ptychography. A coherent illuminating beam called probe is moved respect to the specimen, which creates a sequential array of overlapping illuminated areas [71]. Then the phase of the object is recovered by an iterative phase retrieval algorithm, such as extended ptychographic iterative engine (ePIE) supplied by Phase Focus Ltd. A similar technique is Fourier ptychographic microscopy (FPM) [72]. In FPM, the illumination angle is changed by using, for example, an LED array, so the scan is in the spatial frequency domain. It is a combination of phase retrieval and synthetic aperture microscopy. Scanning-based QPI techniques are slow in both measurement and computation, but they can support high resolution, wide field-of-view, and deep depth-of-focus. In addition, the hardware can be easily modified from standard microscopes and these methods can be used in conjunction with fluorescence microscopy, so the cost of extra hardware is low.

The third 2D QPI category is based on defocus. It scans the image plane of the optical system, so that both the in-focus and some defocused (out-of-focus) images are

captured, and then used to reconstruct the object phase. Experimentally, defocus can be controlled by either moving the sample, the objective, or the camera (CCD) along the optical axis of the optical system. One reconstruction method is based on iterative algorithms, such as iterative wave function reconstruction (IWFR) [73]. It iteratively searches the object phase that can provide the defocused intensities as close to the measured intensities as possible. The iterative nature makes IWFR computationally expensive and not suitable for real-time imaging. More widely used methods are deterministic methods based on linearizing the relation between the object phase and the defocused images. Transport-of-intensity equation (TIE) [74] is a popular linearizing method, which gives the relation between the phase gradient and the longitudinal intensity derivative. The phase gradient is often estimated by a finite difference of two near-focal intensity images. If the object is weakly absorptive, TIE can be simplified and easily Fourier transformed, so the phase can be determined by deconvolution. Contrast transfer function (CTF) [75] is another useful linearizing method, which gives the relation between the phase and the intensity difference of symmetrically defocused images. The phase is also reconstructed by deconvolution [76]. Most of the defocus-based QPI methods are compatible with conventional microscopes. Since a laser is not required, these methods do not suffer from coherent noise. TIE is suitable for weak defocus conditions [77], while CTF works well for objects with weak absorption and slowly varying phase [75]. TIE and CTF can also be combined to retain the advantage of each method [78]. However, linearization usually requires some simplifying object assumption, such as weak absorption and small phase. Furthermore, if only one pair of defocused images is used in TIE or CTF, small defocus distance suffers from noise, while

large defocus distance cannot provide high resolution. Therefore, new methods are developed by combining multiple defocused images. They set up some filters to select the optimal defocus distance for a range of spatial frequency [79]. The TIE and CTF methods are inherently common-path, and they can also be generalized to partial coherent illumination. TIE is already compatible with partially coherent illumination [80, 81], while CTF requires new transfer functions accounting for the effect of partial coherence. Our laboratory has developed a 2D QPI method called multifilter phase imaging with partially coherent light (MFPI-PC) [82], which is based on TIE with multiple defocused planes and partially coherent illumination. Our laboratory has developed another 2D QPI method called phase optical transfer function recovery (POTFR) [83], which is based on CTF with multiple defocused planes and partially coherent illumination. Table 1.1 summarizes some state-of-the-art 2D QPI methods in the literature.

Table 1.1. Characteristic summary of some existing 2D QPI methods. ☑'s indicate presence of desired traits, ☒'s indicate absence of desired traits, and ☐'s indicate a trade-off between desired traits.

2D QPI Method	Published Configuration	Single-shot	High Resolution	Low Noise	Common-Path	No Laser	Existing Microscope	No iteration
Interference	OA-DHM [58]	☑	☒	☑	☒	☒	☒	☑
	HPM [66]	☑	☑	☑	☒	☒	☒	☑
	wDPM [60]	☑	☒	☑	☑	☑	☒	☑
	PS-DHM [63]	☒	☑	☑	☒	☒	☒	☑
	OQM [67]	☑	☑	☑	☒	☒	☒	☑
	SLIM [62]	☒	☑	☑	☑	☑	☒	☑
	DICM [69]	☒	☑	☑	☑	☒	☒	☑
	QWLSI [70]	☑	☑	☑	☑	☑	☒	☑
Ptychography	Ptychog. [71]	☒	☑	☑	☑	☒	☑	☒
	FPM [72]	☒	☑	☑	☑	☒	☑	☒
Defocus	IWFR [73]	☒	☑	☑	☑	☒	☑	☒
	TIE [74]	☒	☐	☐	☑	☑	☑	☑
	WOTF [76]	☒	☐	☐	☑	☑	☑	☑
	OFS [79]	☒	☑	☑	☑	☑	☒	☑
	TIE-CTF [78]	☒	☑	☑	☑	☑	☒	☑
	MFPI-PC [82]	☒	☑	☑	☑	☑	☑	☑
	POTFR [83]	☒	☑	☑	☑	☑	☑	☑

1.2.2 3D QPI Methods

3D QPI includes methods which resolve RI information in both lateral and axial dimensions [20]. In addition to 3D QPI, it is also called variously optical diffraction tomography, quantitative phase tomography, or tomographic phase microscopy [84].

A conventional realization of 3D QPI is based on optical tomography [85]. First, a 2D QPI method is used to measure the phase of the object, which is proportional to the RI integrated along the light propagation direction. For a thick object, the phase is different at various directions, so either the object or the illumination beam should be rotated, and

the phase is measured at different angles. After that, filtered backprojection based on the Fourier slice theorem [8, 86] or filtered backpropagation based on the Fourier diffraction theorem [87] is used to reconstruct the RI of the object from the phase information. Projection tomography (PT) based on filtered backprojection is simpler and faster than diffraction tomography (DT) based on filtered backpropagation. On the other hand, DT is usually more accurate than projection tomography, because filtered backprojection does not account for the diffraction effect, which is usually not negligible at optical wavelength. Nevertheless, DT also requires some simplifying object assumptions, such as weak absorption and small RI contrast. Essentially any 2D QPI method can be used in optical tomography, but holography is the most popular one. OAH [86, 87] and PSH [8, 64] are widely used in 3D QPI. Other 2D QPI methods are also applicable, such as TIE [88]. Some advanced methods are continuously being developed, such as structured illumination microscopy (SI-DPM) [89], which is a common-path off-axis interferometer whose source is formed and rotated by a spatial light modulator (SLM). Tomography requires rotation of either the object or the illumination beam. Object rotation is usually achieved by mechanical rotation stage, while beam rotation can be achieved by mechanical mirror scanning [64] including microelectromechanical systems (MEMS), sequential LED array [90], or SLM [89], so beam rotation can be much faster than object rotation. In addition, object rotating is prone to alignment error, but the resulting spatial resolution is isotropic. If the illuminating beam is rotated, usually it cannot cover the entire range of angles, because the available illumination angle is limited by the numerical aperture (NA) of the system. Therefore, some frequency information is missing, which is often called the “missing cone” problem [91]. This problem makes

isotropic resolution difficult to obtain when beam rotation is used. The “missing cone” problem can be solved somehow by iterative regularization algorithms and *a priori* knowledge of object domain constraints [92], such as edge-preserving [93, 94] or total variation algorithms [95, 96], but at the cost of increased computational complexity. Reflection-mode measurements can fill the missing cone region, but the reflected light is usually very weak and is very difficult to observe [84]. Scanning color optical tomography (SCOT) [97] is a different tomographic method, in which the wavelength of the illumination beam, rather than the angle of the beam or of the object, is scanned by an acousto-optic tunable filter, so no rotation is needed, but the “missing cone” problem also exists. Notably, a drawback in all these holographic optical tomography methods is that they require stand-alone optical systems, so the cost to the potential user is high. In addition, since coherent light is required, coherent noise may degrade the resulting images [98].

Another category of 3D QPI is based on through-focal scanning. Instead of rotation, multiple 2D images are captured by moving the focal plane through the object along the optical axis of the system, so the system is similar to defocus-based 2D QPI methods. Taken together, the multiple 2D images enable a 3D image of the object to be formed. This is accomplished by the optical sectioning capability of incoherent light, so no coherent light is used. Moreover, similar to defocus-based 2D QPI methods, 3D QPI methods based on through-focal scanning are inherently common-path, and they can also be generalized to partial coherent illumination. Three-dimensional deconvolution is usually used to reconstruct the RI from the 3D intensity image. Through-focal scanning can be done by a mechanical rotation stage, electrically tunable lens [7], or a piezo-

electric transducer [99]. Example through-focal scanning methods include white-light diffraction tomography (WDT) [100] and deconvolved spatially incoherent illumination quantitative phase microscopy (SII-QPM) [101]. Through-focal scanning can be implemented on a conventional microscope, which means its cost is relatively low. However, without rotation, the measured 3D RI distribution is not isotropic and it leads to the "missing cone" problem. Recently, new methods combining axial scanning and object rotation have been developed to obtain the advantages of both approaches, such as multifocus tomography (MFT) [102]. Our laboratory has developed a combination method, tomographic deconvolution phase microscopy (TDPM) [99]. However, these methods are very slow due to the extremely large amount of data that needs to be collected. Table 1.2 summarizes some state-of-the-art 3D QPI methods in the literature.

Table 1.2. Characteristic summary of some existing 3D QPI methods. ☑'s indicate presence of a desired trait and ☒'s indicate absence of a desired trait.

3D QPI Method	Published Configuration	Pointwise Resolution	High Resolution	No Laser	Microscopy Compatible	Few Rotations	No iteration
Tomography	TPM [8]	☑	☒	☒	☒	☒	☑
	PT-OAH [86]	☑	☒	☒	☒	☒	☑
	DT-PSH [64]	☑	☑	☒	☒	☒	☒
	DT-OAH [87]	☑	☑	☒	☒	☒	☑
	SI-DPM [89]	☑	☑	☒	☒	☑	☒
	SCOT [97]	☑	☑	☒	☒	☑	☒
	QPM [88]	☑	☑	☑	☑	☒	☑
Through-focal Scanning	WDT [100]	☒	☑	☑	☑	☑	☒
	SII-QPM [101]	☒	☑	☑	☑	☑	☑
Combination	MFT [102]	☑	☑	☒	☒	☒	☑
	TDPM [99]	☑	☑	☑	☑	☒	☑

1.3 Thesis Overview

Until now, the majority of QPI methods have been developed using an integrated approach, in which equipment and algorithm innovations are examined simultaneously. This approach has resulted in a number of commercial QPI products from companies such as Phase Holographic Imaging, Lyncée Tec, Ovizio Imaging Systems, 4Deep, Phi Optics, Phasics, and Phase Focus Limited. However, the integrated approach commonly results in expensive custom hardware systems, so it is not cost-efficient to the primary end-users of QPI, namely microscopists in biology and biomedicine. Therefore, QPI methods based on commercial microscope platforms are more welcome. The resulting methods will then be implemented as computer algorithms, so the cost is generally much lower than custom hardware.

It is a popular notion that coherent illumination is required for phase recovery. Recent work, however, indicates that it is not only possible but in many cases desirable to recover sample phase information using partially coherent illumination, especially partial spatial coherence [81, 82, 103, 104]. Partial coherence effectively enlarges the NA of the microscope, so it results in higher resolution since the resolvable size is inversely proportional to the NA. In addition, coherent noise such as speckle and ringing effects can be largely eliminated, so phase stability is improved. Meanwhile, the cost is also reduced, because no laser is required and the original light source of a commercial microscope can be used. Therefore, partially coherent light source is used in the QPI development in our laboratory. Furthermore, large apertures are usually incorporated in a microscope in order for high spatial resolution, which indicates that the paraxial approximation is not valid. Thus, the nonparaxial property has to be treated for accurate phase imaging [105-107].

The Optics Laboratory has developed several QPI methods, including MFPI-PC [82], POTFR [83], and TDPM [99]. They are all based on a standard commercial microscope, so the extra hardware cost is low if the user already has a microscope, which is typical for a biological laboratory. They all use partially coherent illumination. They have other advantages that are not simultaneously achieved by other QPI methods in the literature. Nevertheless, these methods have some shortcomings. MFPI-PC is developed under paraxial approximation, so it is not very accurate in high NA systems. TDPM requires a large number of images, so the measurement speed is slow. In all of them, the shape of the condenser aperture is limited to a disk. Furthermore, these methods cannot be applied directly in some specific applications, such as fiber Bragg grating (FBG) characterization.

The object of my doctoral research is to develop and generalize QPI methods to enable their more widespread use as well as applications of QPI to new classes of objects. Chapter 2 gives a brief introduction of some important background knowledge and an overview of existing QPI methods developed by the Optics Laboratory. In Chapter 3, a linear partially coherent 3D imaging theory is generalized to the nonparaxial condition, and the 3D phase optical transfer function (POTF) is first derived in an integral form and then analytical integrated. This theory enables MFPI-PC to be generalized to the nonparaxial condition without increasing computational load, which is shown in Chapter 4. Chapter 5 is about another method modified from MFPI-PC, and it is particularly suitable for annular illumination. Chapter 6 summarizes the improvements to the original MFPI-PC and POTFR and compares the improved methods using simulations. In Chapter 7, an iterative regularization algorithm is developed for TDPM, so that the RI can be

reconstructed with high accuracy and with fewer tomography angles, which enables faster measurements. Chapter 8 proposed a procedure to characterize FBGs using 3D QPI, which necessitate significant digital imaging processing algorithms. After a summary of my research outcomes in Chapter 9, some potential future work is proposed in Chapter 10.

CHAPTER 2. BACKGROUND

The main purpose of this chapter is to briefly introduce some QPI methods that were developed in the Optics Laboratory before I came. They are multifilter phase imaging with partially coherent light (MFPI-PC), phase optical transfer function recovery (POTFR), and tomographic deconvolution phase microscopy (TDPM). My developed QPI methods are based on these methods, so it is important to introduce them before presenting my research outcomes. In addition, 3D image formation is very important in all of the QPI methods discussed in this thesis, so a brief overview is presented in the first section of this chapter.

2.1 3D Image Formation Overview

All the QPI methods developed in our laboratory are based on 3D diffraction of partially coherent light. The object is normally represented by a refractive index (RI) distribution $n(\boldsymbol{r})$, but scattering potential (SP)

$$v(\boldsymbol{r}) \triangleq k_0^2[n(\boldsymbol{r})^2 - n_0^2] \tag{2.1}$$

is often used instead of RI in 3D diffraction theory for the ease of linearization. In this equation, $\boldsymbol{r} = (\boldsymbol{x}, z)$ is the 3D spatial coordinate, $k_0 = 2\pi/\lambda$ is the freespace wavevector magnitude, n is the RI of the object, and n_0 is the background RI. For easier discussion, the object is assumed to be immersed in the air by default, so $n_0 = 1$. Nevertheless, the discussion is easily generalized to the condition where $n_0 \neq 1$. One example generalization method is to replace the wavelength λ with the effective wavelength λ/n_0

and to replace the refractive index n with the normalized refractive index n/n_0. For a general object, the SP is a complex quantity and can be expressed as

$$v(\boldsymbol{r}) = v_P(\boldsymbol{r}) + iv_A(\boldsymbol{r}). \tag{2.2}$$

The real part is often called the phase part and is related to the real part of RI. The imaginary part is often called the absorption part and is related to absorption.

In order to linearize the problem fully, the object needs to satisfy the weak absorption property and the first Born approximation [108]. The first Born approximation requires that the object RI be very close to the background RI, *i.e.* $|n - n_0| \ll 1$. When these two requirements are satisfied, the optical system performs as a linear, spatially invariant system, so the 3D intensity distribution $I(\boldsymbol{r})$ can be expressed as a convolution of the SP with the system point-spread functions (PSFs) [108]

$$I(\boldsymbol{r}) = B + h(\boldsymbol{r}) * v_P(\boldsymbol{r}) + h_A(\boldsymbol{r}) * v_A(\boldsymbol{r}), \tag{2.3}$$

where $h(\boldsymbol{r})$ and $h_A(\boldsymbol{r})$ are PSFs for the phase part and absorption part, B is the uniform background intensity, and "*" denoted convolution [108]. Using Fourier transform, Eq. (2.3) can be equivalently described by multiplications with optical transfer functions (OTFs) in the spatial frequency domain as

$$\tilde{I}(\boldsymbol{f}) = B\delta(\boldsymbol{f}) + H(\boldsymbol{f})V_P(\boldsymbol{f}) + H_A(\boldsymbol{f})V_A(\boldsymbol{f}), \tag{2.4}$$

where $\delta(\cdot)$ is the Dirac delta function, $\boldsymbol{f}$ is the 3D spatial frequency, and $\tilde{I}(\boldsymbol{f})$, $H(\boldsymbol{f})$, $H_A(\boldsymbol{f})$, $V_P(\boldsymbol{f})$, and $V_A(\boldsymbol{f})$ are the 3D Fourier transforms of $I(\boldsymbol{r})$, $h(\boldsymbol{r})$, $h_A(\boldsymbol{r})$, $v_P(\boldsymbol{r})$, and

$v_A(\boldsymbol{r})$. The quantities $H(\boldsymbol{f})$ and $H_A(\boldsymbol{f})$ are OTFs for the phase part and absorption part, also called phase optical transfer function (POTF) and absorption optical transfer function (AOTF), respectively.

Usually, the uniform background is not of interest and can be easily removed by subtracting average intensity, so it will be ignored in the following discussions by default. In practice, many objects are essentially phase-only with negligible absorption and so $v_A = 0$ is a very good approximation. In this case, both RI and SP are real quantities, and Eqs. (2.3) and (2.4) can be simplified as

$$I(\boldsymbol{r}) = h(\boldsymbol{r}) * v(\boldsymbol{r}), \tag{2.5}$$

$$\tilde{I}(\boldsymbol{f}) = H(\boldsymbol{f})V(\boldsymbol{f}), \tag{2.6}$$

where the subscript P is dropped because $v(\boldsymbol{r}) = v_P(\boldsymbol{r})$ and $V(\boldsymbol{f}) = V_P(\boldsymbol{f})$.

2.2 Multifilter Phase Imaging With Partially Coherent Light (MFPI-PC)

Multifilter phase imaging with partially coherent light (MFPI-PC) is a deterministic propagation-based 2D QPI method, developed by Jenkins *et al.* [82]. MFPI-PC can be directly implemented on a modern microscope without hardware modification. This method was inspired by the transport-of-intensity equation (TIE), but it also incorporates the concept of the transfer function in the image recovery process.

TIE describes the relation between the longitudinal derivative of the intensity I and the phase ϕ. It is expressed as Eq. (1) in Ref. [82], which is rewritten here,

$$\partial_z I(\boldsymbol{x}, z) = -(\lambda/2\pi)\nabla_\perp \cdot [I(\boldsymbol{x}, z)\nabla_\perp \phi(\boldsymbol{x}, z)], \tag{2.7}$$

where λ is the wavelength, $\boldsymbol{x}$ and z are lateral and longitudinal spatial coordinates, and ∂_z means longitudinal derivative. When the object is transparent, the intensity is approximately constant in the focal plane, and thus, TIE can be simplified. Using Fourier transform, the simplified TIE can be expressed using a transfer function,

$$\partial_z I(\boldsymbol{\rho}) = T(\boldsymbol{\rho})\Phi(\boldsymbol{\rho}), \tag{2.8}$$

where $\boldsymbol{\rho}$ is the lateral spatial frequency, and $\Phi(\boldsymbol{\rho})$ is the spatial spectrum of the phase. The TIE transfer function is expressed as Eq. (7b) in Ref. [82], which is rewritten here,

$$T_{\mathrm{TIE}}(\boldsymbol{\rho}) = 2\pi\lambda B\rho^2, \tag{2.9}$$

In MFPI-PC, multiple pairs of symmetrically defocused images are captured and combined to estimate the in-focus intensity derivative using Savitzky–Golay differentiation filters (SGDF) via Eq. (4) in Ref. [82], which is rewritten here,

$$\partial_z I(\boldsymbol{x}, 0) = \sum_{i=-n}^{n} a_i^{(k)} I_{i\Delta z}(\boldsymbol{x}), \tag{2.10}$$

where $a_i^{(k)}$ are the coefficients (impulse response) of (2k-1)th order SGDF, Δz is the distance between neighboring defocus planes, n is the number of symmetrically defocused image pairs, and $I_{i\Delta z}(\boldsymbol{x})$ is the intensity at plane $z = i\Delta z$. Intensity derivatives estimated from different SGDF orders are slightly different, so strictly speaking, the phase contrast transfer function (PCTF) $T(\boldsymbol{\rho})$ is Eq. (2.8) should be correspondingly

different. The PCTF for the (2k-1)th order SGDF, $T_k(\rho)$, is calculated as Eq. (5b) in Ref. [82], which is rewritten here,

$$T_k(\rho) = \frac{4\pi}{\lambda \Delta z} \int H_{SG,k}\left(e^{2\pi i \eta \Delta z}\right) H(\rho, \eta) \mathrm{d}\eta, \tag{2.11}$$

where η is the longitudinal spatial frequency, ρ is the magnitude of $\boldsymbol{\rho}$, $H_{SG,k}\left(e^{2\pi i \eta}\right)$ is the transfer function of the (2k-1)th order SGDF, and $H(\rho, \eta)$ is the 3D POTF discussed in the previous section. This formula shows that the PCTF is a 1D integral of the 3D POTF.

The phase is recovered by inversely filtering the intensity derivative by the PCTF. In transfer function inversion, the PCTF can be approximated by the weakly defocused PCTF (WD-PCTF), as shown by Eq. (6) in Ref. [82] and is rewritten here,

$$T_W(\rho) = \frac{4\pi}{\lambda} \int 2\pi i \eta H(\rho, \eta) \mathrm{d}\eta. \tag{2.12}$$

Analytical derivation shows that the WD-PCTF $T_W(\rho)$ equals the TIE-PCTF $T_{TIE}(\rho)$ for $\rho < (\mathrm{NA_o} - \mathrm{NA_c})/\lambda$ under paraxial approximation.

Different orders of SGDFs can be applied in phase recovery, and they have their advantages and disadvantages. Low-order PCTFs are better at denoising, while high-order PCTFs can retain more spatial frequencies. Therefore, it is better to use a low-order SGDF to recover low spatial frequency information and use a high-order SGDF to recover high spatial frequency information. In MFPI-PC, a series of binary filters $\xi^{(k)}(\rho)$ are used to select the optimal SGDF order for each spatial frequency. Using the phase transfer function (PTF) defined as

$$\mathrm{PTF_k}(\rho) = T_k(\rho)/T_W(\rho), \tag{2.13}$$

the SGDF order chosen for μ is the lowest order that has a $\mathrm{PTF_k}(\rho)$ larger than a threshold $1-\epsilon$. Ref. [82] chose $\epsilon = 0.01$. Mathematically, define intermediate filters

$$\xi_0^{(k)}(\rho) = \begin{cases} 1, & \text{if } \mathrm{PTF_k}(\rho) > 1-\epsilon \\ 0, & \text{if } \mathrm{PTF_k}(\rho) < 1-\epsilon' \end{cases} \tag{2.14}$$

and then the binary filters $\xi^{(k)}(\rho)$ are defined as

$$\xi^{(1)}(\rho) = \xi_0^{(1)}(\rho), \tag{2.15}$$

$$\xi^{(k+1)}(\rho) = \xi_0^{(k+1)}(\rho) - \xi_0^{(k)}(\rho) \quad (\text{for } 1 < k < m), \tag{2.16}$$

$$\xi^{(m)}(\rho) = 1 - \xi_0^{(m-1)}(\rho). \tag{2.17}$$

where m is the maximum selected SGDF order.

However, although PCTFs for various SGDF orders are calculated to determine the PTFs, the actual transfer function inversion in MFPI-PC is still based on the TIE-PCTF. A complete flow chart of the MFPI-PC method can be found in Figure 1 in Ref. [82].

Despite its success, MFPI-PC has some disadvantages:

a. It uses the paraxial approximation. In fact, it uses TIE, which is only applicable to paraxial situations.

b. The error for TIE-PCTF is too large for $\rho > \mathrm{NA_o} - \mathrm{NA_c}$, so the maximum recoverable spatial frequency is $(\mathrm{NA_o} - \mathrm{NA_c})/\lambda$, which is small and decreases with increased $\mathrm{NA_c}$.

c. It uses a set of binary filters to choose the optimal SGDF order. However, another set of filters with smooth transition may increase the accuracy.

d. It requires uniform defocus plane separation.

e. It requires a purely transparent object.

In this thesis, I will improve MFPI-PC by overcoming these disadvantages.

2.3 Phase Optical Transfer Function Recovery (POTFR)

Phase optical transfer function recovery (POTFR) is another deterministic propagation-based 2D QPI method, developed by Jenkins and Gaylord [83]. Similar to MFPI-PC, POTFR can also be directly implemented on a modern microscope without hardware modification. Different from MFPI-PC, the intensity difference between symmetrically defocused images are calculated instead of the intensity derivative, which is related to the object by transfer functions. The object can be described by planar transmittance function or a screen function

$$t(\boldsymbol{x}) = \exp[i\phi(\boldsymbol{x}) - a(\boldsymbol{x})], \tag{2.18}$$

where $\phi(\boldsymbol{x})$ represents the phase retardation and $a(\boldsymbol{x})$ represents the absorption. Assuming the absorption is weak and the phase is small, the relation between resulting defocused intensity and the object functions can be linearized using Tylor expansion. It can be shown that the defocused intensity at the defocus distance z can be expressed by

$$I_z(\boldsymbol{x}) = B + h_z(\boldsymbol{x}) * \phi(\boldsymbol{x}) + h_{A,z}(\boldsymbol{x}) * a(\boldsymbol{x}), \tag{2.19}$$

where $h_z(\boldsymbol{r})$ and $h_{A,z}(\boldsymbol{r})$ are 2D PSFs for the phase part and absorption part at plane z, and B is the uniform background intensity. Similar to the 3D case, using Fourier transform, this equation can be equivalently described by multiplications with optical transfer functions (OTFs) in the spatial frequency domain as

$$\tilde{I}_z(\boldsymbol{\rho}) = B\delta(\boldsymbol{\rho}) + H_z(\boldsymbol{\rho})\Phi(\boldsymbol{\rho}) + H_{A,z}(\boldsymbol{\rho})A(\boldsymbol{\rho}), \tag{2.20}$$

where $\tilde{I}_z(\boldsymbol{\rho})$, $H_z(\boldsymbol{\rho})$, $H_{A,z}(\boldsymbol{\rho})$, $\Phi(\boldsymbol{\rho})$, and $A(\boldsymbol{\rho})$ are the 2D Fourier transforms of $I_z(\boldsymbol{x})$, $h_z(\boldsymbol{x})$, $h_{A,z}(\boldsymbol{x})$, $\phi(\boldsymbol{x})$, and $a(\boldsymbol{x})$. The quantities $H_z(\boldsymbol{\rho})$ and $H_{A,z}(\boldsymbol{\rho})$ are OTFs for the phase part and absorption part, also called phase optical transfer function (POTF) and absorption optical transfer function (AOTF), respectively. In order to distinguish the 3D and 2D OTFs, the dimension is often spelled out, but this thesis uses the 3D POTF much more often than the 2D POTF.

It can be shown that the 2D AOTF is an even function of z, and the 2D POTF is an odd function of z, which is similar to the 3D case. Therefore, by subtracting intensities from symmetrically defocused planes, the background and the absorption terms can be canceled out, leaving only the phase term. The result is

$$\Delta\tilde{I}_z(\boldsymbol{\rho}) = \tilde{I}_z(\boldsymbol{\rho}) - \tilde{I}_{-z}(\boldsymbol{\rho}) = 2H_z(\boldsymbol{\rho})\Phi(\boldsymbol{\rho}). \tag{2.21}$$

Therefore, as long as the POTF $H_z(\boldsymbol{\rho})$ is known, after the intensity difference $\Delta\tilde{I}_z(\boldsymbol{\rho})$ is determined, the object phase can be calculated by transfer function inversion, $\Phi(\boldsymbol{\rho}) =$

$\Delta\tilde{I}_z(\boldsymbol{\rho})/2H_z(\boldsymbol{\rho})$. However, choosing the optimal defocus distance z is a problem. In fact, there is a tradeoff. Small defocus distance retains more high spatial frequencies, but large defocus distance is more robust under noise. Therefore, the best option is to combine results from multiple defocus distances and retain their advantages. POTFR uses a least-squares filter,

$$\xi_z(\rho) = \frac{|H_z(\rho)|^2}{\sum_z |H_z(\rho)|^2 + \alpha}, \tag{2.22}$$

where α is a regularization parameter, so that the final phase $\Phi(\boldsymbol{\rho})$ is the weighted combination of the phases recovered from different defocus distances $\Phi_z(\boldsymbol{\rho})$ as

$$\Phi(\boldsymbol{\rho}) = \sum_z \xi_z(\rho)\Phi_z(\boldsymbol{\rho}). \tag{2.23}$$

The 2D POTF was derived in Ref. [83] in a form of 2D integration, which is slow to calculate. In this thesis, a semi-analytical form of the 2D POTF is derived, which takes only a 1D integral and is much faster to calculate.

2.4 Tomographic Deconvolution Phase Microscopy (TDPM)

Tomographic deconvolution phase microscopy (TDPM) is a 3D QPI method developed by Jenkins and Gaylord [99]. By exploiting the optical sectioning capability of partially spatially coherent light, this method measures a through-focal series of images, which, taken together, enables the formation of a 3D image of the object. The relation between the 3D intensity image and the SP of the object is represented by the 3D POTF,

as represented by Eqs. (2.5) and (2.6). Therefore, the object SP can be easily estimated using 3D deconvolution by

$$v(\boldsymbol{f}) = \tilde{I}(\boldsymbol{f})/H(\boldsymbol{f}). \tag{2.24}$$

However, the measurement from a single angle suffers from significant missing cone problem, which will be discussed in more detail in Chapter 7. In order to solve the missing cone problem, the object is rotated over 15 angles, and the measurement and calculation are repeated at each angle. All the estimated SPs are rotated back to the same orientation, and they are combined using a filter derived from least-squares fitting to give the final SP, which is then converted to the RI of the object. The actual image processing procedure is slightly different from the description above to make the result more stable, but the spirit is the same. A complete flow chart can be found in Figure 4 in Ref. [99].

TDPM has many advantages. It can be implemented on a commercial microscope platform, which significantly reduces the extra cost to the user. It does not require laser or coherent illumination, which means that it does not suffer from coherent noise such as speckle artifact. However, the measurement time is usually long due to the total number of measured images being very large. In this thesis, I will present an iterative optimization algorithm to reduce the number of angles while maintain high accuracy.

2.5 Experimental Configuration

The experimental configuration used in this thesis is shown in Figure 2.1. It is based on a commercial bright-field microscope with slight hardware modifications. The major advantage of using a commercial microscope is the cost to users. The most

important application of QPI is biomedical imaging, and most biological and biomedical laboratories are already equipped with microscopes. Making QPI methods compatible with their existing microscopes can greatly decrease their hardware cost. Only a piezoelectric scanner and a stepping motor are add-on modules used specifically for QPI. A mercury arc lamp rather than a laser is used as the light source, which not only decreases the cost but also eliminates coherent noise caused by lasers.

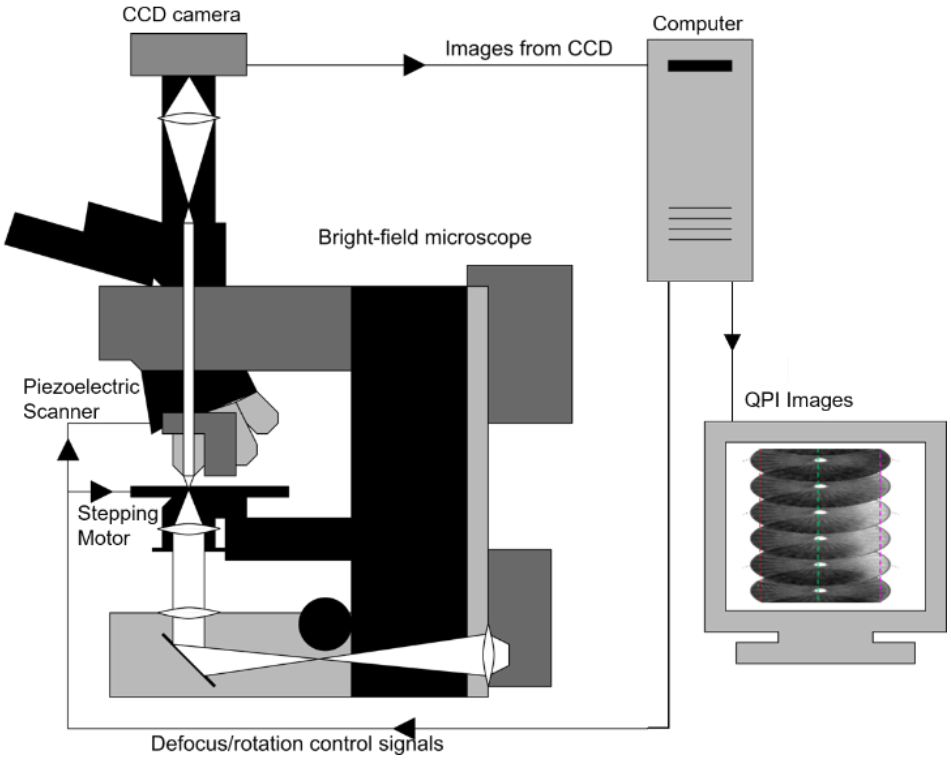

Figure 2.1. The experimental configuration used in this thesis. It includes a bright-field microscope, a CCD camera, a computer, a piezoelectric microscope objective scanner, and a stepping motor to rotate the fiber.

The bright-field microscope utilized in this thesis is an Olympus BX60. The objective lens is a UPlanFl 40×/0.75 objective, so its magnification is 40, and its numerical aperture is 0.75. The camera used was an QImaging Retiga 1300R. The pixel size is 9.8 μm, so after demagnification, the effective resolution of the camera is 245 nm.

The illumination is provided by the green spectral line of a mercury arc lamp filtered with a green interference filter. The central wavelength of the filtered light is 546 nm. The full width at half maxima (FWHM) bandwidth is about 10 nm. The illumination pattern is controlled by a condenser lens. Usually, the measurement in this thesis uses disk illumination, which is produced by a disk condenser with a variable aperture (Olympus U-POC-2). The microscope is configured in the way that Köhler illumination is satisfied. A piezoelectric microscope objective scanner (Physik Instrumente P-721.SL2) is used to shift the objective lens along the optical axis of the microscope. Since the microscope is an infinity-corrected microscope, shifting the objective lens is equivalent to shifting the object, which is a way of defocus. In some other modern microscopes, the focus control is an intrinsic capability of the microscope, so if that kind of microscope is used, the piezoelectric scanner is not needed. In 3D QPI, a stepping motor (Newport Universal Motion Controller ESP 300) is used to rotate the object about an axis perpendicular to the optical axis of the microscope. The defocus and rotation are both automatically controlled by a LabVIEW program. The intensity images measured by the camera are then processed by a MATLAB program containing the QPI algorithm to provide the phase or the RI of the object.

CHAPTER 3. ANALYTICAL NONPARAXIAL 3D PHASE OPTICAL TRANSFER FUNCTION

As mentioned in Chapter 2, All the QPI methods developed in our laboratory are based on 3D diffraction of partially coherent light. The 3D image is formed by the multiplication of the 3D POTF and the SP in the spatial frequency domain. Therefore, determining the 3D POTF is fundamental to our work. In 1985, Streibl *et al.* derived the 3D POTF using the paraxial approximation [108]. However, the paraxial approximation is not very accurate for optical systems with large numerical apertures (NAs). In this chapter, the nonparaxial version of the 3D POTF is derived based on Streibl's original work. This work has been published in Ref. [109].

3.1 Paraxial Partially Coherent 3D POTF

In Ref. [108], the paraxial partially coherent POTF is derived by solving the Helmholtz equation using the Green's function method. The Green's function is a spherical wave and is the often used as the basis of the solutions of the Helmholtz equation. Its angular spectrum representation is Eq. (16) in Ref. [108] and is repeated here

$$\tilde{G}(\boldsymbol{\rho}, z) = \frac{1}{4\pi i\sqrt{\lambda^{-2} - \boldsymbol{\rho}^2}} \exp\left(2\pi i|z|\sqrt{\lambda^{-2} - \boldsymbol{\rho}^2}\right). \tag{3.1}$$

The mutual-intensity function is used to describe a quasi-monochromatic partially coherent field. The van Cittert-Zernike theorem, the propagation laws for the mutual

intensity, and weak object approximation are used in the derivation. After mathematical calculations, the spatial spectrum of the mutual intensity is Eq. (19) in Ref. [108] and is repeated here

$$\begin{aligned}\tilde{J}_{OBJ}(\boldsymbol{\rho}_1;\boldsymbol{\rho}_2) &= \tilde{S}(\boldsymbol{\rho}_1)\delta(\boldsymbol{\rho}_1-\boldsymbol{\rho}_2)\\ &+\frac{\tilde{S}(\boldsymbol{\rho}_2)}{4\pi i\sqrt{\lambda^{-2}-\boldsymbol{\rho}_1^2}}V\left(\boldsymbol{\rho}_1-\boldsymbol{\rho}_2,\sqrt{\lambda^{-2}-\boldsymbol{\rho}_1^2}-\sqrt{\lambda^{-2}-\boldsymbol{\rho}_2^2}\right)\\ &-\frac{\tilde{S}(\boldsymbol{\rho}_1)}{4\pi i\sqrt{\lambda^{-2}-\boldsymbol{\rho}_2^2}}V^*\left(\boldsymbol{\rho}_2-\boldsymbol{\rho}_1,\sqrt{\lambda^{-2}-\boldsymbol{\rho}_2^2}-\sqrt{\lambda^{-2}-\boldsymbol{\rho}_1^2}\right),\end{aligned} \tag{3.2}$$

where $\tilde{S}(\boldsymbol{\rho})$ is the source function, "*" denotes complex conjugate, and $\delta(\cdot)$ is the Dirac delta function. The $\sqrt{\lambda^{-2}-\boldsymbol{\rho}^2}$ terms come from the Green's function Eq. (2.13).

The paraxial approximation is introduced after deriving Eq. (19) in Ref. [108]. Paraxial approximation ensures that the magnitude of spatial frequencies $\boldsymbol{\rho}_1$ and $\boldsymbol{\rho}_2$ are much smaller than λ^{-1}, so $(\lambda^{-2}-\boldsymbol{\rho}^2)^{1/2}$ can be approximated by its first order Taylor expansion $1/\lambda-\lambda\boldsymbol{\rho}^2/2$ in the argument of V function and even approximated with $1/\lambda$ in the denominators. After the paraxial approximation, the mutual intensity becomes

$$\begin{aligned}\tilde{J}_{OBJ}(\boldsymbol{\rho}_1;\boldsymbol{\rho}_2) &= \tilde{S}(\boldsymbol{\rho}_1)\delta(\boldsymbol{\rho}_1-\boldsymbol{\rho}_2)+\frac{\lambda}{4\pi i}\tilde{S}(\boldsymbol{\rho}_2)V\left(\boldsymbol{\rho}_1-\boldsymbol{\rho}_2,\frac{\lambda}{2}(\boldsymbol{\rho}_2^2-\boldsymbol{\rho}_1^2)\right)\\ &-\frac{\lambda}{4\pi i}\tilde{S}(\boldsymbol{\mu}_1)V^*\left(\boldsymbol{\rho}_2-\boldsymbol{\rho}_1,\frac{\lambda}{2}(\boldsymbol{\rho}_1^2-\boldsymbol{\rho}_2^2)\right).\end{aligned} \tag{3.3}$$

The 3D spectrum of the image intensity can be calculated by using the following projection law (combining Eqs. (22) and (23) in Ref. [108])

$$\tilde{I}(\boldsymbol{\rho},\eta) = \int \tilde{p}(\boldsymbol{\rho}' + \boldsymbol{\rho}/2)\tilde{J}_{OBJ}(\boldsymbol{\rho}' + \boldsymbol{\rho}/2, \boldsymbol{\rho}' - \boldsymbol{\rho}/2)\tilde{p}^*(\boldsymbol{\rho}' - \boldsymbol{\rho}/2) \times \delta(\eta + \lambda\boldsymbol{\rho}\cdot\boldsymbol{\rho}')\mathrm{d}^2\boldsymbol{\rho}', \tag{3.4}$$

where $\tilde{p}(\boldsymbol{\rho})$ is the pupil function. In this equation, the term $\lambda\boldsymbol{\rho}\cdot\boldsymbol{\rho}'$ comes from the term $\frac{\lambda}{2}(\boldsymbol{\rho}_1^2 - \boldsymbol{\rho}_2^2)$by replacing $\boldsymbol{\rho}_1 = \boldsymbol{\rho}' + \boldsymbol{\rho}/2$ and $\boldsymbol{\rho}_2 = \boldsymbol{\rho}' - \boldsymbol{\rho}/2$, so it is also a result from the paraxial approximation. After further calculation, the paraxial 3D POTF is derived as Eq. (27) in Ref. [108] and is repeated here

$$H(\boldsymbol{\rho},\eta) = \frac{i\lambda}{4\pi}\int \tilde{p}(\boldsymbol{\rho}' + \boldsymbol{\rho}/2)\tilde{p}^*(\boldsymbol{\rho}' - \boldsymbol{\rho}/2) \times \left[\tilde{S}(\boldsymbol{\rho}' + \boldsymbol{\rho}/2) - \tilde{S}(\boldsymbol{\rho}' - \boldsymbol{\rho}/2)\right]\delta(\eta + \lambda\boldsymbol{\rho}\cdot\boldsymbol{\rho}')\mathrm{d}^2\boldsymbol{\rho}'. \tag{3.5}$$

3.2 Elimination of Paraxial Approximation

If the paraxial approximation is not used, Eq. (3.3) should be used instead of Eq. (3.2), and the term $\lambda\boldsymbol{\rho}\cdot\boldsymbol{\rho}'$ in Eq. (3.4) should also be replaced by its nonparaxial version $\sqrt{\lambda^{-2} - (\boldsymbol{\rho}' - \boldsymbol{\rho}/2)^2} - \sqrt{\lambda^{-2} - (\boldsymbol{\rho}' + \boldsymbol{\rho}/2)^2}$. The general 3D POTF, Eq. (3.5), would then become

$$H(\boldsymbol{\rho},\eta) = \frac{i\lambda}{4\pi}\int \tilde{p}(\boldsymbol{\rho}' + \boldsymbol{\rho}/2)\tilde{p}^*(\boldsymbol{\rho}' - \boldsymbol{\rho}/2) \tag{3.6}$$

$$\times \left[\frac{\tilde{S}(\boldsymbol{\rho}' + \boldsymbol{\rho}/2)}{\sqrt{1-\lambda^2(\boldsymbol{\rho}' - \boldsymbol{\rho}/2)^2}} - \frac{\tilde{S}(\boldsymbol{\rho}' - \boldsymbol{\rho}/2)}{\sqrt{1-\lambda^2(\boldsymbol{\rho}' + \boldsymbol{\rho}/2)^2}} \right]$$

$$\times \delta\left(\eta + \sqrt{\lambda^{-2} - (\boldsymbol{\rho}' - \boldsymbol{\rho}/2)^2} - \sqrt{\lambda^{-2} - (\boldsymbol{\rho}' + \boldsymbol{\rho}/2)^2}\right) \mathrm{d}^2\boldsymbol{\rho}',$$

which is now the general nonparaxial 3D POTF.

To be fully consistent with the nonparaxial case, the obliquity factor (OF) [110] should be incorporated into the Green's function. The OF was introduced by Kirchhoff in his diffraction integral and later modified by Rayleigh and Sommerfeld using different boundary conditions [110]. For the paraxial case, the OF is approximated by unity. The OF modification is to introduced to overcome the different object requirements in 2D and 3D diffraction theories. A detailed explanation of the OF can be found in Appendix A. In order to be consistent with the conventional angular spectrum representation [111], the first Rayleigh-Sommerfeld obliquity factor is chosen. Its angular spectrum is

$$K(\boldsymbol{\rho}) = \sqrt{1-\lambda^2\boldsymbol{\rho}^2}. \tag{3.7}$$

After being multiplied by this factor, the angular spectrum of the Green's function, Eq. (3.1), becomes the angular spectrum of the modified Green's function

$$\widetilde{G}'(\boldsymbol{\rho}, z) = \tilde{G}(\boldsymbol{\rho}, z)K(\boldsymbol{\rho}) = \frac{\lambda}{4\pi i}\exp\left(2\pi i|z|\sqrt{\lambda^{-2} - \boldsymbol{\rho}^2}\right). \tag{3.8}$$

Applying this modification, the nonparaxial 3D POTF given by Eq. (3.6) becomes

$$H(\boldsymbol{\rho}, \eta) = \frac{i\lambda}{4\pi}\int \tilde{p}(\boldsymbol{\rho}' + \boldsymbol{\rho}/2)\tilde{p}^*(\boldsymbol{\rho}' - \boldsymbol{\rho}/2) \tag{3.9}$$

$$\times \left[\tilde{S}(\boldsymbol{\rho}' + \boldsymbol{\rho}/2) - \tilde{S}(\boldsymbol{\rho}' - \boldsymbol{\rho}/2)\right]$$

$$\times \delta\left(\eta + \sqrt{\lambda^{-2} - (\boldsymbol{\rho}' - \boldsymbol{\rho}/2)^2} - \sqrt{\lambda^{-2} - (\boldsymbol{\rho}' + \boldsymbol{\rho}/2)^2}\right) \mathrm{d}^2\boldsymbol{\rho}',$$

In fact, this is the same equation as Eq. (4) in Ref. [112] derived by Noda *et al.*. However, Noda *et al.* did not explain the origin of the equation, so the concept of the obliquity factor does not appear in their paper.

It is interesting to note that the form of Eq. (3.9) is clearly simpler than that of Eq. (3.6). This seems to be consistent with the philosophy that a correct physical principle is often mathematically concise. An equivalent statement of the OF modification is that the paraxial approximation of replacing $\sqrt{\lambda^{-2} - \boldsymbol{\rho}^2}$ with $1/\lambda$ is retained in the denominators. However, this does not represent correct physical understanding.

3.3 Analytical Integration

The most common case is when the illumination is uniform and the apertures are circular, i.e. the pupil function is

$$\tilde{p}(\boldsymbol{\rho}) = \begin{cases} 1, & \text{if} \quad |\boldsymbol{\rho}| \le \rho_p \\ 0, & \text{if} \quad |\boldsymbol{\rho}| > \rho_p \end{cases}, \tag{3.10}$$

and the source function is

$$\tilde{S}(\boldsymbol{\rho}) = \begin{cases} 1, & \text{if} \quad |\boldsymbol{\rho}| \le \rho_s \\ 0, & \text{if} \quad |\boldsymbol{\rho}| > \rho_s \end{cases}. \tag{3.11}$$

Here $\rho_p = \mathrm{NA_o}/\lambda$ and $\rho_s = \mathrm{NA_c}/\lambda$, where $\mathrm{NA_o}$ and $\mathrm{NA_c}$ are the numerical apertures of objective and condenser lenses. Also, it is assumed $\mathrm{NA_o} \geq \mathrm{NA_c}$. In this case, the POTF is axially symmetric, so $\boldsymbol{\rho}$ in the argument can be represented by its magnitude ρ (ρ >0). In this case, the 3D POTF can be derived analytically. The integration of the paraxial POTF is not difficult to calculate, and the result is Eq. (32) in Ref. [108] and is repeated here

$$H(\rho,\eta) = \frac{i}{2\pi\rho}\mathrm{Re}\left[\sqrt{\frac{1}{2}\left(\rho_p^2+\rho_s^2\right)-\frac{1}{4}\rho^2-\left(\frac{\eta}{\lambda\rho}\right)^2-\left|\frac{\eta}{\lambda}-\frac{1}{2}\left(\rho_p^2-\rho_s^2\right)\right|}\right. \\ \left. +\sqrt{\frac{1}{2}\left(\rho_p^2+\rho_s^2\right)-\frac{1}{4}\rho^2-\left(\frac{\eta}{\lambda\rho}\right)^2-\left|\frac{\eta}{\lambda}+\frac{1}{2}\left(\rho_p^2-\rho_s^2\right)\right|}\right]. \tag{3.12}$$

Calculating the integration of the nonparaxial POTF is much more difficult. Appendix B has a detailed derivation, definition of quantities, and geometric interpretation. Here only the resulting formulas are listed. The nonparaxial 3D POTF with OF modification is

$$H(\rho,\eta) = \frac{i\lambda}{4\pi}[F(\rho,\eta) - F(-\rho,-\eta)], \tag{3.13}$$

where

$$F(\rho,\eta) = \frac{\rho^2}{(\rho^2+\eta^2)^{3/2}}\rho'_{y,\max}\sqrt{\gamma^2-\rho'^2_{y,\max}} \\ +\left[\frac{\rho^2}{(\rho^2+\eta^2)^{3/2}}\gamma^2-\frac{\eta^2}{2\sqrt{\rho^2+\eta^2}}\right]\arcsin\left(\frac{\rho'_{y,\max}}{\gamma}\right), \tag{3.14}$$

where

$$\gamma = \sqrt{\lambda^{-2} - (\mu^2 + \eta^2)/4}, \tag{3.15}$$

$$\rho'_{y,\max} = \sqrt{\gamma^2 - \frac{\rho^2 + \eta^2}{\eta^2} {\rho'_{x,c}}^2}. \tag{3.16}$$

When $0 < |\rho| \le \rho_p - \rho_s$

$$\rho'_{x,c} = \frac{\eta}{\rho}\left(\frac{\eta}{2} - \sqrt{\lambda^{-2} - \rho_s^2}\right) \left(\begin{array}{c}\text{if} \quad \sqrt{\lambda^{-2} - \rho_s^2} - \sqrt{\lambda^{-2} - (\rho_s - |\rho|)^2} \\ \le \eta \le \sqrt{\lambda^{-2} - \rho_s^2} - \sqrt{\lambda^{-2} - (\rho_s + |\rho|)^2}\end{array}\right) \tag{3.17}$$

and when $\rho_p - \rho_s < |\rho| \le \rho_p + \rho_s$

$$\rho'_{x,c} = \begin{cases} \dfrac{\eta}{\rho}\left(\dfrac{\eta}{2} - \sqrt{\lambda^{-2} - \rho_s^2}\right) \left(\begin{array}{c}\text{if} \quad \sqrt{\lambda^{-2} - \rho_s^2} - \sqrt{\lambda^{-2} - (\rho_s - |\rho|)^2} \\ \le \eta \le \sqrt{\lambda^{-2} - \rho_s^2} - \sqrt{\lambda^{-2} - \rho_p^2}\end{array}\right) \\ \dfrac{\eta}{\rho}\left(-\dfrac{\eta}{2} - \sqrt{\lambda^{-2} - \rho_p^2}\right) \left(\begin{array}{c}\text{if} \quad \sqrt{\lambda^{-2} - \rho_s^2} - \sqrt{\lambda^{-2} - \rho_p^2} \\ < \eta \le \sqrt{\lambda^{-2} - \left(\rho_p - |\rho|\right)^2} - \sqrt{\lambda^{-2} - \rho_p^2}\end{array}\right) \end{cases}. \tag{3.18}$$

If η is outside of the above region, $\rho'_{y,\max} = 0$.

In order to evaluate the effect of the OF modification, the POTF is calculated with and without the OF. The only difference appears in the quantity $F(\rho,\eta)$. Including the OF, it is calculated by Eq. (3.14). Without the OF it is calculated using

$$F(\rho,\eta)=\frac{2|\rho|}{\lambda(\rho^2+\eta^2)}{\rho'}_{y,\max}-\frac{\eta}{\lambda\sqrt{\rho^2+\eta^2}}\arcsin\left(\frac{{\rho'}_{y,\max}}{\gamma}\right). \tag{3.19}$$

The three versions of 3D POTFs, namely the paraxial POTF (P-POTF) calculated using Eq. (3.12), the nonparaxial POTF without OF modification (nP-POTF) calculated using Eqs. (3.13) and (3.15)-(3.19), and the nonparaxial POTF with OF modification (nP-POTF-OF) calculated using Eqs. (3.13)-(3.18), are plotted in Figure 3.1 for comparison. The imaginary parts are plotted, since the POTF is purely imaginary. In plotting these POTFs, the parameters are $\lambda = 0.546$ μm, $\mathrm{NA_c} = 0.375$, $\mathrm{NA_o} = 0.75$. The POTFs are plotted in a 400×400 discrete grid, and thus the frequency resolution is $1/(400 \times 0.245\ \mu\mathrm{m})$, where 0.245 μm is the effective pixel size of the camera. The results show that the nonparaxial POTFs are wider than the paraxial POTF. Thus, a greater range of spatial frequencies is included in the imaging process. At the same spatial frequency, the P-POTF is the largest in absolute value, while the nP-POTF-OF is the smallest in absolute value. The shapes of the POTFs are explained in detail in Appendix B.

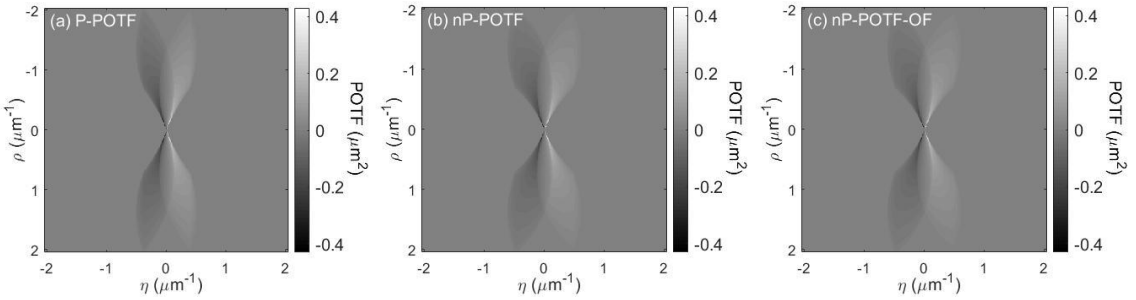

Figure 3.1. Imaginary parts of three versions of 3D POTFs. The horizontal and vertical axes are longitudinal and transverse spatial frequencies $\boldsymbol{\eta}$ and $\boldsymbol{\rho}$ respectively. The colorbars represent the imaginary values of the POTFs. (a) The paraxial POTF (P-POTF); (b) the nonparaxial POTF without OF modification (nP-POTF); (c) the nonparaxial POTF with OF modification (nP-POTF-OF).

In addition to the POTF, the absorption optical transfer function (AOTF) can also be extended to the nonparaxial case using the procedure described above. Although it is not used in this paper, it is nevertheless presented here for completeness. The general expression for the AOTF is

$$H_A(\boldsymbol{\rho},\eta) = \frac{\lambda}{4\pi}\int \tilde{p}(\boldsymbol{\rho}'+\boldsymbol{\rho}/2)\tilde{p}^*(\boldsymbol{\rho}'-\boldsymbol{\rho}/2)$$
$$\times\left[\tilde{S}(\boldsymbol{\rho}'+\boldsymbol{\rho}/2)+\tilde{S}(\boldsymbol{\rho}'-\boldsymbol{\rho}/2)\right] \tag{3.20}$$
$$\times\,\delta\left(\eta+\sqrt{\lambda^{-2}-(\boldsymbol{\rho}'-\boldsymbol{\rho}/2)^2}-\sqrt{\lambda^{-2}-(\boldsymbol{\rho}'+\boldsymbol{\rho}/2)^2}\right)\mathrm{d}^2\boldsymbol{\rho}'.$$

For the case of uniform illumination and circular apertures, the expression is

$$H_A(\rho,\eta) = \frac{\lambda}{4\pi}[F(\rho,\eta)+F(-\rho,-\eta)], \tag{3.21}$$

where $F(\rho,\eta)$ is still calculated using Eqs. (3.14)-(3.18).

The nP-POTF-OF can be applied to some QPI methods that use 3D POTF to extend them to nonparaxial conditions. Due to their analytic nature, there will be negligible increase in computation time. One example application is nP-MFPI-PC-OF method, which will be discussed in Chapter 4. It has also been used by other research groups [113]. However, the original equations published in Ref. [109] has some typos, some of which are corrected by an erratum paper [114] and some of which are mentioned in Ref. [115].

CHAPTER 4. NONPARAXIAL MULTI-FILTER PHASE IMAGING WITH PARTIALLY COHERENT LIGHT

Multifilter phase imaging with partially coherent light (MFPI-PC) is a deterministic propagation-based QPI method developed by Jenkins *et al.* [82]. Chapter 2 has a brief overview of it. However, this original POTF is based on the paraxial approximation, which is not very accurate for optical systems with large numerical apertures (NAs). However, using the nonparaxial 3D POTF derived in Chapter 3, the MFPI-PC can be extended to the nonparaxial condition. This work has been published in Ref. [109].

4.1 Theory

With the development of the nonparaxial POTF, the calculation of the nonparaxial PCTF is now enabled. The only modification is to use the nonparaxial 3D POTF to be the $H(\rho,\eta)$ in Eqs. (2.11) and (2.12). When the nonparaxial POTF and PCTF are used instead of the paraxial ones, the MFPI-PC becomes a nonparaxial method.

Figure 4.1 displays three versions of WD-PCTFs, namely the paraxial WD-PCTF (P-WD-PCTF), the nonparaxial WD-PCTF without OF correction (nP-WD-PCTF), and the nonparaxial WD-PCTF with OF correction (nP-WD-PCTF-OF). The inset in the upper right corner shows the ratios of the nP-WD-PCTF and the P-WD-PCTF to the nP-WD-PCTF-OF. It is obvious that the P-WD-PCTF is smaller than the nP-WD-PCTF-OF, while the nP-WD-PCTF is larger than the nP-WD-PCTF-OF.

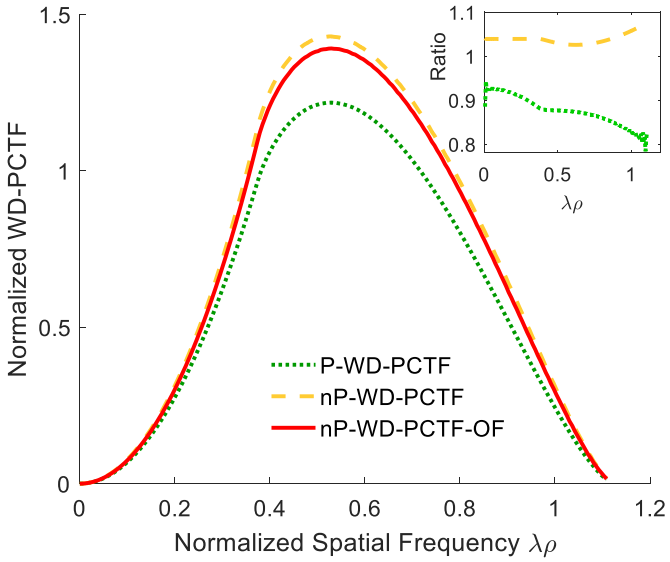

Figure 4.1. Three versions of WD-PCTFs. The horizontal axis is the normalized longitudinal spatial frequency $\lambda\rho$ and the vertical axis is the normalized WD-PCTF defined in Ref. [82]. The green dotted curve is the paraxial WD-PCTF. The yellow dashed curve is the nonparaxial WD-PCTF without OF correction. The red curve is the nonparaxial WD-PCTF with OF correction. The inset in the upper right corner shows the ratios of the P-WD-PCTF and the nP-WD-PCTF to the nP-WD-PCTF-OF.

Based on simulations and experimental results presented in this chapter, the relative amplitudes of the WD-PCTFs are shown to be important in determining the error in the recovered quantitative phase. Therefore, further consideration of the amplitude of the WD-PCTF is appropriate. The nP-WD-PCTF-OF is smaller than the nP-WD-PCTF, because the multiplication of the OF makes the POTF smaller. However, similar reasoning does not explain why the P-WD-PCTF is the smallest, especially given that the P-POTF is largest. The reason lies in the fact that the paraxial POTF is narrower than it is in the nonparaxial case, as shown in Figure 3.1. In calculating the WD-PCTF from the POTF using Eq. (2.12), integration along η axis, weighted by η, is required, so the narrow shape of the P-POTF results in a smaller integration interval and smaller weight, which together lead to the small P-WD-PCTF.

Figure 4.2 is a flowchart showing the basic process of the nonparaxial MFPI-PC. The process is very similar to the original paraxial MFPI-PC, except that the TIE inversion is replaced by the transfer function inversion over the WD-PCTF $T_W(\rho)$. In this way, the nonparaxial effect is included. Another advantage is that the WD-PCTF is much more accurate than the TIE-PCTF for $(\mathrm{NA_o} - \mathrm{NA_c})/\lambda < \rho < (\mathrm{NA_o} + \mathrm{NA_c})/\lambda$, so the maximum recoverable spatial frequency is increased from $(\mathrm{NA_o} - \mathrm{NA_c})/\lambda$ to $(\mathrm{NA_o} + \mathrm{NA_c})/\lambda$. Another consequence of using WD-PCTF is that TIE is not directly involved in the actual phase recovery anymore. Since TIE is only valid in paraxial approximation, eliminating TIE is necessary to incorporate nonparaxial effect. Despite that the nonparaxial model is more accurate, the computation time essentially does not increase because of the analytical nature of the 3D POTF.

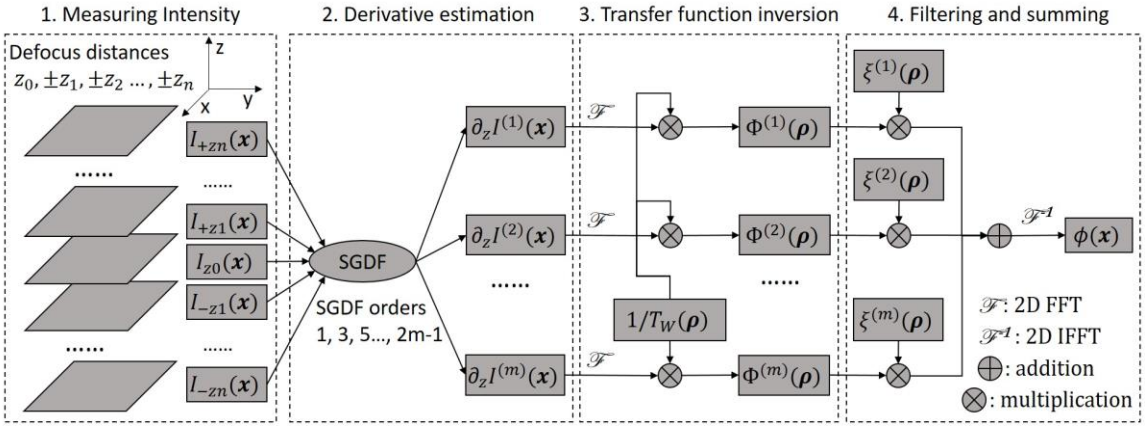

Figure 4.2. Flow chart showing the basic process of the nonparaxial MFPI-PC. $I_z(x)$ is the image intensity at defocus distance z. $\partial_z I^{(k)}(x)$ is the longitudinal intensity derivative at the focal plane, calculated using the (2k-1)th order SGDF [79]. $T_W(\rho)$ is the WD-PCTF. $\Phi^{(k)}(\rho)$ is the recovered phase in the spatial frequency domain corresponding to the (2k-1)th order SGDF. $\xi^{(k)}(\rho)$ is a filter aiming to select the optimal SGDF order for each frequency component.

4.2 Simulation Results

In order to quantify the improvement associated with the nonparaxial MFPI-PC method, simulations were performed comparing its phase recovery with that from the paraxial MFPI-PC method. The metric used to quantify the recovery accuracy is the normalized root-mean-square error (NRMSE), defined as

$$\mathrm{NRMSE} = \left(\frac{\sum [\phi_r(x,y) - \phi_0(x,y)]^2}{\sum \phi_0(x,y)^2} \right)^{1/2}. \tag{4.1}$$

The quantity $\phi_0(x,y)$ is the ideal phase and $\phi_r(x,y)$ is the recovered phase of the object. The summation is over all of the discrete pixels.

The simulation results of the first object (Object 1) are shown in Figure 4.3. Since the MFPI-PC cannot recover the zero frequency component, the mean values are subtracted from all the images. The phase of the original Object 1 is shown in Figure 4.3(a). It is a pure phase object with no absorption. The object has a size of 400×400 pixels and a maximum phase difference of 0.3 radians. As can be seen, it is a complicated object with significant high spatial frequency components. The NA of the objective lens was NA_o= 0.75 and that of the condenser lens was NA_c= 0.375. Intensity images at 31 equally distributed planes (the focal plane and 15 pairs of symmetrically defocused planes) were simulated and then used in the recovery of the quantitative phase image.

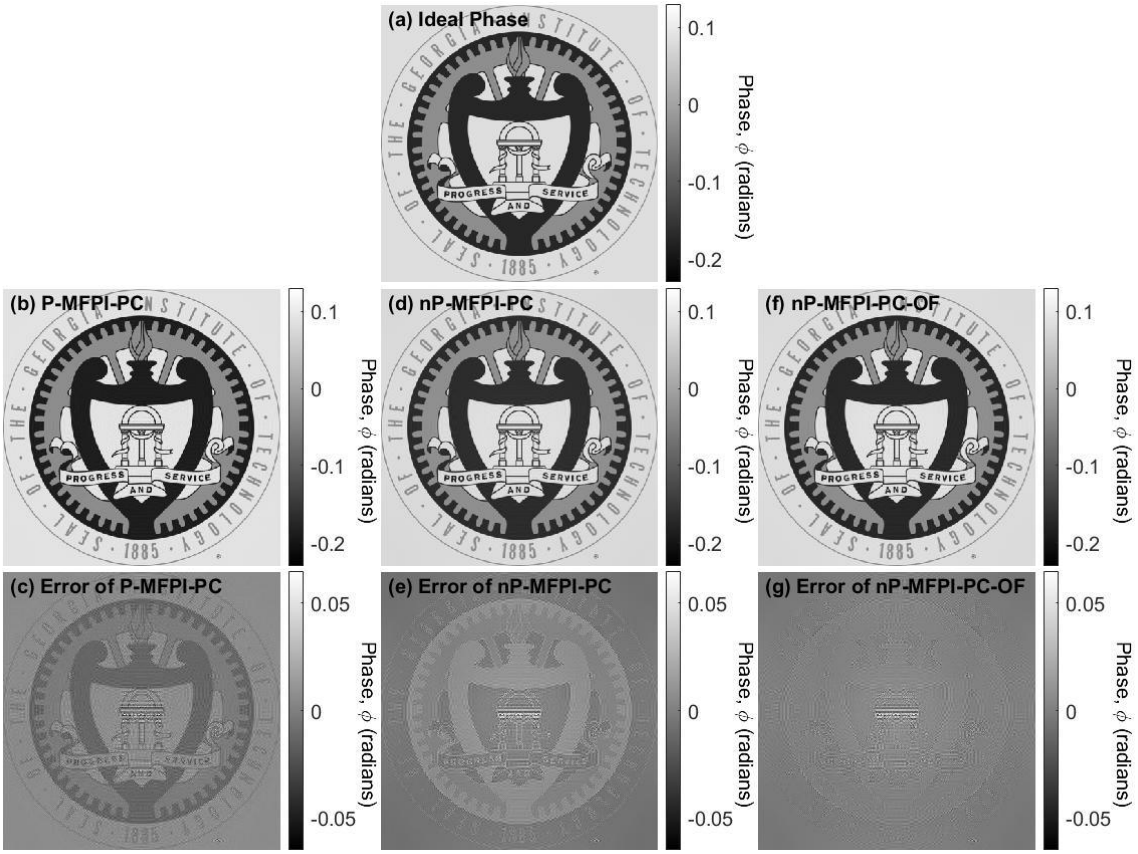

Figure 4.3. Simulation of the phases recovered from various versions of MFPI-PCs using Object 1. The units on the colorbars are radians. The ranges of the ideal phase and the three recovered phases are all from -0.23 to +0.13. The ranges of the three error maps are all from -0.065 to +0.065. (a) The ideal phase image to be simulated. (b) The phase recovered by the P-MFPI-PC. (c) The error of (b) compared to (a). The NRMSE was 0.085. (d) The phase recovered by the nP-MFPI-PC. (e) The error of (d) compared to (a). The NRMSE was 0.071. (f) The phase recovered by the nP-MFPI-PC-OF. (g) The error of (f) compared to (a). The NRMSE was only 0.052.

Figure 4.3(b) shows the recovered phase from the paraxial MFPI-PC (P-MFPI-PC) and Figure 4.3(c) shows its error map relative to the ideal phase (recovered phase minus ideal phase). The NRMSE was 0.085. The error map shows that the P-MFPI-PC overestimated the phase. Figure 4.3(d) shows the recovered phase from the nonparaxial MFPI-PC without OF correction (nP-MFPI-PC) Figure 4.3(e) shows its error map. The NRMSE was 0.071. The error map shows that the nP-MFPI-PC underestimated the phase. Figure 4.3(f) and (g) show the recovered phase from the nonparaxial MFPI-PC

with OF correction (nP-MFPI-PC-OF), as well as its error map. The NRMSE was only 0.052. The error map shows that the nP-MFPI-PC-OF only slightly underestimated the phase. Although the P-MFPI-PC and the nP-MFPI-PC recovered the phase reasonably well, the nP-MFPI-PC-OF was clearly the best of the three.

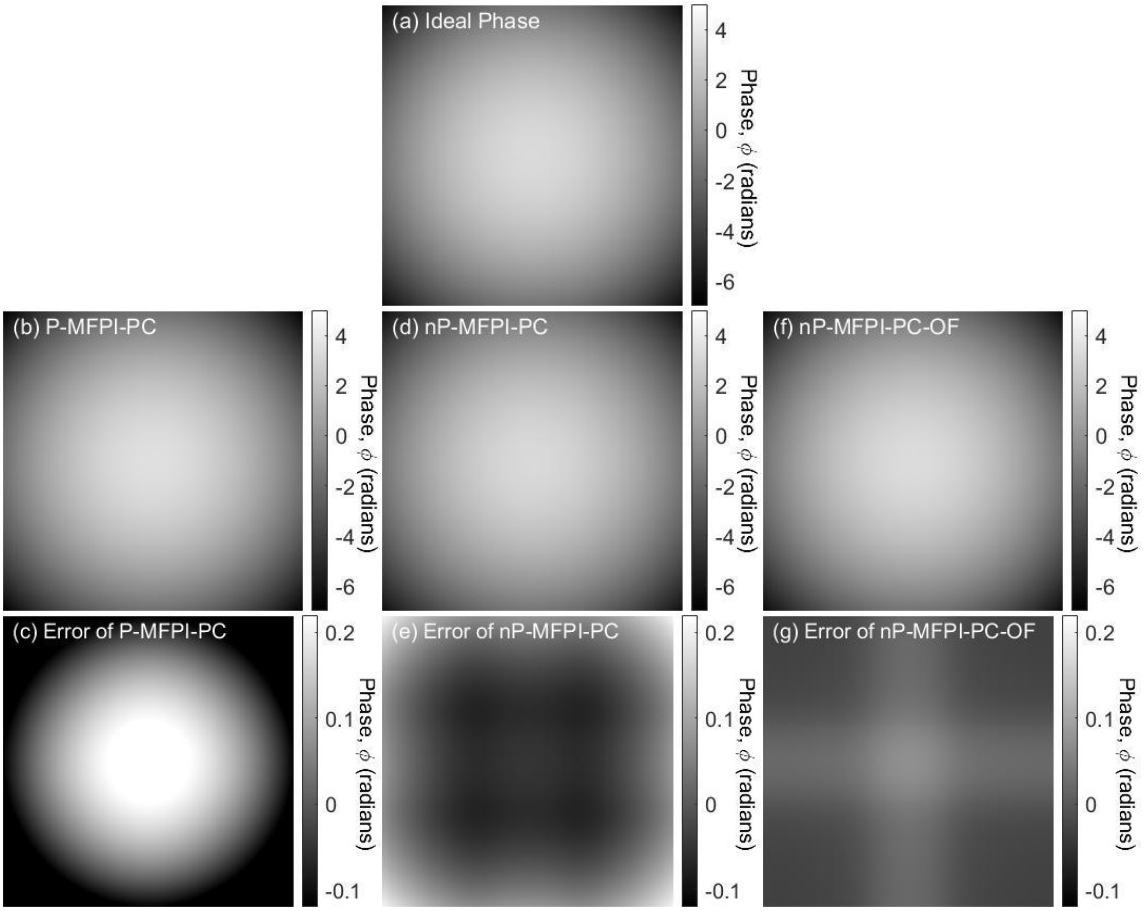

Figure 4.4. Simulation of the phases recovered from various versions of MFPI-PCs using Object 2. The units on the colorbars are radians. The ranges of the ideal phase and the three recovered phases are all from -7 to +5. The ranges of the three error maps are all from -0.12 to +0.22. (a) The ideal phase image to be simulated. (b) The phase recovered by the P-MFPI-PC. (c) The error of (b) compared to (a). The NRMSE was 0.076. (d) The phase recovered by the nP-MFPI-PC. (e) The error of (d) compared to (a). The NRMSE was 0.028. (f) The phase recovered by the nP-MFPI-PC-OF. (g) The error of (f) compared to (a). The NRMSE was only 0.013.

To evaluate and compare the three methods applied to a simple but realistic object, a parabolic profile was chosen (Object 2). The phase of the original object is

shown in Figure 4.4(a). It is also a pure phase object with no absorption. The object had a size of 612×612 pixels and the maximum phase difference is 11 radians. It is a simple object, but one with a very large range of the phase. The numerical apertures were the same as in the previous simulation. Intensity images at 31 planes, as before, were simulated and then used in the recovery of the quantitative phase image.

The recovered phase images, as well as the errors, are shown in Figure 4.4 in the same format as Figure 4.3. The NRMSE of the P-MFPI-PC was 0.076. In this case, the phase was greatly overestimated. The error was so large that it exceeded the range of the colorbar selected. The NRMSE of the nP-MFPI-PC was 0.028. In this case, the phase was underestimated. The error was low at the center of the image, but large away from the center. By contrast, the NRMSE of the nP-MFPI-PC-OF was only 0.013. The error map shows small error over the whole image. The phase was only slightly overestimated. These simulations further validate that the nP-MFPI-PC-OF method is more accurate than the other two methods.

From the above error maps, it is possible to draw some systematic conclusions about the three methods. The P-MFPI-PC usually overestimates the phase, because the P-WD-PCTF is the smallest of the three PCTFs. The nP-MFPI-PC usually underestimates the phase, because the nP-WD-PCTF is the largest of the three PCTFs. In contrast, the nP-MFPI-PC-OF method only slightly underestimates the phase of Object 1 and only slightly overestimates the phase of Object 2. Not only is the nP-WD-PCTF-OF method the most accurate, but also there is a lack of any noticeable systematic error. These results indicate that the new nP-POTF-OF used in the present work, with its relaxation of the

paraxial approximation and its incorporation of the obliquity factor, provides a more reliable and accurate representation of the imaging than the other two POTFs.

Furthermore, noise sensitivity is important and also needs to be considered and evaluated. This is especially true since the MFPI-PC is an inverse filtering method and noise can produce degradation when a spatial frequency component has a small transfer function value [116]. In order to reduce noise sensitivity, a low-pass filter is designed to filter out the high-frequency component whose ideal value is less than the noise. At present, the filter is chosen to be simply

$$\mathrm{LPF}(\rho) = \begin{cases} 1, & \text{when} \quad \rho \le \beta(\rho_s + \rho_p) \\ 0, & \text{when} \quad \rho > \beta(\rho_s + \rho_p) \end{cases}, \tag{4.2}$$

where β is a constant close to but less than unity. The best choice of β is related to the magnitude of the noise and the spectrum width of the object. For larger values of noise and smaller widths of the spectra of the objects, the value of β should be chosen correspondingly smaller. However, determining the optimal value of β is left to future work. In this paper, β is chosen to be 0.95.

Simulations with noise were performed for Object 2. At each noise level, 10 simulations were done for each of the three methods and the average NRMSEs were calculated. When the signal-to-noise ratio (SNR) was 50 dB, the average NRMSE of the P-MFPI-PC was 0.077, of the nP-MFPI-PC was 0.029, and of the nP-MFPI-PC-OF was only 0.013. When the SNR was 30 dB, the average NRMSE of the P-MFPI-PC was 0.091, of the nP-MFPI-PC was 0.048, and of the nP-MFPI-PC-OF was only 0.043. The results show that the nP-MFPI-PC-OF method is stable under noisy conditions. In

addition, the accuracy advantage of the nP-MFPI-PC-OF over the other two methods is retained in the presence of significant noise.

4.3 Experimental Results

The new nP-MFPI-PC-OF method was also applied to experimental data. The experimental configuration is described in Chapter 2. The phase pattern of a periodic microlens array (Thorlabs MLA150-7AR) was quantitatively imaged. The pattern was similar to simulation Object 2. The smallest defocus distance was 0.6 μm. The apertures were the same as those used in the simulations. Intensity images at 31 equally distributed planes (the focal plane and 15 pairs of symmetrically defocused planes) were captured and then used in the recovery of the quantitative phase image.

Figure 4.5(a) shows the recovered phase from the P-MFPI-PC. Figure 4.5(b) shows the recovered phase from the nP-MFPI-PC. Figure 4.5(c) shows the recovered phase from the nP-MFPI-PC-OF. Figure 4.5(d) shows the line profiles of the phases along the center columns (shown in dashed lines) of the previous three figures, as well as the phase from the thickness as directly measured by a profilometer (KLA-Tencor P-15). Consistent with the simulation section above, the P-MFPI-PC overestimated the phase and the nP-MFPI-PC underestimated the phase. Clearly, the nP-MFPI-PC-OF was still the most accurate. These results are similarly consistent with the simulation results of Object 2.

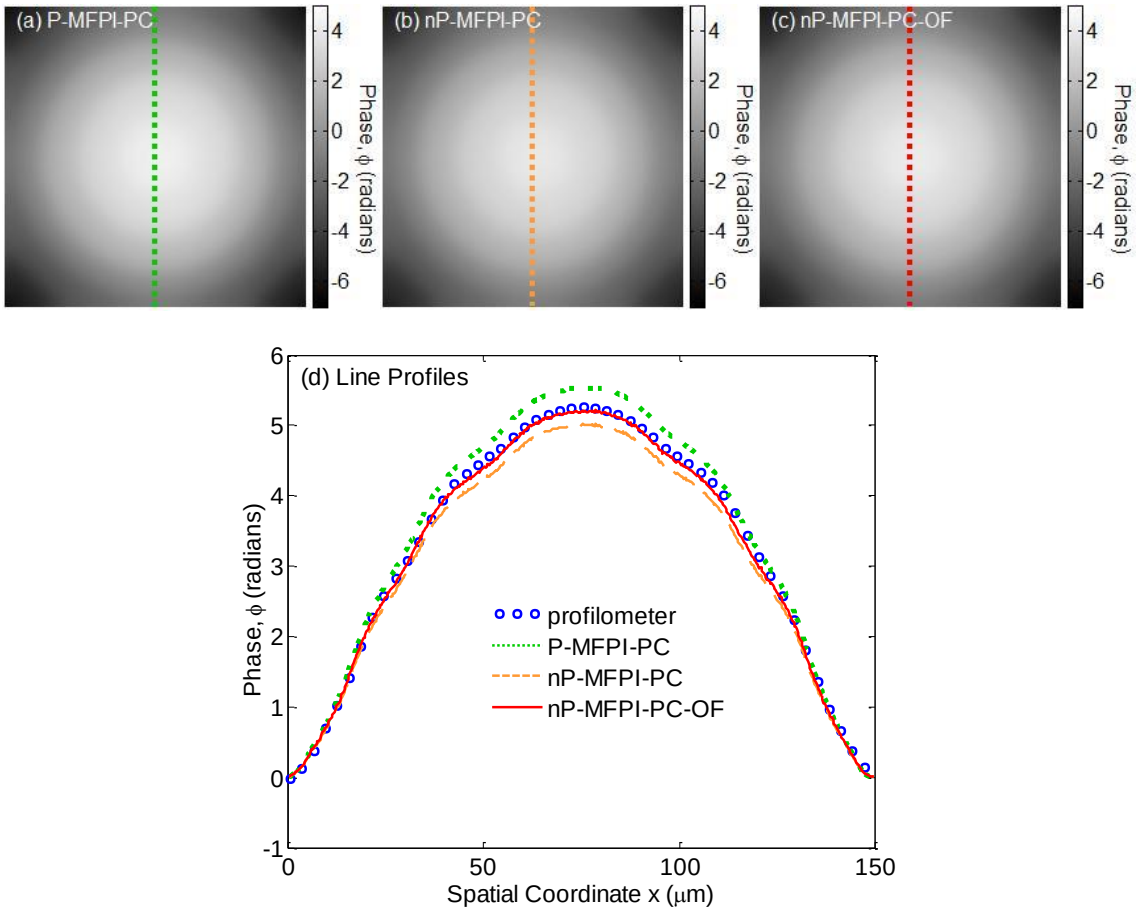

Figure 4.5. Experimentally measured quantitative phase images of a microlens. (a) The phase recovered by the P-MFPI-PC; (b) the phase recovered by the nP-MFPI-PC; (c) the phase recovered by the nP-MFPI-PC-OF. (d) The line profiles of the phases along the center columns (dotted lines) of (a), (b) and (c), as well as the phase from the thickness as directly measured by the profilometer. The vertical axis and colorbars are the phase delay relative to the edge of the microlens, whose unit is radians.

4.4 Discussion

The simulations of Object 2 and the experimental measurements of the microlens indicate that the phase changes over those objects are quite large (~10 radians). Thus, the first Born approximation would no longer seem to be applicable [83]. Therefore, in principle, the derivation of the POTF that has been used should not be reliable since it incorporates the Born approximation [108]. However, the apparent accuracy of the results

brings the “weakly scattering” assumption into question. It appears that the “slowly varying phase” requirement is sufficient. Perhaps this conclusion is not surprising since indeed a similar result is found when applying the CTF [75, 117]. Although the MFPI-PC is developed based on the TIE, Eq. (5) in Ref. [82] shows that it is also similar to the CTF. Thus, a possible explanation is the Born approximation can be replaced by the Rytov approximation, if the derivations of the governing relationships are properly modified [83, 107]. However, this fundamental modification in the theory is left to future work.

The simulations and experimental results presented in this paper show, in general, that nP-MFPI-PC-OF is more accurate than either P-MFPI-PC or nP-MFPI-PC. However, it is possible to find situations where this general result may be violated. This is illustrated and discussed in Appendix C.

CHAPTER 5. WEIGHTED-LEAST-SQUARES MULTI-FILTER PHASE IMAGING WITH PARTIALLY COHERENT LIGHT: CHARACTERISTICS OF ANNULAR ILLUMINATION

5.1 Introduction

While most of the QPI methods use disk illumination, other shapes of illumination, such as annular illumination, have also attracted the interest of researchers. In fact, annular illumination has a long history of applications in various microscopy techniques and has shown a number of advantages. For example, in the fluorescent imaging of single molecules, annular illumination was found to reduce spot size and enhance longitudinal fields, resulting in the generation of stronger observable patterns [118]. In the terahertz frequency regime, annular beam profiles have been found to be focusable beyond the diffraction limit, resulting in extreme resolution imaging. This has found practical use in security and biology [119]. Similar results of increased resolution have been found in solid emersion microscopy [120], adaptive optics scanning light ophthalmoscopy [121], and scanning electron microscopy [122]. In localized surface plasmon microscopy, annular illumination was able to improve the observed fluorescence of samples by approximately 1.8 times over that of disk illumination [123]. It also improved the signal-to-background noise ratio by 30% in multiphoton microscopy [124]. The benefits of annular illumination in other microscopy techniques extend well into phase imaging. In phase contrast microscopy, annular illumination is used to increase the illuminance of the background light [2]. Generally, in phase imaging microscopy, using an annular source has been found to provide higher resolution due to the extension of the lateral resolution

to twice that of the coherent diffraction limit [125-128]. In transport-of-intensity QPI, in addition to increased resolution, annular illumination also has been found to require fewer measurement data [129]. Other benefits include shorter and lower intensity exposures and compatibility with conventional microscopy techniques due to not requiring coherent illumination [129]. The phase-to-intensity ratio response of annular illumination is generally better than that of disk illumination [112]. Additionally, using annular illumination allows for the adjustment of phase contrast by tuning the annulus inner radius to focus on specific spatial frequencies [130] and obtain high contrast images of objects with small phase variation [131].

In these previously published results, the annular illumination was usually investigated numerically, since the impact of the annular source is often described by a complex integral. On the other hand, analytical formulas are explicit relationships that inherently contain more information, and so provide a deeper understanding of the physical problem. In addition, the calculation speed is much faster than that of a numerical integration, which is very important in real-time applications. However, due to the frequent mathematical challenges, analytical formulas may be difficult to derive.

In this chapter, annular illumination is analyzed by QPI MFPI-PC [82]. The analytical transfer function for annular illumination is derived explicitly and discussed. Since there is a significant noise magnification problem in using annular illumination in MFPI-PC, an improved algorithm, weighted-least-squares MFPI-PC (WLS-MFPI-PC) is developed to solve this problem. Simulations and microlens experiments are used to validate the new QPI method for annular illumination. This work has been published in Ref. [132].

5.2 Annular Illumination QPI Theory

In order to apply annular illumination in MFPI-PC, the transfer functions for annular illumination should be derived. Fortunately, the integral form of the 3D POTF, Eq. (3.9), is not only valid for disk illumination but also valid for annular illumination, as long as the annular source function is used. When the numerical apertures (NAs) of the outer and inner annular rings are $\mathrm{NA_c}$ and $\mathrm{NA_{ci}}$ respectively, the annular source function is

$$\tilde{S}(\boldsymbol{\rho}) = \begin{cases} 0, & \text{if } |\boldsymbol{\rho}| < \rho_{si} \\ 1, & \text{if } \rho_{si} \le |\boldsymbol{\rho}| \le \rho_s, \\ 0, & \text{if } |\boldsymbol{\rho}| > \rho_s \end{cases} \tag{5.1}$$

where $\rho_s = \mathrm{NA_c}/\lambda$ and $\rho_{si} = \mathrm{NA_{ci}}/\lambda$. The source function can be represented schematically in Figure 5.1. The 3D POTF of a configuration with a uniform annular source can be expressed as $H(\boldsymbol{\rho}, \eta; \rho_{si}, \rho_s)$ to include the inner and outer boundaries of the annulus. Using this notation, $H(\boldsymbol{\rho}, \eta; 0, \rho_s)$ is the corresponding 3D POTF for disk illumination.

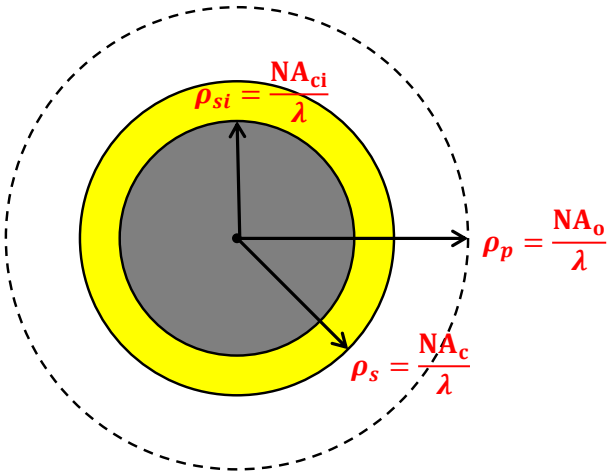

Figure 5.1. Schematic representation of annular illumination source function in spatial frequency domain. The central ring is the annular illumination area. The radii of outer and inner circles of the annulus are determined by their corresponding numerical apertures (NAs), NA_c and NA_{ci}. For reference, The NA of the objective lens, NA_o, is plotted as a dashed circle.

Due to the linearity of Eq. (3.9) to $\tilde{S}(\boldsymbol{\rho})$ stemming from Köhler illumination, the annular 3D POTF can be easily calculated from the disk 3D POTF using the superposition principle, and the result is

$$H(\boldsymbol{\rho}, \eta; \rho_{si}, \rho_s) = H(\boldsymbol{\rho}, \eta; 0, \rho_s) - H(\boldsymbol{\rho}, \eta; 0, \rho_{si}). \tag{5.2}$$

This equation indicates that the POTF of an annular source is the difference of two POTFs of disk sources with the corresponding numerical apertures. However, this generalization does not account for the variation of background intensity. When first Born approximation is applied, the intensity distribution in the 3D image space is given by Eq. (2.3). If the object does not absorb light, it can be simplified to

$$I(\boldsymbol{r}) = B + h(\boldsymbol{r}) * v(\boldsymbol{r}). \tag{5.3}$$

As mentioned in Chapter 2, B is the uniform background intensity. It is usually not of interest. Meanwhile, since B equals the average intensity, it can be easily removed by subtracting average intensity. However, its effect has to be considered now. The formula to calculate B is [108]

$$B = \int \tilde{S}(\boldsymbol{\rho}')\mathrm{d}^2\boldsymbol{\rho}'. \tag{5.4}$$

It indicates that B equals the spatial frequency area of the source function. For an annular source, it can be simplified to

$$B = \pi(\rho_s^2 - \rho_{si}^2). \tag{5.5}$$

Disk source can be considered as the case where $\rho_{si} = 0$.

For computational convenience, the average intensity is usually normalized to unity in simulation and experiment. Therefore, the frequently-used POTF is the normalized POTF $\widetilde{H}$, which is defined as

$$\widetilde{H} = H/B. \tag{5.6}$$

Combining Eqs. (5.2), (5.5), and (5.6), the normalized 3D POTF for the annular source can be written as the weighted difference of the normalized 3D POTFs for the corresponding disk sources,

$$\widetilde{H}(\boldsymbol{\rho}, \eta; \rho_{si}, \rho_s) = \frac{\rho_s^2 \cdot \widetilde{H}(\boldsymbol{\rho}, \eta; 0, \rho_s) - \rho_{si}^2 \cdot \widetilde{H}(\boldsymbol{\rho}, \eta; 0, \rho_{si})}{\rho_s^2 - \rho_{si}^2}. \tag{5.7}$$

With this analytical 3D POTF for annular illumination, the WD-PCTF can be calculated using Eq. (2.12) by a 1D integration. Apparently, the resulting WD-PCTF is also the weighted difference of the normalized WD-PCTF for the corresponding disk sources,

$$T_W(\rho;\rho_{si},\rho_s)=\frac{\rho_s^2\cdot T_W(\rho;0,\rho_s)-\rho_{si}^2\cdot T_W(\rho;0,\rho_{si})}{\rho_s^2-\rho_{si}^2}. \tag{5.8}$$

Using this result, MFPI-PC can be applied to annular illumination.

5.3 Preliminary Simulation Results and Problems

In order to quantify the advantages of MFPI methods applied to annular illumination, simulations were performed with various inner numerical aperture values, and their respective phase recoveries were compared. White Gaussian noise with $\sigma = 0.01$ (the intensity ratio of the noise and the uniform background) was added. The metric used to quantify the recovery accuracy is again NRMSE.

5.3.1 Preliminary Simulation Results

The simulation results using the standard Lenna image as the test object are shown in Figure 5.2. Since the MFPI-PC cannot recover the zero frequency component, the mean values are subtracted from all the images. The phase of the original Lenna is shown in Figure 5.2(a). It is a pure phase object with no absorption. The object has a size of 512×512 pixels. The pixel size was 245 nm. The wavelength of light is 546 nm. The numerical aperture of the objective lens was NA_o = 0.55. The condenser lens had an outer ring numerical aperture of $\mathrm{NA_c}$ = 0.46 and inner ring numerical apertures of $\mathrm{NA_{ci}}$ = 0.1, 0.2, and 0.3 respectively. Intensity images at 31 equally distributed planes

(the focal plane and 15 pairs of symmetrically defocused planes) were simulated and then used in the recovery of the quantitative phase image.

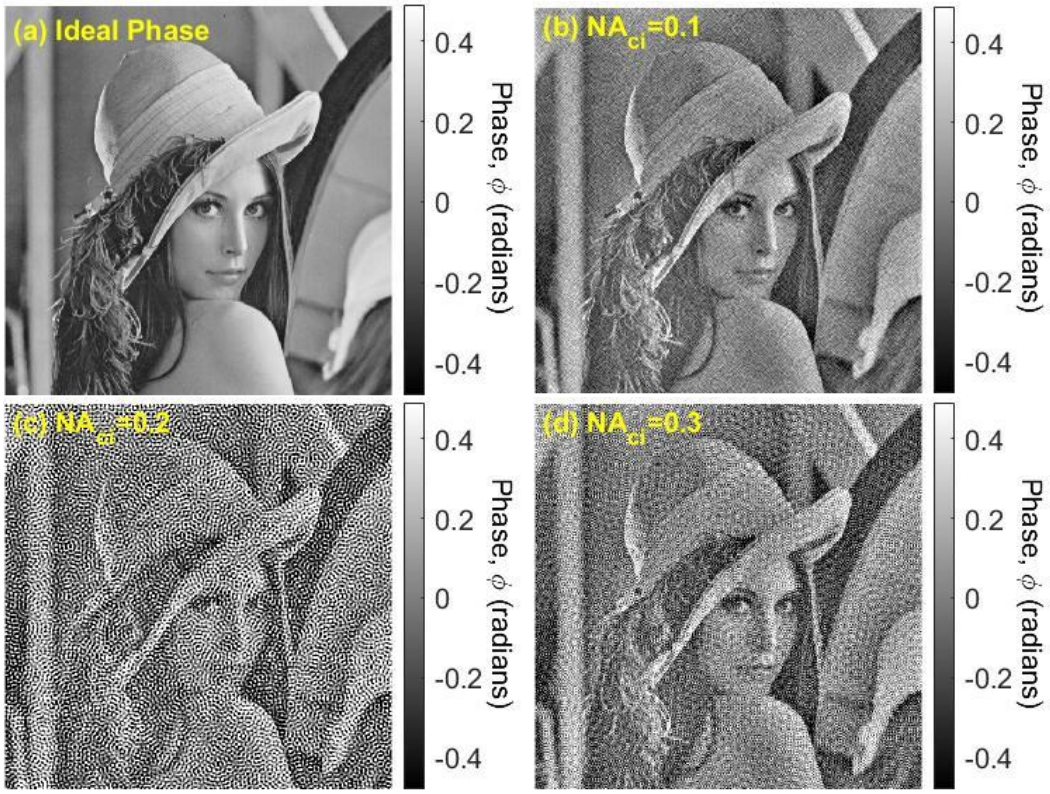

Figure 5.2. Simulation of the phases recovered for various NA_{ci} at a constant NA_c using MFPI-PC. The units on the colorbars are radians. The ranges of the ideal phase and the three recovered phases are all from -0.48 to +0.49 radians. (a) The ideal phase image to be simulated; (b)-(d) the phases recovered at NA_{ci} = 0.1, 0.2, and 0.3 respectively.

Figure 5.2(b) shows the recovered phase when NA_{ci} = 0.1. The NRMSE was 0.65. Figure 5.2(c) shows the recovered phase when NA_{ci} = 0.2. The NRMSE was 2.30. Figure 5.2(d) shows the recovered phase when NA_{ci} = 0.3. The NRMSE was 1.15. The phase maps show that the recovered phase of NA_{ci} = 0.1 was closest to the ideal phase. The recovered phase of NA_{ci} = 0.3 was worse than NA_{ci} = 0.1 but still significantly better than NA_{ci} = 0.2, which was shown to have by far the worst results. The result shows clearly that the error does not vary monotonically with NA_{ci}.

In order to characterize the relation of the error and the numerical apertures in a larger scope, the simulation results for various combinations of inner and outer numerical apertures are shown in Figure 5.3. These results were generated using a scaled down 128×128 version of the original Lenna object. The NA_c values range from 0.01 to 0.55 at 0.01 intervals along the y-axis. The NA_{ci} values range from 0 to 0.54 at 0.01 intervals along the x-axis. The values represented are the logarithm of the NRMSE of the recovered phase compared to the ideal phase image. The case of $NA_c = 0.55$ and $NA_{ci} = 0.0$ has been removed from the plot, since the transfer function is zero for all spatial frequencies. Since NAci must be smaller than NAc, the upper right triangle part is nonphycical. The range of the colorbar is from -1.05 to 0. The log(NRMSE) above zero are cropped, because an NRMSE greater than 1 means the error is larger than the information itself and is considered useless.

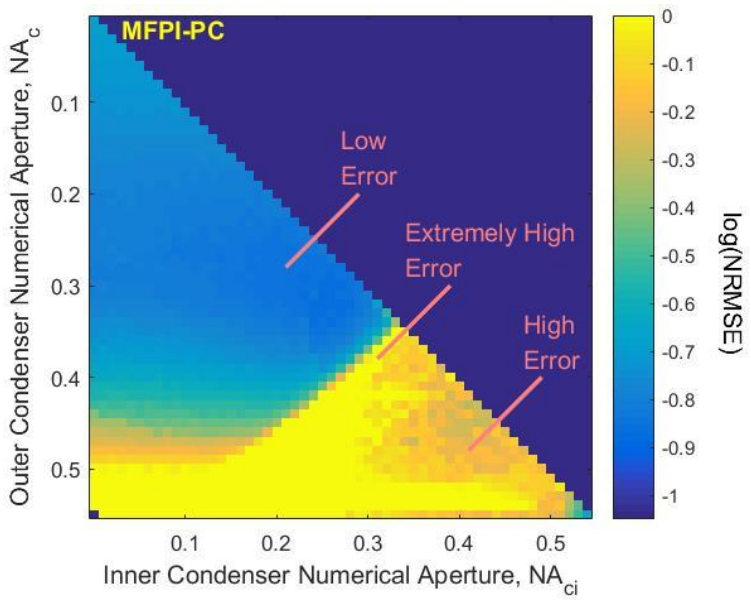

Figure 5.3. Logarithm of NRMSE of the recovered phases at various inner and outer numerical apertures. The $\mathrm{NA_c}$ ranges from 0.01 to 0.55 and the $\mathrm{NA_{ci}}$ ranges from 0 to 0.54. The colorbar scale is from -1.05 to 0. The values above zero are cropped.

From the 2D log NRMSE plot, three separate regions can be identified. A low-error region exists in the upper left while a high-error region exists in the lower right. These two distinct regions are separated by an extremely-high-error narrow band region. The extremely-high-error band is located near a line $\mathrm{NA_{ci}}/2 + \mathrm{NA_c} = \mathrm{NA_o}$. The three cases in Figure 5.2 are examples of the three regions.

5.3.2 Reason for Large Error

The reason for the large errors in the previous results can be explained by the WD-PCTF. Figure 5.4 shows the WD-PCTFs for four different $\mathrm{NA_{ci}}$. All the WD-PCTFs are approximately the same (exactly the same if the paraxial approximation is used) in the interval $\lambda\rho \leq \mathrm{NA_o} - \mathrm{NA_c}$, and start to deviate from disk illumination as ρ increases. A center valley forms with nonzero $\mathrm{NA_{ci}}$. As $\mathrm{NA_{ci}}$ increases, the local minimum value of

the central valley decreases, and when $\mathrm{NA_{ci}}$ is large enough, this value can be negative. The local minimum is close to zero when $\mathrm{NA_{ci}}/2 + \mathrm{NA_c} \approx \mathrm{NA_o}$.

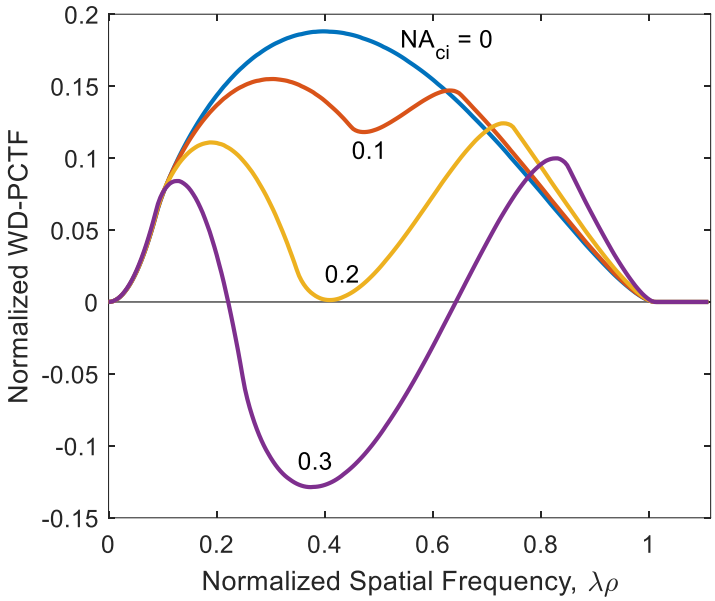

Figure 5.4. WD-PCTFs ($T_W(\rho)$) for four different $\mathrm{NA_{ci}}$. The horizontal axis is the normalized longitudinal spatial frequency $\lambda\rho$ and the vertical axis is the normalized WD-PCTF. The normalization makes these quantities dimensionless. Other parameters are fixed and are the same as in the simulation of Figure 5.2.

Since MFPI-PC is based on transfer function inversion, a WD-PCTF close to zero causes significant noise magnification. Usually, a regularization method, such as hard cutoff or Wiener filtering, has to be applied to deal with the noise magnification problem. The previous results are obtained by hard cutoff, that is, if the absolute value of the WD-PCTF is too small (smaller than 0.01 times the maximum absolute value of WD-PCTF), the corresponding frequency component is manually set to be zero. By using this hard cutoff, the error is already much smaller in the high-error region, but it is still much larger than the error in the low-error region. When the WD-PCTF is close to zero in a

larger interval, the error tends to be larger, so the error tends to be the largest at $\mathrm{NA_{ci}}/2 + \mathrm{NA_c} \approx \mathrm{NA_o}$, which is in the extremely-high-error band.

5.4 Improved MFPI-PC Theory

In order to apply MFPI-PC to general annular illumination situations, some improvement of the QPI algorithm is necessary. Notice that in MFPI-PC, multiple intensity derivatives are calculated using multiple SGDF orders, but the Fourier transforms of them are divided by the same transfer function, the WD-PCTF. This is because the PCTF for the (2k-1)th SGDF order is approximated by the WD-PCTF. The ratio of $T_W(\rho)$ and $T_k(\rho)$ is called the phase transfer function (PTF) in Ref. [82]. For each spatial frequency component, only one SGDF order is selected to calculate the phase at that spatial frequency. The order selected is the lowest order that has a PTF greater than a critical value. Since $T_W(\rho)$ is used instead of $T_k(\rho)$ in phase recovery, the difference between them should be small enough, so the PTF must be greater than a critical value. When their difference is sufficiently small, a lower-order SGDF is preferred because it is better able to provide noise reduction. Figure 5.5 shows WD-PCTF ($T_W(\rho)$) and PCTFs ($T_k(\rho)$) for other SGDF orders for $\mathrm{NA_{ci}}$ = 0.2. As the SGDF order increases, $T_k(\rho)$ approaches $T_W(\rho)$.

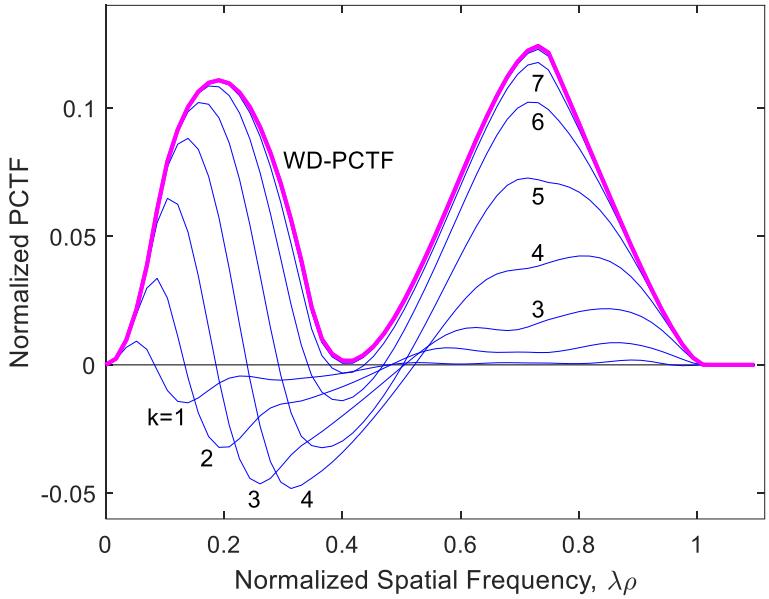

Figure 5.5. WD-PCTF ($T_W(\rho)$) and PCTFs ($T_k(\rho)$) for various SGDF orders for NA_{ci} = 0.2. The horizontal axis is the normalized longitudinal spatial frequency $\lambda\rho$ and the vertical axis is the normalized PCTF. The normalization makes these quantities dimensionless. Other parameters are fixed and are the same as in the simulation of Figure 5.2. Curves for $k \geq 8$ are nearly the same as WD-PCTF.

Approximating $T_k(\rho)$ by $T_W(\rho)$ works well in disk illumination, because a higher-order PCTF is always larger than a lower-order PCTF, and they are all positive. However, in annular illumination, the PCTF can be negative, and lower-order PCTFs can have larger absolute values than higher-order PCTFs and the WD-PCTF. In some midrange frequencies, the WD-PCTF and higher-order PCTFs have very small absolute values, which cause significant noise magnification, but lower-order PCTFs may not have this problem. For example, in Figure 5.5, when $\lambda\rho = 0.4$, the best SGDF order is 4, because its corresponding PCTF has the largest absolute value. On the contrary, WD-PCTF has much smaller absolute values than low-order PCTFs.

With this disadvantage of the WD-PCTF approximation, it is beneficial to use $T_k(\rho)$ directly rather than $T_W(\rho)$ in annular illumination. In fact, in the calculation of the

PTF, $T_k(\rho)$ is already calculated within MFPI-PC. A possible reason for not using $T_k(\rho)$ directly might be its low accuracy attributed to the numerical calculation method used when Ref. [82] was published. However, the calculation method can be improved as discussed in Appendix D. As a result, and the computational accuracy of $T_k(\rho)$ is very good now, so there is no penalty in using $T_k(\rho)$ directly. In addition to fewer approximations, there is another important advantage of using $T_k(\rho)$ rather than $T_W(\rho)$. Transfer functions $T_k(\rho)$ with different order k have different zero crossings, so even when some $T_k(\rho)$ and $T_W(\rho)$ are very close to zero, other orders with larger $T_k(\rho)$ can be chosen to recover the phase more accurately.

In order to solve the problem of dividing by zero, the set of binary filters used in the original MFPI-PC to combine results from various SGDF orders cannot be used anymore. Instead, we have to find some smooth filters that are weighted according to the magnitude of the PCTFs. A good candidate is least squares filtering. That is, the individual recovered phases are averaged with weight equaling the modules square of their PCTFs $T_k(\rho)$ [83, 125]. That is

$$\Phi(\boldsymbol{\rho}) = \frac{\sum_k |T_k(\rho)|^2 \Phi^{(k)}(\boldsymbol{\rho})}{\sum_k |T_k(\rho)|^2 + \alpha}, \tag{5.9}$$

where k is the SGDF order, and α is a regularization parameter in Wiener filtering to avoid small denominator. If written in a form compatible with the original method as

$$\Phi(\boldsymbol{\rho}) = \sum_k \xi^{(k)}(\rho) \Phi^{(k)}(\boldsymbol{\rho}), \tag{5.10}$$

the weighting filter $\xi^{(k)}(\rho)$ is

$$\xi_{LS}^{(k)}(\rho) = \frac{|T_k(\rho)|^2}{\sum_k |T_k(\rho)|^2 + \alpha}. \tag{5.11}$$

This method will be called least-squares MFPI-PC (LS-MFPI-PC) in this paper.

However, LS-MFPI-PC does not account for the fact that a lower-order SGDF is better at denoising than a higher-order SGDF, even if their $T_k(\rho)$ values are very close. This is an important fact, which dominates the binary filter design in the original MFPI-PC. In order to account for this fact, we should give lower-order results extra weight and give higher-order results smaller weight. This extra weighting should demonstrate the denoising capability of SGDF. Mathematically, the noise magnification capability of any finite impulse response filter is represented by the sum of the modulus squares of the impulse response function [133, 134]. Denoising capability is the inverse of noise magnification capability. Therefore, the extra weighting should be $1/\sum_i \left|a_i^{(k)}\right|^2$, where $a_i^{(k)}$ is the impulse response of the (2k-1)th order SGDF. The modified weighting filter $\xi^{(k)}(\rho)$ is then

$$\xi_{WLS}^{(k)}(\rho) = \frac{\left|T_{P,k}^{(2)}(\rho)\right|^2 / \sum_i \left|a_i^{(k)}\right|^2}{\sum_k \left[\left|T_{P,k}^{(2)}(\rho)\right|^2 / \sum_i \left|a_i^{(k)}\right|^2\right] + \alpha}. \tag{5.12}$$

Figure 5.6 is the flow chart of the LS-MFPI-PC and WLS-MFPI-PC algorithms. It is very similar to Figure 3 in Ref. [109], except that the WD-PCTF is replaced by the PCTFs for the corresponding SGDF orders, and the weighting filter $\xi^{(k)}(\rho)$ is changed.

The weighting filter $\xi^{(k)}(\rho)$ is also the only difference between LS-MFPI-PC and WLS-MFPI-PC.

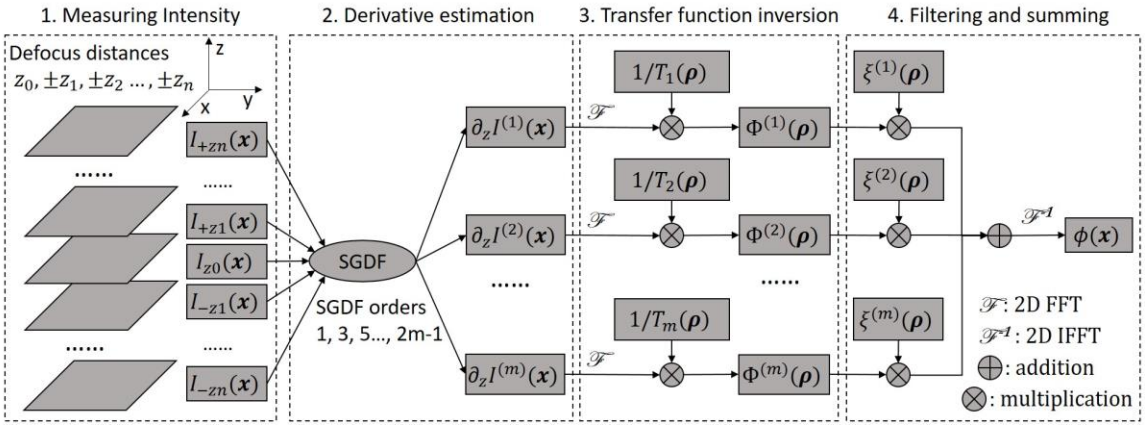

Figure 5.6. Flow chart showing the basic procedure of the modified MFPI-PC (for LS-MFPI-PC, $\xi^{(k)}(\rho)$ is $\xi_{LS}^{(k)}(\rho)$, and for WLS-MFPI-PC, $\xi^{(k)}(\rho)$ is $\xi_{WLS}^{(k)}(\rho)$, where $\xi^{(k)}(\rho)$ is the weighting filter). $I_z(r)$ is the image intensity at defocus distance z. $\partial_z I^{(k)}(r)$ is the longitudinal intensity derivative at the focal plane, calculated using the (2k-1)th order SGDF [79]. $T_k(\rho)$ is the PCTF for the (2k-1)th order SGDF. $\phi^{(k)}(\rho)$ is the recovered phase in the spatial frequency domain corresponding to the (2k-1)th order SGDF.

5.5 Simulation Results from the Improved Methods

In order to quantify the improvement associated with the WLS-MFPI-PC method, simulations were performed comparing its phase recovery with that of the original MFPI-PC method. The metric used will continue to be the NRMSE. The simulation results for WLS-MFPI-PC are shown in Figure 5.7. The phase of the original Lenna is shown in Figure 5.7(a) again. All the simulation parameters are the same as in Figure 5.2.

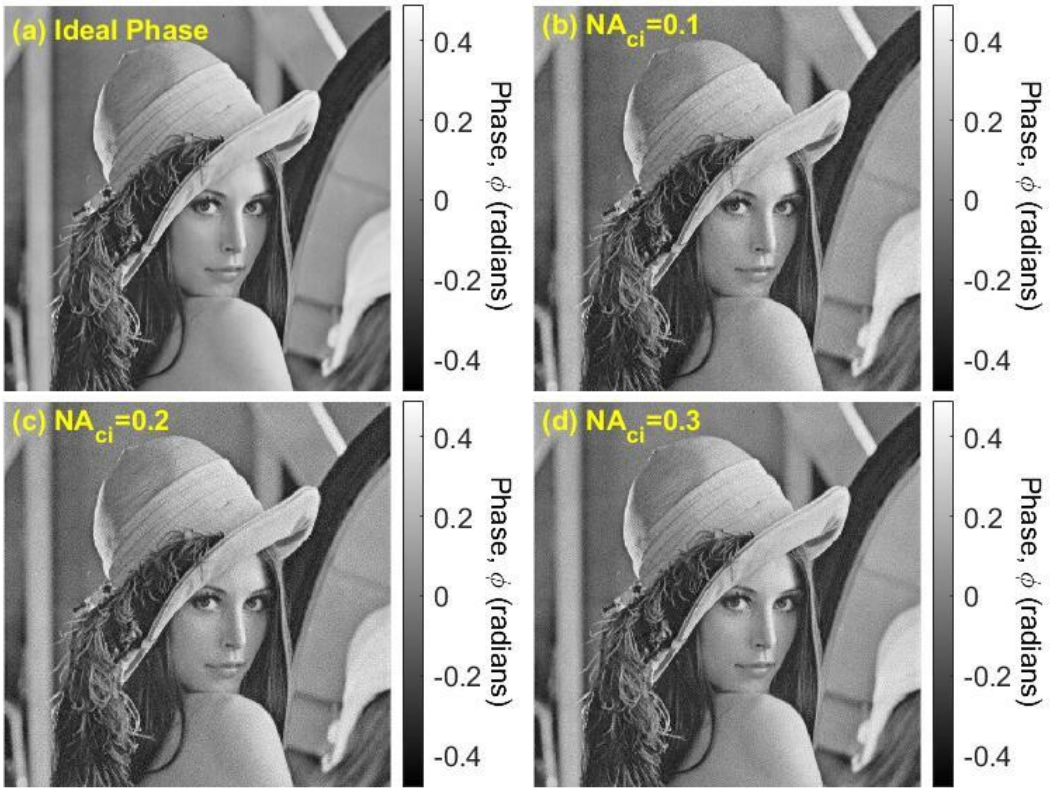

Figure 5.7. Simulation of the phases recovered for various NA_{ci} at a constant NA_c using WLS-MFPI-PC. The units on the colorbars are radians. The ranges of the ideal phase and the three recovered phases are all from -0.48 to +0.49 radians. (a) The ideal phase image to be simulated; (b)-(d) the phases recovered at NA_{ci} = 0.1, 0.2, and 0.3 respectively.

Figure 5.7(b) shows the recovered phase when NA_{ci} = 0.1. The NRMSE was 0.157. Figure 5.7(c) shows the recovered phase when NA_{ci} = 0.2. The NRMSE was 0.177. Figure 5.7(d) shows the recovered phase when NA_{ci} = 0.3. The NRMSE was 0.155. The NRMSE values for WLS-MFPI-PC for each NA_{ci} value are close to each other, and they are significantly lower than their original MFPI-PC counterparts in Figure 5.2.

The simulation results for various combinations of inner and outer numerical apertures for both LS-MFPI-PC and WLS-MFPI-PC are shown in Figure 5.8. Figure 5.8(a) shows LS-MFPI-PC result and (b) shows WLS-MFPI-PC result. The simulation

parameters are the same as in Figure 5.3. The two NRMSE plots show that the LS-MFPI-PC method appears to be an improvement over the MFPI-PC method, while the WLS-MFPI-PC method appears to be a further improvement. In addition, the distinct regions found in the NRMSE plot for MFPI-PC are much less significant for LS-MFPI-PC and completely disappear for WLS-MFPI-PC.

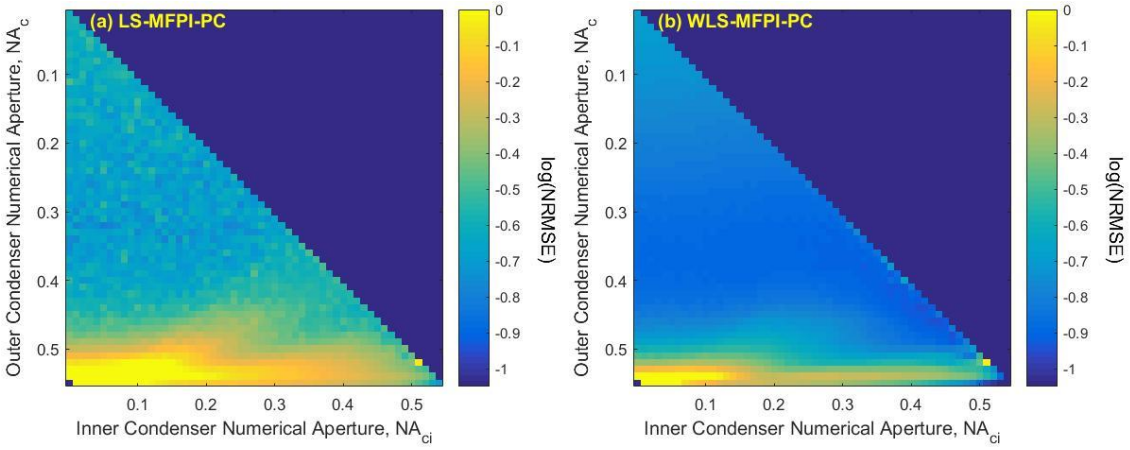

Figure 5.8. Logarithm plots of the NRMSE of the recovered phases at various inner and outer numerical apertures using LS-MFPI-PC and WLS-MFPI-PC. The NA_c ranges from 0.01 to 0.55 and the NA_{ci} ranges from 0 to 0.54. (a) The NRMSEs of the recovered images using LS-MFPI-PC. (b) The NRMSEs of the recovered images using WLS-MFPI-PC. The colorbar scales are from -1.05 to 0. The values above zero are cropped.

To further demonstrate the benefits of LS-MFPI-PC and WLS-MFPI-PC, every NRMSE value in each of the plots in Figure 5.8 has been compared to their respective NRMSE value in the plot for the original MFPI-PC method as shown in Figure 5.3. In each of the comparisons, an indicator P is used to show the positivity of the NRMSE difference, which is defined as

$$P(\Delta\text{NRMSE}) = \begin{cases} -1, & \text{if } \Delta\text{NRMSE} < -0.01 \\ 0, & \text{if } |\Delta\text{NRMSE}| \leq 0.01 \\ 1, & \text{if } \Delta\text{NRMSE} > 0.01 \end{cases}. \tag{5.13}$$

The absolute value of the NRMSE difference must be greater than the threshold of 0.01 to have a nonzero positivity indicator value, because an NRMSE difference smaller than such a threshold can be considered not noticeable, since it might simply be a result of random noise. Figure 5.9(a) shows the difference when the NRMSE values of LS-MFPI-PC are subtracted from those of MFPI-PC, Figure 5.9(b) shows the difference when the NRMSE values of WLS-MFPI-PC are subtracted from those of MFPI-PC, and Figure 5.9(c) shows the difference when the NRMSE values of WLS-MFPI-PC are subtracted from those of LS-MFPI-PC.

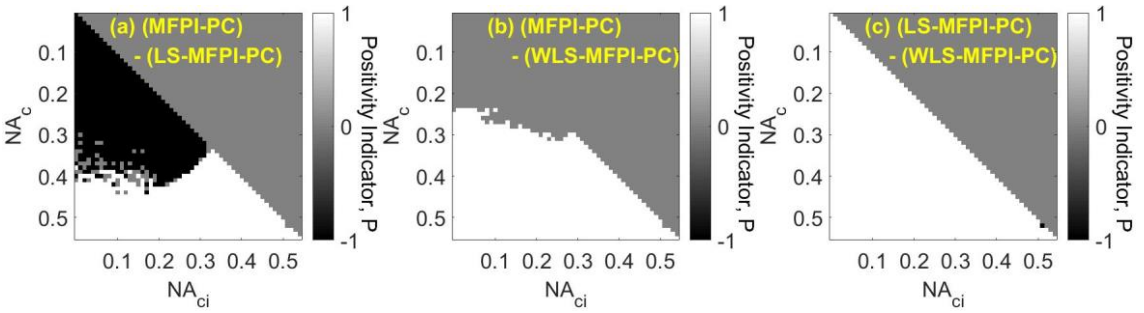

Figure 5.9. 2D Plots of the differences in NRMSE between the three methods: MFPI-PC, LS-MFPI-PC, and WLS-MFPI-PC. The NA_c ranges from 0.01 to 0.55 and the NA_{ci} ranges from 0 to 0.54. The colorbar scales have three indicator values, where 1 represents all positive values, -1 represents all negative values, and 0 represents values near 0. (a) The difference when the NRMSE values of LS-MFPI-PC are subtracted from those of MFPI-PC. (b) The difference when the NRMSE values of WLS-MFPI-PC are subtracted from those of MFPI-PC. (c) The difference when the NRMSE values of WLS-MFPI-PC are subtracted from LS-MFPI-PC.

Figure 5.9(a) shows P = 1 in the high NA_c region and P = -1 in the low NA_c region. Therefore, LS-MFPI-PC is better than the original MFPI-PC in the previous high-error region, but it is generally worse in the previous low-error region. This is because LS-MFPI-PC solves the problem of dividing by zero in the previous high-error region, but it does not place appropriate weight for different SGDF orders, so it is generally worse than the original MFPI-PC when the problem of dividing by zero does not exist in

the previous low-error region. Figure 5.9(b) shows P = 1 in the high NA_c region and P = 0 in the low NA_c region, and Figure 5.9(c) shows mostly P = 1. Therefore, while WLS-MFPI-PC does not always produce the lowest NRMSE, it never produces a noticeably higher NRMSE than its counterparts. This indicates that WLS-MFPI-PC is the optimal method of the three, because it solves the problem of dividing by zero and still keeps the appropriate weight for different SGDF orders.

The relationship between NRMSE and NA_c and NA_{ci} is further expanded upon in Figure 5.10. Figure 5.10(a) shows NRMSE plotted against NA_{ci} at three selected NA_c values, and Figure 5.10(b) shows NRMSE plotted against NA_c at four selected NA_{ci} values. From these curves, we can tell that NRMSE is almost independent of NA_{ci}. When NA_c increases, NRMSE decreases first and then increases.

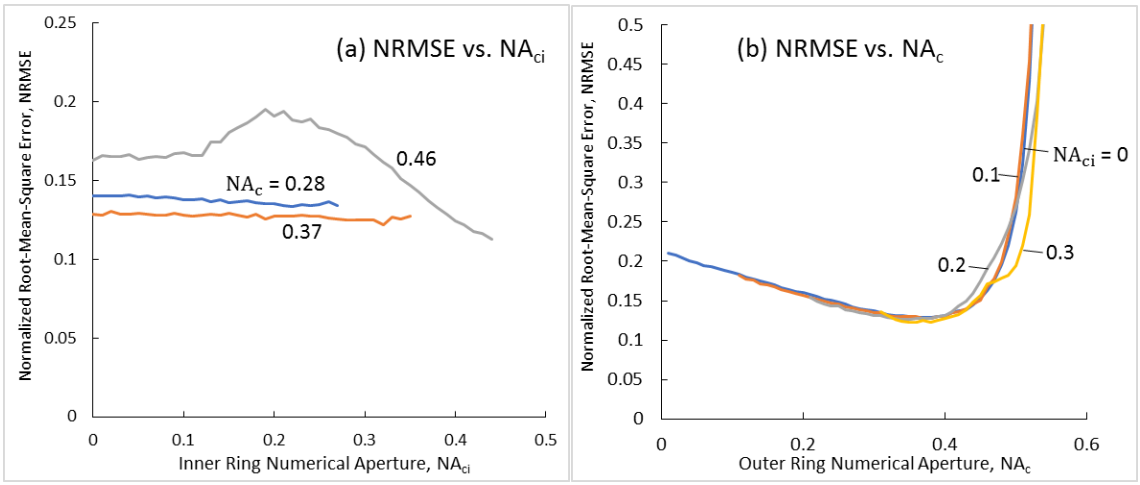

Figure 5.10. NRMSE plots of various values of NA_c and NA_{ci}. (a)NRMSE vs NA_{ci} at various NA_c. The NRMSE scale is from 0 to 0.25. The selected constant NA_c are 0.28, 0.37, and 0.46. The NA_{ci} values range from 0 to NA_c. (b) NRMSE vs NA_c at various NA_{ci}. The NRMSE scale is from 0 to 0.5. The selected constant NA_{ci} are 0, 0.1, 0.2, and 0.3. The NA_c values range from NA_{ci} to 0.55.

5.6 Experimental Validation

The new QPI method WLS-MFPI-PC with annular illumination was also applied to experimental data. The phase pattern of a periodic microlens array (Thorlabs MLA150-7AR) was quantitatively imaged. The experimental configuration is described in Chapter 2, except the condenser lens. The annular illumination is shaped by a phase contrast condenser, Olympus U-PCD2. In order to match the magnification with the objective lens, the annulus 40X was chosen. The numerical apertures of the condenser are measured to be NA_c = 0.331 and NA_{ci} = 0.292. They are determined by measuring the inner and outer radii of the annuli under another microscope, and comparing their radii to the radius of NA equaling 0.75, because the NA is proportional to the radius. See Appendix D for a detailed explanation. Intensity images at 31 equally distributed planes (the focal plane and 15 pairs of symmetrically defocused planes) were captured and then used in the recovery of the quantitative phase image.

Figure 5.11(a) shows the recovered phase from the WLS-MFPI-PC. Figure 5.11(b) shows the line profiles of the phase along the center row (shown in dashed lines) of Figure 5.11(a) and the phase from the thickness as directly measured by a profilometer (KLA-Tencor P-15). The result shows that WLS-MFPI-PC with annular illumination can recover the phase of the microlens accurately.

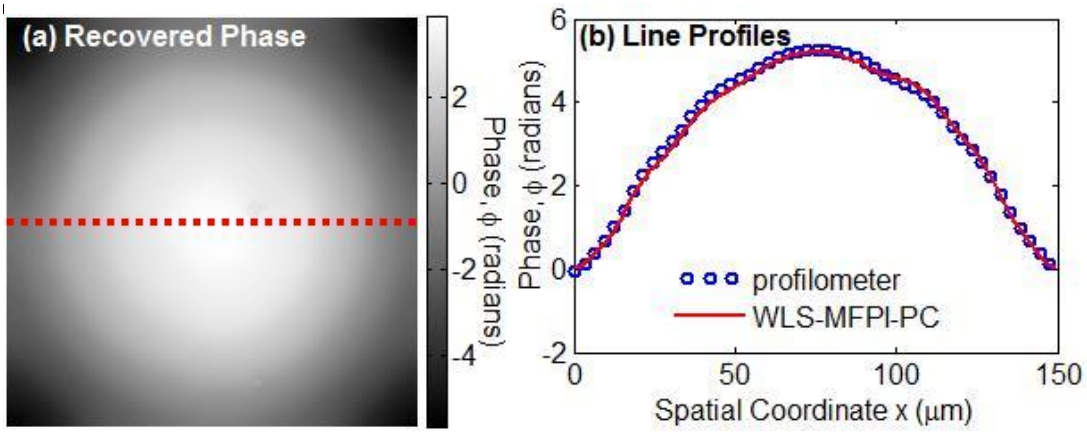

Figure 5.11. Experimentally measured quantitative phase images of a microlens. The units on the colorbars are radians. (a) The phase recovered by the WLS-MFPI-PC for a single microlens. (b)The line profiles of the phase along the center row (dotted line) of (a) and the phase from the thickness as directly measured by the profilometer. The vertical axis is the phase delay relative to the edge of the microlens.

5.7 Summary and Discussion

From the WD-PCTF curves in Figure 5.4, we observe some potential advantages of annular illumination compared to disk illumination. In the low-spatial-frequency region ($\lambda\rho \leq \mathrm{NA_o} - \mathrm{NA_c}$), the WD-PCTF are almost the same for various $\mathrm{NA_{ci}}$ (actually exactly the same if the paraxial approximation is used). In the midrange-frequency region ($\mathrm{NA_o} - \mathrm{NA_c} < \lambda\rho < \mathrm{NA_o} + \mathrm{NA_{ci}}$), the WD-PCTF for annular illumination is smaller than that for disk illumination. However, in the high-frequency region ($\mathrm{NA_o} + \mathrm{NA_{ci}} \leq \lambda\rho < \mathrm{NA_o} + \mathrm{NA_c}$), the WD-PCTF for annular illumination is larger than that for disk

illumination. This can be seen from the analytical expression of WD-PCTF, Eq. (5.8). Since $T_W(\rho; 0, \rho_{si}) = 0$ when $\lambda\rho \geq \mathrm{NA_o} + \mathrm{NA_{ci}}$, Eq. (5.8) can be simplified as $T_W(\rho; \rho_{si}, \rho_s) = \frac{\rho_s^2}{\rho_s^2 - \rho_{si}^2} T_W(\rho; 0, \rho_s)$, which clearly indicates that the WD-PCTF for annular illumination is larger than that of disk illumination. A large transfer function is often preferred, because it can lead to a higher signal-to-noise ratio. Therefore, annular illumination has advantages over disk illumination for high-spatial-frequency information recovery, which may lead to a better resolution.

In addition to annular illumination, WLS-MFPI-PC can also be used in other QPI applications even if disk illumination is used. For example, in Chapter 8, WLS-MFPI-PC is used in the 2D QPI of short-period gratings, and it provides smoother and less noisy phase recovery than the original MFPI-PC and POTFR [83].

Although MFPI-PC is inspired by TIE, its formulation does not directly involve TIE or variations of it. Computation times for MFPI-PC and WLS-MFPI-PC are generally faster than those for TIE-based QPI methods. Another important advantage of MFPI-PC is that it has been generalized to include nonparaxial conditions. This increases the accuracy of QPI in high NA systems.

In summary, a new QPI method, weighted-least-squares multi-filter phase imaging with partially coherent light (WLS-MFPI-PC) has been introduced and demonstrated to produce superior images for the important case of annular illumination. We have shown that the analytical 3D POTF derived in Ref. [109, 114] can be extended to annular illumination by Eq. (5.7). Based on that, the QPI method nonparaxial MFPI-PC can also be extended to annular illumination. However, the WD-PCTF may have zero

crossings in annular illumination, which causes significant noise magnification. In order to solve this problem, LS-MFPI-PC and WLS-MFPI-PC are developed by using the PCTFs for various SGDF orders instead of the approximated WD-PCTF and combining resulting phases from various SGDF orders by proper weighting filters. The simulation results show that WLS-MFPI-PC is better than the original MFPI-PC and LS-MFPI-PC. The microlens measurement also validates this new QPI method. Thanks to the analytical 3D POTF, the computation time is still very short. Specifically, the entire process can be calculated in a few seconds using Matlab on a typical personal computer. This short computation time enables potentially real-time calculation speeds for the characterization of fast phenomena.

CHAPTER 6. COMPARISON AND DEVELOPMENT OF MFPI-PC AND POTFR

6.1 Comparison of Original MFPI-PC and POTFR

MFPI-PC [82] and POTFR [83] are both defocus-based 2D QPI methods developed in Optics Laboratory. Both of them are developed for partially coherent optical systems and can be implemented with a commercial microscope. Apparently, there is some difference in their recovery results, since their principles are not the same. Although both methods are based on transfer function inversion in practice, MFPI-PC is based on the relation between the intensity derivative and the object phase, while POTFR is based on the relation between the intensity difference and the object phase. MFPI-PC was initially developed using paraxial approximations, while POTFR was originally developed for nonparaxial conditions. Although both of them use filters to combine results from different sets of data, MFPI-PC uses binary bandpass filters determined by cutoff frequencies, while POTFR uses weighting filters derived from least-squares fitting. Another difference is that MFPI-PC requires equally distanced defocused planes, while POTFR is flexible with defocused distances. In addition, the derivation of MFPI-PC requires a purely transparent object, while POTFR has taken weak object absorption into account. However, MFPI-PC has an advantage in that it can use semi-analytical transfer functions while those in POTFR are calculated using numerical simulations. Table 6.1 summarized the differences between the original MFPI-PC and POTFR.

Table 6.1. Comparisons of some properties of original MFPI-PC and POTFR. The bold terms have advantages.

Property	MFPI-PC	POTFR
Target quantity	Intensity derivative	Intensity difference
Paraxial or not	Paraxial approximations	**Nonparaxial condition**
Filters	Binary bandpass filters	**Least-squares filters**
Defocus distances	Equally spaced planes	**Flexible distances**
Object absorption	No absorption	**Weak absorption**
Transfer functions	**Semi-analytical**	Numerical

From the above comparison, it seems that POTFR is better than MFPI-PC in general, since it has fewer disadvantages. However, all of these disadvantages can be overcome. In this chapter, the solutions to overcome these disadvantages are presented, and the improved MFPI-PC and POTFR are then compared by simulations.

6.2 Improved MFPI-PC

6.2.1 Nonparaxial MFPI-PC

The original MFPI-PC uses the paraxial approximation. In fact, it used TIE, which is only applicable to paraxial situations. As a consequence, the maximum recoverable spatial frequency is $(\mathrm{NA_o} - \mathrm{NA_c})/\lambda$, which is small and decreases with increased NAc. In order to overcome this disadvantage, nonparaxial MFPI-PC with OF modification (nP-MFPI-PC-OF) is developed in Chapter 4, in which the analytical nonparaxial 3D POTF derived in Chapter 3 is used to generalize MFPI-PC to the nonparaxial condition. The

maximum recoverable spatial frequency becomes $(\mathrm{NA_o} + \mathrm{NA_c})/\lambda$, which is large and increases with increased $\mathrm{NA_c}$.

6.2.2 Weighted-Least-Squares MFPI-PC

The original MFPI-PC uses a set of binary bandpass filters to choose the optimal SGDF order. It generally cannot give the optimal result from the tradeoffs among various SGDF orders. Particularly, it has a large error when annular illumination is used. In order to overcome this disadvantage, weighted-least-squares MFPI-PC (WLS-MFPI-PC) is developed in Chapter 5. A set of filters derived from least-squares fitting, further multiplied by an extra weight inversely proportional to the noise magnification factor of the SGDF orders, is used to replace the binary filters.

6.2.3 Nonuniform Plane Separation

The original MFPI-PC uses SGDF to determine the intensity derivative from defocused images. SGDF only works for equally distributed samples, which requires equally distributed defocus planes. However, using uniform defocused planes is usually inefficient. In fact, some papers have shown that exponential distribution is the optimal strategy in similar QPI methods [135, 136]. Therefore, it is necessary to extend SGDF to nonuniformly spaced planes. Fortunately, the solution has been found in Ref. [137] by using discrete orthogonal polynomials, and Jenkins has used this solution in Ref. [83] to describe MFPI-PC with nonuniform plane separation, although it is only briefly mentioned and not published as a separate paper.

6.2.4 Weak Object Absorption

The original MFPI-PC is based on the simplified TIE, Eq. (2.8), which approximates the in-focus intensity to be uniform, so a purely transparent object is required. However, after the previous improvements, the improved MFPI-PC does directly rely on TIE anymore, and it should be applicable to weakly absorptive objects without modification.

The rigorous analysis starts with the 3D image formation scheme described by Eqs. (2.3) and (2.4). In addition to POTF, the AOTF has to be considered as well for absorptive objects. The formula to calculate AOTF is Eq. (3.20) or (3.21). An important difference between POTF and AOTF is that the POTF is an odd function while the AOTF is an even function [108]. Therefore, the absorption term can often be eliminated by subtraction of symmetric intensities, which is done in POTFR. On the other hand, MFPI-PC is based on the PCTF calculated from Eq. (2.11). The quantities $H_{SG,k}\left(\mathrm{e}^{2\pi i\eta\Delta z}\right)$ and $H(\rho,\eta)$ are both odd functions, so the integration is generally non-zero. However, when absorption is considered, a corresponding transfer function, which might be called absorption transfer function, should be calculated as

$$T_{A,k}(\rho)=\frac{4\pi}{\lambda\Delta z}\int H_{SG,k}\left(e^{2\pi i\eta\Delta z}\right)H_A(\rho,\eta)\mathrm{d}\eta. \tag{6.1}$$

In this equation, the AOTF $H_A(\rho,\eta)$ replaces the POTF $H(\rho,\eta)$. Since AOTF is an even function, the resulting integration becomes zero, *i.e.*, $T_{A,k}(\rho)=0$. Therefore, weak absorption does not affect the SGDF-fitted intensity derivative, and so MFPI-PC and WLS-MFPI-PC can also be applied to weakly absorptive objects without modifications.

With these three disadvantages overcome, MFPI-PC is more powerful. The improved MFPI-PC will also be called WLS-MFPI-PC in the rest of this chapter, which actually can combine the WLS-MFPI-PC defined in Chapter 5 with nonuniform defocused planes.

6.3 Improved POTFR: Semi-analytical 2D POTF

POTFR is based on the relation of the intensity of the defocused image and the object phase via Eq. (2.20). The computation of the transfer function, 2D POTF $H_z(\boldsymbol{\rho})$ is critical. The original paper uses a 2D integral, Eq. (16) in Ref. [83], to calculate the 2D POTF, and a two-fold loop is required, so the computation is very slow. On the contrary, in MFPI-PC, the transfer function, PCTF, is calculated by a 1D integral, Eq. (2.11), which is much faster than 2D integral with the help of analytical 3D POTF. Moreover, Eq. (2.11) can be calculated without a loop in MATLAB, which further enlarges the difference between their computation time. Therefore, if a semi-analytical formula of calculating the 2D POTF similar to Eq. (2.11) can be derived, it will greatly increase the computation speed. This section will provide such a formula.

The semi-analytical nature of MFPI-PC is enabled by the analytical 3D POTF, so in order to derive a semi-analytical formula for the 2D POTF, we should relate the 2D defocused image $I_z(\boldsymbol{x})$ to the 3D image $I(\boldsymbol{r})$. In fact, the relation is trivial,

$$I_z(\boldsymbol{x}) = I(\boldsymbol{x}, z). \tag{6.2}$$

Plugging in the linearized relations, Eqs. (2.3) and (2.19), we can know that the background, phase term, and absorption term all should be equal correspondingly. For our interest, only the phase term is listed here,

$$h_z(\boldsymbol{x}) * \phi(\boldsymbol{x}) = [h(\boldsymbol{x}, z') * v(\boldsymbol{x}, z')]_{z'=z}. \tag{6.3}$$

Then the relation between the phase and the SP must be found. Since the object is thin, if it is described by a 3D RI distribution, it must be proportional to $\delta(z)$. Since the phase equals the integrated RI difference along the z direction multiplied with k_0, the object can be represented as

$$\Delta n(\boldsymbol{x}, z') = \phi(\boldsymbol{x})\delta(z')/k_0, \tag{6.4}$$

where

$$\Delta n = n - n_0 \tag{6.5}$$

is the RI difference between the object and the immersion medium. When Δn is small, Eq. (2.1) can be simplified by Tylor expansion as (considering $n_0 = 1$ as before)

$$v(\boldsymbol{r}) = -2k_0^2 \Delta n(\boldsymbol{r}). \tag{6.6}$$

Combining Eqs. (6.4) and (6.6), the relation between the SP and the phase can be found as

$$v(\boldsymbol{x}, z') = -2k_0 \phi(\boldsymbol{x})\delta(z'). \tag{6.7}$$

Combining Eqs. (6.3) and (6.7), we know

$$h_z(\boldsymbol{x}) * \phi(\boldsymbol{x}) = -2k_0[h(\boldsymbol{x}, z') * \delta(z')]_{z'=z} * \phi(\boldsymbol{x}). \tag{6.8}$$

Therefore, we can conclude that

$$h_z(\boldsymbol{x}) = -2k_0 h(\boldsymbol{x}, z). \tag{6.9}$$

This simple equation relates the 2D PSF with the 3D PSF. Taking 2D Fourier transform of Eq. (6.9), the left-hand side becomes the 2D POTF $H_z(\boldsymbol{\rho})$, while the right-hand side can also be calculated by a 1D inverse Fourier transform from the 3D POTF $H(\boldsymbol{\rho}, \eta)$, so the result is

$$H_z(\boldsymbol{\rho}) = -2k_0 \int H(\boldsymbol{\rho}, \eta) \exp(2\pi i \eta z)\, \mathrm{d}\eta. \tag{6.10}$$

This is the semi-analytical formula of the 2D POTF. It is significantly simpler than Eq. (16) in Ref. [83] in calculation, because it only requires a 1D integral of the analytical 3D POTF, and the computation does not require a loop in MATLAB. In fact, the 1D integral is an inverse Fourier transform, so there can be even more advantages if the 2D POTFs in a large number of equally distributed defocused planes are required. Also notice that if z is small, $\exp(2\pi i \eta z)$ can be approximated using first-order Tylor expansion, and the resulting formula is almost the same as Eq. (2.12), the weakly-defocused PCTF in MFPI-PC, except a coefficient z. In fact, the phrase "weak defocus" exactly means small z. This result can be easily understood, since if z is small, the intensity difference can be used to

approximate the intensity derivative. This similarity also shows the MFPI-PC and POTFR have some intrinsic similarities.

By default, the analytical 3D POTF mentioned above refers to the one calculated by Eqs. (3.13)-(3.18), which is the analytical 3D POTF for a nonparaxial partially coherent system with a disk illumination. If annular illumination is used, Eq. (5.7) also ensures that the analytical 2D POTF can be calculated by a weighted difference similar to Eq. (5.8) used in MFPI-PC. The improved POTFR will sometimes be still called POTFR in the rest of this chapter.

6.4 Comparison of WLS-MFPI-PC and Improved POTFR

After the improvements discussed above, all the disadvantages shown in Table 6.1 have been overcome. These improvements make WLS-MFPI-PC and improved POTFR close to each other, and no significant difference can be found easily. Nevertheless, it is worthwhile to test the improved methods by simulations to show which can be better. Both disk illumination and annular illumination are tested, and both uniformly distributed planes and nonuniformly distributed planes are tested.

6.4.1 Disk Illumination

The simulation is performed using the standard Lenna image as the test object, similar to that done in Chapter 5. The mean values are subtracted from all the images. NRMSE is used to quantify the error.

The phase of the original Lenna is the same as Figure 5.2(a). It is a pure phase object with no absorption. The object has a size of 512×512 pixels. The pixel size was

245 nm. The wavelength of light is 546 nm. The numerical aperture of the objective lens was NA_o = 0.55. The disk condenser lens had a numerical aperture of NA_c = 0.4. Intensity images at 31 equally distributed planes (the focal plane and 15 pairs of symmetrically defocused planes) were simulated and then used in the recovery of the quantitative phase image. The distance between neighboring planes is $\Delta z = 0.6$ μm. White Gaussian noise with $\sigma = 0.01$ (SNR = 40 dB) was added.

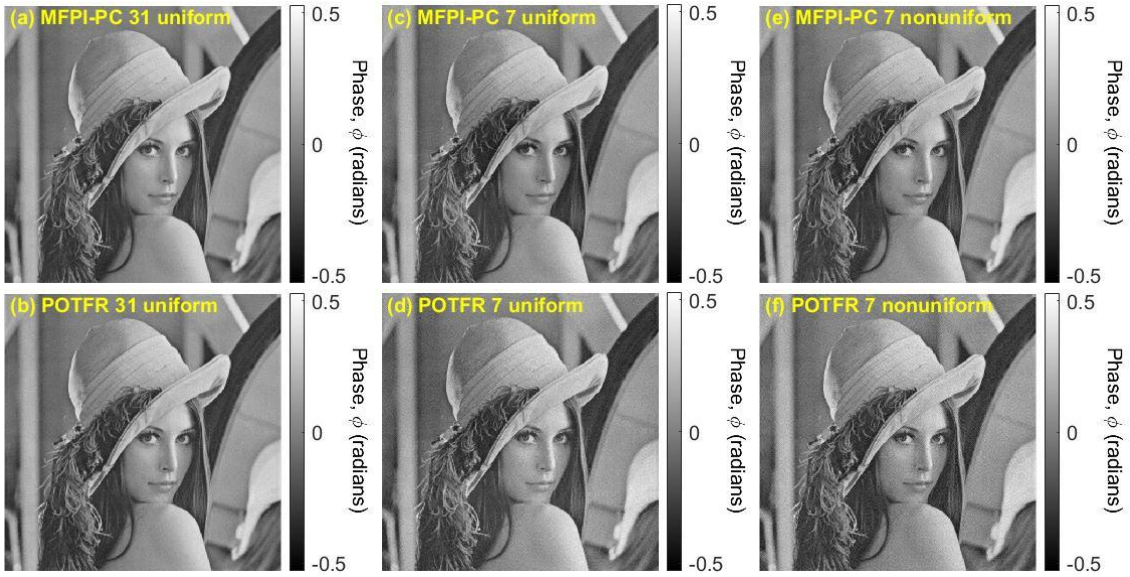

Figure 6.1. Simulation of the phases recovered from WLS-MFPI-PC and improved POTFR using disk illumination. The units on the colorbars are radians. The ranges of the phases are all from -0.53 to +0.53 radians. (a) The phase recovered from WLS-MFPI-PC using 31 uniform planes. NRMSE = 0.107. (b) The phase recovered from improved POTFR using 31 uniform planes. NRMSE = 0.118. (c) The phase recovered from WLS-MFPI-PC using 7 uniform planes. NRMSE = 0.184. (d) The phase recovered from improved POTFR using 7 uniform planes. NRMSE = 0.230. (e) The phase recovered from WLS-MFPI-PC using 7 nonuniform planes. NRMSE = 0.172. (f) The phase recovered from improved POTFR using 7 nonuniform planes. NRMSE = 0.216.

Although intensities at 31 planes are simulated, not all of them have to be used in phase recovery. Usually, imaging short-time process prefers a small number of measured images. When all 31 images are used, the phases recovered from WLS-MFPI-PC and

improved POTF are shown in Figure 6.1(a) and (b) respectively. The NRMSE was 0.107 for WLS-MFPI-PC and 0.118 for POTFR. Figure 6.1(c) and (d) use intensities at 7 uniformly distributed planes, a focal plane and 3 pairs of symmetrically defocused planes whose defocus distances are $\pm 3\Delta z$, $\pm 6\Delta z$, and $\pm 9\Delta z$. The NRMSE of the WLS-MFPI-PC result (Figure 6.1(c)) is 0.184, and the NRMSE of the improved POTFR result (Figure 6.1(d)) is 0.230. Figure 6.1(e) and (f) use intensities at 7 nonuniformly distributed planes, whose defocus distances are $\pm \Delta z$, $\pm 4\Delta z$, and $\pm 15\Delta z$. The NRMSE of the WLS-MFPI-PC result (Figure 6.1(e)) is 0.172, and the NRMSE of the improved POTFR result (Figure 6.1(f)) is 0.216. Using NRMSE values, the accuracy of these results can be compared quantitatively. The results from WLS-MFPI-PC are better than those from improved POTFR in general. When 31 uniform planes are used, they are very close. However, when 7 number planes are used, WLS-MFPI-PC is significantly better than improved POTFR. The errors from 7 planes are larger than that from 31 planes.

In order to characterize the relation of the error and the numerical apertures in a larger scope, the simulation results for various combinations of $\mathrm{NA_o}$ and $\mathrm{NA_c}$ are shown in Figure 6.2. These results are generated using a scaled down 128×128 version of the original Lenna object. White Gaussian noise with $\sigma = 0.01$ (SNR = 40dB) was added. The $\mathrm{NA_o}$ values range from 0.01 to 0.55 at 0.01 intervals along the y-axis. The $\mathrm{NA_c}$ values have the same range and interval along the x-axis. The values represented are the logarithm of the NRMSE of the recovered phase compared to the ideal phase image. Only the cases of $\mathrm{NA_c} < \mathrm{NA_o}$ are shown, since this is the assumption used in the derivation of 3D POTF and is usually satisfied in practice. Therefore, the upper right triangle part is nonphycical. The range of the colorbar is from -0.88 to 0. WLS-MFPI-PC

is used in Figure 6.2(a), (c), and (e), and improved POTFR is used in Figure 6.2(b), (d), and (f). In addition, different numbers of defocused planes are also tested. Figure 6.2(a) and (b) are simulated using 31 uniform planes. Figure 6.2(c) and (d) are simulated using 7 uniform planes. Figure 6.2(e) and (f) are simulated using 7 nonuniform planes. The planes are selected to be the same as those used in Figure 6.1.

Figure 6.2 shows some useful information. In general, the results from WLS-MFPI-PC and improved POTFR are close. When a fewer number of planes are used, both methods result in larger errors. When the 7 planes become nonuniform, both methods result in slightly larger errors when both $\mathrm{NA_c}$ and $\mathrm{NA_o}$ are large. The behaviors are mostly consistent with the results in Figure 5.2. When $\mathrm{NA_o}$ increases, the errors in all cases decrease. When $\mathrm{NA_c}$ increases, the errors decrease first and then increase, so there is an optimal $\mathrm{NA_c}$ for a specific $\mathrm{NA_o}$.

In order to quantitatively compare the difference between WLS-MFPI-PC and improved POTFR, the relative difference of their NRMSEs, defined as

$$D = \frac{\mathrm{NRMSE_1}}{\mathrm{NRMSE_2}} - 1. \tag{6.11}$$

is calculated, where $\mathrm{NRMSE_1}$ is for WLS-MFPI-PC and $\mathrm{NRMSE_2}$ is for improved POTFR. The result is shown in Figure 6.3. A positive D means improved POTFR is better, and a negative D means WLS-MFPI-PC is better. Relative differences of 31 uniform planes, 7 uniform planes, and 7 nonuniform planes are shown in Figure 6.3(a)-(c) respectively. The colorbar scales are cropped from -0.1 to 0.1.

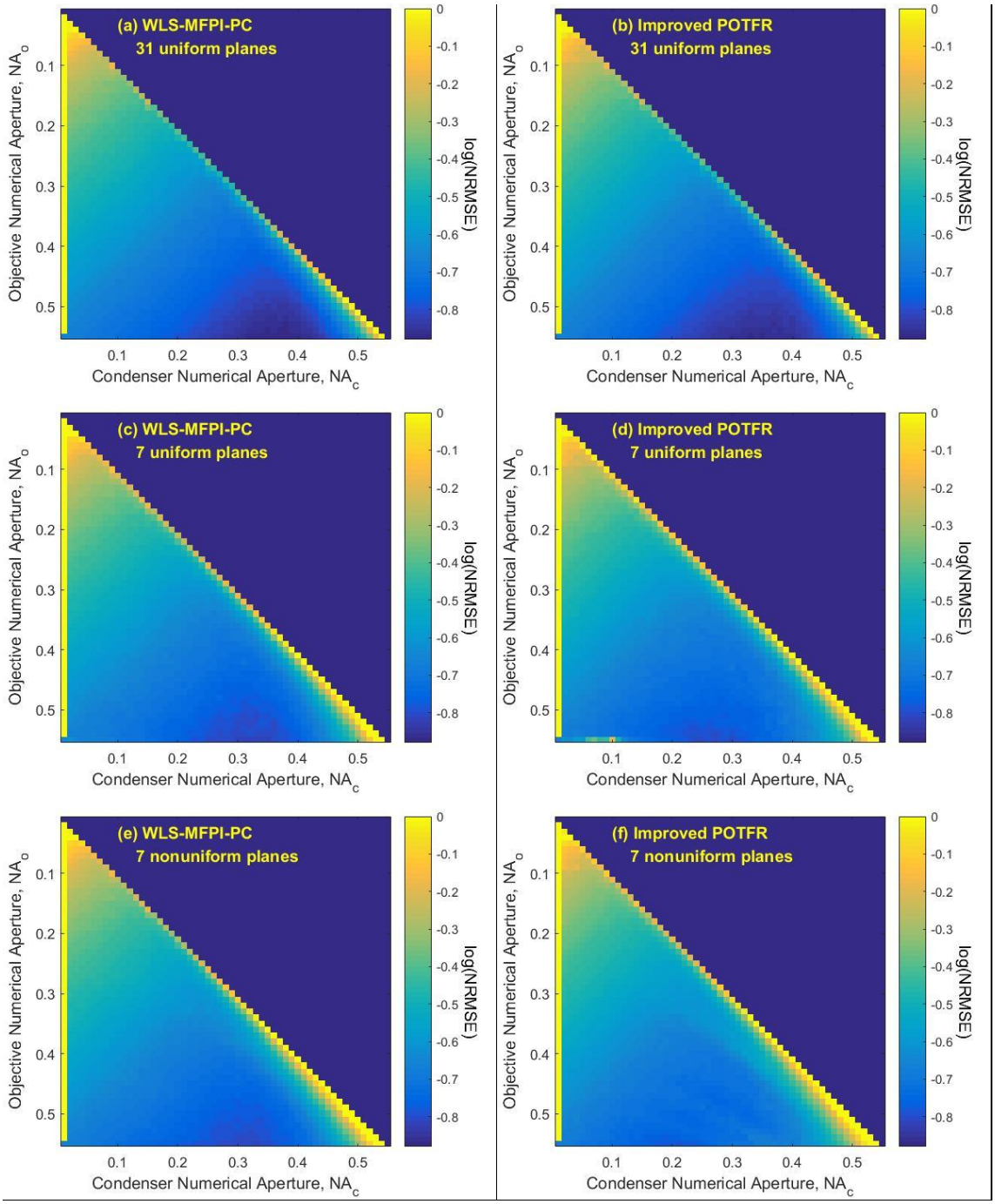

Figure 6.2. Logarithm plots of the NRMSEs of the recovered phases with disk illumination at various NA_o and NA_c using WLS-MFPI-PC and improved POTFR. Both the NA_o and NA_c range from 0.01 to 0.55. The scales of all colorbars are from -0.88 to 0. (a) The NRMSEs from WLS-MFPI-PC using 31 uniform planes. (b) The NRMSEs from improved POTFR using 31 uniform planes. (c) The NRMSEs from WLS-MFPI-PC using 7 uniform planes. (d) The NRMSEs from improved POTFR using 7 uniform planes. (e) The NRMSEs from WLS-MFPI-PC using 7 nonuniform planes. (f) The NRMSEs from improved POTFR using 7 nonuniform planes.

Figure 6.3 shows that when NA_c is large and when only 7 planes are used, WLS-MFPI-PC is significantly better than improved POTFR. Since higher NA_c brings higher spatial resolution and thus usually higher accuracy, the region where WLS-MFPI-PC is better is usually useful. When 31 planes are used, the advantage of WLS-MFPI-PC is small, and improved POTFR becomes better when $NA_c \approx NA_o$. However, the region where improved POTFR is better is associated with large errors, so it is usually not used.

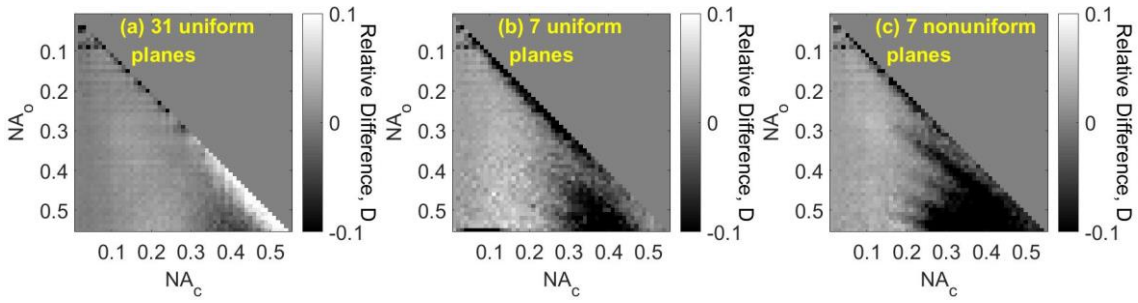

Figure 6.3. 2D Plots of the relative differences in NRMSE between WLS-MFPI-PC and improved POTFR for disk illumination. Both the NA_o and NA_c range from 0.01 to 0.55. The colorbar scales are cropped from -0.1 to 0.1. (a) Intensities at 31 uniform planes are used. (b) Intensities at 7 uniform planes are used. (c) Intensities at 7 nonuniform planes are used.

6.4.2 Annular Illumination

Similar simulation is also performed using annular illumination. The simulation conditions are the same, except that the annular condenser lens had an outer ring numerical aperture of $NA_c = 0.46$ and inner ring numerical aperture of $NA_{ci} = 0.3$. The results are shown in Figure 6.4 in the same pattern as Figure 6.1. The NRMSEs are written in the figure caption. Almost the same behaviors as disk illumination can be found. The results from WLS-MFPI-PC are better than those from improved POTFR in general. When 31 uniform planes are used, they are very close. However, when 7 number

planes are used, WLS-MFPI-PC is significantly better than improved POTFR. The errors from 7 planes are larger than that from 31 planes.

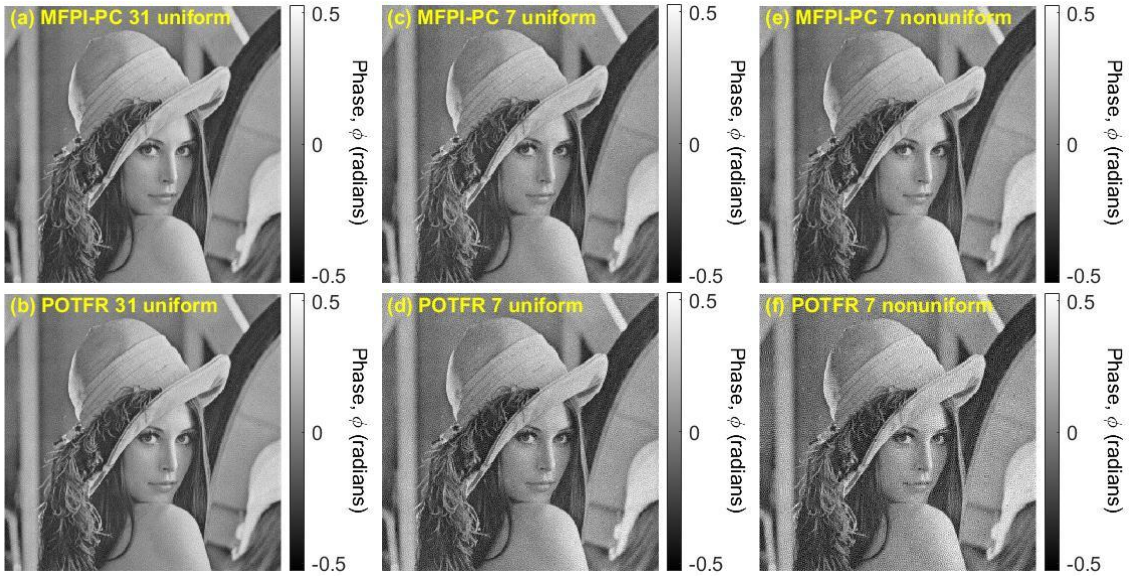

Figure 6.4. Simulation of the phases recovered from WLS-MFPI-PC and improved POTFR using annular illumination. The units on the colorbars are radians. The ranges of the ideal phase and the three recovered phases are all from -0.53 to +0.53 radians. (a) The phase recovered from WLS-MFPI-PC using 31 uniform planes. NRMSE = 0.153. (b) The phase recovered from improved POTFR using 31 uniform planes. NRMSE = 0.171. (c) The phase recovered from WLS-MFPI-PC using 7 uniform planes. NRMSE = 0.250. (d) The phase recovered from improved POTFR using 7 uniform planes. NRMSE = 0.360. (e) The phase recovered from WLS-MFPI-PC using 7 nonuniform planes. NRMSE = 0.247. (f) The phase recovered from improved POTFR using 7 nonuniform planes. NRMSE = 0.522.

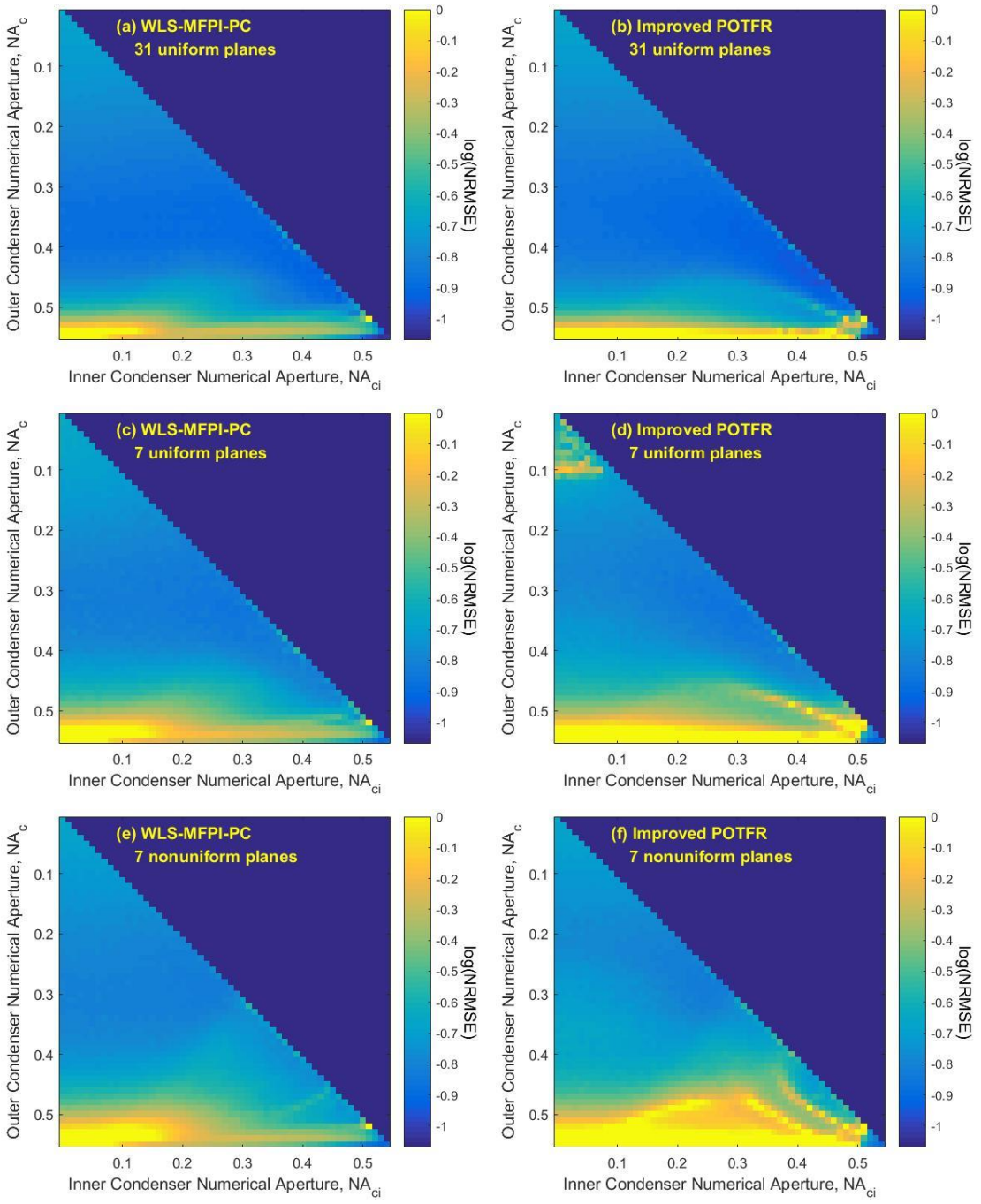

Figure 6.5. Logarithm plots of the NRMSEs of the recovered phases with annular illumination at various NA_c and NA_{ci} using WLS-MFPI-PC and improved POTFR. The NA_c ranges from 0.01 to 0.55, and the NA_{ci} ranges from 0.00 to 0.54. The scales of all colorbars are from -1.07 to 0. (a) The NRMSEs from WLS-MFPI-PC using 31 uniform planes. (b) The NRMSEs from improved POTFR using 31 uniform planes. (c) The NRMSEs from WLS-MFPI-PC using 7 uniform planes. (d) The NRMSEs from improved POTFR using 7 uniform planes. (e) The NRMSEs from WLS-MFPI-PC using 7 nonuniform planes. (f) The NRMSEs from improved POTFR using 7 nonuniform planes.

In order to characterize the relation of the error and the numerical apertures in a larger scope, the simulation results for various combinations of NA_c and NA_{ci} are also performed and shown in Figure 6.5. The NA_c values range from 0.01 to 0.55 at 0.01 intervals along the y-axis. The NA_{ci} values range from 0. to 0.54 at 0.01 intervals along the x-axis. The ranges are set so that $NA_c \leq NA_o$ is always satisfied. The values represented are the logarithm of the NRMSE of the recovered phase compared to the ideal phase image. Only the physical cases of $NA_{ci} < NA_c$ are shown. The range of the colorbar is from -1.07 to 0. The log(NRMSE) above zero are cropped, because an NRMSE greater than 1 means the error is larger than the information itself and is considered useless. The results are shown in Figure 6.5 in the same pattern as Figure 6.2.

Figure 6.5 shows that WLS-MFPI-PC is better than improved POTFR when NA_c is close to NA_o, although the NRMSEs are still close in other areas. When a fewer number of planes are used, both methods result in larger errors. When the 7 planes become nonuniform, both methods result in slightly larger errors. The behaviors are consistent with the results in Figure 6.4. Generally, NA_{ci} does not significantly affect the error when NA_c is not very close to NA_o. When NA_c increases, the errors decrease first and then increase, so there is an optimal NA_c, which is consistent with disk illumination case.

In order to quantitatively compare the difference between WLS-MFPI-PC and improved POTFR, the relative difference of their NRMSEs is also calculated, and the result is shown in Figure 6.6 in the same pattern as Figure 6.3. When 31 planes are used, WLS-MFPI-PC and improved POTFR are close, and one is better in some regions and

the other is better in some other regions. When only 7 planes are used, WLS-MFPI-PC is significantly better than improved POTFR in most cases. Therefore, WLS-MFPI-PC is generally better than improved POTFR.

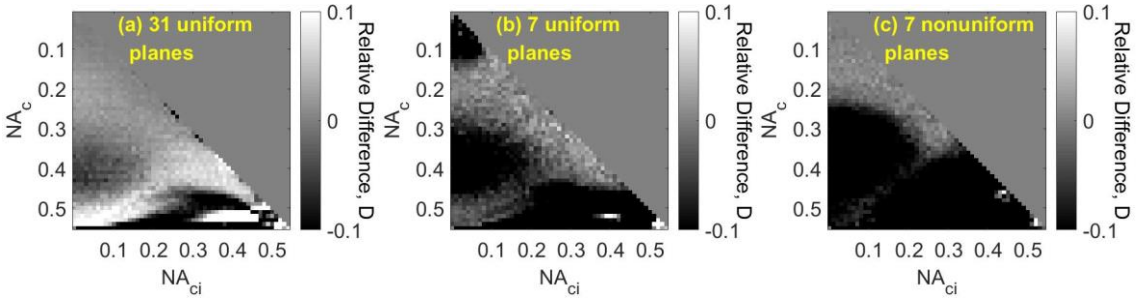

Figure 6.6. 2D Plots of the relative differences in NRMSE between WLS-MFPI-PC and improved POTFR for annular illumination. The NA_c ranges from 0.01 to 0.55, and the NA_{ci} ranges from 0.00 to 0.54. The colorbar scales are cropped from -0.1 to 0.1. (a) Intensities at 31 uniform planes are used. (b) Intensities at 7 uniform planes are used. (c) Intensities at 7 nonuniform planes are used.

6.4.3 Absorptive Object

In addition to a purely transparent object, simulations using absorptive objects are performed to verify the ability of WLS-MFPI-PC and improved POTFR in weakly absorptive case. The numerical apertures are chosen to be $NA_o = 0.75$, $NA_c = 0.375$, and $NA_{ci} = 0$. White Gaussian noise with $\sigma = 0.01$ (SNR = 40 dB) was added. Other conditions are the same as before. The transmittance function of the object is

$$t(\boldsymbol{x}) = \exp[i\phi(\boldsymbol{x}) - \beta a(\boldsymbol{x})], \tag{6.12}$$

where $\phi(\boldsymbol{x})$ is the regular phase function, and $\beta a(\boldsymbol{x})$ is the absorption function of the object. Here $a(\boldsymbol{x})$ is chosen to be a fixed pattern, and β is a varying absorption coefficient to control the strength of the absorption.

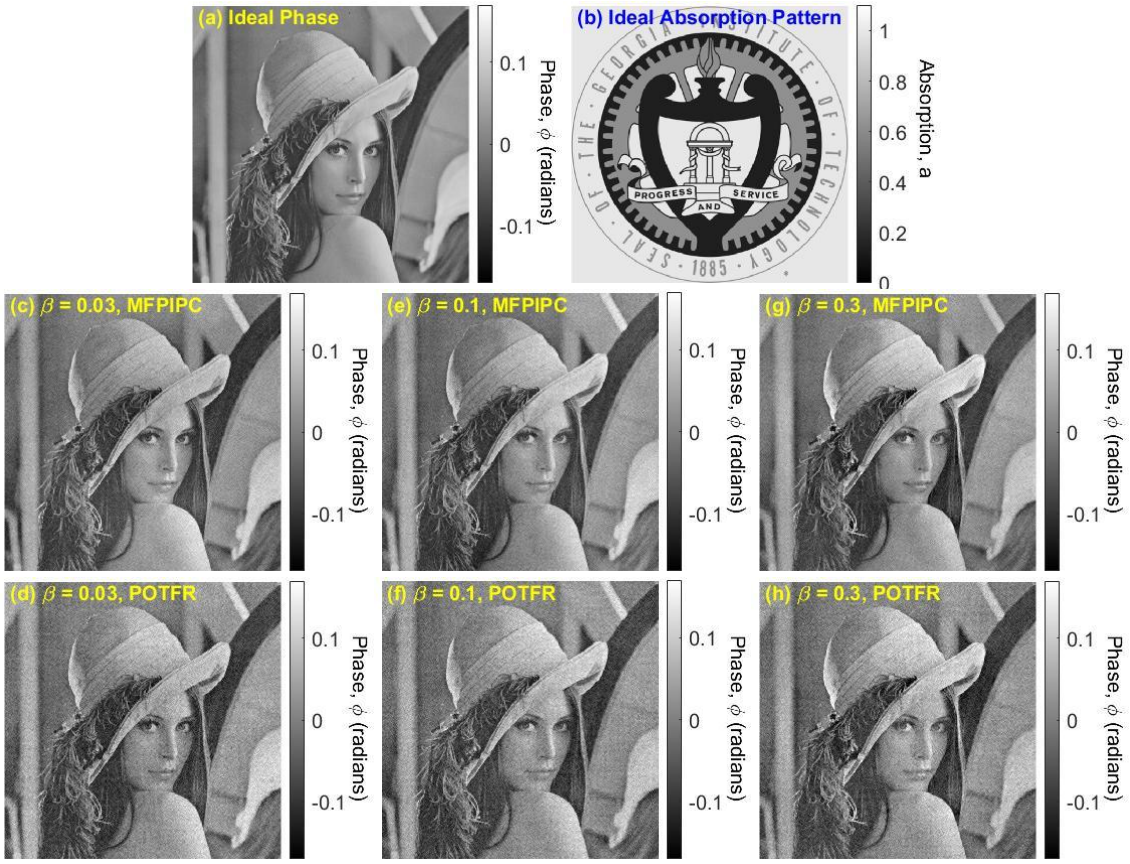

Figure 6.7. Simulation of the phases recovered from WLS-MFPI-PC and improved POTFR using absorptive objects. The units on the colorbars are radians, except that in (b) is dimensionless. The ranges of the phases are all from -0.17 to +0.17 radians. (a) The ideal phase. (b) The absorption pattern $a(x)$. (c) The phase recovered from WLS-MFPI-PC when $\beta = 0.03$. NRMSE = 0.273. (d) The phase recovered from improved POTFR when $\beta = 0.03$. NRMSE = 0.345. (e) The phase recovered from WLS-MFPI-PC when $\beta = 0.1$. NRMSE = 0.288. (f) The phase recovered from improved POTFR when $\beta = 0.1$. NRMSE = 0.336. (g) The phase recovered from WLS-MFPI-PC when $\beta = 0.3$. NRMSE = 0.293. (h) The phase recovered from improved POTFR when $\beta = 0.3$. NRMSE = 0.371.

The results are shown in Figure 6.7. Figure 6.7(a) is the phase of the object, $\phi(x)$, and Figure 6.7(b) is the fixed absorption pattern, $a(x)$. The object has a size of 512×512 pixels. The absorption coefficient β is chosen to be 0.03 in Figure 6.7(c) and (d), 0.1 in Figure 6.7(e) and (f), and 0.3 in Figure 6.7(g) and (h). WLS-MFPI-PC is used in Figure 6.7(c), (e), and (g), and improved POTFR is used in Figure 6.7(d), (f), and (h). The resulting NRMSEs are shown in the figure caption. As a comparison, when there is no

absorption ($\beta = 0$), the NRMSE from WLS-MFPI-PC is 0.258, and that from improved POTFR is 0.322. We can see that the errors increase slightly when the absorption coefficient β increases, but the difference is small. Therefore, both WLS-MFPI-PC and improved POTFR work well for weakly absorptive objects. In addition, we see that WLS-MFPI-PC has smaller errors than improved POTFR, again.

In order to characterize the relation of the error and the absorption coefficient in a larger scope, the simulation results for various combinations of β are performed under different noise levels. The results are shown in Figure 6.8. The horizontal axis shows the β values. The vertical axis represents the logarithm of the NRMSE of the recovered phase compared to the ideal phase image. Noise level is represented by the SNR, which can be 30 dB, 40 dB, 50 dB, 60 dB, and no noise. Each data point is simulated five times and the average NRMSE is calculated and plotted in the figure.

Figure 6.8 shows that the errors increase with increasing absorption coefficient, which is not surprising. However, when the absorption coefficient is very small, the curves are almost flat, and the increase becomes faster when the absorption coefficient is large. This trend further supports the claim that both WLS-MFPI-PC and improved POTFR work for weakly absorptive objects. When the absorption coefficient increases, the absorption is no longer weak, and the weak absorption approximation in the fundamental 3D image formation theory is violated, so the error becomes larger at a faster speed. These behaviors are consistent with the results in Figure 6.7. In addition, we see that WLS-MFPI-PC and improved POTFR have very close errors when noise is small, but in larger noise, WLS-MFPI-PC has smaller errors than improved POTFR. The better noise robustness might be attributed to more intensity planes used at a time, since

more data can cancel random noise at some level. POTFR uses only two symmetrically defocused planes to calculate a phase at a time, while MFPI-PC uses all intensity images each time.

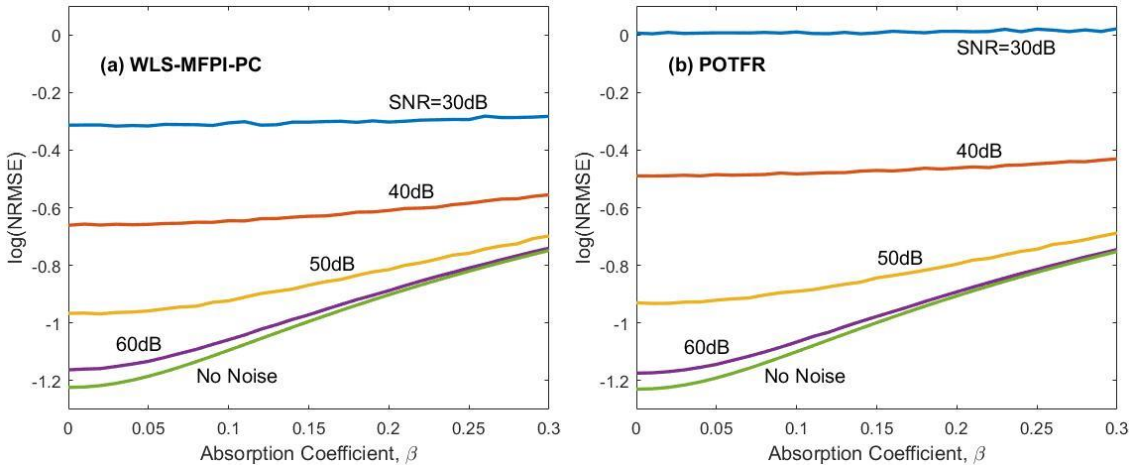

Figure 6.8. Logarithm plots of the NRMSEs of the recovered phases with absorption coefficient β using WLS-MFPI-PC and improved POTFR. The absorption coefficient β ranges from 0 to 0.3, and the logarithm of NRMSE ranges from -1.3 to 0.1. Different noise level is labeled with different colors, as shown in the figure legend. (a) The NRMSEs from WLS-MFPI-PC. (b) The NRMSEs from improved POTFR.

6.5 Summary and Discussion

As a side note, Ref. [82] claims that the optimal $\mathrm{NA_c}$ is approximately $\mathrm{NA_o}/2$ for MFPI-PC. It is based on the simulation results in that paper. However, I think this result is not appropriately explained. In Ref. [82], when $\mathrm{NA_c} = \mathrm{NA_o}/2$, it also makes the maximum spatial frequency the optical system can pass, $(\mathrm{NA_o} + \mathrm{NA_c})/\lambda$, very close to the maximum frequency the camera can measure, $1/(2\Delta x)$. When $\mathrm{NA_c}$ further increases, some spatial frequency cannot be received by the camera correctly, which results in aliasing. Therefore, the smallest error in that paper is not caused by $\mathrm{NA_c} = \mathrm{NA_o}/2$, but is

caused by $(\mathrm{NA_o} + \mathrm{NA_c})/\lambda = 1/(2\Delta x)$. In fact, as shown in Figure 6.4, the optimal $\mathrm{NA_c}$ is usually larger than $\mathrm{NA_o}/2$.

In summary, the original MFPI-PC and POTFR are compared and their relative advantages and disadvantages are compared in Table 6.1. All of these disadvantages are then overcome. The improvements of MFPI-PC are presented either in previous chapters or in Ref. [83]. The improvement of POTFR is presented in this chapter. After these improvements, the resulting WLS-MFPI-PC and improved POTFR are compared using simulations, and both uniformly distributed planes and nonuniformly distributed planes are tested. The results show that generally, the errors decrease with increasing $\mathrm{NA_o}$, decrease and then increase with increasing $\mathrm{NA_c}$, and do not vary significantly with $\mathrm{NA_{ci}}$. Using a small number of planes decreases the accuracy, which is the natural cost of faster measurement. WLS-MFPI-PC is generally as good as or better than improved POTFR, and it is more robust under noise.

CHAPTER 7. ITERATIVE OPTIMIZATION IN TOMOGRAPHIC DECONVOLUTION PHASE MICROSCOPY

As mentioned in Chapter 2, the measurement procedure of tomographic deconvolution phase microscopy (TDPM) is relatively time-consuming, because it requires many illumination angles. However, if the number of the rotation angle is not large enough, it may suffer from missing cone problem. In this chapter, an edge-preserving iterative regularization algorithm is developed and applied to TDPM to solve the missing cone problem, so that the required number of illumination angles is reduced from 15 to 3, while the measurement accuracy remains high. This work has been published in Ref. [138].

7.1 Problem Description

As introduced in Chapter 2, The 3D intensity $I(\boldsymbol{r})$ and the scattering potential (SP) $v(\boldsymbol{r})$ of the object is related by a point spread function (PSF) $h(\boldsymbol{r})$ via convolution or a phase optical transfer function (POTF) $H(\boldsymbol{f})$ via multiplication in the spatial-frequency domain. Therefore, by measuring the 3D image intensity $I(\boldsymbol{r})$ and calculating its Fourier transform $\tilde{I}(\boldsymbol{f})$, then $V(\boldsymbol{f})$ can be simply estimated from $\tilde{I}(\boldsymbol{f})/H(\boldsymbol{f})$. In practice, the division is computed in the regularized form using, for example, a Wiener filter, in order to avoid the problem of dividing by a very small number. However, the POTF has limited coverage in the spatial frequency domain, as shown in Figure 7.1(a), so only the frequency support of the POTF can be successfully recovered, and the frequency information outside the support is totally lost. This is called the missing cone problem

[92, 139]. This problem can be solved using object rotation. In TDPM, the object is rotated through 15 angles. The total frequency support of the 15-angle TDPM is shown in Figure 7.1(b), which effectively covers all the frequencies within the effective numerical aperture. However, if the number of angles is reduced, for example, to 3, then the new total frequency support is that shown in Figure 7.1(c), which still have some spatial frequency areas either equal to zero or have a very small value, so the deconvolution process will have greatly magnified noise.

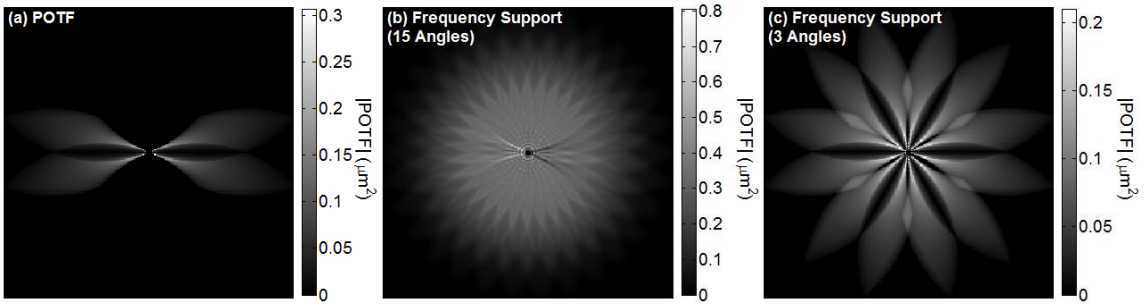

Figure 7.1. Cross section of 3D POTF and frequency support. (a) The absolute value of the POTF. (b) Sum of the absolute values of the POTFs in 15 angles, which shows the frequency support of 15 angles. (c) Sum of the absolute values of the POTFs in 3 angles, which shows the frequency support of 3 angles. The POTF is calculated according to [109], and has an objective numerical aperture of $\mathbf{NA_o = 0.75}$ and a condenser numerical aperture of $\mathbf{NA_c = 0.375}$.

7.2 Algorithm Description

7.2.1 Edge-Preserving Minimization

In the literature, iterative optimization is a popular class of algorithms to overcome the missing cone problem and thus to denoise the RI image [12, 92, 96, 140-142]. Instead of direct deconvolution in the frequency domain, these algorithms iteratively search the SP so as to provide the expected image intensities as close to the

measured images as possible. In the problem of this work, it is mathematically described by

$$v(\boldsymbol{r}) = \underset{v(\boldsymbol{r})}{\operatorname{argmin}} \left|\left|h(\boldsymbol{r}) * v(\boldsymbol{r}) - I(\boldsymbol{r})\right|\right|^2, \tag{7.1}$$

where $\left|\left|a(\boldsymbol{r})\right|\right|$ is the L^2 norm of $a(\boldsymbol{r})$ defined as

$$\left|\left|a(\boldsymbol{r})\right|\right|^2 \triangleq \int |a(\boldsymbol{r})|^2 d\boldsymbol{r}. \tag{7.2}$$

For the convenience of further discussion, v can be viewed as an element in a linear function space, and the convolution of h can be viewed as a linear imaging operator A, *i.e.*

$$Av \triangleq h(\boldsymbol{r}) * v(\boldsymbol{r}). \tag{7.3}$$

Alternatively, the convolution can also be calculated in the frequency domain by

$$Av = F^{-1}HFv, \tag{7.4}$$

where F is the Fourier transform operator, F^{-1} is the inverse Fourier transform operator, and H indicates multiplication by the POTF. In TDPM, there are multiple angles, so the minimization should be satisfied for the average value over all angles.

However, some constraints have to be applied to the minimization. Some widely used constraints include known spatial support, piecewise smoothness, and nonnegativity [92]. Known spatial support has been already incorporated into this minimization

problem. Nonnegativity is usually satisfied for biological samples, but not necessarily satisfied for other objects such as optical fibers. Therefore, in the following discussion, only the piecewise smoothness constraint is considered specifically. It is described by a minimization of a regularization function $J(v)$. The regularization function is usually in the form $J(v) = \int \psi(|\nabla v|)\mathrm{d}\boldsymbol{r}$, where $|\nabla v|$ is the gradient magnitude of $v(\boldsymbol{r})$, and $\psi(\cdot)$ is a function satisfying various requirements to preserve edges [143]. In the present paper, it is chosen to be $\psi(|\nabla v|) = \sqrt{|\nabla v|^2 + \varepsilon^2}$, where ε is a small number to avoid divisions by zero when the gradient is very small or null. This choice makes $J(v)$ the total variation function of v [144].

Including the regularization term, the total cost function to be minimized is

$$\Psi(v, I) = \frac{1}{2N}\sum\nolimits_m \left||A_m v_m - I_m|\right|^2 + \alpha J(v), \tag{7.5}$$

where N is the total number of angles, m is the angle number, and α is a regularization parameter to adjust the relative importance of the two minimization terms, and the summation is over all of the m angles. The first term $\frac{1}{2N}\sum_m \left||A_m v_m - I_m|\right|^2$ is called the similarity term, and the second term $\alpha J(v)$ is called the regularization term. Due to the rotations, in addition to 3D image intensity I_m, the object SP v_m and the convolution operator A_m may also vary with angle. The detailed forms of v_m and A_m will be discussed in the next subsection. The optimal v is then

$$v = \underset{v}{\operatorname{argmin}}\, \Psi(v, I). \tag{7.6}$$

7.2.2 Rotation Representation

In the TDPM experiment, the object is rotated while the camera is fixed, so the object and the images are in different relative orientations at each angle. Therefore, the cost function should account for rotation compensations at each angle. There are two possible solutions: The first solution is maintaining the positions of images I and rotating the object v, which mimics the experimental situation; the second solution is using a fixed position of object v and rotating the images I back to the corresponding position. The two solutions should be equivalent physically, but their behaviors can differ in practical numerical calculations. In the present paper, the first solution is called object rotation, and the second solution is called image rotation.

In order to account for the rotations in the cost function, a rotation operator Θ_m is defined, which simply rotates the object or image by the m-th angle. Therefore, in object rotation, the new cost function becomes

$$\Psi_{\mathrm{o}}(v, I) = \frac{1}{2N}\sum_m \left||A\Theta_m v - I_m|\right|^2 + \alpha J(v). \tag{7.7}$$

In image rotation, the new cost function becomes

$$\Psi_{\mathrm{i}}(v, I) = \frac{1}{2N}\sum_m \left||A_{-m} v - \Theta_{-m} I_m|\right|^2 + \alpha J(v). \tag{7.8}$$

where Θ_{-m} means rotating in the opposite direction by the m-th angle. In image rotation, the imaging operator is A_{-m} and is different at each angle, because the illumination beam has to be rotated by the same angle as the image I_m to keep the source, object, and

camera in a straight line. Specifically, A_{-m} can be calculated by rotating the PSF $h(\boldsymbol{r})$. The rotation direction in image rotation is opposite to that in object rotation, so that the relative angular positions of the source, object, and camera are equivalent.

Image rotation is perhaps easier to use, because A_{-m} and $\Theta_{-m}I_m$ can be determined before the iterative optimization starts, so an explicit rotation operation is not needed within the iterative optimization procedure. By comparison, object rotation is generally more difficult, because Θ_m has to be applied at each iteration step. It is perhaps not straightforward to calculate the effect of $A\Theta_m$ as a whole, unless an extra rotation is applied so that the problem is reduced to image rotation. On the other hand, since the image I usually occupies a larger and more irregular space than v does, rotating I in a limited cubic space may require some truncation, but this problem can be avoided by rotating v. Therefore, both rotation solutions have advantages and disadvantages. We can expect that image rotation requires less computation time, but object rotation is more accurate. In the following sections, most of the simulation and experiment results will use object rotation only, except for the direct comparison of the two rotation schemes.

7.2.3 Optimization Algorithm

There are many potential algorithms to minimize the nonlinear cost function $\Phi(v, I)$. In the present work, a simple gradient descent algorithm was chosen. Nevertheless, other algorithms could also be applied. If object rotation is used, the gradient of the cost function is

$$\nabla\Psi_{\mathrm{o}}(v, I) = \frac{1}{N}\sum\nolimits_m \left[\Theta_m^{\dagger}A^{\dagger}A\Theta_m v - \Theta_m^{\dagger}A^{\dagger}I_m\right] + \alpha\nabla J(v). \tag{7.9}$$

In this formula, $\nabla J(v)$ can be calculated according to [144], so the remaining problem is to calculate the adjoint operators $\Theta_m^\dagger$ and $A^\dagger$. A natural approach is to represent the operators in their matrix representations. However, the matrices are usually very large, and they are not even sparse matrices, so the memory requirement in the computation and thus the storage is excessively large. Therefore, a better approach is to continue with the operator forms. Fortunately, by using the definition of the adjoint operators [145], analytic expressions of $\Theta_m^\dagger$ and $A^\dagger$ in this problem can be derived. The details are given in Appendix E. The results are

$$A^\dagger = -A, \tag{7.10}$$

$$\Theta_m^\dagger = \Theta_{-m}. \tag{7.11}$$

These expressions require that the numbers of pixels in all dimensions are the same for the object and each 3D image, a condition that can be easily satisfied. Although it is possible to combine $\Theta_m^\dagger A^\dagger A \Theta_m$ as a single operator, the simulation results show that it is not as accurate as applying them in sequence, so this possibility is not further explored in the present paper.

If image rotation is used, the gradient of the cost function is

$$\nabla \Psi_{\mathrm{i}}(v, I) = \frac{1}{N} \sum\nolimits_m [A_{-m}^\dagger A_{-m} v - A_{-m}^\dagger \Theta_{-m} I_m] + \alpha \nabla J(v). \tag{7.12}$$

where $A_{-m}^\dagger = -A_{-m}$ is calculated in the same way as $A^\dagger$. By continuing with operator forms rather than using the matrix form, the operation on and storage of huge matrices

are avoided, so the memory requirement of this algorithm is relatively small [94]. This algorithm can be implemented on a typical personal computer.

A flow chart showing the entire process using object rotation is shown in Figure 7.2. The initial scattering potential $v^{(0)}$ can be calculated using the original TDPM or can be simply set to any arbitrary function. The quantity τ is the step length in the descent, which can vary in each iteration by line search. The parameter α should be chosen carefully to balance the two components of the cost function and optimize the imaging accuracy. Since the domain of v must cover the entire object in all rotation angles, the object must have a finite support region, and the SP must be zero sufficiently far from the center. Therefore, after each step in which the SP is updated, the object constraint should be applied, which means that the SP outside of the object support is reset to zero. The outside region can be defined as the region that can be truncated after rotation, or whose distance from the rotation axis is larger than the radius of the inscribed circle of the cubic domain. This reset step eliminates truncation errors arising from the object rotation. If the nonnegativity constraint is satisfied for the object, which means the RI of the object is always greater than or equal to that of the surrounding media, it can also be applied in this step. The process using image rotation is very similar, so its flow chart is not shown explicitly.

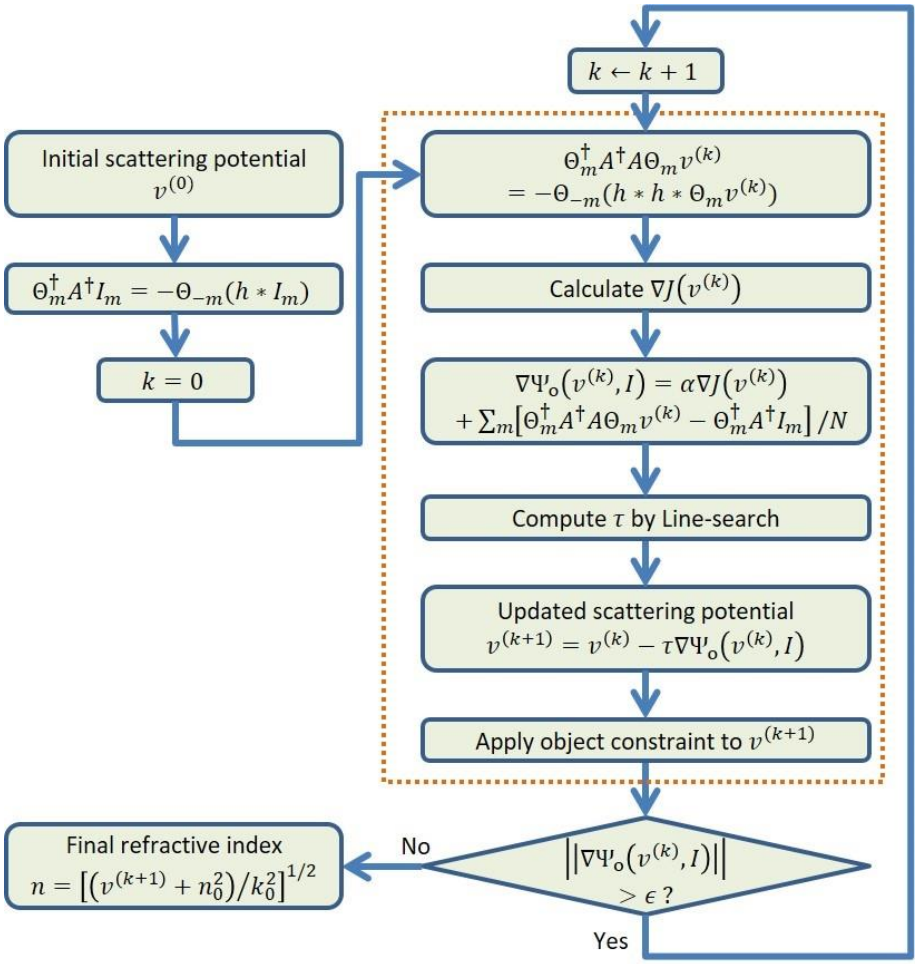

Figure 7.2. Flow chart of the iterative TDPM algorithm using object rotation.

7.3 Simulation Validation

In order to quantify the accuracy of the iterative TDPM (ITDPM), simulations were performed comparing its RI recovery with that from the original TDPM. The metric used to quantify the recovery accuracy is the normalized root-mean-square error (NRMSE), defined as

$$\text{NRMSE} = \left(\frac{\sum [n_r(x,z) - n_i(x,z)]^2}{\sum [n_i(x,z) - n_0^2]^2} \right)^{1/2}. \tag{7.13}$$

The summation is over all of the discrete pixels. The quantity $n_i(x,z)$ is the ideal RI, $n_r(x,z)$ is the recovered RI, and n_0 is the background RI.

The simulation results are shown in Figure 7.3. The object to be simulated was a cylinder whose cross section is a modified phantom. The RI cross section of the ideal object was shown in Figure 7.3(a). The RI of the background media was 1. The object field cross section had a size of 256×256 pixels and a maximum RI difference of 0.004. The objective numerical aperture is $NA_o = 0.75$, and the condenser numerical aperture is $NA_c = 0.375$. All the parameters were the same as in Ref. [99], except that only 3 angles were simulated and then used in the recovery of the quantitative RI. The PSF used here is simulated using the split-step beam propagation method (SSBPM) [99].

Figure 7.3(b) shows the reconstructed RI using the original TDPM. Although a large regularization parameter in the Wiener filter was used, the reconstructed RI is very noisy. The RI in some areas is actually much lower than the lower bound of the colorbar. The NRMSE is 0.94, which indicates that the error is at almost the same level as the RI variation itself. If the regularization parameter in the Wiener filter is not very large, the reconstructed RI consists almost only of noise. Figure 7.3(c) shows the reconstructed RI using the iterative TDPM with object rotation, in which $\alpha = 0.004$. The noise is effectively removed and the result is very clean. The NRMSE is reduced to 0.16. Figure 7.3(d) shows the reconstructed RI using the iterative TDPM with image rotation, in which $\alpha = 0.004$. The NRMSE is reduced to 0.22. The results show clearly that the iterative optimization algorithm successfully overcomes the missing cone problem caused

by the small number of angles in TDPM. In addition, the object rotation approach performs better than image rotation.

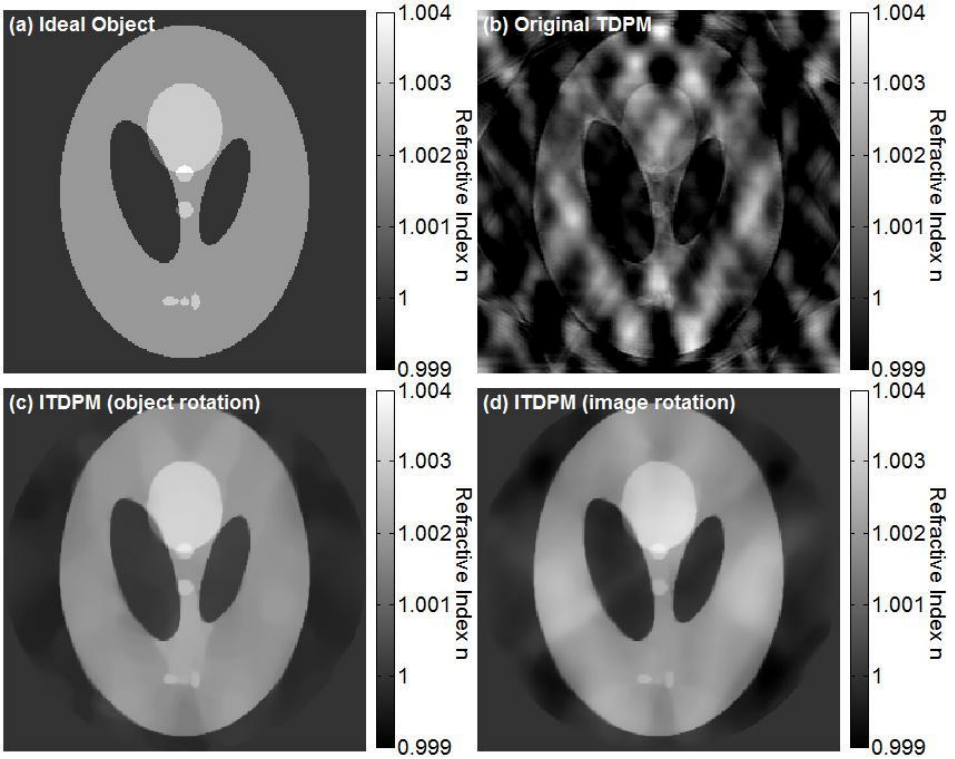

Figure 7.3. Simulation results for a modified phantom cylinder. The units on the colorbars are RI units. The ranges of the ideal RI and the recovered RIs are all from 0.999 to 1.004. (a) The ideal RI cross section to be simulated. (b) The RI cross section recovered by the original TDPM. The NRMSE is 0.94. (c) The RI cross section recovered by iterative TDPM using object rotation. The NRMSE is 0.16. (d) The RI cross section recovered by iterative TDPM using image rotation. The NRMSE is 0.22.

In order to select the optimal total number of angles N, simulations of various total numbers of angles were performed and compared. The results are shown in Figure 7.4. The ideal RI cross section is again shown in Figure 7.4(a), and the ITDPM reconstructed RI cross sections from 2-6 angles are shown in Figure 7.4(b)-(f) respectively. The NRMSEs are 0.34, 0.16, 0.17, 0.16, and 0.11 respectively. The results show that the $N \geq 3$ provides good recovery, but $N = 2$ are not sufficient. The NRMSEs

of 3-5 angles are very similar. Therefore, $N = 3$ represents a good tradeoff between measurement speed and reconstruction accuracy. Nevertheless, other N can be chosen depending on the optical system and the relative importance of speed and accuracy for a specific application. Appendix E provides a discussion of the effect of the total number of angles.

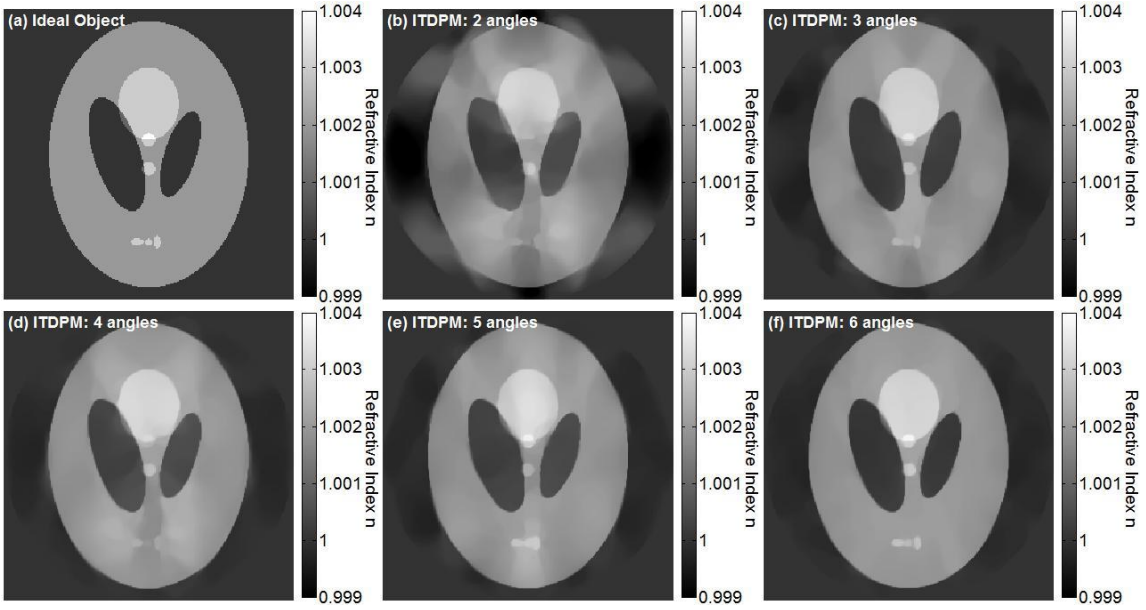

Figure 7.4. Simulation results for a modified phantom cylinder using iterative TDPM with various numbers of angles. The units on the colorbars are RI units. The ranges of the ideal RI and the recovered RIs are all from 0.999 to 1.004. (a) The ideal RI cross section to be simulated. (b) - (f) The RI cross sections recovered by iterative TDPM using 2 - 6 illumination angles. The NRMSEs are 0.34, 0.16, 0.17, 0.16, and 0.11 respectively.

7.4 Experimental Validation

The iterative TDPM method presented in this work was also applied to experimental data. Various optical fibers were used as test objects. The experimental configuration is described in Chapter 2. The condenser numerical aperture is $NA_c = 0.375$. Through-focal images at 3 equally distributed angles were captured and then used

in the recovery of the RI distribution. Each angle is 60° away from its neighbor. At each angle, a stack of 147 images was taken with a defocusing step size of 980 nm. The fibers are immersed in refractive index matching oil with a refractive index of $n_0 = 1.46$. Except for the number of angles (3), other experimental parameters are the same as those in Ref. [99].

The measurement was done for three fibers: a single-mode fiber (Corning SMF-28), a polarization-maintaining fiber (Thorlabs HB980T), and a photonic crystal fiber (Blaze Photonics ESM-12-01). The PSF used here is simulated using SSBPM with a Gaussian-fitted source function [99]. The results are shown in Figure 7.5. The images in the left column are reconstructed by the original TDPM, while the images in the right column were reconstructed by the iterative TDPM with object rotation, in which $\alpha = 0.004$. The data used in the iterative TDPM is a subset of the data used in the original TDPM. The improvement of imaging quality due to the iterations is significant. The results are consistent with [99] and other literature [82, 146, 147]. It is also consistent with the datasheet of the single-mode fiber, which specifies that the RI difference between the core and the cladding is 0.36% (0.0053). The RI reconstructed from an angularly offset set of angles with same angle separation are essentially the same.

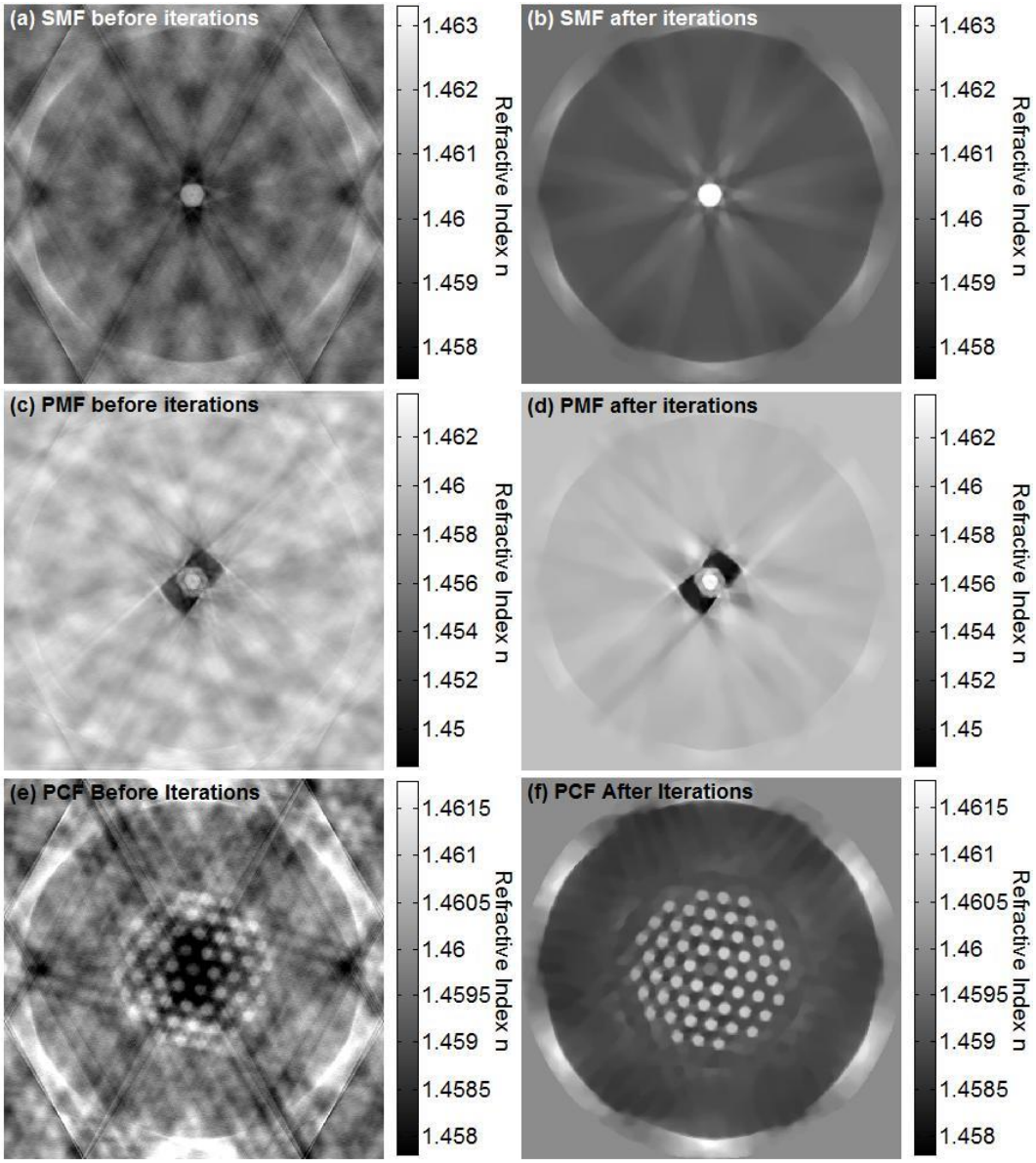

Figure 7.5. Experimental results for some optical fibers using iterative TDPM. The units on the colorbars are RI units. The RI ranges of the same fiber are the same. (a) and (b) The reconstructed RI cross section of a single-mode fiber (SMF) before (a) and after (b) iterations. (c) and (d) The reconstructed RI cross section of a polarization-maintaining fiber (PMF) before (c) and after (d) iterations. (e) and (f) The reconstructed RI cross section of a photonic crystal fiber (PCF) before (e) and after (f) iterations.

7.5 Summary and Discussion

The accuracy of the recovered RI depends on the regularization parameter α. For an objective comparison between image rotation and object rotation, they should be performed with correspondingly different α's that optimize them respectively. By properly choosing the appropriate α, object rotation consistently outperforms image rotation. The main reason is that object rotation can effectively avoid the truncation error during rotations. Moreover, in practical simulations, the cost function in image rotation may not monotonically decrease, even if the descent direction is the negative gradient direction. This phenomenon is mainly due to the extra step of resetting the SP outside the area of interest to be zero. Although object rotation should also be affected by this resetting theoretically, a similar phenomenon has not been observed in our simulations. Overall, object rotation outperforms image rotation except that its computation speed is slower.

As stated in Eqs. (7.3) and (7.4), the convolution can be realized either in the spatial domain or in the frequency domain. Usually, convolution in the frequency domain is much faster, but this convolution is inherently a circular convolution, which is not appropriate for the situation in this thesis. Therefore, in order to make use of the fast calculation of frequency domain convolution, it is necessary to zero-pad the matrices to be convolved before Fourier transformation, and then to truncate the convolution result to the original size after inverse Fourier transformation.

In summary, a new regularized iterative algorithm has been developed, which can be used to reduce the number of rotation angles in the 3D QPI method TDPM from 15 to 3. The strong denoising capability of the iterative algorithm is validated by both simulations and experiments. The resulting iterative TDPM method requires much less

measurement time than the original TDPM, so it can be used to detect some dynamic processes that are too fast to be captured in the original TDPM.

CHAPTER 8. QUANTITATIVE PHASE IMAGING OF FIBER BRAGG GRATINGS IN MULTICORE FIBERS

8.1 Background, Motivation, and Impact

The fiber Bragg grating (FBG) is one of the most important fiber-based devices. FBGs are formed by periodically perturbing the refractive index (RI) in the core of a fiber on a sub-wavelength scale. The most notable characteristic of an FBG is its band rejection property. When propagating light encounters an FBG, the light in a narrow wavelength band about the Bragg wavelength is reflected (diffracted), but the light of other wavelengths passes. FBGs have widespread applications, particularly in telecommunications and sensing [148, 149]. In telecommunications, FBGs are used as band-rejection filters in wavelength-selective devices, such as in optical multiplexers and demultiplexers [150-153]. Furthermore, since the Bragg wavelength is sensitive to temperature and strain, FBGs can be utilized as sensors for measuring temperature [154], strain [155-157], or both simultaneously [158, 159]. Additionally, other physical properties that affect temperature or strain, such as gas or liquid pressure [160], bend angle [161], and shear force [162], can be inferred. FBGs are also used as highly reflective mirrors in fiber lasers and fiber resonators [163-165].

The highest performance FBGs are usually designed with nonuniform RI modulation rather than with simple constant-amplitude sinusoidal profiles [166, 167]. Chirped FBGs have a varying grating period along the grating length, so that light of various wavelengths is reflected at a series of locations along the fiber. A particularly

important application is dispersion compensation [168-171]. Apodized FBGs are engineered with nonuniform RI modulation amplitude along the grating, such as a Gaussian or raised cosine function, which reduces undesirable side lobes in the reflection spectrum [172-174]. Importantly, even if the FBG is not designed in this way, some level of apodization naturally exists in realistic fabrication processes.

Writing FBGs in multicore fibers (MCFs) is a relatively new but rapidly growing field. The MCF is a good candidate for increasing the transmission capacity of a communication system by space division multiplexing [175, 176]. In an MCF, one fiber contains several cores, each supporting their own channel, so the transmission capacity is significantly increased. Furthermore, FBGs in MCFs open a new dimension in sensing. An MCF with FBGs can fulfill sensing tasks that otherwise would require multiple single core fibers with FBGs, and the sensing results are more stable and accurate [177]. Since the multiple FBGs in a single MCF have fixed relative positions and the same environment, the sensing results are more stable and accurate [177]. One significant FBG MCF sensing example is the two-axis bend measurement, or vector curvature measurement [178-180], which enables high-accuracy shape sensing [181] and position sensing [182]. These are fundamental in providing haptics for minimally invasive surgery [183, 184].

Accompanying the wider applications of FBGs, the manufacturing tolerances have become tighter to ensure the required performance. Engineers need reliable techniques to test fabricated FBGs. Since the most important property of the FBG is its reflection spectrum, most characterizations focus on accurately measuring reflection spectrum. However, the reflection spectrum does not fully characterize the FBG; the RI

distribution is more fundamental. In fact, the reflection spectrum can be calculated numerically based on the RI distribution using coupled mode theory [167]. Therefore, characterizing the RI distribution in FBGs is needed to close the loop between design and fabrications. This work has been published in Ref. [115].

8.2 FBG Characterization Methods Review

Unfortunately, it has been very difficult to measure directly the RI distribution in FBGs. The two major difficulties in characterizing FBGs are its transparency and its short period. Since FBGs are transparent to visible light, images formed in conventional optical systems have very poor contrast and can hardly give any useful information. The typical period is very close to the diffraction-limited resolution of typical imaging systems using visible light, but a resolution much smaller than the period is required for reliable direct imaging, so a conventional optical microscope cannot provide sufficient resolution. Nevertheless, researchers have developed several methods in overcoming the difficulties of measuring the RI variations.

One category focuses on high-resolution imaging through near-field imaging, such as apertured photon scanning tunneling microscopy [185] and scanning near-field optical microscopy [186]. Light in the near field contains evanescent wave, which contains high-spatial-frequency information of the fiber. However, these two methods require the cladding be removed, so the measured object is not a native FBG, since the residual stress is significantly changed in the removal process.

Beyond high-resolution techniques, there are also non-imaging approaches. Side diffraction is such a method for characterizing gratings [174, 187]. Coherent light

transversely incident on the FBG is diffracted. For incidence at the Bragg angle, the relative strengths of the zero- and first-order diffracted beams depend on the magnitude of the RI modulation of the grating [188]. This method has been further improved by measuring the interference pattern of the two beams, with the intensity of the zero-order beam appropriately attenuated [189]. The RI accuracy can be 5×10^{-6} [190]. The resolution of side diffraction is determined by the width of the probe beam, which is typically about 10 μm [188]. However, side diffraction is highly sensitive to the alignment of the FBG and the beam. The quantitative relation between the RI variation and the intensity ratio depends on the beam polarization and the beam shape [191]. It does not measure the average value of the refractive index [192]. It can only measure a one-dimensional (1D) RI modulation, so it cannot detect any cross-sectional pattern. When several FBGs in an MCF are measured, they have to be measured sequentially, and the FBG being measured cannot be blocked by any other FBGs. Therefore, the alignment difficulty is further increased, and the efficiency is low.

Another non-imaging technique is based on calculating the RI modulation from reflection spectra. However, the complex reflection spectrum, including both the amplitude and the phase, is required in reconstructing the RI distribution. It can be measured by low-coherence interferometry [193-195] or by frequency-resolved optical-gating technique [196]. If the complex reflection spectrum is measured, the RI modulation can be calculated by an inverse scattering algorithm [197], such as layer peeling [198, 199] or numerically solving Gel'fand–Levitan–Marchenko equations [200]. However, the resolution is 12~20 μm [193, 194], which is on the same order as side diffraction. It is also possible to recover the RI modulation by measuring two amplitude

reflection spectra for the same FBG with two different thermal modulations [201] or with two different strain distributions [202]. Then the RI profile can be calculated by an optimization algorithm, which searches for the best-fit RI distribution. However, this approach requires the knowledge of the apodization function type. Similar to side diffraction, both inverse scattering and optimization approaches based on the spectra can only measure a 1D RI modulation.

In order to attempt to characterize 2D RI structures, differential interference contrast (DIC) has been applied to FBG characterization. DIC provides image intensities proportional to the phase gradients. DIC has been applied to image FBGs and shows Talbot patterns induced by the UV laser in the FBG writing process [203-205]. However, since DIC is a direct optical imaging approach, it is unable to resolve the small FBG periods. In characterizing MCFs using DIC, the FBG cores should not overlap, so that they can be imaged simultaneously. Table 8.1 summarizes the existing RI characterization methods, as well as their advantages and disadvantages.

Table 8.1: Summary of the existing RI characterization methods for FBGs.

Method	Published Papers	Non-invasive	High Spatial Resolution	Quantitative	No *A Prior* Knowledge	Control Simplicity	2D Imaging	3D Imaging
Atomic Force Microscope	[206]	☒	☑	☒	☑	☑	☑	☒
Near-Field Imaging	[185, 186]	☒	☑	☑	☑	☒	☑	☒
Side Diffraction	[174, 187-189, 191]	☑	☒	☑	☒	☒	☒	☒
Inverse Scattering	[193-200]	☑	☒	☑	☑	☑	☒	☒
Optimization	[201, 202]	☑	☒	☑	☒	☒	☒	☒
Differential Interference Contrast	[203-205]	☑	☑	☒	☑	☑	☑	☒

Based on the shortcomings of the state-of-the-art research, a new approach is needed that can detect 2D, and even 3D variations in FBG structures quantitatively. QPI

is a promising technique for achieving this goal. It can overcome the transparency difficulty. However, there are still many challenges associated with the short-grating-period difficulty. Goh *et al.* [207] applied QPI to some FBG characterization in 2014. However, their results appear to be qualitative, since many of the challenges were not resolved. In this section, we address these important challenges and provide suggested solutions for each of them. After that, we present a complete procedure that directly characterizes, for the first time, the RI distribution of FBGs in single-core and multi-core fibers using both 2D and 3D QPI techniques. This procedure is then supported by simulation of 2D and 3D gratings. This work has been published in Ref. [208].

8.3 Challenges and Solutions

Although measuring the RI distribution in FBGs using QPI techniques seems very attractive, there are numerous challenges associated with this approach, most of which stem from the very short grating period. This is the main reason why QPI has seldom been used for FBG characterization. However, if we do not attempt to measure the RI distribution point by point, but focus on the important characteristics, such as the period, the average RI, and the RI modulation, these challenges can be overcome. In this section, we will identify the major challenges associated with short-period gratings, including the pixel integration effect, the aliasing effect, the numerical aperture requirement, and characteristic functions recovery, and then we will describe our solutions to each of these challenges. Although short-grating-period difficulty can be solved by using a suitably high-resolution camera, such cameras are not readily available, and it is therefore necessary to address each of these challenges directly. This is the approach used in the present work. In the following discussion, we will denote the center period of the grating

as Λ_0, the freespace light wavelength as λ, and the camera resolution as Δx. Since we use a microscope, the camera resolution here, which might be better called the effective camera resolution, is the actual camera resolution divided by the microscope magnification factor.

8.3.1 Pixel Integration Effect

The intensity function $I(x, y)$ is a continuous function in the real world, but it has to be discretized into pixels when measured by a camera, so the camera acts as an analog-to-digital converter. Each pixel is measured by a sensor in the camera. However, the camera does not really sample the intensity but calculates the average intensity over each finite sensor area. This is called the pixel integration effect [209]. This does not represent a difficulty when the intensity varies slowly, but is a major challenge for the short-period FBG measurement, because the intensity variation of the FBG is significant in a sensor area.

Accounting for the pixel integration effect, the measured average intensity is the convolution of the actual intensity with a window function representing the sensor area [209]. This relation can also be written in the spatial frequency domain as

$$\hat{I}(\rho_x, \rho_y) = \tilde{I}(\rho_x, \rho_y)\widetilde{\Pi}(\rho_x, \rho_y), \tag{8.1}$$

where $\widetilde{\Pi}(\rho_x, \rho_y)$ is the Fourier transform of the window function $\Pi(x, y)$, and is often called the modulation transfer function (MTF). For a rectangular window, the MTF can be written analytically as [210]

$$\widetilde{\Pi}(\rho_x, \rho_y) = \frac{\sin(\pi\rho_x\Delta x')}{\pi\rho_x\Delta x'}\frac{\sin(\pi\rho_y\Delta y')}{\pi\rho_y\Delta y'}, \tag{8.2}$$

where $\Delta x'$ and $\Delta y'$ are the size of a sensor in each direction. Notice that they are different from the camera resolution, Δx and Δy, which is determined by the distance between neighboring sensors. If fill factor FF is defined as

$$FF = \frac{\Delta x'}{\Delta x}, \tag{8.3}$$

it is usually smaller than unity due to restrictions of practical camera technology. In the y-direction, the intensity variation is not significant, so most high-frequency components are nearly zero. However, since the x-direction is the direction of the grating periodicity, a significant part of the spatial frequency is near $\pm 1/\Lambda_0$, so the MTF plays an important role. Therefore, the MTF can be simplified to a function of only ρ_x and denoted as $\gamma(\rho_x)$,

$$\gamma(\rho_x) = \frac{\sin(\pi\rho_x\Delta x')}{\pi\rho_x\Delta x'}. \tag{8.4}$$

In fact, if Λ_0 is known, the effect of MTF can be further simplified to two numbers. For the low-frequency (DC) part, the MTF can be approximated by unity. For the high-frequency (AC) part, it is approximately

$$\gamma_0 = \frac{\sin(\pi\Delta x'/\Lambda_0)}{\pi\Delta x'/\Lambda_0}. \tag{8.5}$$

When $\Delta x'$ is comparable to Λ_0, this factor cannot be ignored, and $\gamma_0$can even become zero when $\Delta x' = \Lambda_0$.

In order to compensate for the pixel integration effect, the measured intensity spectrum should be divided by the MTF, so that the result is a closer estimation of the actual intensity distribution spectrum.

8.3.2 Random Sampling Effect

Another effect associated with the camera is its random sampling. The center position of each camera sensor representing a pixel is random. However, when sampling is considered, the entire system is not shift-invariant anymore [211]. For example, if $\Delta x = \Lambda_0/2$, then the centers of the sensors can be at the tops and bottoms of the sinusoidal wave, which detects the maximum contrast, or can be at the zero-crossings of the sinusoidal wave, which cannot detect any contrast. Therefore, the measured contrast depends on the alignment of the sensors and the intensity peaks. This problem is particularly significant when $\Lambda_0/\Delta x$ equals or is very close to a ratio of two small integers. On the other hand, if $\Lambda_0/\Delta x$ is far from any ratio of two small integers, the sampling positions of neighboring sensors are different, and sampled results from multiple periods can reach the maximum and minimum intensities.

Therefore, a reliable characterization requires that $\Lambda_0/\Delta x$ is far from any ratio of two small integers. However, even if this condition is satisfied, the measured contrast in each local period can be less than the actual contrast. Therefore, recovery of the modulation amplitude in a larger scale is essential. The last subsection will come back to this problem.

8.3.3 Aliasing Effect

In order to get important characteristic functions such as the apodization function, we need to focus on the gratings and their images in the spatial-frequency domain. The RI distribution of an ideal grating may be written as

$$n(x) = n_D + n_A \cos(2\pi\, x/\Lambda_0 + \psi_0), \tag{8.6}$$

which is composed of a uniform background and a sinusoidal function, so its spectrum is the sum of three delta functions at 0 and$\pm f_c$, where $f_c = 1/\Lambda_0$. For practical gratings, those three bands cannot be infinitesimally narrow, so n_D and n_A will be functions of x. In fact, many FBGs are designed with a slowly varying apodization $n_A(x)$, as described in the first section of this chapter. Therefore, the measured intensity spatial spectra are mainly composed of three frequency bands centered at 0 and $\pm f_c$, which are usually narrow.

If the effective camera resolution is larger than the Nyquist sampling period $\Lambda_0/2$, we cannot fully recover the information about a general object, due to the aliasing effect [110]. However, since the spectra are only composed of three bands, which are typically narrow, bandpass sampling allows us to recover the full information [212, 213], if the appropriate parameters are chosen properly so that these three bands can be distinguished and are not overlapping. Usually, bandpass sampling shifts the high-frequency bands to the baseband. However, in the present case, there is another low-frequency band, so many of these conclusions cannot be directly implied. Furthermore, we need to restore the aliased bands to their correct positions, rather than down-convert them to the

baseband as is usually done in telecommunications, because we need to apply a QPI algorithm to the correct frequency. Therefore, we need to provide an algorithm specifically satisfying the above situation to invert the bandpass sampling procedure.

In order to apply the QPI algorithm correctly, we need to upsample the defocused images so that the new pixel size is $\delta x < \Lambda_0/2$. The upsampling factor $u = \Delta x/\delta x$ is an integer. This step has to be done before applying any QPI algorithm, otherwise, the frequency domain operations in QPI will be applied to wrong components. Since we are able to recover the information of the FBG completely, the upsampling can be accurate provided the three bands do not overlap after aliasing and there is no noise. It is straightforward to show that the shifting index m can be calculated as $m = \mathrm{round}(\Delta x/\Lambda_0)$, where $\mathrm{round}(x)$ indicates the nearest integer to x. When round-down is applied, the left and right bands retain their relative positions, so we left shift the left band by mf_s, and right shift the right band by mf_s, where $f_s = 1/\Delta x$ is the sampling frequency. When round-up is applied, the left and right bands exchange their relative positions, so we left shift the right band by mf_s, and right shift the left band by mf_s.

To ensure that the high- and low-frequency bands are well separated, we must make sure that the measured center frequency f_c' is far from either 0 or $f_s/2$ with respect to the high- and low-frequency bandwidths. This requires that $2\Delta x/\Lambda_0$ is away from any integer. In practice, however, it is recommended to make $\Delta x/\Lambda_0 < 1$ and not close to 1 or $1/2$, otherwise, γ_0 will be very small, which degrades the intensity contrast. The non-overlapping requirement of the three measured bands limits the resolution of the algorithm. Ideally, each band can have a bandwidth of $f_s/3$, so the corresponding ideal

resolution of the apodization and average RIs is $3\Delta x$, which is close to 1 μm. Generally, using a higher-resolution camera (smaller Δx) will improve the resolution, but of course, the resolution cannot be better than the resolution determined by the QPI method, which inherently must be equal to or lower than the diffraction-limited resolution.

8.3.4 Numerical Aperture Requirement

If the illuminating light is a normally incident plane wave on the side of the fiber, the NA of the pupil of the objective lens should satisfy $\mathrm{NA_o} > \lambda/\Lambda_0$ to ensure the first-order diffracted light passes the pupil. However, this requirement can be relaxed if partially spatially coherent light is used for illumination. Partially spatially coherent illumination is provided by an extended source, whose size is determined by $\mathrm{NA_c}$, the numerical aperture of the condenser lens. Even if the first-order diffracted light of the normally incident component does not pass the pupil of the objective lens, some oblique light contained in the extended source might have a portion of its first-order diffracted light pass the pupil. If partially spatially coherent light is used as illumination, the numerical aperture requirement is relaxed to

$$\mathrm{NA_o} + \mathrm{NA_c} > \lambda/\Lambda_0. \tag{8.7}$$

Nevertheless, this requirement is critical. If the numerical aperture of the condenser and the objective lenses are small, a correspondingly shorter wavelength should be used to satisfy this requirement.

8.3.5 Characteristic Functions Recovery

We are typically interested in the characteristic functions of the grating rather than the point-by-point RI distribution. Indeed, the point-by-point RI distribution may not even show the actual RI modulation correctly. Thus, we need to find the DC component and the profile of the AC component (apodization function). For chirped gratings, the local period is also an important characteristic function. These functions should be obtained after the entire RI distribution is recovered.

First, the 1D RI profile in an FBG core can be extracted as $n(x)$. The DC component $n_D(x)$ and AC component $n_h(x)$ can be separated by low-pass and high-pass filtering. The apodization and chirp functions should be recovered from the AC component. One convenient way to recover them is using the Hilbert transform [214] from which a complex analytic function $\tilde{n}_A(x)$ can be obtained as

$$\tilde{n}_h(x) = n_h(x) + iHT\big(n_h(x)\big), \tag{8.8}$$

where $i = \sqrt{-1}$, and $HT(\cdot)$denotes the Hilbert transform. A convenient way to calculate it is

$$\tilde{n}_h(x) = F^{-1}\left(F\big(n_h(x)\big) \cdot \big(1 + \mathrm{sgn}(\rho_x)\big)\right), \tag{8.9}$$

where ρ_x is the spatial frequency corresponding to x, F and F^{-1} denotes Fourier transform and inverse Fourier transform, and $\mathrm{sgn}(\rho_x)$ is the sign function

$$\mathrm{sgn}(\rho_x) = \begin{cases} 1 & \text{if } \rho_x > 0 \\ 0 & \text{if } \rho_x = 0 \\ -1 & \text{if } \rho_x < 0 \end{cases}. \tag{8.10}$$

Then the apodization function is

$$|n_A(x)| = |\tilde{n}_h(x)| \tag{8.11}$$

The local period is related to the angle of $\tilde{n}_h(x)$,

$$\tilde{\psi}(x) = \text{angle}\big(\tilde{n}_h(x)\big). \tag{8.12}$$

It has to be unwrapped, but the phase changes between neighboring pixels are so large that direct unwrapping is not very reliable. Fortunately, since most of the frequency components are close to $1/\Lambda_0$, by subtracting $2\pi x/\Lambda_0$ from $\tilde{\psi}(x)$, the remaining part is slowly varying and is much more reliable for unwrapping. The final unwrapped phase $\psi(x)$ can be obtained by adding $2\pi x/\Lambda_0$ back to the unwrapped remaining part. The local period is then

$$\Lambda(x) = 2\pi/D\big(\psi(x)\big). \tag{8.13}$$

where $D(\cdot)$ denotes differentiation. In discretized functions, it is usually obtained by the finite difference between neighboring pixels, but other differentiation methods can also be applied.

8.4 Proposed Method

Having identified the foregoing solutions to the challenges, we now present a detailed description of the steps to implement the proposed method.

1) Capture a stack of defocused intensity images $I_z(\boldsymbol{r})$, whose effective resolution is Δx.

2) Calculate the Fourier transform of each defocused image $\tilde{I}_z(\boldsymbol{\rho})$.

3) If $\Delta x > \Lambda_0/2$, upsample the defocused images by a factor of u.

    a. Zero-pad the spectrum by a factor of $u = \Delta x/\delta x$, where u is an integer and $\delta x < \Lambda_0/2$.

    a. Separate the DC band and the AC bands by filtering.

    b. Calculate the shifting index $m = \mathrm{round}(\Delta x/\Lambda_0)$.

    c. Shift the AC bands to the correct positions. If $m < \Delta x/\Lambda_0$, we left shift the left band by $m/\Delta x$ and right shift the right band by $m/\Delta x$. If $m > \Delta x/\Lambda_0$, we right shift the left band by $m/\Delta x$ and left shift the right band by $m/\Delta x$.

    d. Recombine the shifted AC bands with the DC band to obtain the upsampled intensity spectrum $\tilde{I}_z''(\boldsymbol{\rho})$.

4) Divide the intensity spectrum $\tilde{I}_z(\boldsymbol{\rho})$ or $\tilde{I}_z''(\boldsymbol{\rho})$ by the MTF $\gamma(\rho_x)$.

5) Inverse Fourier transform the spectrum $\tilde{I}_z'(\boldsymbol{\rho})$ to generate the compensated (and upsampled) image $I_z'(\boldsymbol{r})$.

6) Calculate the RI distribution of the FBG using a QPI algorithm based on the compensated (and upsampled) defocused images.

7) Recover the DC component, the envelope profile of the AC component, and the local period. This step can be done for multiple FBG cores in the same 3D RI distribution image.

   a. Extract the RI value in the central line of an FBG core $n(x)$.

   b. Low-pass filter the line RI to get the DC component $n_D(x)$. High-pass filter the line RI to get the AC component $n_h(x)$.

   c. Calculate complex analytic $\tilde{n}_h(x)$ using the Hilbert transform of $n_h(x)$.

   d. The profile of the AC component (apodization function) is $|n_A(x)| = |\tilde{n}_h(x)|$.

   e. Calculate the angle function of $\tilde{n}_h(x)$, and unwrap it to get $\psi(x)$.

   f. The local period (chirp function) is $\Lambda(x) = 2\pi/D\big(\psi(x)\big)$.

Figure 8.1 is a flowchart of this procedure. The overall flowchart is shown in Figure 8.1(a). A total of k defocused images are taken by the camera. Each image is processed by the sub-flowchart in Figure 8.1(b) to compensate for the pixel integration effect and is upsampled if $\Delta x > \Lambda_0/2$. The revised images are input to a QPI algorithm to calculate the RI distribution of the FBG. The RIs of the j-th FBG cores can be extracted from the recovered RI distributions. Each line RI is processed by the sub-flowchart in Figure 8.1(c) to calculate the average RI, apodization function, and the chirp function.

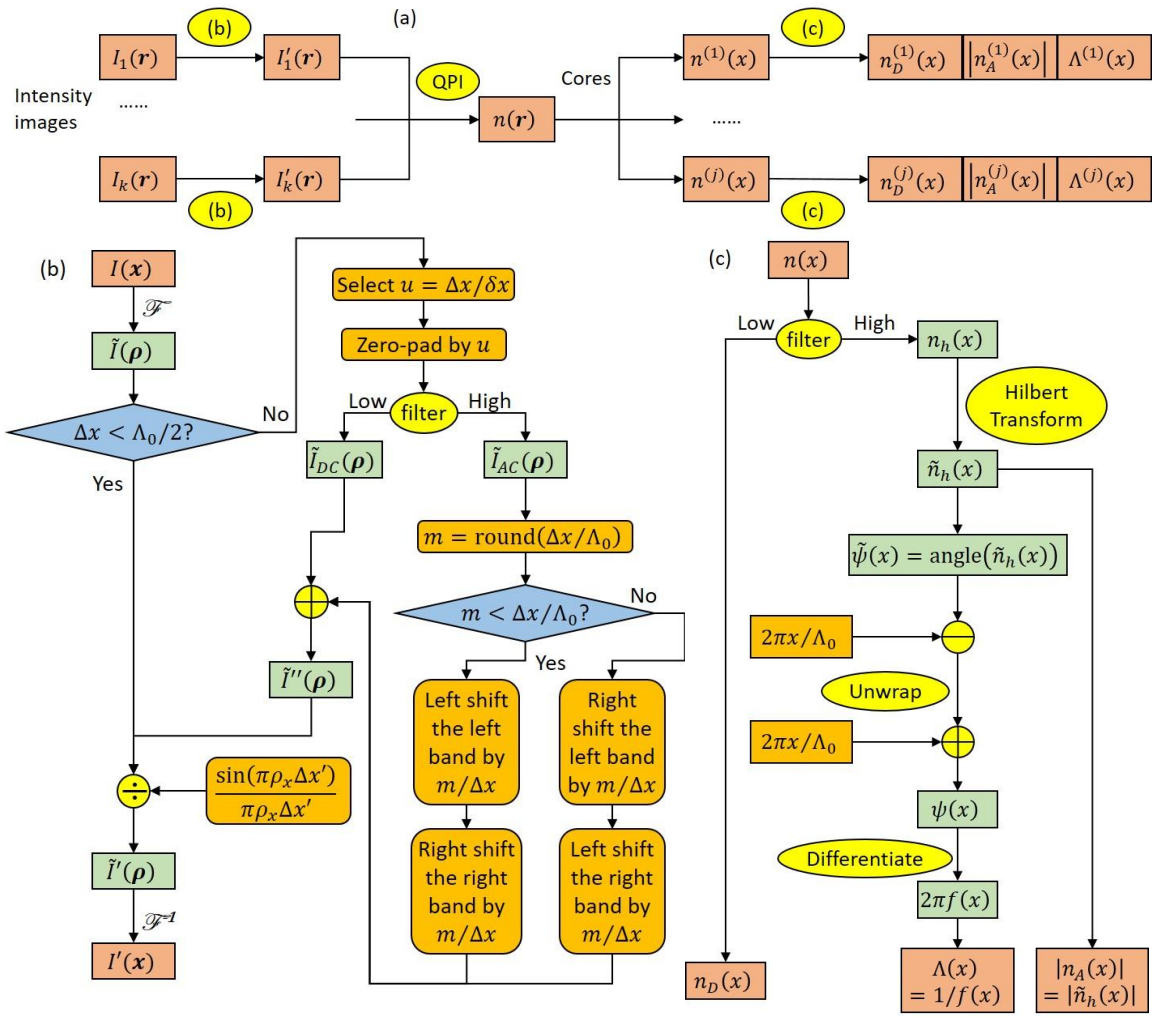

Figure 8.1. Flowchart showing the basic procedure of characterizing FBGs using QPI. (a) The overall flowchart, which calls sub-flowcharts (b) and (c). The QPI algorithm can be any appropriate method in the literature. (b) Sub-flowchart for processing the defocused images, including the compensation for the pixel integration effect and the necessary upsampling. (c) Sub-flowchart to recover the average RI, the apodization function, and the local period for a given line RI profile in an FBG.

There are some necessary requirements for this procedure, as summarized in the following.

- The numerical apertures must satisfy $\text{NA}_\text{o} + \text{NA}_\text{c} > \lambda/\Lambda_0$. Shorter wavelength and larger NAs are usually better.

- The camera resolution should better satisfy $\Delta x < \Lambda_0$, and $2\Delta x/\Lambda_0$ must be away from any integer.

- The DC and AC components must have sufficiently narrow bandwidths. This means the average and the apodization functions are not varying rapidly within a grating period. This gives the theoretical limit of the spatial resolution of the average RI and the apodization function, which is close to 1 μm.

- No discrete phase shift can exist within the FBG.

Though challenging, these requirements are achievable.

8.5 Simulation Validation

In order to quantify the accuracy of the proposed algorithm, simulations were performed comparing recovered characteristic functions with the ideal characteristic functions. The metric used to quantify the recovery accuracy is the normalized root-mean-square error (NRMSE), defined as

$$\mathrm{NRMSE} = \left(\frac{\sum [n_r(x) - n_i(x)]^2}{\sum [n_i(x) - n_0]^2} \right)^{1/2}. \tag{8.14}$$

The summation is over all of the discrete pixels. The quantity $n_i(x)$ is the ideal RI (can be average or apodization), $n_r(x)$ is the corresponding recovered RI. The NRMSE is only appropriate for line profiles, but not appropriate for the entire fiber, because if the FBG is shifted along the fiber axis, it is essentially the same object, but the NRMSE can be very large.

The first simulation was performed on two planar misaligned phase gratings and is shown in Figure 8.2. Although this 2D object is not an MCF with integrated FBGs, it is conceptually similar, so the reconstruction of the phase of this object also helps us evaluate the proposed algorithm. Instead of 3D QPI, a 2D QPI method should be used to reconstruct the phase distribution of the object. Here we use WLS-MFPI-PC, introduced in Chapter 5. The gratings have nonuniform average phases and apodization functions and can have varying local periods. The apodization function of Grating (1) is a flat-top raised-cosine function, while that of Grating (2) is a Gaussian function, both of which are commonly occurring in practice [167]. The object has a size of 512×512 pixels. The grating period is the typical Λ_0 = 531 nm, which is the same as many telecommunication FBGs. The wavelength of the illuminated light is λ = 546 nm, which simulates the green light of a mercury lamp. The pixel size is δx = 196 nm. The effective camera resolution is Δx = 392 nm, so an upsampling factor u = 2 is required in the image processing. The NA of the objective lens is $\mathrm{NA_o}$ = 0.75, and that of the condenser lens is $\mathrm{NA_c}$ = 0.5. In light propagation simulations, the intensities in 2×2 neighboring discrete sub-pixels are averaged to represent the (pixel-integrated) measured intensity in the camera pixel area. This average is different from the actual camera average but is more suitable for simulation. In order to model it accurately, the window function should be correspondingly changed, so the MTF becomes $\gamma(\rho_x) = \sin(\pi\rho_x\Delta x)/[2\sin(\pi\rho_x\Delta x/2)]$.

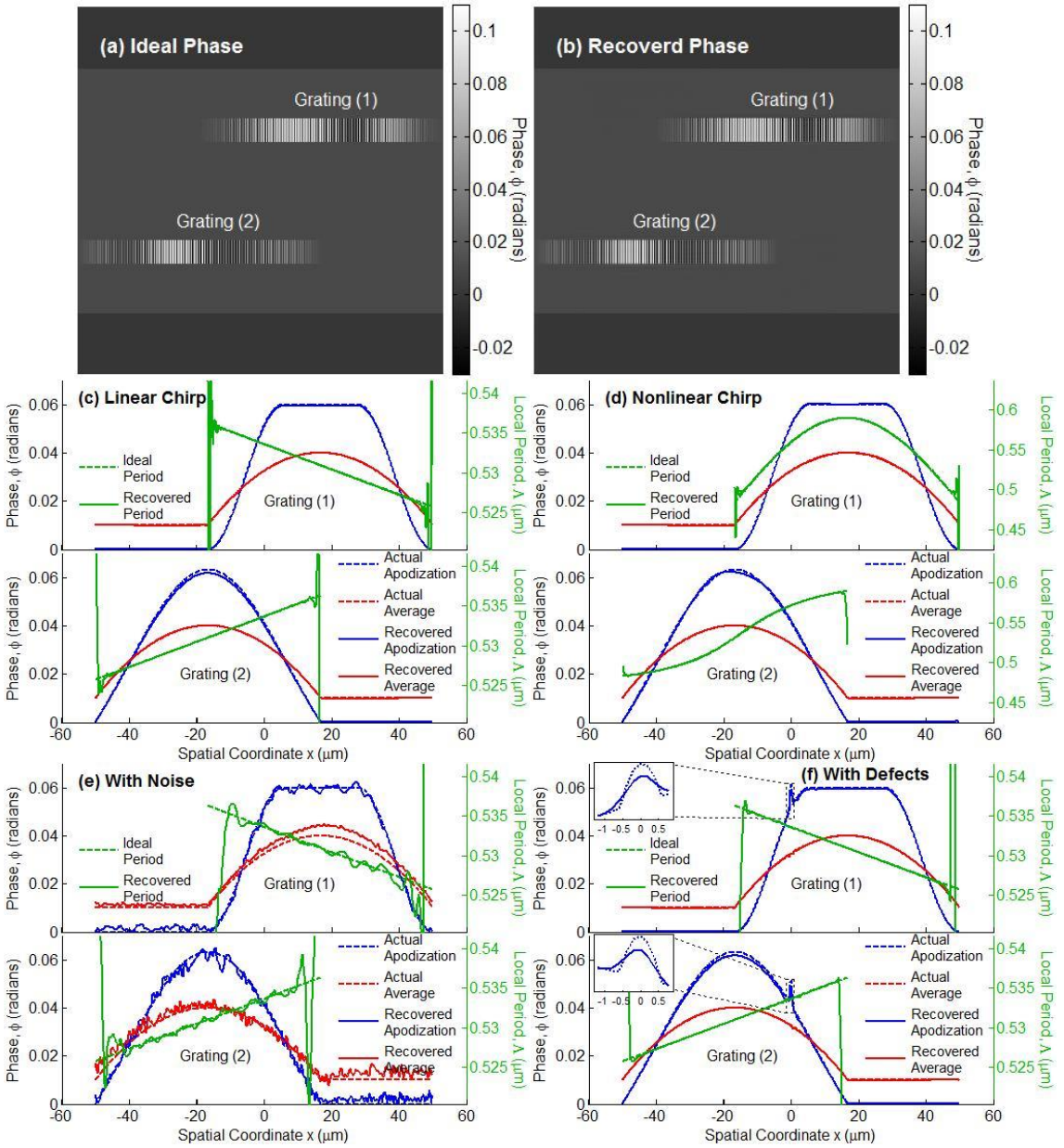

Figure 8.2. Simulation results for a 2D grating. (a) The ideal phase (with 1% chirp) to be simulated. (b) The recovered phase (with 1% chirp) from the proposed algorithm. (c) The ideal and recovered line profiles with 1% chirp. (d) The ideal and recovered line profiles with 10% nonlinear chirp. (e) The ideal and recovered line profiles with 1% chirp and 0.1% noise. (f) The ideal and recovered line profiles with 1% chirp and small artifacts. Upper left corners show zoomed artifact regions. In (a) and (b), the phases are both from -0.03 to 0.11 rad. In (c)-(f), the red lines represent the average functions (unit radians), the blue lines represent the apodization functions (unit radians), and the green lines represent the chirp functions (unit microns). The dashed lines represent the ideal functions, and the solid lines represent the recovered functions. In all the figures, the first grating is on the upper half, and the second grating is on the bottom half.

The first test object has a linear period variation of 1% of the center period, which is ±5.31 nm. The ideal phase is shown in Figure 8.2(a). The reconstructed object is shown in Figure 8.2(b). The structure is recovered clearly and remains almost the same as the ideal object. The characteristic functions are compared in Figure 8.2(c). The red lines represent the average functions, the blue lines represent the apodization functions, and the green lines represent the chirp functions. The dashed lines represent the ideal functions, and the solid lines represent the recovered functions. The recovered phases match the ideal phases so well that dashed and solid curves are almost indistinguishable. The NRMSEs of the apodization functions are both 0.023 for two gratings respectively, and that of the average phases are both 0.002. These results mean that the reconstructed curves deviate from the actual apodization by only 2.3% and from the actual average by only 0.2%. Furthermore, the error is sensitive to neither the shape of the apodization function nor the initial phase of the sinusoidal function. The recovered chirp function is also very close to the ideal line, except in the regions where the apodization is very small. This is understandable, and in the extreme case in which RI modulation is zero, the local period is meaningless. Therefore, the NRMSE is not used for local period comparison, because the local period recovery has large errors when the RI modulation is small, so NRMSE cannot show the recovery accuracy in the reliable region.

The second object has a nonlinear period variation of 10% of the center period, which is ±53.1 nm and is a very large chirp. The characteristic functions are compared in Figure 8.2(d). The NRMSEs of the apodization functions are 0.012 and 0.015 respectively, which are even smaller than in Figure 8.2(c) (although this is not typical). The NRMSEs of the average functions are 0.005 and 0.002 respectively, which are still

very small. The result shows that large and nonlinear chirps are also recovered successfully.

In realistic measurements, there is always some noise, so the recovery under noise is also tested. The object used is the first object with 1% chirp. Additive white Gaussian noise with $\sigma = 0.001$ (the intensity ratio of the noise and the uniform background) is added in all defocused intensity images. Notice that in the differentiation step in calculating the local period, the conventional finite difference is extremely sensitive to noise, so other differentiation algorithms that are more stable under noise should be employed. Here we use the first-order Savitzky–Golay differentiation filter (SGDF) [134] with length 27. The recovered characteristic functions are compared in Figure 8.2(e). The NRMSEs of the apodization functions are 0.037 and 0.059 respectively, and that of the average functions are 0.098 and 0.100 respectively. The recovered curves are still very close to the ideal curves, although there are some irregular oscillations due to noise.

The third test object also has a linear period variation of 1% of the center period, but it has artifacts in each grating. The artifact has a larger RI modulation than its neighboring region. The size is only 1.176 μm ($3\Delta x$). The first-order SGDF with length 27 is used as the differentiator again. The recovered characteristic functions are compared in Figure 8.2(f). The NRMSEs of the apodization functions are 0.012 and 0.024 respectively, and that of the average functions are both 0.003, which are similar to the other two objects. The insets in the upper left corners show the artifact regions. It is clear that the small artifacts are detected successfully. This simulation shows that the resolution of the proposed algorithm can reach $3\Delta x$ (about 1 μm).

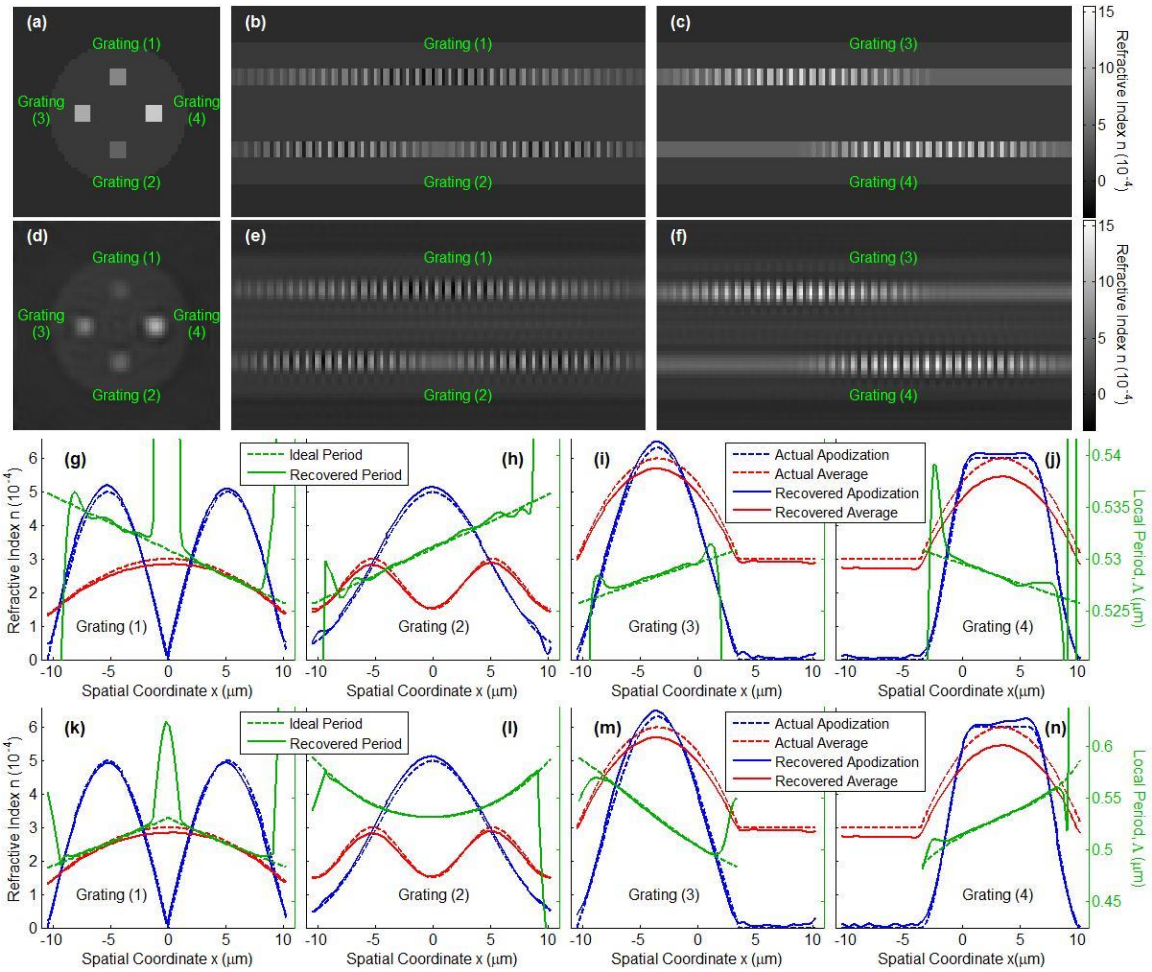

Figure 8.3. Simulation results of a four-core fiber, each of whose core is an FBG. The quantity shown in the figures is the RI difference between the fiber and the medium. (a)-(c) The three orthogonal center cross sections of the original object. (d)-(f) The three orthogonal center cross sections of the recovered RI. (g)-(j) The actual (dashed) and reconstructed (solid) characteristic functions, including average (red), apodization (blue), and chirp (green) functions, in the center of the four FBGs. (k)-(n) The actual (dashed) and reconstructed (solid) characteristic functions, including average (red), apodization (blue), and chirp (green) functions, in the center of another four-core fiber.

The second simulation is performed on a four-core fiber, and all the cores are inscribed with FBGs with different characteristic functions. The grating period and wavelength are the same as in the 2D simulation. The pixel size is δx = 163 nm. The effective camera resolution is Δx = 326 nm, so the upsampling factor is also u = 2. The numerical apertures are $\mathrm{NA_o}$ = 0.9 and $\mathrm{NA_c}$ = 0.55. The $\mathrm{NA_o}$ is chosen to be a large

number, because a large NA_o gives a better spatial resolution. The NA_c is chosen to be slightly larger than $\lambda/2\Lambda_0$, according to a criterion discussed in Appendix F. The object is assumed to be immersed in a refractive index matching medium, whose RI is 1.46. The object has a size of 64×64×128 voxels. In this case, the object is a 3D object, so a 3D QPI method should be used. Here we use tomographic deconvolution phase microscopy (TDPM) developed in Ref. [99]. Through-focal images at 15 equally distributed angles were simulated. Although a multi-core fiber with FBGs is typically much larger than the depth of field of a typical optical system, TDPM does not require focusing of the object, but it uses the optical sectioning capability of the extended light source (spatially incoherent source) to resolve a 3D image of the object. Only after processing are the high-resolution images obtained. Figure 8.3(a)-(c) show the three orthogonal center cross sections of the ideal object. The quantity shown in the figures is the RI difference between the fiber and the medium. The chirp is 1% linear chirp. Figure 8.3(d)-(f) show the three orthogonal center cross sections of the recovered object. The structure is reconstructed clearly and is very close to the ideal object. The reconstructed characteristic functions of each grating core are also shown in Figure 8.3(g)-(j) in solid lines. The first-order SGDF with length 15 is used for differentiation. The recovered characteristic functions match the ideal characteristic functions (dashed lines) very well. The average NRMSEs of the four apodization functions are 0.042, and the average NRMSEs of the four average functions are 0.055. The error is not sensitive to the initial phase of the sinusoidal function. Another object with 10% nonlinear chirp is also tested, and the comparisons of the characteristic functions are shown in Figure 8.3(k)-(n). The average NRMSEs of the four apodization functions are 0.046, and the average NRMSEs of the

four average functions are 0.055. The results clearly show that the recovery of RI and characteristic functions are successful.

8.6 Summary and Discussion

The majority of this chapter has been devoted to the digital signal processing techniques needed to overcome the short-grating-period challenges. Nevertheless, the importance of the QPI itself should not be overlooked, since it solves the transparency difficulty associated with FBGs. Diffraction effects are inherently included in the QPI procedure. The fact that QPI is represented by only a single step in the flowchart in Figure 8.1 is indicative of the fact that QPI is independent of the overall procedure. Therefore, the presented approach to solve the short-period difficulty in FBG characterization is not limited only to the QPI methods used in the simulation section, but applies to many other QPI methods as well, although some details may vary from method to method. For example, QPI methods based on phase-shifting holography or transport-of-intensity equation can use algorithms presented here without any modification, since the image processing procedures are performed separately in these methods as well. On the other hand, for QPI methods based on off-axis holography [216], the procedure presented here cannot be applied directly, because the intensity spectrum is more complicated, and image processing (such as spatial filtering) has to be done concurrently with phase recovery. Nevertheless, the spatial resolution of off-axis holography is limited by the off-axis angle of the reference beam and is lower than the diffraction-limited resolution. Thus, off-axis holography may not be a good option for FBG characterization due to the short-grating-period difficulty.

In conclusion, a new FBG characterization method based on QPI is proposed and supported by 2D and 3D simulations. The theoretical resolution is approximately 1 μm. The method is non-invasive and quantitative, and it does not require *a priori* knowledge. It is capable of measuring simultaneously 3D RI distributions of multiple FBGs in a single MCF with high resolution, and directly enables their average, apodization, and chirp functions to be determined.

CHAPTER 9. RESEARCH SUMMARY

The object of my thesis is to develop and generalize QPI methods to enable their more widespread use as well as applications of QPI to new classes of objects. the Optics Laboratory has developed several QPI methods, including MFPI-PC [82], POTFR [83], and TDPM [99]. They are all based on a standard commercial microscope, so the extra hardware cost is low if the user already has a microscope, which is typical for a biological laboratory. They have other advantages that are not simultaneously achieved by other QPI methods in the literature. Nevertheless, these methods have some shortcomings. In this thesis, some improved QPI methods are developed to overcome these shortcomings. In addition, some theories are developed to form the basis of the new QPI methods. Finally, the QPI methods are applied to FBG characterization.

9.1 Theory: Nonparaxial Partially Coherent 3D POTF

In Chapter 3, a linear partially coherent 3D imaging theory based on 3D OTFs is generalized to the nonparaxial condition. The 3D POTF is first derived in an integral form and then analytically integrated for disk and annular source functions. Due to the analytical nature, the increase of computation time can be almost neglected, but the accuracy improvement is significant for high-NA systems.

Along with the development of the 3D POTF, obliquity factor (OF) modification is used to eliminate the systematic error. The OF modification is to introduced to overcome the different object requirements in 2D and 3D diffraction theories, which will be explained in more details in Appendix A. In addition, Appendix A also represents a

presentation of a unified, complete, and consistent description of the use of OF and OF modifications in 2D and 3D imaging of thin and thick objects.

9.2 Development: Several 2D and 3D QPI Methods

9.2.1 2D QPI: Nonparaxial MFPI-PC with OF Modification

The original MFPI-PC uses the paraxial approximation. In fact, it used TIE, which is only applicable to paraxial situations. As a consequence, the maximum recoverable spatial frequency is $(\mathrm{NA_o} - \mathrm{NA_c})/\lambda$, which is small and decreases with increased $\mathrm{NA_c}$. In Chapter 4, nonparaxial MFPI-PC with OF modification (nP-MFPI-PC-OF) is developed, which generalize MFPI-PC to the nonparaxial condition using the analytical nonparaxial 3D POTF derived in Chapter 3. The maximum recoverable spatial frequency becomes $(\mathrm{NA_o} + \mathrm{NA_c})/\lambda$, which is large and increases with increased $\mathrm{NA_c}$. The computation time is almost the same due to the analytical nature of the nonparaxial 3D POTF. The improved accuracy due to the nonparaxial 3D POTF with OF modification is validated by both simulations and experiments. The simulation results show that nP-MFPI-PC-OF does not have a systematic error, while P-MFPI-PC and nP-MFPI-PC do.

9.2.2 2D QPI: Weighted-Least-Squares MFPI-PC

The original MFPI-PC uses a set of binary filters to choose the optimal SGDF order. It generally cannot give the optimal result from the tradeoffs among various SGDF orders. Particularly, it has a large error when annular illumination is used. In Chapter 5, weighted-least-squares MFPI-PC (WLS-MFPI-PC) is developed. A set of filters derived from least-squares fitting, further multiplied by an extra weight inversely proportional to

the noise magnification factor of the SGDF orders, is used to replace the binary filters. The benefits from least-squares fitting and the extra weight are validated in both simulations and experiments.

9.2.3 2D QPI: Comparison and Improvement of MFPI-PC and POTFR

In addition to the two previously-mentioned disadvantages, the original MFPI-PC requires intensities measured at uniformly distributed planes due to the nature of SGDF. However, nonuniformly distributed planes can be more efficient than uniformly distributed planes. Fortunately, Ref. [83] already generalized MFPI-PC to nonuniformly distributed planes by using a generalization of SGDF. After overcoming all the three disadvantages, the MFPI-PC is significantly improved and is then called WLS-MFPI-PC.

Another disadvantage of MPFI-PC is that its derivation requires a purely transparent object, since it uses simplified TIE. However, after the previous improvement, the improved MFPI-PC does directly rely on TIE anymore, and further analysis shows that it is applicable to weakly absorptive objects without modification.

Compared to MFPI-PC, POTFR has a disadvantage in that the calculation of the 2D POTF is based on a 2D integral and thus slow. In Chapter 6, a semi-analytical form of the 2D POTF is developed, which is based on a 1D integral of the analytical 3D POTF. The computation time is much faster. The semi-analytical 2D POTF is available for both disk and annular illuminations.

After all the improvements, WLS-MFPI-PC and improved POTFR are compared in Chapter 6 by simulations. Both disk and annular illuminations are simulated. Recoveries

from uniformly and nonuniformly distributed planes are both simulated and compared. Absorptive objects are also tested. The results show that generally, the errors decrease with increasing $\mathrm{NA_o}$, decrease and then increase with increasing $\mathrm{NA_c}$, and do not vary significantly with $\mathrm{NA_{ci}}$. WLS-MFPI-PC is generally not worse than improved POTFR, and it is more robust under noise. Using a small number of planes decreases the accuracy, which is the natural cost of faster measurement.

9.2.4 3D QPI: Iterative TDPM

The measurement time of the original TDPM is usually long due to the total number of measured images being very large. In Chapter 7, iterative TDPM (ITDPM) is developed, which uses an iterative regularization algorithm to overcome the "missing cone" problem. The iterative regularization is based on minimizing the cost function, which aims to minimize the difference between the expected intensities and the measured intensities while maintaining piece-wise smoothness of the RI (SP) distribution. ITDPM can reduce the number of rotation angles from 15 to 3, so the measurement time is significantly shortened, which makes ITDPM more suitable for characterizing live cells and investigating dynamic processes. The image quality of ITDPM has been validated using simulations and experiments.

9.3 Application: FBG Characterization

FBG is a widely-used transparent object, but it is difficult to characterize using QPI because of its short grating period. There are several problems associated with the short-period difficulty. In Chapter 8, some digital image processing techniques are developed

to overcome the problems. A complete procedure of characterizing FBG using QPI is proposed and supported by simulations of 2D and 3D objects.

CHAPTER 10. FUTURE WORK

10.1 Experimental Fiber Bragg Grating Characterization

In Chapter 8, an FBG characterization algorithm based on QPI has been developed and supported by simulation. We will test the proposed algorithm experimentally. First, we have purchased some commercial FBGs in single-mode fibers from Femto Fiber Tec and from Technica, so they will be used as our first test objects. It is a fortunate that the FBGs from the two companies have different periods, RI modulations, and lengths, and they are written using different techniques, so their measurement can be a good comparison. Some specially fabricated FBGs, such as sampled FBG [217] and superimposed FBG [218] can also be tested. In addition, we also want to characterize FBGs in multi-core fibers. Since multi-core fibers with FBGs are difficult to obtain, we plan to fuse a bundle of single-core FBGs together to mimic a multi-core fiber with FBGs. All of the FBGs can have varying average RI, apodization, and chirp.

In order to better perform the FBG characterization, some optimization in experimental devices is helpful. We propose to use annular illumination in FBG characterization. As is mentioned in Chapter 5, annular illumination has advantages in recovering high-spatial-frequency information, so it is particularly of interest in FBG characterization. Although annular illumination has only been applied in 2D QPI in our laboratory up to now, the application in 3D QPI is easy because the 3D POTF for annular illumination has already been developed as Eq. (5.7). In the experiment, we propose to first test the annular illumination using single-mode fiber, polarization-maintaining fiber,

and photonic crystal fiber. If the results are consistent with those using disk illumination, then annular illumination can be used in experimental FBG characterization.

The objective lens also requires optimization. A larger $\mathrm{NA_o}$ ensures higher resolution and is generally wanted. The magnification should ensure that the entire fiber cross section is within the field-of-view of the camera, and it should also ensure that the effective camera resolution is far away from integer multiples of $\Lambda_0/2$. Among the existing objective lenses in our laboratory, the best one is UMPlanFL 50X/0.75 BDP. The magnification is 50, and the $\mathrm{NA_o}$ is 0.75. We also propose to incorporate an oil-immersion objective lens in the future. Oil-immersion can greatly increase the NA of the objective lens. It increases the spatial resolution of imaging, which can be a great help, particularly in FBG characterization.

Some other preparations have been done. The fill factor of the camera sensor array has been measured, which is $FF = 78\%$, so the MTF can be calculated. Furthermore, since the measured intensity can be sensitive to the spatial shift of the FBG, a rotation mechanism ensuring more fixed fiber position is essential. Therefore, a new rotation mechanism has been proposed, which uses two synchronized rotators on both ends of fibers. By fixing both ends of the fiber, the spatial shift of the FBG can be reduced significantly. In addition to hardware changes, corresponding software modifications are also required. A new version of the LabVIEW program has been made particularly for FBG characterization. For example, the distance between the through-focal images is set smaller, from $\Delta z = 4\Delta x$ in the original program [99] to $\Delta z = \Delta x$. Since the FBG varies very rapidly in space, a smaller sampling distance is essential. The rotation module has also been modified to enable synchronized two-axis rotation.

The QPI method may require specific modification as well. The simulation in Chapter 8 uses TDPM. However, as mentioned in Appendix F, TDPM suffers from low-POTF problem along the ρ_y axis. The problem becomes more significant as the size of the problem increases. Properly choosing $\mathrm{NA_c}$ relieves this problem in simulation, but we are not sure whether it works in experiments as well. If TDPM cannot overcome the low-POTF problem in the experiment, we may try to use iterative optimization to fill the low-POTF region. However, ITDPM cannot be applied directly, because it requires piecewise smooth RI distribution, which is not true for FBG. Nevertheless, modifying the iterative regularization procedure to overcome the missing cone problem might be a possibility. I propose to use iterative optimization separately for low-frequency and high-frequency bands. For high-frequency bands, they should be downconverted to low frequency to ensure piecewise smooth. However, if the entire high-frequency bands fall into the missing cone rather than the low-POTF region, an iterative algorithm does not help, so $\mathrm{NA_c} > \lambda/2\Lambda_0$ should still be satisfied. As a final note, since our FBG characterization algorithm is compatible with a variety of 3D QPI methods, if TDPM and modified ITDPM are both considered not good after our preliminary test, we can switch to other QPI methods, such as optical diffraction tomography based on both beam rotation and object rotation. However, it requires more hardware modification to enable beam rotation.

Furthermore, there are more difficulties in the experiments that may not exist in simulations. There is more noise in the experiment, so a noise-robust differentiator such as SGDF must be used. The problem size is larger than the existing simulation, so the hardware cost is much more significant. Due to the larger problem size, the low-POTF

problem is also more significant. In addition, actual FBGs are longer than the field-of-view, so the boundary of the field-of-view may have large errors. Moreover, how to characterize the entire FBG is another difficulty. We cannot simply connect images from two field-of-views to form a larger image, because there can easily be some discrete phase shift between neighboring images. We may have to connect characteristic functions rather than RI distribution directly. Finally, the structures of actual FBGs are more complicated than the simulated ones. There is nonuniform cross-sectional RI distribution, such as Talbot pattern [204]. These difficulties have to be overcome to get a good experimental result.

10.2 3D Biological Cell Imaging

QPI has wide application in biology and biomedicine. All of the methods developed in our laboratory should be applicable to imaging biological cells. The capability of 2D QPI has been validated in Ref. [83]. Moreover, we also want to apply our 3D QPI methods to cell imaging. However, since TDPM and ITDPM require object rotation, it is a significant challenge to rotate cells in a controllable way. If we want to image living cells in their natural environment, which is a major advantage of QPI, the challenge is even more significant. Holographic optical tweezer is an amazing technology [219], but the cost is high. In order to reduce the cost, we still want to perform the rotation mechanically.

The current plan is to use a capillary tube to store the cells, so that the tube can be rotated like a fiber. The cells can be immobilized in the capillary tube with agarose gel. The capillary tube is made of transparent material, which can be glass or polymer. Since

glass is usually fragile, polymer is preferred. Agarose gel can be mixed with cells in its liquid state, and then filled into the capillary tube. Capillary action is sufficient to absorb a sufficient amount of gel. After the gel solidifies, the cells can be kept immobilized but still alive. In the process of gel absorption, the capillary can be heated to prevent the gel from solidifying too fast. If this attempt will succeed, we can quantitatively measure the RI distribution of living cells. We can also use microspheres or micropowders as test objects before actually doing cell experiments. This is a collaboration work done by three undergraduate students and me as an Opportunity Research Scholars (ORS) project.

In general, we want the RI of the capillary tube to be close to that of the solvent. There are some major requirements from our measurement hardware and software limitations:

a. The RIs of the capillary material, cells, gel, and the immersion liquid should all be close.

b. The outer diameter of the capillary should not be greater than the range of the Piezo objective scanner.

c. The inner diameter of the capillary should be at least larger than the size of cells.

However, it is difficult to satisfy all the requirements. Up to now, we have not found a commercial capillary tube that satisfies all the requirements. As a compromise, we may ignore either the RI requirement or the size requirement. If the RI requirement is ignored, it is still possible to partly compensate for the large RI contrast by taking the

difference between the recovered RI of gel mixed with cells and that of pure gel [220]. Another way of compensation is to explicitly consider the refraction at the boundaries with large RI contrast [221]. If the size requirement is ignored, the simplest approach is to make the RI of the capillary and the gel as close as possible and thus assume their RI are exactly the same.

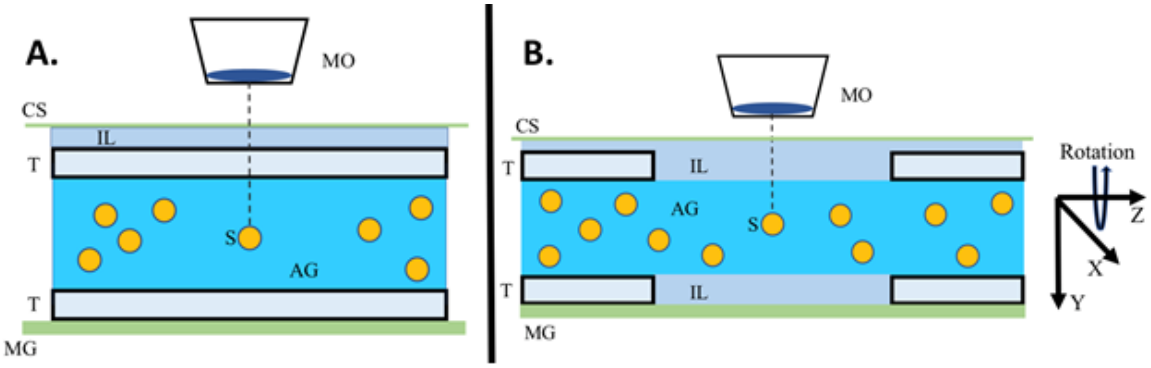

Figure 10.1. Conventional sample preparation (left) and hanging-gel preparation (right). A. shows the microscope objective (MO) measuring the refractive properties of some sample (S) which is fixed in an agarose gel (AG) and embedded inside a capillary tube (T). B. (hanging-gel configuration) shows the same process in A, but with two capillaries holding the sampled portion of agar gel in suspension.

Another approach to overcoming this difficulty is to use a specially designed configuration. Figure 10.1 shows two possible configurations that may be used in the experiments. Configuration A is the conventional one, which has some requirements that cannot be satisfied simultaneously now. Configuration B is called the “hanging-gel” configuration. It is similar to some configurations used in light-sheet microscopy. The idea is to remove the capillary from the light path, so that there is no requirement about the RI of the capillary. Meanwhile, the size of the capillary can be larger, because there is no requirement about the outer diameter. Instead, the inner diameter should not be greater than the range of the Piezo objective scanner. Therefore, Configuration B has fewer

restrictions on equipment parameters. There is already a capillary tube satisfying all the requirements for “hanging-gel” configuration in our laboratory.

Despite the promising advantages, the “hanging-gel” configuration also brings some new challenges. The rotation mechanism has been updated, so that capillary on both sides of the hanging gel are hold on different rotators, and the two rotators are controlled by the same LabVIEW program and can be rotated simultaneously. This two-axis rotation configuration has advantages of less spatial shift after rotation, so it can also be applied to other objects. Meanwhile, we must make sure that the hanging gel is not dissolved in the immersion liquid.

The major challenge, however, is to create the hanging gel properly. The first problem is how to separate the two capillaries after the gel solidifies. It is unrealistic to cut a capillary in two after the gel is formed inside it, since there is no way to cut the capillary perfectly but not cut the gel at all. It is more reasonable to connect two capillaries before the gel is formed, and separate them after the gel solidifies. In this way, however, a way to align the two capillary perfectly and firmly before the gel enters is a critical problem. Another problem is how to control the shape of the hanging gel. Ideally, the hanging gel should maintain approximately a cylindrical shape. A natural idea to push gel out of the capillary is using a syringe. However, preliminary test shows that the gel will not maintain a cylindrical shape but will become more like a spherical shape due to surface tension, whose diameter will be much larger than the allowed size of our hardware limit.

In order to solve these problems, we propose using specially-designed molds to form the shape of the gel and set appropriate separation between the two capillaries. The shape of the proposed mold is shown in Figure 10.2. The mold can be made using nanoscribe technology. Two pieces of this mold are used to fix the size of the hanging gel. The grooves of the two pieces form a channel of the capillary and hanging gel. The small middle groove is for the hanging gel, so the diameter equals the inner diameter of the capillary. The larger outer grooves are for capillary, so the diameters equal the outer diameter of the capillary, and taper structures are applied on both ends. The convex and concave hexagons are paired from the two pieces to prevent shift between two the pieces. Anti-adhesion coating may be required to prevent the adhesion between the hanging gel and the molds. After the two capillaries are inserted into the grooves, the two molds are closed, and then the gel can be absorbed by capillary attraction. After the gel solidifies, the two molds can be separated and moved away, and then a cylindrical hanging gel should be formed between two capillaries.

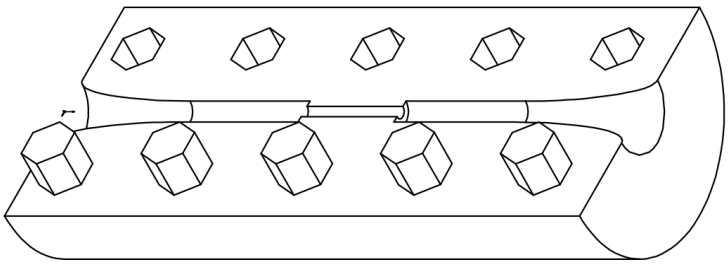

Figure 10.2. Model of the proposed mold used for creating hanging gel. Two pieces of this mold are used to fix the size of the hanging gel. The grooves of the two pieces form a channel of the capillary and hanging gel. The convex and concave hexagons are paired from the two pieces to prevent shift between two the pieces.

We may try both configurations in Figure 10.1 to find out which is better, and may propose new configurations as well.

10.3 2D QPI on Other Test Objects

In the previous 3D QPI measurements, various fibers are tested, but in 2D QPI measurements, only a microlens array is used as the test object. However, it is beneficial to test more objects. Therefore, it is proposed to test our 2D QPI methods using other transparent thin objects. Although biological cell imaging is a major application of QPI, the cells cannot be used to quantify the imaging accuracy, because we do not know the actual phase to determine the measurement error. In the literature, a standard US air force (USAF) resolution target is often used to test the resolution of the imaging methods [222]. However, the USAF resolution target absorbs light significantly, so it is not a very good object to test QPI. Phase-modulated spatial light modulator (SLM) [223] is an excellent controllable object, but it can only work on reflection configuration.

A transmission diffraction grating is a good phase object. However, the thickness is typically 3 mm, which is larger than the focal length of the condenser lens and is larger than the working distance of the objective lens that we often use. Therefore, the grating side of the sample should face down towards the condenser lens, and we should use another objective lens with a larger working distance, so that Köhler illumination can be satisfied. Another disadvantage is that a grating has a lot of high-spatial-frequency information, which can be lost due to finite apertures. Modulation transfer function similar to that described in Chapter 8 should be used to compensate for the pixel-integration effect. However, the preliminary result now is not satisfactory, so more analysis has to be done to achieve good accuracy.

Some research groups use some custom-created structures, such as silicon wafer [224], silicon wafer etched by an electron beam [225, 226], laser-written microstructures [227], geometry pattern etched on polymethyl methacrylate (PMMA) substrate [228], nanopillars on the quartz substrate [229], etc.. We are also creating our own test phase object using an Elionix electron beam lithography system. An USAF resolution test chart is etched onto silica substrates. The thickness of the substrate is 1 mm. Two test patterns, whose phases are 1 rad and 3 rad respectively, are being fabricated. The smallest feature size is 1 μm. Due to equipment restriction, sub-micrometer feature size cannot be created. After the test objects are obtained, we will use it to test various 2D QPI methods, including disk illumination and annular illumination with various NAs. It is expected that annular illumination can achieve higher accuracy for small feature sizes.

10.4 Gaussian Illumination

Disk and annular illuminations are not the only illumination types that are of interest. Other types of sources have been used in many papers, such as LED array [127], half-disk illumination [130], and Gaussian illumination [230]. These sources have different POTFs. For deconvolution-based QPI methods, low transfer function values often cause magnified noise, so large POTF values are generally welcome. Annular illumination has larger POTF values for high spatial frequency components [125, 129, 215], so it is a good source to recover objects with great high-frequency information, such as FBGs. On the other hand, Gaussian illumination has smaller low-value regions in the POTF, particularly when the NA_c is close to NA_o [230], which is often desired to improve the spatial resolution. Therefore, we propose to incorporate Gaussian illumination in both theory and experiment.

Theoretically, the integral form of POTF, Eq. (3.9), is compatible with any source type. Gaussian illumination is a type of circularly symmetric source, whose source function can be represented as a function of the spatial frequency magnitude only,

$$\tilde{S}(\boldsymbol{\rho}) = \tilde{S}(\rho). \tag{10.1}$$

It can be decomposed into a series of narrow annulus using delta function decomposition,

$$\tilde{S}(\boldsymbol{\rho}) = \int \tilde{S}(|\boldsymbol{\rho}'|)\frac{\delta(|\boldsymbol{\rho}'| - |\boldsymbol{\rho}|)}{2\pi|\boldsymbol{\rho}|}\mathrm{d}\boldsymbol{\rho}' = \int \tilde{S}(\rho')\delta(\rho' - \rho)\mathrm{d}\rho'. \tag{10.2}$$

In order to normalize the background intensity, it is convenient to normalize the source function so that

$$B = \int \tilde{S}(\boldsymbol{\rho})\mathrm{d}\boldsymbol{\rho} = \int \tilde{S}(\rho)2\pi\rho\mathrm{d}\rho = 1. \tag{10.3}$$

If the source is a narrow annulus, it can be represented as

$$\tilde{S}(\boldsymbol{\rho}) = \frac{1}{2\pi\rho_s}\delta(|\boldsymbol{\rho}| - \rho_s) = \frac{1}{2\pi\rho_s}\delta(\rho - \rho_s), \tag{10.4}$$

which is the limit function of normalized Eq. (5.1) when ρ_{si} approaches ρ_s. The corresponding normalized 3D POTF $\widetilde{H}(\boldsymbol{\rho}, \eta; \rho_s, \rho_s)$ can then be written as

$$\begin{aligned}\widetilde{H}(\boldsymbol{\rho},\eta;\rho_s,\rho_s) &= \lim_{\rho_{si}\to\rho_s}\frac{1}{\pi\rho_s^2-\pi\rho_{si}^2}H(\boldsymbol{\rho},\eta;\rho_{si},\rho_s)\\ &= \frac{1}{2\pi\rho_s}\frac{\mathrm{d}H(\boldsymbol{\rho},\eta;0,\rho_s)}{\mathrm{d}\rho_s}.\end{aligned} \tag{10.5}$$

In this way, the POTF of the system with a narrow annular source can also be expressed analytically, but it is more complicated. Combining Eqs. (10.2), (5.7), and (10.5) and using the superposition principle again, the POTF for a circularly symmetric source can be mathematically expressed as

$$H(\boldsymbol{\rho},\eta) = \int \tilde{S}(\rho_s)\frac{\mathrm{d}H(\boldsymbol{\rho},\eta;0,\rho_s)}{\mathrm{d}\rho_s}\mathrm{d}\rho_s. \tag{10.6}$$

However, the dependence of $H(\boldsymbol{\rho},\eta;0,\rho_s)$ with respective to ρ_s is not elementary. As ρ_s varies, the nonzero boundary of the 3D POTF also varies, which makes the derivative not practical. Therefore, the integration cannot be calculated analytically, but numerical evaluation using the finite difference is practical and should be performed. Nevertheless, compared to the conventional 2D integration, this calculation is still simpler since only 1D integration is required.

Experimentally, Gaussian illumination can be obtained by inserting a Gaussian apodizing filter placed over the condenser's diaphragm plane [230]. With the theoretical and experimental development, we should be able to incorporate Gaussian illumination in our QPI methods.

10.5 ITDPM Development

The current ITDPM program introduced in Chapter 7 is elementary. The iterative minimization algorithm is based on gradient descent, which is simple but converges slowly. More sophisticated algorithms can be used for the minimization. Potential algorithms include Newton's method, nonlinear conjugate gradient, and multigrid algorithm [231]. Multigrid algorithm is a powerful iterative optimization algorithm. The convergence speed almost does not vary with problem size, so it is particularly suitable for multi-dimensional problems. I propose to implement the multigrid algorithm, so that ITDPM is adequate for full 3D problems.

In the previous simulations, α was a fixed number. However, it is an important parameter for adjusting the tradeoff between the intensity similarity and piecewise smoothness. It needs to be appropriately chosen to obtain optimized behaviors. For the case when the ideal object is known, the optimized α can be found by minimizing the NRMSE between the ideal RI and the reconstructed RI. The optimized value may depend on many factors, such as the size of the problem (number of pixels in each dimension), the range of RI, the number of angles, and the noise level. It can also be different for object rotation and image rotation. An elementary criterion is that the selected α should ensure that the values of the similarity term and the regularization term for the optimized v are of the same order of magnitude.

Some preliminary simulations were done to investigate the properties of the optimized α. Using the average rather than the sum of $\left|\left|A_m v - I_m\right|\right|^2$ ensures that the optimized α is approximately independent of the total number of angles N. This was verified by simulations. On the other hand, our simulations also show that the optimized

α increases when the problem size (the number of pixels in each dimension) increases. This is because the similarity term is approximately proportional to the total number of pixels in the area (in the volume in 3D), while the regularization term is approximately proportional to the number of pixels on the edge (on the surface in 3D). Our simulations also show that the optimized α also increases when the maximum RI contrast of the object increases, which can be explained by the same reasoning. I hope more quantified results can be found with further simulations.

A more attracting development is to measure the RI without rotating the object, *i.e.* ITDPM with a single angle of rotation. If it is developed successfully, the hardware modification is further reduced since the rotator is not needed any more. The current 3D QPI methods require object rotation, which is slow because the fiber may need to be realigned to the center of the camera field of view after each rotation. The rotation is an even bigger problem in 3D biological cell imaging, because it is very difficult to rotate cells in a controllable way. However, ITDPM with a single angle of rotation is not currently workable, because the missing cone problem is too severe. Even two angles of rotation bring significant errors, as shown in Figure 7.4(b). However, the errors should be smaller if the NAs can be increased. The size of the region with zero POTF can be reduced with a larger $\mathrm{NA_c}$. However, on the other hand, a large $\mathrm{NA_c}$ will increase the size of the low-value POTF region, which is also problematic. Since Gaussian illumination reduces the size of the low-value POTF region, it can be very helpful in single-angle ITDPM. Therefore, if the $\mathrm{NA_c}$ and $\mathrm{NA_o}$ are sufficiently large and Gaussian illumination is used, it should be possible to reconstruct the RI reasonably well from a single angle of rotation. In fact, Soto *et. al.* [113] did some similar work on 3D QPI based on through-

focal scanning without rotation. They can image the cells reasonably well by using $NA_o = 1.4$, even without iterative regularization. I think the major difference is from the NAs. Since ITDPM without rotation enables much simpler experimental equipment and much faster measurement, we want to adjust both our microscopes and our programs to enable higher NAs. Therefore, we propose to add an oil-immersion objective lens to our microscope, which can make the NA_o larger than 1. Another difference from Soto *et. al.* is that they assume that the weak absorption is proportional to refractive index contrast, so that an effective POTF containing the absorption part is used [113]. It helps to reduce the error caused by zero POTF along the y-axis in the frequency domain. This is also something we can try. We expect to recover the RI by ITDPM without rotation, and the improved method can be called non-tomographic deconvolution phase microscopy (NTDPM), since tomography is not used anymore.

10.6 3D QPI on Weakly Absorptive Objects

In the previous QPI simulations and measurements, the objects are usually assumed to be pure phase objects, which means that they do not absorb light at all. However, realistic objects often have slight absorption. Although the absorption can be safely ignored in most objects, taking absorption into account can make the QPI results more accurate. In Chapter 6, WLS-MFPI-PC is proved to be workable for absorptive objects, and improved POTFR already takes weak absorption into account. The simulation results support that both methods work for weakly absorptive objects. Furthermore, we propose to modify our 3D QPI methods to be suitable for objects with weak absorption and then test these methods using simulation and experiments.

As analyzed in Chapter 6, the absorption term can often be eliminated by subtraction of symmetric intensities. Therefore, in TDPM, we can use a rotation of 360° instead of 180°. In this way, two stacks of 3D images whose illumination are from opposite directions can be measured. By subtracting them, the absorption parts cancel out, and only the phase parts are retained. Simulations and experiments should be done to validate this modification.

APPENDIX A. CLARIFICATION AND UNIFICATION OF THE OBLIQUITY FACTOR IN DIFFRACTION AND SCATTERING THEORIES: DISCUSSION

A.1 Introduction

The underlying basis of QPI theories is the diffraction and scattering of light by objects. This is particularly apparent for the case of single-beam non-interferometric QPI methods. Diffraction usually refers to interaction with thin objects, whereas scattering refers to interaction with thick objects. Since they are similar in concept and are closely related, as will be shown later, they are collectively called diffraction in the present thesis. 2D diffraction theories describe the propagation of light beyond a planar screen or a thin object, which is a conventional concept of diffraction. 3D diffraction theories describe the propagation of light beyond a thick object, which is more commonly known as scattering. Although in some literature, 2D diffraction refers to diffraction in the 2D space (x-z plane, incident propagation in the z direction with no variation in y direction), and 3D diffraction refers to diffraction in the complete 3D space, these definitions are not used in the present thesis.

The 2D and 3D theories are similar in concept, but they have been developed from different points of view and are usually applied separately. 2D theories are applied to thin objects, and 3D theories are applied to thick objects. Nevertheless, in the literature, there are some mixed uses of 2D and 3D diffraction theories. For example, some 3D theories are developed by applying 2D theories slice by slice repeatedly [232-

235]. Some 2D theories are developed by integrating some 3D quantity along a single dimension [77]. Some 2D theories use 3D theories simply by defining the thin object as a Dirac delta distribution in the 3D space [82, 236].

In spite of the existence and value of mixed uses in the literature, the validity of them cannot be taken for granted, because 2D and 3D theories are developed independently based on different object types with different requirements. The present appendix discusses the relationship between the two theories. Particularly, we will emphasize that one needs an obliquity factor (OF) modification to ensure the correctness in some mixed uses, particularly when the paraxial approximation is not valid. Although this type of concept has already been applied in some papers [99, 237], the present appendix, which distinguishes two types of OF modifications, provides a more complete and unified theory. The discussion is concluded with a comprehensive table that summarizes the use of the OF modifications in 2D and 3D diffraction theories as applied to thin and thick objects. This work is published in Ref. [114].

A.2 The 2D and 3D Diffraction Theories

A.2.1 2D Diffraction Theory

Classical 2D diffraction theory [110] models an object as a planar transmittance function or a screen function

$$t(\boldsymbol{x}) = \exp[i\phi(\boldsymbol{x})]. \tag{A.1}$$

The real part of $\phi(\boldsymbol{x})$ represents the phase retardation. Since 2D diffraction theory models the object as a 2D function, it requires that the object is very thin. A thin object usually means that the light exits the object approximately at the same lateral coordinate as it enters the object, or the transversal deviation of light can be neglected [110].

The diffraction integral gives the amplitude of the diffracted light as

$$u(\boldsymbol{x}, z) = \int u_{IN}(\boldsymbol{x}', 0) t(\boldsymbol{x}') h^{(2)}(\boldsymbol{x}, z; \boldsymbol{x}') \mathrm{d}\boldsymbol{x}', \tag{A.2}$$

where $u_{IN}(\boldsymbol{x}', z')$ is the incident light amplitude, $u(\boldsymbol{x}, z)$ is the diffracted light amplitude, and z is the longitudinal spatial coordinate. The quantity $h^{(2)}(\boldsymbol{x}, z; \boldsymbol{x}') = h^{(2)}(\boldsymbol{x} - \boldsymbol{x}', z)$ is the 2D point spread function (PSF) of the optical system. It is given explicitly as

$$h^{(2)}(\boldsymbol{x}, z; \boldsymbol{x}') = \frac{1}{i\lambda} \frac{\exp\left(ik_0[(\boldsymbol{x} - \boldsymbol{x}')^2 + z^2]^{1/2}\right)}{[(\boldsymbol{x} - \boldsymbol{x}')^2 + z^2]^{1/2}} K(\boldsymbol{x}, z; \boldsymbol{x}'). \tag{A.3}$$

where $k_0 = 2\pi/\lambda$ is the freespace wavevector magnitude and K is the obliquity factor (OF). The OF was first introduced by Kirchhoff in his diffraction integral. Later Rayleigh and Sommerfeld modified it, aiming to overcome the inconsistent Kirchhoff boundary conditions (BCs) [110]. The three versions of OFs are summarized in the following as [238]

$$K(\theta, \theta') = \begin{cases} \cos\theta & \text{Dirichlet BC} \\ \cos\theta' & \text{Neumann BC} \\ (\cos\theta + \cos\theta')/2 & \text{Kirchhoff BCs} \end{cases}. \tag{A.4}$$

In the above equation, θ is the diffracting angle, defined by the angle between the diffracted light and the positive z-axis. The quantity θ' is the incident angle, defined by the angle between the incident light and the positive z-axis. The first two solutions are Rayleigh-Sommerfeld solutions. All of the OFs are very close to unity for paraxial conditions, so they make no difference in the simplified paraxial theories.

The difference between the two Rayleigh-Sommerfeld solutions of OFs is analogous to two orthogonal linear polarizations of light, transverse electric (TE) and transverse magnetic (TM) respectively. The Kirchhoff solution is analogous to the unpolarized light, which is the equal mixture of the two polarizations. The preferred choice is the first OF using Dirichlet BC (first Rayleigh-Sommerfeld OF), because it is the simplest, and is the only one consistent with the widely used angular spectrum theory [111]. Considering the relation between the propagation angle and the spatial frequency,

$$\rho = \sin\theta\,/\lambda. \tag{A.5}$$

the first Rayleigh-Sommerfeld OF can be written in the spatial frequency domain

$$K(\boldsymbol{\rho}) = \sqrt{1-\lambda^2\boldsymbol{\rho}^2}. \tag{A.6}$$

or

$$K(\boldsymbol{x}, z; \boldsymbol{x}') = K(\boldsymbol{x}-\boldsymbol{x}', z) = \frac{z}{[(\boldsymbol{x}-\boldsymbol{x}')^2 + z^2]^{1/2}}. \tag{A.7}$$

A.2.2 3D Diffraction Theory

Classical 3D diffraction theory [5] starts from the 3D Helmholtz equation for an inhomogeneous material

$$\nabla^2 \boldsymbol{E} + 2\nabla(\boldsymbol{E} \cdot \nabla n/n) + n^2 k_0^2 \boldsymbol{E} = 0. \tag{A.8}$$

The term containing the refractive index gradient is usually ignored for simplicity. However, this simplification requires that the refractive index gradient is small, which can be mathematically represented as

$$\lambda |\nabla n(\boldsymbol{r})| \ll 1. \tag{A.9}$$

The simplified scalar Helmholtz equation is solved via the Green's function method. Usually, the delta function decomposition in that method uses SP instead of RI.

After some mathematical steps, the diffracted light amplitude can be expressed as

$$u(\boldsymbol{r}) = u_{IN}(\boldsymbol{r}) + \int u(\boldsymbol{r}')v(\boldsymbol{r}')G(\boldsymbol{r};\boldsymbol{r}')\mathrm{d}\boldsymbol{r}', \tag{A.10}$$

where $u_{IN}(\boldsymbol{r})$ is the amplitude of the incident light and $u(\boldsymbol{r})$ is the amplitude of the diffracted light. $G(\boldsymbol{r};\boldsymbol{r}') = G(\boldsymbol{r}-\boldsymbol{r}')$ is the Green's function as defined as a solution of

$$\nabla^2 G(\boldsymbol{r}) + k_0^2 G(\boldsymbol{r}) = \delta(\boldsymbol{r}) \tag{A.11}$$

and can be written explicitly as

$$G(\boldsymbol{r};\boldsymbol{r}') = -\frac{\exp(ik_0|\boldsymbol{r}-\boldsymbol{r}'|)}{4\pi|\boldsymbol{r}-\boldsymbol{r}'|}. \tag{A.12}$$

For an object with an arbitrary shape, calculating Eq. (A.10) requires further approximation. The most commonly used approximation is the single-scattering approximation, also called the first Born approximation. This approximation, given the prerequisite of the 3D Helmholtz equation Eq. (A.9), requires the SP to be small, which can be expressed as

$$|n(\boldsymbol{r}) - 1| \ll 1. \tag{A.13}$$

With this approximation, the propagating light amplitude $u(\boldsymbol{r}')$ in the perturbation integral term can be approximated by the incident light amplitude $u_{IN}(\boldsymbol{r}')$. As a result, the diffracted light amplitude Eq. (A.10) becomes

$$u(\boldsymbol{r}) = u_{IN}(\boldsymbol{r}) + \int u_{IN}(\boldsymbol{r}')V(\boldsymbol{r}')G(\boldsymbol{r};\boldsymbol{r}')\mathrm{d}\boldsymbol{r}'. \tag{A.14}$$

A.2.3 Intrinsic Difference in 2D and 3D Diffraction Theories

Although many researchers are familiar with 2D and 3D diffraction theories, few may notice that the basic object requirements in 2D and 3D diffraction theories are different. 2D diffraction theory requires a very thin object. Nevertheless, for an ideal thin phase object, the RI of the thin object can be described in the 3D space as

$$\Delta n(\boldsymbol{x}, z) = \phi(\boldsymbol{x})\delta(z)/k_0. \tag{A.15}$$

where $\delta(z)$ is the Dirac delta function. The quantity Δn is the RI difference between the object and the background media, i.e.,

$$\Delta n(\boldsymbol{x}, z) = n(\boldsymbol{x}, z) - 1. \tag{A.16}$$

This means that if the phase is finite, which is always true for a realistic meaningful object, the refractive index values and gradients are large. 3D diffraction theory, on the other hand, is valid for a thick object but requires that the refractive index values and gradients are small, as described by Eqs. (A.13) and (A.9).

As can be seen, the basic object requirements in 2D and 3D diffraction theories are different. Although a delta function can be used to express a 2D phase distribution by a 3D refractive index distribution, the object does not satisfy the basic requirements of 3D diffraction theory.

A.2.4 Explicit Difference for a Thin Object

In order to show clearly the different results due to the different object requirements, we apply 2D and 3D diffraction theories respectively to a thin object. The test object is an infinitesimally thin object, whose phase $\phi(\boldsymbol{x})$ is small. It is placed at the plane $z = 0$. In principle, only the 2D theory should be applied to a thin object, but applying the 3D theory is also mathematically possible, even though the refractive index requirement is not met.

Firstly, the 2D theory is applied. Since $\phi(\boldsymbol{x})$ is small, the screen function Eq. (A.1) can be approximated by

$$t(\boldsymbol{x}) = 1 + i\phi(\boldsymbol{x}). \tag{A.17}$$

As a result, the final expression of the diffracted light Eq. (A.2) becomes

$$u(\boldsymbol{x}, z) = u_{IN}(\boldsymbol{x}, z) + \frac{1}{\lambda}\int u_{IN}(\boldsymbol{x}', 0)\phi(\boldsymbol{x}')\frac{\exp\left(ik_0[(\boldsymbol{x}-\boldsymbol{x}')^2 + z^2]^{1/2}\right)}{[(\boldsymbol{x}-\boldsymbol{x}')^2 + z^2]^{1/2}}K(\boldsymbol{x}, z; \boldsymbol{x}')\mathrm{d}\boldsymbol{x}' \tag{A.18}$$

Secondly, the 3D theory is applied. The SP can be determined from the phase using Eq. (5.7). As a result, the final expression of the diffracted light Eq. (A.14) becomes

$$u(\boldsymbol{x}, z) = u_{IN}(\boldsymbol{x}, z) + \frac{1}{\lambda}\int u_{IN}(\boldsymbol{x}', 0)\phi(\boldsymbol{x}')\frac{\exp\left(ik_0[(\boldsymbol{x}-\boldsymbol{x}')^2 + z^2]^{1/2}\right)}{[(\boldsymbol{x}-\boldsymbol{x}')^2 + z^2]^{1/2}}\mathrm{d}\boldsymbol{x}'. \tag{A.19}$$

By inspection of Eqs. (A.18) and (A.19), the only difference between the diffracted light amplitudes of the thin object due to different diffraction theories is the obliquity factor (OF), which only appears in the 2D result. This is the consequence of the dissimilar object requirements. This explanation is consistent with the verbal description in Chap. 1.8 of Cowley's book *Diffraction Physics* [239] but is mathematically justified here.

A.3 Conversions Between 2D and 3D Theories

The equations in the previous section show that 2D and 3D diffraction theories are based on different object requirements. Therefore, they should be used according to their own applicabilities, i.e., the 2D theory is used for thin objects, and the 3D theory is used for thick objects. However, 2D and 3D diffraction theories are not independent of each other. This section will show that they can be linked together.

A.3.1 Application of 2D Theory to 3D Objects

This subsection will show that 3D diffraction theory can be derived from 2D diffraction theory, and the OF is eliminated at the same time. A thick object can be decomposed into a series of slices normal to the z-axis. The slices are very thin and satisfy the thin object requirement. With the first Born approximation, the perturbations due to each slice, described by Eq. (A.18), can be linearly superposed. Since the position of the slice is not fixed, another parameter z' describing the longitudinal position of the slice should be introduced. Therefore, Eq. (A.18) should be rewritten accordingly as

$$u(\boldsymbol{x}, z) = u_{IN}(\boldsymbol{x}, z) + \iint u_{IN}(\boldsymbol{x}', z')\mathrm{d}\phi(\boldsymbol{x}', z') \times \frac{1}{\lambda}\frac{\exp\left(ik_0[(\boldsymbol{x}-\boldsymbol{x}')^2 + (z-z')^2]^{1/2}\right)}{[(\boldsymbol{x}-\boldsymbol{x}')^2 + (z-z')^2]^{1/2}} K(\boldsymbol{x}, z; \boldsymbol{x}', z')\mathrm{d}\boldsymbol{x}'. \tag{A.20}$$

where the definition of the OF is now

$$K(\boldsymbol{x}, z; \boldsymbol{x}', z') = K(\boldsymbol{x}-\boldsymbol{x}', z-z') = \frac{z-z'}{[(\boldsymbol{x}-\boldsymbol{x}')^2 + (z-z')^2]^{1/2}}. \tag{A.21}$$

where the propagation angle θ' is now a function of $\boldsymbol{x}, z, \boldsymbol{x}'$ and z. Since the refractive index is small, each thin slice produces an infinitesimal phase. The important point is that these slices satisfy both thin object requirement in the 2D theory and the small SP requirement Eq. (A.13) in the 3D theory. This is the key to connect the two theories. However, this is only possible when the phase is infinitesimal, but one should be aware that a realistic thin object cannot really have infinitesimal phase.

For off-axis illumination, the induced phase of a slice should not be simply

$$\mathrm{d}\phi(\boldsymbol{x}', z') = k_0 \Delta n(\boldsymbol{x}', z')\mathrm{d}z'. \tag{A.22}$$

Instead, it should be replaced by the effective phase, which is

$$\mathrm{d}\phi'(\boldsymbol{x}', z') = k_0 \Delta n(\boldsymbol{x}', z')\mathrm{d}z'/K(\boldsymbol{x}, z; \boldsymbol{x}', z'). \tag{A.23}$$

The division of the OF enlarges the effective phase, because the light path length in the slice is $\mathrm{d}z'/K$ for off-axis light. This behavior was also recognized in Ref. [237] and [99]. When combined with Eqs. (A.17) and (A.23), Eq. (A.20) becomes

$$\begin{aligned} u(\boldsymbol{x}, z) = u_{IN}(\boldsymbol{x}, z) - \iint u_{IN}(\boldsymbol{x}', z')V(\boldsymbol{x}', z') \\ \times \frac{1}{4\pi} \frac{\exp\left(ik_0[(\boldsymbol{x}-\boldsymbol{x}')^2 + (z-z')^2]^{1/2}\right)}{[(\boldsymbol{x}-\boldsymbol{x}')^2 + (z-z')^2]^{1/2}} \mathrm{d}\boldsymbol{x}'\mathrm{d}z'. \end{aligned} \tag{A.24}$$

The two OF terms cancel out, so there is no OF in this result. Given Eq. (A.12) and 3D coordinate $\boldsymbol{r} = (\boldsymbol{x}, z)$, Eq. (A.24) is the same as Eq. (A.14). So far, 3D diffraction theory is derived from the 2D theory successfully.

Nemoto *et al.* provided a similar derivation going from 2D diffraction theory to 3D diffraction theory [240], but that derivation is limited to the paraxial case, where the OF is not an issue. Similar situations can be found in other papers [232-235]. The extension to the nonparaxial case shows that the OF term in the 2D theory disappears in the 3D result, which is the consequence of the effective phase Eq. (A.23). The introduction of the effective phase is defined here as the Type-1 OF modification.

However, the induced phase of a thin object in the conventional 2D diffraction theory remains as defined by Eq. (A.22). Since the phase is finite rather than infinitesimal, but the thickness of an ideally thin object is infinitesimal, in order to satisfy the finite phase, the refractive index is correspondingly infinitely large. As a result, the light propagating in the object is always in the normal direction after refraction, so the light path length does not vary with the incident angle. This is, again, because of the different properties for thin and thick objects.

A.3.2 Application of 3D Theory to 2D Objects

Unlike the development of 3D diffraction theory from the 2D theory presented in the previous subsection, the 2D theory cannot be derived from the 3D theory in similar ways, since the object requirements cannot be made to be compatible. As shown in Sec. 2D, it is their different object requirements that result in the OF. However, we can still find a modification method to equivalently express the 2D theory from the 3D theory.

For this purpose, a modified Green's function can be defined as the standard Green's function multiplied by the OF

$$G'(\boldsymbol{r};\boldsymbol{r}') = G(\boldsymbol{r};\boldsymbol{r}')K(\boldsymbol{r};\boldsymbol{r}'). \tag{A.25}$$

This is inspired by the PSF Eq. (A.3) in the 2D theory. In fact, the Green's function Eq. (A.12) is the impulse response function of the 3D Helmholtz equation, whereas the PSF Eq. (A.3) is the impulse response function of a 2D diffraction system. Therefore, it is not surprising that the two impulse response functions have similar forms. Except for a constant multiplication factor, the modified Green's function in the 3D theory is the same as the PSF in the 2D theory. When this modified Green's function is used in the 3D theory instead of the standard Green's function, the result will include the OF and be the same as that from the 2D theory. The introduction of the modified Green's function is defined here as the Type-2 OF modification. Unlike the Type-1 OF modification, the Type-2 OF modification has not been recognized by previous researchers.

This modification enables the application of some results from 3D diffraction theory to 2D cases. Section A.3.4 will apply this modification to explain the derivation of the nonparaxial POTF.

A.3.3 Relationship between the Two Types of Obliquity Factor Modifications

The two types of OF modifications are developed using different logical reasoning, so they have some significant differences. The effective phase in the Type-1 OF modification has a clear physical meaning, whereas the modified Green's function in the Type-2 OF modification represents a mathematical construct, since it is not directly based on physical boundary conditions. This difference stems, again, from dissimilar

object requirements in 2D and 3D diffraction theories, which will be explained in more detail below.

A thick object must satisfy Eq. (A.13), which is the requirement of 3D diffraction theory. For the application of 2D diffraction theory, a thick object can be divided into multiple thin slices, with each slice satisfying thin object requirement of 2D diffraction theory. Therefore, it is physically correct to apply the 2D theory to each slice and integrate the results to achieve a 3D result, provided the appropriate phase is used. In this case, the effective phase has a clear physical meaning as it accounts for the longer propagation distances of the off-axis rays.

A thin object must be thin enough to satisfy the requirement of 2D diffraction theory. Therefore, its thickness l must be small. If the refractive index relative to the surrounding index Δn is small, then its induced phase will be $\phi = \int_0^l k\Delta n \mathrm{d}z \approx kl\Delta n$, and it can be neglected since it contains the product of two very small numbers. A negligible ϕ means that the object does not produce any measurable effect. Therefore, a realistic meaningful thin object cannot satisfy Eq. (A.13), the requirement of 3D diffraction theory. Although a thin object can be modeled in 3D space using a delta function, it does not change the fact that Eq. (A.13) is not satisfied due to the nature of the delta function. As a result, there is no realistic physical modification enabling the correct application of 3D diffraction theory to a thin object. However, a mathematical modification can be synthesized that produces correct results. The modified Green's function does not have a clear physical meaning, but it indeed leads to correct results in this situation.

In spite of the significant differences between them, both types of OF modifications represent the incorporation of nonparaxial obliquity effects into the corresponding diffraction theories. Applying the Type-1 OF modification results in the original equation being divided by the OF, while applying the Type-2 OF modification results in the original equation being multiplied by the OF. From this point of view, one OF modification is, in some sense, equivalent to the inverse of the other modification. However, the division and multiplication are not trivial, because the definition of the OF, Eq. (A.21), is a function of the coordinates of both the object space and the image space, and the OFs are inside integrals. Therefore, the two types of OF modifications are not true inverses of each other. However, the inverse-like relationship between them provides a level of understanding and unifies them within a common framework.

A.3.4 Application of Obliquity Factor Modification in Nonparaxial POTF

MFPI-PC is a 2D QPI method for recovering the phase of a thin object, so it uses 2D diffraction theory in the development. However, it also uses the 3D POTF derived from 3D diffraction theory. The different object requirements of 2D and 3D diffraction theories increase the difficulty in making MFPI-PC self-consistent. However, it is obvious now that the derivation of the nonparaxial MFPI-PC falls into a category discussed in Sec. A.3.2. Therefore, the Type-2 OF modification should be introduced. Although the full unmodified 3D POTF does not contain the OF, when we apply it to recover the phase of a thin object, we need the OF to modify the Green's function. This modification is a part of the approach in Chapter 3, as shown in Eq. (3.8)(3.11), and the resulting theory gives improved accuracy as determined by both simulations and experimental measurements.

Two versions of nonparaxial POTFs were derived in Chapter 3, namely the nonparaxial POTF without OF modification (nP-POTF) and the nonparaxial POTF with OF modification (nP-POTF-OF). The theories in the present apprndix predict the applicability of each POTF. The artificial nP-POTF-OF is more accurate when applied to 2D diffraction cases or thin objects, which was already validated in Chapter 3. On the other hand, the realistic nP-POTF should be more accurate when applied to 3D diffraction cases or thick objects.

A.4 Summary and Discussion

The present work clarifies the applicability of 2D and 3D diffraction theories. 2D diffraction theory models the object as a planar transmittance function, which requires the object to be very thin. 3D diffraction theory employs the Born approximation, which requires that the difference of the refractive index of the object relative to the surrounding index is very small, as described by Eq. (A.13). These two object requirements are different and cannot be satisfied simultaneously by a real object. Therefore, if one theory is applied to an object that satisfies the requirement of the other theory, some modification is required for consistent uses. The present apprndix shows that the OF modifications link the two theories and make the mixed uses possible. When the 2D theory is applied to a thick object, the effective phase including the OF should be used. When the 3D theory is applied to a thin object, the modified Green's function including the OF should be included. The OF modifications are not needed if the 2D theory is applied to a thin object or the 3D theory is applied to a thick object. Table A.1 summarizes the conditions when the OF should and should not be used.

Table A.1: The usage of the OF modifications when 2D and 3D theories are applied to thin and thick objects.

Theory	Thin objects	Thick objects
2D diffraction	(inherent OF) No modification needed. Use Eq. (A.2) as is.	(the Type-1 OF modification) Use effective phase $\mathrm{d}\phi'$. $\mathrm{d}\phi' = \mathrm{d}\phi/K$ [Eq. (A.23)].
3D diffraction (scattering)	(the Type-2 OF modification) Use modified Green's function G'. $G' = GK$ [Eq. (A.25)].	(no OF) No modification needed. Use Eq. (A.14) as is.

An important application of these conclusions is in the nonparaxial POTF. The POTF is derived from 3D diffraction theory. If it is applied in phase imaging of a thin object, the Type-2 OF modification should be included, which was already validated in Chapter 3 by simulations and experimental results. On the other hand, if the POTF is applied in imaging the refractive index of a thick object, the OF modification should not be used.

The conclusions in this discussion appendix do not overturn the existing theories and applications but, on the contrary, support them. Most of the existing theories are based on the paraxial approximation, in which the OF is approximated by unity, so the OF modifications make no differences there. In addition, most of the existing theories only apply the 2D theory to thin objects or apply the 3D theory to thick objects, so no modifications are needed in these cases. For other situations, in which the mixed use of the 2D and 3D theories is applied in nonparaxial conditions, the OF modifications should be included for more accurate results. Some authors have used the Type-1 OF modification when they generalized the paraxial theory to the nonparaxial conditions [99, 237]. However, the Type-2 OF modification has not been proposed by previous

researchers before me [109]. The present appendix supports the previous work both where the OF modifications are not needed and where they have been applied.

This appendix represents a presentation of a unified, complete, and consistent description of the use of OF and OF modifications in 2D and 3D imaging of thin and thick objects. Without this four-fold 2D-3D description, researchers may logically and inadvertently adopt an inappropriate approach leading to erroneous results.

APPENDIX B. NONPARAXIAL 3D POTF: MORE DETAILS

B.1 Analytical Integration of Nonparaxial 3D POTF

In Chapter 3, the general equation for the nP-POTF-OF is given as Eq.(3.9). By defining

$$F(\boldsymbol{\rho},\eta) \triangleq \int \tilde{p}(\boldsymbol{\rho}'+\boldsymbol{\rho}/2)\,\tilde{S}(\boldsymbol{\rho}'+\boldsymbol{\rho}/2)\tilde{p}^{*}(\boldsymbol{\rho}'-\boldsymbol{\rho}/2) \times \delta\left(\eta+\sqrt{\lambda^{-2}-\left(\boldsymbol{\rho}'-\frac{\boldsymbol{\rho}}{2}\right)^{2}}-\sqrt{\lambda^{-2}-\left(\boldsymbol{\rho}'+\frac{\boldsymbol{\rho}}{2}\right)^{2}}\right)\mathrm{d}^{2}\boldsymbol{\rho}', \tag{B.1}$$

it is clear that

$$H(\boldsymbol{\rho},\eta)=\frac{i\lambda}{4\pi}[F(\boldsymbol{\rho},\eta)-F^{*}(-\boldsymbol{\rho},-\eta)]. \tag{B.2}$$

When the conditions for uniform illumination and circular apertures are applied as described by Eqs. (3.10)-(3.11), the POTF is axially symmetric, so it can be assumed $\boldsymbol{\rho}=(\rho,0)$ for simplicity, and $F(\rho,\eta)$ is real. Therefore,

$$H(\rho,\eta)=\frac{i\lambda}{4\pi}[F(\rho,\eta)-F(-\rho,-\eta)]. \tag{B.3}$$

Meanwhile, the $\boldsymbol{\rho}'$ is represented by $\boldsymbol{\rho}'=(\rho_x',\rho_y')$. Since it is assumed $\rho_p \geq \rho_s$, the integral can be rewritten as

$$F(\rho,\eta)=\iint \tilde{S}(\rho_x'+\rho/2\,,\mu_y')\tilde{p}(\rho_x'-\rho/2\,,\rho_y') \tag{B.4}$$

$$\times \delta(\eta + \sqrt{\lambda^{-2} - \left(\rho_x' - \frac{\rho}{2}\right)^2 - {\rho_y'}^2} - \sqrt{\lambda^{-2} - \left(\rho_x' + \frac{\rho}{2}\right)^2 - {\rho_y'}^2})\mathrm{d}\rho_x'\mathrm{d}\rho_y'.$$

In the $\rho_x' - \rho_y'$ plane, $\tilde{S}(\rho_x' + \rho/2, \rho_y')$ represents a disk with radius ρ_s and $\tilde{p}(\rho_x' - \rho/2, \rho_y')$ represents a disk with radius ρ_p. Letting the argument of the delta function be zero,

$$\eta + \sqrt{\lambda^{-2} - (\rho_x' - \rho/2)^2 - {\rho_y'}^2} - \sqrt{\lambda^{-2} - (\rho_x' + \rho/2)^2 - {\rho_y'}^2} = 0, \qquad \text{(B.5)}$$

so the following equation can be derived

$${\rho_y'}^2 + \left(1 + \frac{\rho^2}{\eta^2}\right){\rho_x'}^2 = \gamma^2, \qquad \text{(B.6)}$$

where γ is defined as

$$\gamma(\rho, \eta) \triangleq \sqrt{\lambda^{-2} - (\rho^2 + \eta^2)/4}\,, \qquad \text{(B.7)}$$

It is clear that the delta function represents an ellipse in the $\rho_x' - \rho_y'$ plane. The integral is only performed in the segment of the ellipse inside both of the two disks (the common area). Figure B.1 shows the positions of the ellipse and the two disks with some different parameters. In the figures, S, P, and D represent the source function, the pupil function, and the delta function respectively.

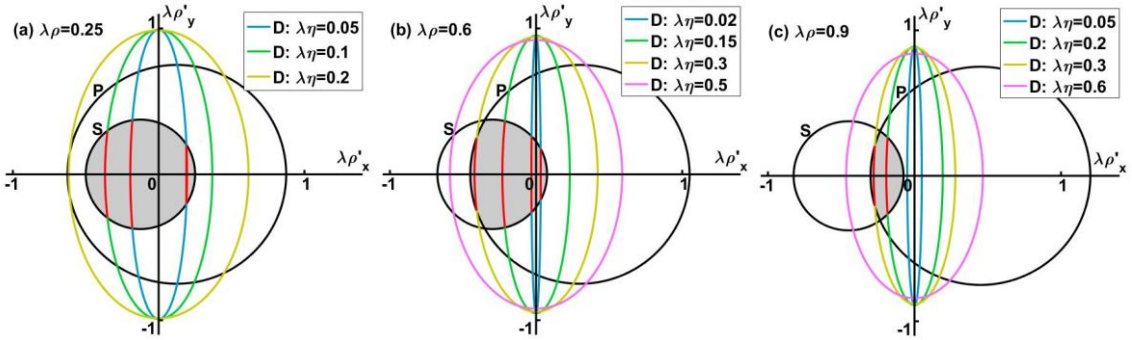

Figure B.1: The positions of the source, pupil and delta functions in the spatial frequency $\rho'_x - \rho'_y$ plane. The variables are multiplied by λ so both axes are dimensionless. S represents the source function $\tilde{S}(\rho'_x + \rho/2, \rho'_y)$. P represents the pupil function $\tilde{p}(\rho'_x - \rho/2, \rho'_y)$. D represents the delta function $\rho'^2_y + \left(1 + \frac{\rho^2}{\eta^2}\right)\rho'^2_x = \gamma^2$. The shaded area is the area where $\tilde{S}(\rho'_x + \rho/2, \rho'_y)$ and $\tilde{p}(\rho'_x - \rho/2, \rho'_y)$ are both unities. The red segment of the ellipse is the integral region of Eq. (B.4). In all of the figures, $\lambda\rho_s = 0.375$ and $\lambda\rho_p = 0.75$. (a) $\lambda\rho = 0.25$. The blue ellipse corresponds to $\lambda\eta = \pm 0.05$, where $\lambda\eta = 0.05$ corresponds to the left red segment, and $\lambda\eta = -0.05$ corresponds to the right red segment. The green ellipse corresponds to $\lambda\eta = 0.1$. The yellow ellipse corresponds to $\lambda\eta = 0.2$. (b) $\lambda\rho = 0.6$. The blue ellipse corresponds to $\lambda\eta = \pm 0.02$, where $\lambda\eta = 0.02$ corresponds to the left red segment, and $\lambda\eta = -0.02$ corresponds to the right red segment. The green ellipse corresponds to $\lambda\eta = 0.15$. The yellow ellipse corresponds to $\lambda\eta = 0.3$. The magenta ellipse corresponds to $\lambda\eta = 0.5$. (c) $\lambda\rho = 0.9$. The blue ellipse corresponds to $\lambda\eta = 0.05$. The green ellipse corresponds to $\lambda\eta = 0.2$. The yellow ellipse corresponds to $\lambda\eta = 0.3$. The magenta ellipse corresponds to $\lambda\eta = 0.6$. If $\rho < 0$, S, P, and D are flipped horizontally, and positive η corresponds to the right segment.

In order to perform the integral of Eq. (B.4), a detailed analysis of the positions of S, P, and D is needed. When $|\rho| \leq \rho_p - \rho_s$, S is completely inside P, so the common area of S and P is S itself. When $\rho_p - \rho_s < |\rho| \leq \rho_p + \rho_s$, S and P are intersected. When $|\rho| < 2\rho_s$, the origin point is inside S, so D may have two segments inside the common area for small η. But notice that actually only a half of the ellipse is effective. If $\rho > 0$, then for $\eta > 0$, only the left half ellipse is effective, while for $\eta < 0$, only the right half ellipse is effective. If $\rho < 0$, then for $\eta > 0$, only the right half ellipse is effective, while for $\eta < 0$, only the left half ellipse is effective. This property is lost when Eq. (B.5)

evolves into Eq. (B.6). When $|\rho| > 2\rho_s$, the origin point is outside of S, so D can have at most one segment inside the common area. When η is large, it is also possible that D does not intersect with the common area. The positions for various cases are shown in Figure B.1.

Since ρ_y' is single valued in the integral segment, Eq. (B.4) is simplified to involve the integration over only ρ_y' using the property of two-dimensional delta function

$$\iint \delta(f(x,y)=0)g(x,y)\mathrm{d}x\mathrm{d}y = \int_{f(x,y)=0} \frac{g(x,y)}{\left|\frac{\partial f(x,y)}{\partial x}\right|}|\mathrm{d}y|. \tag{B.8}$$

After integrating ρ_y', Eqs. (3.13)-(3.18) can be derived, and the notations in those equations can be explained now. The quantity $\rho_{y,\max}'$ is the maximum possible ρ_y' properly determined by one of the red segments in Figure B.1. The quantity $\rho_{x,c}'(\rho,\eta)$ is the ρ_x' of the intersection points of D and the boundary of the shaded area.

B.2 Shapes of the POTFs

Equations (3.13)-(3.18) describe the nP-POTF-OF in abstract analytical expressions. Nevertheless, they can be visualized in the figure of the POTF. Figure B.2 shows the detailed shapes of the POTFs as well as the boundaries of $F(\rho,\eta)$, which can help to understand the properties of the POTFs. The POTFs are odd functions of η but are even functions of ρ. Figure B.2(a) shows the shape of the P-POTF and the boundaries determined by Eq. (32) in Ref. [108]. Figure B.2(b) shows the shape of the nP-POTF-OF and the boundaries of $F(\rho,\eta)$ determined by Eqs. (3.14)-(3.18) in this paper. The

boundaries of the nP-POTF are the same as those of the nP-POTF-OF. The meaning of Eqs. (3.17)-(3.18) can be now clearly interpreted. From the expressions of the boundaries, it can be seen that the boundaries of the nP-POTF-OF are circular arcs, while those of the P-POTF are parabolas. The approximation of using parabolas instead of circular arcs is a typical result of the paraxial approximation. It makes the curves narrower, since the curvatures are underestimated. The narrow property of the P-POTF makes the P-WD-PCTF smaller than the nonparaxial WD-PCTFs, as shown in Figure 4.1.

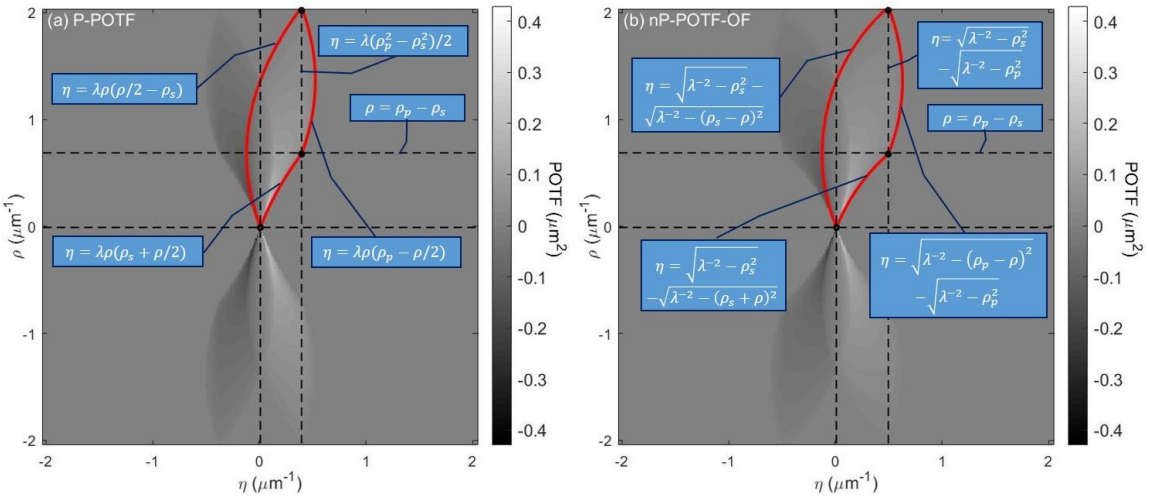

Figure B.2: The shapes and boundaries of the POTFs. The POTFs are the same as those in Figure 3.1. The horizontal axis is the longitudinal spatial frequency η and the vertical axis is the transverse spatial frequency ρ. The three red curve segments show the boundaries of $F(\rho, \eta)$, with the analytical expressions presented nearby. (a) P-POTF. (b) nP-POTF-OF.

APPENDIX C. NONPARAXIAL MFPI-PC: MORE DETAILS

C.1 Restrictions on the nP-MFPI-PC-OF

Although simulations and experimental results show a clear advantage of the nP-MFPI-PC-OF over the P-MFPI-PC and the nP-MFPI-PC, there are still some shortcomings for this method. In some circumstances, it may not give the smallest NRMSE. Some simulations were performed to show this fact.

Firstly, Object 1 used in Figure 4.3 was simulated again, but with noise present. When the SNR was 60 dB, the average NRMSE of the P-MFPI-PC was 0.0904 of the nP-MFPI-PC was 0.071, and of the nP-MFPI-PC-OF was 0.053. When the SNR was 40 dB, the average NRMSE of the P-MFPI-PC was 0.306, of the nP-MFPI-PC was 0.243, and of the nP-MFPI-PC-OF was 0.251. It can be seen that the nP-MFPI-PC-OF gave smallest NRMSE in low noise, but the nP-MFPI-PC became better when the noise became higher. The unexpected behaviors in high noise indicate that the nP-MFPI-PC has a better noise stability than the nP-MFPI-PC-OF. The reason is, without the OF correction, the nP-WD-PCTF is larger, resulting in the underestimation in the recovered phase. However, large transfer function values are effective for limiting noise magnification. As a result, the nP-MFPI-PC can give a smaller NRMSE under high noise condition. However, it does not mean the nP-POTF itself is more accurate under high noise.

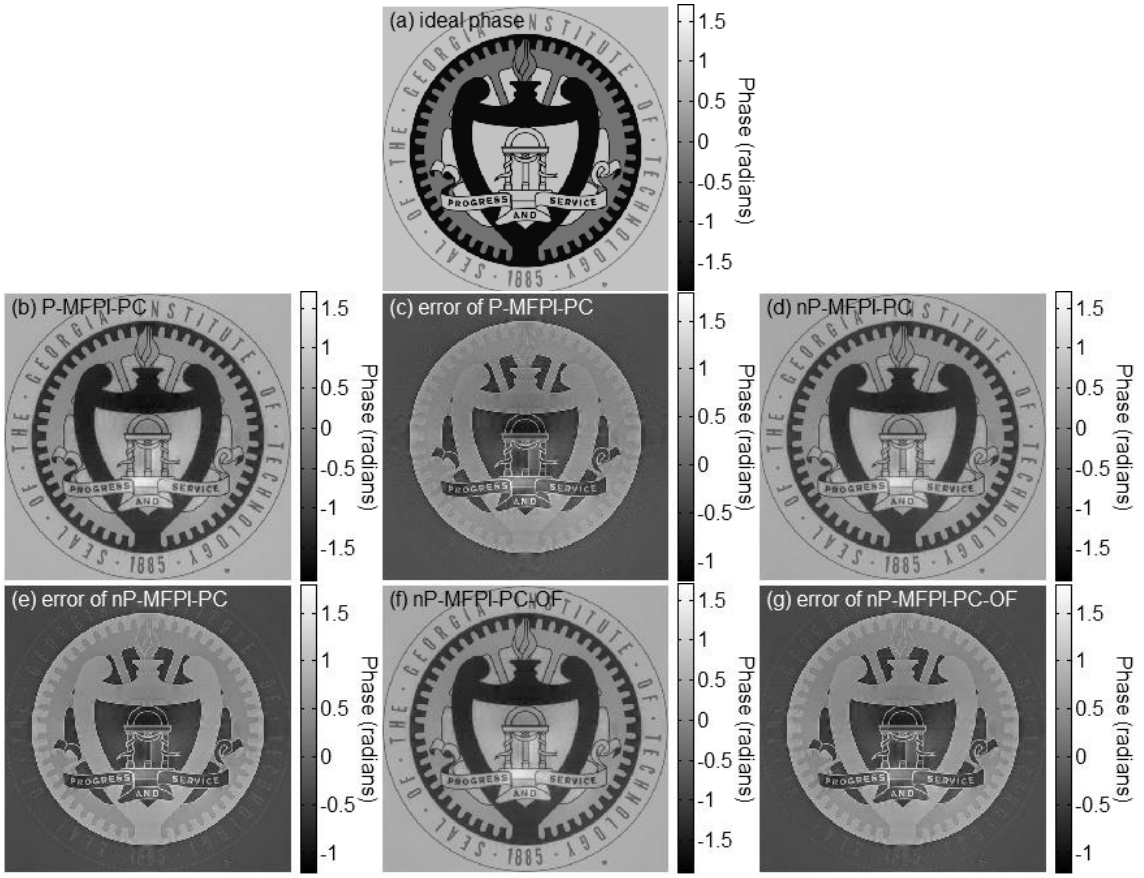

Figure C.1: Simulation of the phases recovered from various versions of MFPI-PCs using Object 3. The units on the colorbars are radians. The ranges of the ideal phase and the three recovered phases are all from -1.9 to +1.7. The ranges of the three error maps are all from -1.2 to +1.8. (a) The ideal phase image to be simulated. (b) The phase recovered by the P-MFPI-PC. (c) The error of (b) compared to (a). (d) The phase recovered by the nP-MFPI-PC. (e) The error of (d) compared to (a). (f) The phase recovered by the nP-MFPI-PC-OF. (g) The error of (f) compared to (a).

Further simulations were done using Object 3. This object is similar to Object 1, except that the phase is enlarged by a factor of 10. The phase difference of this object is now large, which means that both weak object and slowly varying object approximations are violated. The simulation results are shown in Figure C.1, which is also in the same format as Figure 4.3. The NRMSE of the P-MFPI-PC was 0.389, of the nP-MFPI-PC was 0.444, and of the nP-MFPI-PC-OF was 0.427. The simulations show that the violation of the proper object assumptions made all the methods underestimate the phase and give

large errors. Among the three methods, the P-MFPI-PC gave the smallest NRMSE. This is because the P-WD-PCTF is the smallest, so the recovered phase from the P-MFPI-PC is the largest. Since all the three methods underestimate the phase, the largest phase means the smallest underestimation and the smallest error. However, it also does not mean the P-POTF itself is more accurate when the slowly varying object approximation is violated.

In summary, in some circumstances, the systematic error can bring the recovered phase closer to the actual phase. The nP-MFPI-PC tends to be better in high noise, while the P-MFPI-PC tends to be better when the slowly varying phase assumption is violated. These results do not overturn the fact that the nP-POTF-OF is the most accurate description of nonparaxial propagation of light. However, they set restrictions on the nP-MFPI-PC-OF. It is better used in slowly-varying-phase objects with low noise. Although the other two methods may be better when the above conditions are not satisfied, the errors are large anyway. On the other hand, the theory of the MFPI-PC can still be improved, and the noise robustness of the nP-MFPI-PC-OF can be enhanced in the future as well.

APPENDIX D. WLS-MFPI-PC: MORE DETAILS

D.1 Improved Calculation Method for PCTF

As mentioned in Chapter 5, Ref. [82] used the PCTF $T_k(\rho)$ indirectly via PTF. A possible reason for not using PCTF directly in Ref. [82] might be its low accuracy attributed to the numerical calculation method used to integrate Eq. (2.11) when that paper was published. Nevertheless, since PTF is the ratio of the PCTF $T_k(\rho)$ and the WD-PCTF $T_k(\rho)$, although both of them are inaccurately integrated, their ratio is much more reliable, so Ref. [82] used PTF to select the cutoff frequencies. However, in annular illumination, using $T_k(\rho)$ directly is essential, so a numerical calculation method with improved accuracy is necessary. This section presents an improved numerical integration method for accurately calculating $T_k(\rho)$ using Eq. (2.11).

Due to its core role in this section, Eq. (2.11) is repeated here

$$T_k(\rho) = \frac{4\pi}{\lambda \Delta z} \int H_{SG,k}\left(e^{2\pi i \eta \Delta z}\right) H(\rho, \eta) \mathrm{d}\eta, \tag{D.1}$$

where $H(\rho, \eta)$ is the 3D POTF discussed in Chapter 3. The shape of the 3D POTF is shown in Figure 3.1. The 1D integration is about η, so the integration is along a horizontal line. However, the 3D POTF is very narrow near the center, so after discretization, there can be only very few or even no pixels with nonzero POTF. The small number of nonzero pixels causes large errors for integration.

In order to increase the number of pixels for horizontal integration, an intermediate variable, spatial frequency ratio ζ is defined as

$$\zeta = \eta/\rho. \tag{D.2}$$

Since η and the corresponding maximum ρ scale approximately linear near the center of the POTF, their ratio is approximately constant, so there can be a sufficient number of pixels for integration, if the 3D POTF is expressed using ρ and ζ.

Figure D.1 shows the nonparaxial 3D POTFs plotted as functions of (a) ρ and η as well as (b) ρ and ζ. It clearly shows that plotting the 3D POTF as a function of ρ and ζ allows the horizontal integration near the center to be performed on a much larger number of pixels, which makes the integration much more accurate and stable.

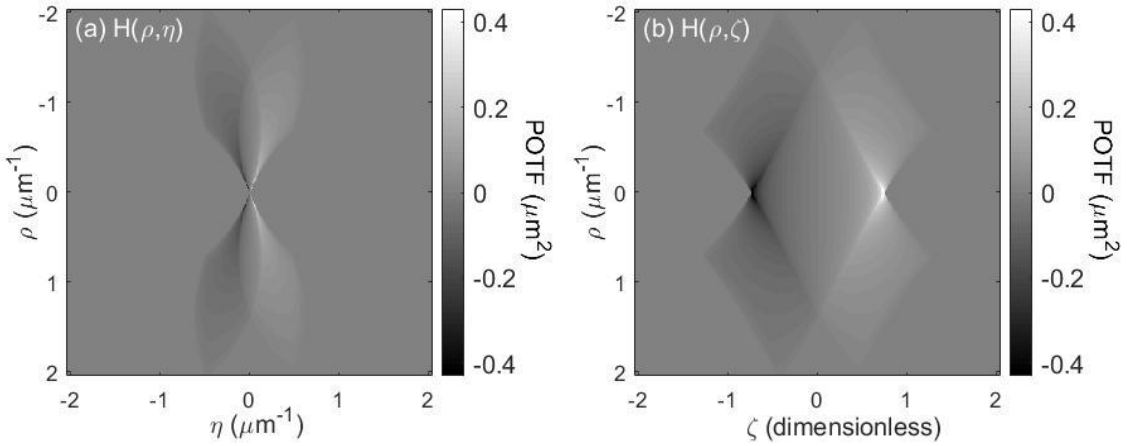

Figure D.1: Nonparaxial 3D POTFs plotted as different variables. (a) Nonparaxial 3D POTF with OF modification plotted as a function of ρ and η. (b) Nonparaxial 3D POTF with OF modification plotted as a function of ρ and ζ.

Using the intermediate quantity ζ, Eq. (2.11) can be easily rewritten as an integral of ζ,

$$T_k(\rho) = \frac{4\pi}{\lambda \Delta z} \int H_{SG,k}\left(e^{2\pi i \rho \zeta \Delta z}\right) H(\rho, \rho\zeta) \rho \mathrm{d}\zeta. \tag{D.3}$$

Since η and ρ scale approximately linear near the center of the POTF, their ratio ζ does not vary significantly, so there can be a sufficient number of pixels for integration, if the 3D POTF is also calculated using ρ and ζ. Figure D.2 shows the WD-PCTF and PCTFs of various orders calculated using integration over (a) η and (b) ζ. The result shows clearly that there are some ripples in all the curves calculated using integration over η, but the curves calculated using integration over ζ are very smooth, so the latter one should be much more accurate and reliable.

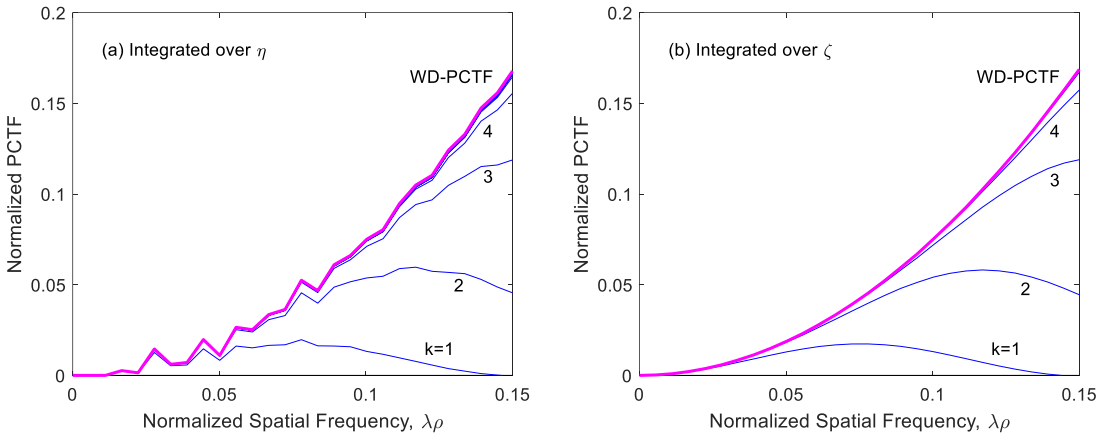

Figure D.2: WD-PCTF ($T_W(\rho)$) and PCTFs ($T_k(\rho)$) for various SGDF orders. The horizontal axis is the normalized longitudinal spatial frequency $\lambda\rho$ and the vertical axis is the normalized PCTF. (a) PCTFs calculated using integration over η, Eq. (2.11). (b) PCTFs calculated using integration over ζ, Eq. (D.3).

D.2 Experimental Measurement of NA_c and NA_{ci}

In the experiment in Chapter 5, the annular illumination is produced by a phase contrast condenser, Olympus U-PCD2. The inner and outer numerical apertures of the condenser are determined by measuring the inner and outer radii of the annuli. The NA values in

the experiment are proportional to their corresponding aperture radii. To determine these NA values, it is necessary to know the radius associated with a known NA. Here, NA_o is chosen to be the known reference NA. With the phase contrast condenser in the QPI microscope, the Bertrand lens was inserted to show the source image in the back focal plane of the microscope. Increasing the iris diaphragm corresponds to increasing the condenser aperture. With this increase, the source radius initially increases and then becomes constant at a maximum value. The transition from increasing to a constant value occurs when $NA_c = NA_o$. In the present configuration, NA_o = 0.75, and thus iris setting for NA_c = 0.75 is determined. The iris diaphragm is then fixed at this NA_c = 0.75 value, and it is subsequently used as the reference NA. With a separate measuring microscope, the reference iris diaphragm radius r_0 is measured. With the inner and outer radii measured, the inner or outer NA is given by $NA = 0.75 \times r/r_o$, where r is the corresponding radius measured by the measuring microscope. These measurements show that the numerical apertures of the 40X annular condenser are NA_c = 0.331 and NA_{ci} = 0.292.

APPENDIX E. ITDPM: MORE DETAILS

E.1 Derivation of Adjoint Operators

In Chapter 7, the definition of the adjoint operator $A^\dagger$ is the operator that satisfies [145]

$$(A^\dagger I, v) = (I, Av). \tag{E.1}$$

for any functions I and v in the same function space. Here $(\cdot,\cdot)$ is the inner product defined as

$$(I, Av) \triangleq \int I^*(\boldsymbol{r}) Av(\boldsymbol{r}) \mathrm{d}\boldsymbol{r}. \tag{E.2}$$

Writing operator A explicitly, we have

$$\begin{aligned}
(I, Av) &= \int I^*(\boldsymbol{r})[h(\boldsymbol{r}) * v(\boldsymbol{r})]\mathrm{d}\boldsymbol{r} \\
&= \int I^*(\boldsymbol{r})\left[\int h(\boldsymbol{r}-\boldsymbol{r}')v(\boldsymbol{r}')\mathrm{d}\boldsymbol{r}'\right]\mathrm{d}\boldsymbol{r} \\
&= -\int v(\boldsymbol{r}')\left[\int h(\boldsymbol{r}'-\boldsymbol{r})I^*(\boldsymbol{r})\mathrm{d}\boldsymbol{r}\right]\mathrm{d}\boldsymbol{r}' \\
&= -\int v(\boldsymbol{r}')[h(\boldsymbol{r}') * I^*(\boldsymbol{r}')]\mathrm{d}\boldsymbol{r}' \\
&= \int [-AI^*(\boldsymbol{r}')]v(\boldsymbol{r}')\mathrm{d}\boldsymbol{r}'.
\end{aligned} \tag{E.3}$$

In this derivation, $h(\boldsymbol{r}-\boldsymbol{r}') = -h(\boldsymbol{r}'-\boldsymbol{r})$ is used because the PSF h is an odd function [108]. On the other hand,

$$(A^{\dagger}I, v) = \int [A^{\dagger *} I^{*}(\boldsymbol{r}')] v(\boldsymbol{r}') \mathrm{d}\boldsymbol{r}'. \tag{E.4}$$

Therefore,

$$A^{\dagger *} = -A. \tag{E.5}$$

Similarly, for the adjoint of the rotation operator Θ_{m}, it satisfies

$$\left(\Theta_{\mathrm{m}}^{\dagger} u, v\right) = (u, \Theta_{\mathrm{m}} v). \tag{E.6}$$

for any u and v in the same function space. Further analysis shows

$$\begin{aligned} (u, \Theta_{\mathrm{m}} v) &= \int u^{*}(\boldsymbol{r}) \Theta_{\mathrm{m}} v(\boldsymbol{r}) \mathrm{d}\boldsymbol{r} \\ &= \int \Theta_{\mathrm{m}} \{[\Theta_{-\mathrm{m}} u^{*}(\boldsymbol{r})] v(\boldsymbol{r})\} \mathrm{d}\boldsymbol{r} \\ &= \int [\Theta_{-\mathrm{m}} u^{*}(\boldsymbol{r})] v(\boldsymbol{r}) \mathrm{d}\boldsymbol{r}, \end{aligned} \tag{E.7}$$

and

$$(\Theta_{\mathrm{m}}^{\dagger} u, v) = \int \left[\Theta_{\mathrm{m}}^{\dagger *} u^{*}(\boldsymbol{r})\right] v(\boldsymbol{r}) \mathrm{d}\boldsymbol{r}. \tag{E.8}$$

Therefore,

$$\Theta_{\mathrm{m}}^{\dagger *} = \Theta_{-\mathrm{m}}. \tag{E.9}$$

Since the object SP, the image intensity, and the PSF are all real functions, the convolution with PSF and the rotation only involve real number operations, so the

complex conjugate does not have any effect. Therefore, Eqs. (E.5) and (E.9) become Eqs. (7.10) and (7.11).

E.2 Optimal Number of Angles and Frequency Support

In Chapter 7, as can be seen from Figure 7.4, the reconstruction accuracy does not monotonically increase with the total number of illumination angles N, since 3 angles gives a better reconstruction than 4 angles. The reason behind this is the frequency support, or the POTF coverage of various angular regions. Figure E.1 shows the frequency support for 1 to 6 observation angles. It is obvious that 6 angle is the best, while 1 or 2 angles are far from sufficient. An interesting phenomenon is that 4 angles has more black regions than 3 angles, which leads to its lower accuracy in RI reconstruction. The black region in Figure E.1(d) actually has nonzero POTF values, but the values are too small compared to the gray regions, so they are still problematic in RI reconstruction. The 4-angle figure has more overlap between the gray regions of the POTFs from different observation angles, which leads to less effective coverage for the black regions in the entire frequency domain. Therefore, the RI reconstruction from 4 angles is less accurate than that from 3 angles. This result is largely dependent on the shape of the POTF, which is determined by the numerical apertures of the objective lens ($\mathrm{NA_o}$) and the condenser lens ($\mathrm{NA_c}$), the wavelength (λ), and the background refractive index (n_0) [109]. Therefore, for different experimental configurations, the optimal number of angles may vary. Usually smaller numerical apertures require larger numbers of angles for effective RI reconstruction.

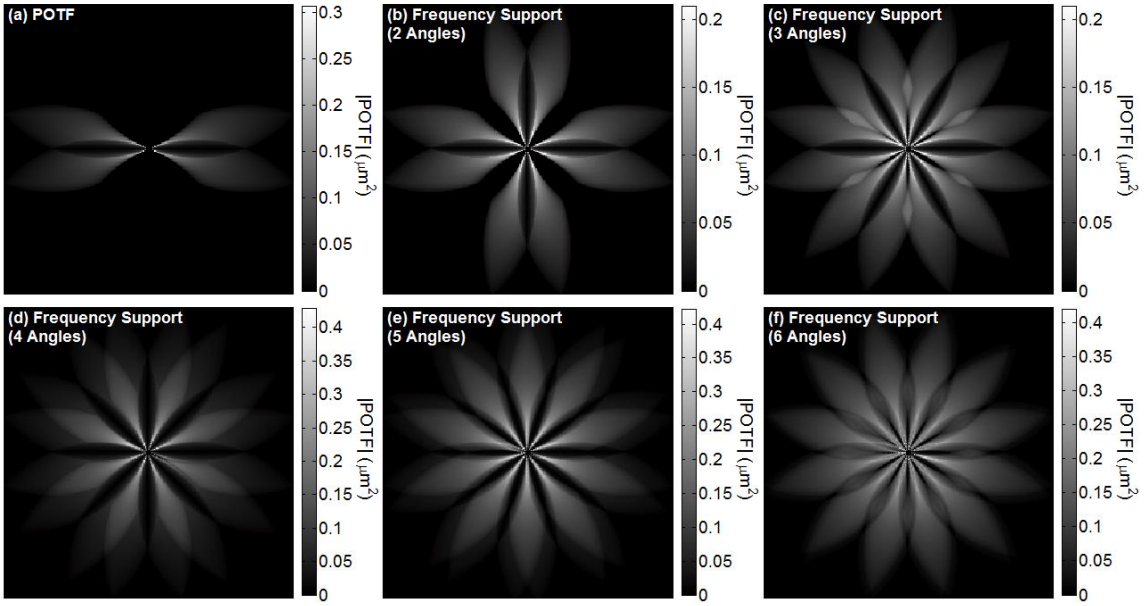

Figure E.1: POTF and frequency support for various number of angles. (a) The absolute value of the POTF. (b) - (f) Sums of the absolute values of the POTFs in 2 - 6 angles, which show the frequency supports of 2 - 6 angles.

APPENDIX F. FBG CHARACTERIZATION: MORE DETAILS

F.1 NAc Selection in 3D FBG Characterization Using TDPM

In Chapter 8, TDPM is used for 3D FBG simulations. However, due to the different topologies between 2D and 3D QPI, there are more difficulties in 3D FBG characterization than in 2D. One of the differences is the selection of $\mathrm{NA_c}$. Eq. (8.7) is a fundamental requirement of the NAs, and it is also a sufficient condition in 2D simulations. However, in 3D simulations using TDPM, this condition is not sufficient yet. As shown in Figure 7.1(a) and Figure B.2(b), the POTF along the ρ axis is zero in the region $|\rho| > 2\rho_s$ and is very small in the region $0 < |\rho| < 2\rho_s$. In three dimension, values near the $\rho_x - \rho_y$ plane are zero or very small, which may cause large errors. This problem does not exist in 2D QPI. In TDPM and ITDPM, since the object is rotated along the y-axis, the spatial frequency information near the ρ_x axis can be covered by POTFs in other angles, but the ρ_y axis is kept constant during object rotation, so the POTF values near the ρ_y axis are always zero or very small. Therefore, the recovered information near the ρ_y axis has large errors. For most conventional fibers, they are uniform along the fiber axis, which is the object rotation axis (y-axis) in our experimental configuration, so the spatial spectrum of the fiber is approximately proportional to $\delta(\rho_x)$, so the problem can be simplified to a 2D problem in the x-z plane ($\rho_x - \eta$ plane), whose POTF coverage is good as shown in Figure 7.1(b). For fibers that do vary along the fiber axis but vary slowly, such as long-period fiber grating (LPFG), most of the useful spatial frequencies are still near the $\rho_x - \eta$ plane, so they are still recoverable. However, for FBGs, their RI varies very rapidly, and the most important information is the high-spatial-frequency

band, which locates near $\rho_y = \pm f_c = \pm 1/\Lambda_0$, which is clearly along the ρ_y axis and far from the origin. Therefore, ensuring the accuracy near $\rho_y = \pm f_c$ is a very important topic. First, we should make sure that $\rho_y = \pm f_c$ does not fall into the zero-POTF region, because the information in that region is totally lost. The corresponding mathematical requirement is $1/\Lambda_0 < 2\rho_s$, which leads to

$$\mathrm{NA_c} > \lambda/2\Lambda_0. \tag{F.1}$$

Since the high-spatial-frequency band has some finite bandwidth, we should not use exactly $\mathrm{NA_c} = \lambda/2\Lambda_0$, otherwise, half of the band will be in the zero-POTF region. Apparently, when this requirement is satisfied, $\rho_y = \pm f_c$ falls into the low-POTF region. Nevertheless, due to the finite bandwidth again, when f_c gets closer to $2\rho_s$, a larger part of the band may fall into the regular-POTF regions. Therefore, it is better to make $1/\Lambda_0$ close to but smaller than $2\rho_s$. That is to say, $\mathrm{NA_c}$ should be chosen to be slightly larger than $\lambda/2\Lambda_0$. Using the parameters for simulating Figure 8.3, the critical $\mathrm{NA_c}$ determined from Eq. (F.1) is 0.514, so $\mathrm{NA_c} = 0.55$ is chosen in the simulation.

F.2 Regularization in 3D FBG Characterization Using TDPM

As mentioned in Chapter 7, dividing by a small POTF often cause noise magnification problem. In order to reduce this problem, the transfer function inversion is often done in a regularized form. Two popular regularization methods are hard cutoff and Wiener filtering. Hard cutoff means that the components whose transfer function magnitudes are smaller than a threshold are ignored while other components are calculated by direct transfer function inversion. Wiener filter means that another term (usually a constant for

simplicity) is added to the denominator of all components in transfer function inversion. Our simulation shows that Wiener filtering can generally give smoother results, but it tends to underestimate the result, and this problem is significant when the transfer function value is very small. For FBG characterization, the high-spatial-frequency bands usually locate at the low-POTF region, so Wiener filtering may significantly underestimate the SP. However, for the low-spatial-frequency band, Wiener filtering is better because it gives smoother results. Therefore, we separate the high- and low-spatial-frequency components, and then we use Wiener filtering for low-spatial-frequency components and use hard cutoff for high-spatial-frequency components.

REFERENCES

[1] R. Yuste, "Fluorescence microscopy today," *Nat. Meth.*, vol. 2, pp. 902-904, 2005.

[2] F. Zernike, "Phase contrast, a new method for the microscopic observation of transparent objects Part II," *Physica*, vol. 9, pp. 974-986, Dec. 1, 1942.

[3] G. Nomarski and A. R. Weill, "Application a la metallographie des methodes interferentielles a deux ondes polarisees," *Revue de Metallurgie*, vol. 52, pp. 121-134, Feb. 1, 1955.

[4] R. Hoffman and L. Gross, "Modulation contrast microscope," *Appl. Opt.*, vol. 14, pp. 1169-1176, May 1, 1975.

[5] G. Popescu, *Quantitative Phase Imaging of Cells and Tissues*. New York: McGraw-Hill Biophotonics, 2011.

[6] K. G. Phillips, S. L. Jacques, and O. J. McCarty, "Measurement of single cell refractive index, dry mass, volume, and density using a transillumination microscope," *Phys. Rev. Lett.*, vol. 109, pp. 118105-1--118105-5, Sep. 14, 2012.

[7] C. Zuo, Q. Chen, W. Qu, and A. Asundi, "High-speed transport-of-intensity phase microscopy with an electrically tunable lens," *Opt. Express*, vol. 21, pp. 24060-24075, Oct. 7, 2013.

[8] W. Choi, C. Fang-Yen, K. Badizadegan, S. Oh, N. Lue, R. R. Dasari, and M. S. Feld, "Tomographic phase microscopy," *Nat. Meth.*, vol. 4, pp. 717-719, Aug. 12, 2007.

[9] M. Mir, Z. Wang, Z. Shen, M. Bednarz, R. Bashir, I. Golding, S. G. Prasanth, and G. Popescu, "Optical measurement of cycle-dependent cell growth," *Proc. Nat. Acad. Sci.*, vol. 108, pp. 13124-13129, Aug. 9, 2011.

[10] R. Wang, Z. Wang, J. Leigh, N. Sobh, L. Millet, M. U. Gillette, A. J. Levine, and G. Popescu, "One-dimensional deterministic transport in neurons measured by dispersion-relation phase spectroscopy," *J. Phys. Condens. Mat.*, vol. 23, p. 374107, 2011.

[11] Y. Park, C. A. Best, T. Auth, N. S. Gov, S. A. Safran, G. Popescu, S. Suresh, and M. S. Feld, "Metabolic remodeling of the human red blood cell membrane," *Proc. Nat. Acad. Sci.,* vol. 107, pp. 1289-1294, Jan. 26, 2010.

[12] Y. Sung, W. Choi, N. Lue, R. R. Dasari, and Z. Yaqoob, "Stain-free quantification of chromosomes in live cells using regularized tomographic phase microscopy," *PLoS One,* vol. 7, p. e45902, Nov. 2012.

[13] P. Bon, S. Lécart, E. Fort, and S. Lévêque-Fort, "Fast label-free cytoskeletal network imaging in living mammalian cells," *Biophys. J.,* vol. 106, pp. 1588-1595, Apr. 15, 2014.

[14] S. M. Baker-Groberg, K. G. Phillips, and O. J. T. McCarty, "Quantification of volume, mass, and density of thrombus formation using brightfield and differential interference contrast microscopy," *BIOMEDO,* vol. 18, pp. 016014-016014, Jan. 1, 2013.

[15] H. Ding, F. Nguyen, S. A. Boppart, and G. Popescu, "Optical properties of tissues quantified by Fourier-transform light scattering," *Opt. Lett.,* vol. 34, pp. 1372-1374, May 1, 2009.

[16] H. F. Ding, L. J. Millet, M. U. Gillette, and G. Popescu, "Actin-driven cell dynamics probed by Fourier transform light scattering," *Biomed. Opt. Express,* vol. 1, pp. 260-267, Aug. 2, 2010.

[17] A. K. Ellerbee, T. L. Creazzo, and J. A. Izatt, "Examining cardiomyocyte development with spectral domain phase microscopy," *Proc. SPIE,* vol. 6441, pp. 644109-1--644109-8, 2007.

[18] C. Joo, E. Ozkumur, M. S. Unlu, and J. F. de Boer, "Spectral-domain optical coherence phase microscopy for label-free multiplexed protein microarray assay," *Biosensors & Bioelectronics,* vol. 25, pp. 275-281, Oct. 2009.

[19] B. Joshi, I. Barman, N. C. Dingari, N. Cardenas, J. S. Soares, R. R. Dasari, and S. Mohanty, "Label-free route to rapid, nanoscale characterization of cellular structure and dynamics through opaque media," *Scientific Reports,* vol. 3, pp. 1-8, Oct. 2, 2013.

[20] K. Lee, K. Kim, J. Jung, J. Heo, S. Cho, S. Lee, G. Chang, Y. Jo, H. Park, and Y. Park, "Quantitative phase imaging techniques for the study of cell pathophysiology: from principles to applications," *Sensors,* vol. 13, pp. 4170-4191, Mar. 28, 2013.

[21] N. Lue, G. Popescu, T. Ikeda, R. R. Dasari, K. Badizadegan, and M. S. Feld, "Live cell refractometry using microfluidic devices," *Opt. Lett.,* vol. 31, pp. 2759-2761, Sep. 15, 2006.

[22] M. Mihailescu, R. C. Popescu, A. Matei, A. Acasandrei, I. A. Paun, and M. Dinescu, "Investigation of osteoblast cells behavior in polymeric 3D micropatterned scaffolds using digital holographic microscopy," *Appl. Opt.,* vol. 53, pp. 4850-4858, Aug. 1, 2014.

[23] M. Mir, S. D. Babacan, M. Bednarz, M. N. Do, I. Golding, and G. Popescu, "Visualizing escherichia coli sub-cellular structure using sparse deconvolution spatial light interference tomography," *PLoS One,* vol. 7, p. e39816, Jun. 28, 2012.

[24] G. Popescu, T. Ikeda, C. A. Best, K. Badizadegan, R. R. Dasari, and M. S. Feld, "Erythrocyte structure and dynamics quantified by Hilbert phase microscopy," *BIOMEDO,* vol. 10, pp. 060503-060503-3, 2005.

[25] G. Popescu, Y. Park, R. R. Dasari, K. Badizadegan, and M. S. Feld, "Coherence properties of red blood cell membrane motions," *Phys. Rev. E,* vol. 76, pp. 031902-1--031902-5, 2007.

[26] V. Tychinsky, A. V. Kretushev, I. V. Klemyashov, V. D. Zverzhkhovskiy, T. V. Vyshenskaya, and A. A. Shtil, "Quantitative phase imaging of living cells: application of the phase volume and area functions to the analysis of "nucleolar stress"," *BIOMEDO,* vol. 18, p. 111413, Nov. 2013.

[27] R. Wang, Z. Wang, L. Millet, M. U. Gillette, A. J. Levine, and G. Popescu, "Dispersion-relation phase spectroscopy of intracellular transport," *Opt. Express,* vol. 19, pp. 20571-20579, Oct. 10, 2011.

[28] K. Creath and G. Goldstein, "Dynamic quantitative phase imaging for biological objects using a pixelated phase mask," *Biomed. Opt. Express,* vol. 3, pp. 2866-2880, Nov. 1, 2012.

[29] M. Mir, Z. Wang, K. Tangella, and G. Popescu, "Diffraction Phase Cytometry: blood on a CD-ROM," *Opt. Express,* vol. 17, pp. 2579-2585, Feb. 16, 2009.

[30] D. Claus, A. M. Maiden, F. Zhang, F. G. R. Sweeney, M. J. Humphry, H. Schluesener, and J. M. Rodenburg, "Quantitative phase contrast optimised cancerous cell differentiation via ptychography," *Opt. Express,* vol. 20, pp. 9911-9918, Apr. 23, 2012.

[31] M. Hunter, V. Backman, G. Popescu, M. Kalashnikov, C. W. Boone, A. Wax, V. Gopal, K. Badizadegan, G. D. Stoner, and M. S. Feld, "Tissue self-affinity and polarized light scattering in the Born approximation: A new model for precancer detection," *Physical Review Letters,* vol. 97, pp. 138102-1--138102-4, Sep. 29, 2006.

[32] Z. Wang, K. Tangella, A. Balla, and G. Popescu, "Tissue refractive index as marker of disease," *J. Biomed. Opt.,* vol. 16, pp. 116017-1--116017-7, Nov. 2011.

[33] V. Backman, M. B. Wallace, L. T. Perelman, J. T. Arendt, R. Gurjar, M. G. Muller, Q. Zhang, G. Zonios, E. Kline, T. McGillican, S. Shapshay, T. Valdez, K. Badizadegan, J. M. Crawford, M. Fitzmaurice, S. Kabani, H. S. Levin, M. Seiler, R. R. Dasari, I. Itzkan, J. Van Dam, and M. S. Feld, "Detection of preinvasive cancer cells," *Nature,* vol. 406, pp. 35-36, Jul. 6, 2000.

[34] S. S. Gorthi and E. Schonbrun, "Phase imaging flow cytometry using a focus-stack collecting microscope," *Opt. Lett.,* vol. 37, pp. 707-709, Feb. 15, 2012.

[35] J. W. Kang, N. Lue, C.-R. Kong, I. Barman, N. C. Dingari, S. J. Goldfless, J. C. Niles, R. R. Dasari, and M. S. Feld, "Combined confocal Raman and quantitative phase microscopy system for biomedical diagnosis," *Biomedical Optics Express,* vol. 2, pp. 2484-2492, Sep. 1, 2011.

[36] J. Klossa, B. Wattelier, T. Happillon, D. Toubas, L. de Laulanie, V. Untereiner, P. Bon, and M. Manfait, "Quantitative phase imaging and Raman micro-spectroscopy applied to malaria," *Diagnostic Pathology,* vol. 8, pp. S42-1--S42-4, 2013.

[37] M. Mir, H. F. Ding, Z. Wang, J. Reedy, K. Tangella, and G. Popescu, "Blood screening using diffraction phase cytometry," *BIOMEDO,* vol. 15, p. 027016, Mar.-Apr. 2010.

[38] L. F. Yu, S. Mohanty, G. J. Liu, S. Genc, Z. P. Chen, and M. W. Berns, "Quantitative phase evaluation of dynamic changes on cell membrane during laser microsurgery," *BIOMEDO,* vol. 13, pp. 050508-1--050508-3, Sep.-Oct. 2008.

[39] C. L. Zheng, K. Scheerschmidt, H. Kirmse, I. Hausler, and W. Neumann, "Imaging of three-dimensional (Si, Ge) nanostructures by off-axis electron holography," *Ultramicroscopy,* vol. 124, pp. 108-116, Jan. 2013.

[40] K. Ishizuka and B. Allman, "Phase measurement of atomic resolution image using transport of intensity equation," *J. Electron Micros.,* vol. 54, pp. 191-197, 2005.

[41] G. Baffou, P. Bon, J. Savatier, J. Polleux, M. Zhu, M. Merlin, H. Rigneault, and S. Monneret, "Thermal imaging of nanostructures by quantitative optical phase analysis," *ACS Nano,* vol. 6, pp. 2452-2458, Mar. 27, 2012.

[42] R. S. Bradley, A. McNeil, and P. J. Withers, "An examination of phase retrieval algorithms as applied to phase contrast tomography using laboratory sources," *Proc. SPIE,* vol. 7804, pp. 780404-1--780404-10, 2010.

[43] L. J. Allen and M. P. Oxley, "Phase retrieval from series of images obtained by defocus variation," *Opt. Commun.,* vol. 199, pp. 65-75, Nov. 15, 2001.

[44] M. A. Beltran, D. M. Paganin, K. Uesugi, and M. J. Kitchen, "2D and 3D X-ray phase retrieval of multi-material objects using a single defocus distance," *Opt. Express,* vol. 18, pp. 6423-6436, Mar. 29, 2010.

[45] A. V. Bronnikov, "Theory of quantitative phase-contrast computed tomography," *J. Opt. Soc. Am. A,* vol. 19, pp. 472-480, Mar. 1, 2002.

[46] A. Burvall, U. Lundström, P. A. C. Takman, D. H. Larsson, and H. M. Hertz, "Phase retrieval in X-ray phase-contrast imaging suitable for tomography," *Opt. Express,* vol. 19, pp. 10359-10376, May 23, 2011.

[47] R. C. Chen, L. Rigon, and R. Longo, "Quantitative 3D refractive index decrement reconstruction using single-distance phase-contrast tomography data," *J. Phys. D: Appl. Phys.,* vol. 44, pp. 495401-1--495401-9, 2011.

[48] M. Endrizzi, F. A. Vittoria, P. C. Diemoz, R. Lorenzo, R. D. Speller, U. H. Wagner, C. Rau, I. K. Robinson, and A. Olivo, "Phase-contrast microscopy at high x-ray energy with a laboratory setup," *Opt. Lett.,* vol. 39, pp. 3332-3335, Jun. 1, 2014.

[49] S. Gasilov, A. Mittone, E. Brun, A. Bravin, S. Grandl, and P. Coan, "On the possibility of quantitative refractive-index tomography of large biomedical samples with hard X-rays," *Biomedical Optics Express,* vol. 4, pp. 1512-1518, Sep. 1, 2013.

[50] T. E. Gureyev and S. W. Wilkins, "On x-ray phase imaging with a point source," *J. Opt. Soc. Am. A,* vol. 15, pp. 579-585, Mar. 1998.

[51] M. Langer, P. Cloetens, J. P. Guigay, and F. Peyrin, "Quantitative comparison of direct phase retrieval algorithms in in-line phase tomography," *Medical Physics,* vol. 35, pp. 4556-66, Sep. 18, 2008.

[52] K. A. Nugent, T. E. Gureyev, D. F. Cookson, D. Paganin, and Z. Barnea, "Quantitative phase imaging using hard x rays," *Physical Review Letters,* vol. 77, pp. 2961-2964, Sep. 30, 1996.

[53] G.-C. Yin, F.-R. Chen, Y. Hwu, H.-P. D. Shieh, and K. S. Liang, "Quantitative phase retrieval in transmission hard x-ray microscope," *Applied Physics Letters,* vol. 90, p. 181118, 2007.

[54] T. Feng, M. H. Jenkins, F. Yan, and T. K. Gaylord, "Joint residual stress/refractive index characterization of large-mode-area erbium-doped fibers," *J. Lightwave Technol.,* vol. 31, pp. 2426-2433, Jul. 15, 2013.

[55] T. Feng, M. H. Jenkins, F. Yan, and T. K. Gaylord, "Arc fusion splicing effects in large-mode-Area single-mode ytterbium-doped fibers," *Appl. Opt.,* vol. 52, pp. 7706-7711, 2013.

[56] M. R. Hutsel and T. K. Gaylord, "Concurrent three-dimensional characterization of the refractive-index and residual-stress distributions in optical fibers," *Appl. Opt.,* vol. 51, pp. 5442-5452, Aug. 1, 2012.

[57] A. D. Yablon, "Multifocus tomographic algorithm for measuring optically thick specimens," *Opt. Lett.,* vol. 38, pp. 4393-4396, Nov. 1, 2013.

[58] U. Schnars and W. Jüptner, "Direct recording of holograms by a CCD target and numerical reconstruction," *Appl. Opt.,* vol. 33, pp. 179-181, Jan. 10, 1994.

[59] G. Popescu, T. Ikeda, R. R. Dasari, and M. S. Feld, "Diffraction phase microscopy for quantifying cell structure and dynamics," *Opt. Lett.*, vol. 31, pp. 775-777, Mar. 3, 2006.

[60] B. Bhaduri, H. Pham, M. Mir, and G. Popescu, "Diffraction phase microscopy with white light," *Opt. Lett.*, vol. 37, pp. 1094-1096, Mar. 15, 2012.

[61] N. Lue, W. Choi, G. Popescu, T. Ikeda, R. R. Dasari, K. Badizadegan, and M. S. Feld, "Quantitative phase imaging of live cells using fast Fourier phase microscopy," *Appl. Opt.*, vol. 46, pp. 1836-1842, Apr. 1, 2007.

[62] Z. Wang, L. Millet, M. Mir, H. Ding, S. Unarunotai, J. Rogers, M. U. Gillette, and G. Popescu, "Spatial light interference microscopy (SLIM)," *Opt. Express*, vol. 19, pp. 1016-1026, Jan. 17, 2011.

[63] I. Yamaguchi and T. Zhang, "Phase-shifting digital holography," *Opt. Lett.*, vol. 22, pp. 1268-1270, Aug. 15, 1997.

[64] Y. Sung, W. Choi, C. Fang-Yen, K. Badizadegan, R. R. Dasari, and M. S. Feld, "Optical diffraction tomography for high resolution live cell imaging," *Opt. Express*, vol. 17, pp. 266-277, Jan. 5, 2009.

[65] M. J. Beran and G. B. Parrent, *Theory of Partial Coherence*. Englewood Cliffs, NJ: Prentice-Hall, 1964.

[66] T. Ikeda, G. Popescu, R. R. Dasari, and M. S. Feld, "Hilbert phase microscopy for investigating fast dynamics in transparent systems," *Opt. Lett.*, vol. 30, pp. 1165-1167, May 15, 2005.

[67] W. S. Rockward, A. L. Thomas, B. Zhao, and C. A. DiMarzio, "Quantitative phase measurements using optical quadrature microscopy," *Appl. Opt.*, vol. 47, pp. 1684-1696, Apr. 1, 2008.

[68] D. C. Ghiglia and M. D. Pritt, *Two-Dimensional Phase Unwrapping: Theory, Algorithms, and Software*. Hoboken, NJ. : Wiley, 1998.

[69] M. R. Arnison, K. G. Larkin, C. J. R. Sheppard, N. I. Smith, and C. J. Cogswell, "Linear phase imaging using differential interference contrast microscopy," *J. Microsc.*, vol. 214, pp. 7-12, Apr. 2004.

[70] P. Bon, G. Maucort, B. Wattellier, and S. Monneret, "Quadriwave lateral shearing interferometry for quantitative phase microscopy of living cells," *Opt. Express,* vol. 17, pp. 13080-13094, Jul. 20, 2009.

[71] J. Marrison, L. Raty, P. Marriott, and P. O'Toole, "Ptychography - a label free, high-contrast imaging technique for live cells using quantitative phase information," *Sci. Repts.,* vol. 3, pp. 1-7, Aug. 2013.

[72] X. Ou, R. Horstmeyer, C. Yang, and G. Zheng, "Quantitative phase imaging via Fourier ptychographic microscopy," *Opt. Lett.,* vol. 38, pp. 4845-4848, Nov. 15, 2013.

[73] L. J. Allen, W. McBride, N. L. O'Leary, and M. P. Oxley, "Exit wave reconstruction at atomic resolution," *Ultramicroscopy,* vol. 100, pp. 91-104, Jul. 2004.

[74] M. R. Teague, "Deterministic phase retrieval: a Green's function solution," *J. Opt. Soc. Am. A,* vol. 73, pp. 1434-1441, Nov. 1, 1983.

[75] J. P. Guigay, "Fourier-transform analysis of Fresnel diffraction patterns and in-line holograms," *Optik,* vol. 49, pp. 121-125, 1977.

[76] S. S. Kou, L. Waller, G. Barbastathis, P. Marquet, C. Depeursinge, and C. J. R. Sheppard, "Quantitative phase restoration by direct inversion using the optical transfer function," *Opt. Lett.,* vol. 36, pp. 2671-2673, Jul. 15, 2011.

[77] E. D. Barone-Nugent, A. Barty, and K. A. Nugent, "Quantitative phase-amplitude microscopy I: Optical microscopy," *J. Microsc.,* vol. 206, pp. 194-203, Jun. 2002.

[78] J. P. Guigay, M. Langer, R. Boistel, and P. Cloetens, "Mixed transfer function and transport of intensity approach for phase retrieval in the Fresnel region," *Opt. Lett.,* vol. 32, pp. 1617-1619, Jun. 15, 2007.

[79] C. Zuo, Q. Chen, Y. J. Yu, and A. Asundi, "Transport-of-intensity phase imaging using Savitzky-Golay differentiation filter - theory and applications," *Opt. Express,* vol. 21, pp. 5346-5362, Mar. 11, 2013.

[80] D. Paganin and K. A. Nugent, "Noninterferometric phase imaging with partially coherent light," *Phys. Rev. Lett.,* vol. 80, pp. 2586-2589, Mar. 23, 1998.

[81] J. C. Petruccelli, L. Tian, and G. Barbastathis, "The transport of intensity equation for optical path length recovery using partially coherent illumination," *Opt. Express,* vol. 21, pp. 14430-14441, Jun. 17, 2013.

[82] M. H. Jenkins, J. M. Long, and T. K. Gaylord, "Multifilter phase imaging with partially coherent light," *Appl. Opt.,* vol. 53, pp. D29-D39, Jun. 1, 2014.

[83] M. H. Jenkins and T. K. Gaylord, "Quantitative phase microscopy via optimized inversion of the phase optical transfer function," *Appl. Opt.,* vol. 54, pp. 8566-8579, Oct. 1, 2015.

[84] D. Jin, R. Zhou, Z. Yaqoob, and P. T. C. So, "Tomographic phase microscopy: principles and applications in bioimaging [Invited]," *J. Opt. Soc. Am. B,* vol. 34, pp. B64-B77, May 1, 2017.

[85] A. C. Kak and M. Slaney, *Principles of computerized tomographic imaging*. Philadelphia, PA. : Society for Industrial and Applied Mathematics, 2001.

[86] F. Charrière, E. Cuche, P. Marquet, and C. Depeursinge, "Biological cell (pollen grain) refractive index tomography with digital holographic microscopy," *Proc. SPIE,* vol. 6090, pp. 609008-1--609008-8, Feb. 23, 2006.

[87] F. Charrière, J. Kühn, T. Colomb, E. Cuche, P. Marquet, and C. Depeursinge, "Sub-cellular quantitative optical diffraction tomography with digital holographic microscopy," *Proc. SPIE,* vol. 6441, pp. 64410K-1--64410K-6, Feb. 19, 2007.

[88] A. Barty, K. A. Nugent, D. Paganin, and A. Roberts, "Quantitative optical phase microscopy," *Opt. Lett.,* vol. 23, pp. 817-819, Jun. 1, 1998.

[89] S. Chowdhury, W. J. Eldridge, A. Wax, and J. Izatt, "Refractive index tomography with structured illumination," *Optica,* vol. 4, pp. 537-545, May 20, 2017.

[90] L. Tian, J. Wang, and L. Waller, "3D differential phase-contrast microscopy with computational illumination using an LED array," *Opt. Lett.,* vol. 39, pp. 1326-1329, Mar. 1, 2014.

[91] F. Macias-Garza, K. R. Diller, and A. C. Bovik, "Missing cone of frequencies and low-pass distortion in three-dimensional microscopic images," *OPTICE,* vol. 27, pp. 276461-276461, Jun. 1988.

[92] J. Lim, K. Lee, K. H. Jin, S. Shin, S. Lee, Y. Park, and J. C. Ye, "Comparative study of iterative reconstruction algorithms for missing cone problems in optical diffraction tomography," *Opt. Express,* vol. 23, pp. 16933-16948, Jun. 29, 2015.

[93] A. H. Delaney and Y. Bresler, "Globally convergent edge-preserving regularized reconstruction: an application to limited-angle tomography," *Image Processing, IEEE Transactions on,* vol. 7, pp. 204-221, Feb. 1998.

[94] Y. Sung and R. R. Dasari, "Deterministic regularization of three-dimensional optical diffraction tomography," *J. Opt. Soc. Am. A,* vol. 28, pp. 1554-1561, Aug. 1, 2011.

[95] J. F. P.-J. Abascal, J. Chamorro-Servent, J. Aguirre, S. Arridge, T. Correia, J. Ripoll, J. J. Vaquero, and M. Desco, "Fluorescence diffuse optical tomography using the split Bregman method," *Medical Physics,* vol. 38, pp. 6275-6284, 2011.

[96] C. H. Chang, J. W. Su, W. C. Hsu, K. B. Sung, and C. Y. Chou, "Quantitative three-dimensional reconstruction of limited-angle experimental measurements in diffraction tomography," in *9th IEEE Int. Symp. Biomed. Imaging (ISBI)*, 2012, pp. 1667-1670.

[97] P. Hosseini, Y. Sung, Y. Choi, N. Lue, Z. Yaqoob, and P. So, "Scanning color optical tomography (SCOT)," *Opt. Express,* vol. 23, pp. 19752-19762, Jun. 27, 2015.

[98] S. Kosmeier, P. Langehanenberg, S. Przibilla, G. von Bally, and B. Kemper, "Multi-wavelength digital holographic microscopy for high resolution inspection of surfaces and imaging of phase specimen," *Proc. SPIE*, vol. 7718, pp. 77180T-1--77180T-7, 2010.

[99] M. H. Jenkins and T. K. Gaylord, "Three-dimensional quantitative phase imaging via tomographic deconvolution phase microscopy," *Appl. Opt.,* vol. 54, pp. 9213-9227, Nov. 1, 2015.

[100] T. Kim, R. Zhou, M. Mir, S. D. Babacan, P. S. Carney, L. L. Goddard, and G. Popescu, "White-light diffraction tomography of unlabelled live cells," *Nat. Photon.,* vol. 8, pp. 256-263, Mar. 1, 2014.

[101] P. Bon, S. Aknoun, S. Monneret, and B. Wattellier, "Enhanced 3D spatial resolution in quantitative phase microscopy using spatially incoherent illumination," *Opt. Express,* vol. 22, pp. 8654-8671, Apr. 7, 2014.

[102] A. D. Yablon, "Novel multifocus tomography for measurement of microstructured and multicore optical fibers," *Proc. SPIE,* vol. 8961, pp. 89610G-1--89610G-6, Feb. 1, 2014.

[103] L. Waller, "Phase imaging with partially coherent light," *Proc. SPIE,* vol. 8589, pp. 85890K-1--85890K-6, 2013.

[104] L. Waller, M. Tsang, S. Ponda, S. Y. Yang, and G. Barbastathis, "Phase and amplitude imaging from noisy images by Kalman filtering," *Opt. Express,* vol. 19, pp. 2805-2815, Jan. 31, 2011.

[105] Y. Sung and C. J. R. Sheppard, "Three-dimensional imaging by partially coherent light under nonparaxial condition," *J. Opt. Soc. Am. A,* vol. 28, pp. 554-559, Apr. 1, 2011.

[106] J. E. Harvey, A. Krywonos, and D. Bogunovic, "Nonparaxial scalar treatment of sinusoidal phase gratings," *J. Opt. Soc. Am. A,* vol. 23, pp. 858-865, Apr. 1, 2006.

[107] Y. Sung, C. J. R. Sheppard, G. Barbastathis, M. Ando, and R. Gupta, "Full-wave approach for x-ray phase imaging," *Opt. Express,* vol. 21, pp. 17547-17557, Jul. 29, 2013.

[108] N. Streibl, "Three-dimensional imaging by a microscope," *J. Opt. Soc. Am. A,* vol. 2, pp. 121-127, Feb. 1, 1985.

[109] Y. Bao and T. K. Gaylord, "Quantitative phase imaging method based on an analytical nonparaxial partially coherent phase optical transfer function," *J. Opt. Soc. Am. A,* vol. 33, pp. 2125-2136, Nov. 1, 2016.

[110] J. W. Goodman, *Introduction to Fourier Optics*. New York: McGraw-Hill, 1996.

[111] G. C. Sherman, "Application of the convolution theorem to Rayleigh's integral formulas," *J. Opt. Soc. Am. A,* vol. 57, pp. 546-547, Apr. 1, 1967.

[112] T. Noda, S. Kawata, and S. Minami, "3-dimensional phase-contrast imaging by an annular illumination microscope," *Appl. Opt.*, vol. 29, pp. 3810-3815, Sep. 10, 1990.

[113] J. M. Soto, J. A. Rodrigo, and T. Alieva, "Label-free quantitative 3D tomographic imaging for partially coherent light microscopy," *Opt. Express*, vol. 25, pp. 15699-15712, Jul. 10, 2017.

[114] Y. Bao and T. K. Gaylord, "Quantitative phase imaging method based on an analytical nonparaxial partially coherent phase optical transfer function: erratum," *J. Opt. Soc. Am. A*, vol. 34, p. 1329, Aug. 1, 2017.

[115] Y. Bao and T. K. Gaylord, "Quantitative phase imaging of fiber Bragg gratings in multicore fibers," *Appl. Opt.*, vol. 57, pp. 10062-10071, Dec. 1, 2018.

[116] R. C. Gonzalez and R. E. Woods, *Digital Image Processing*. Upper Saddle River, NJ: Prentice Hall, 2008.

[117] M. Langer, P. Cloetens, J. P. Guigay, and F. Peyrin, "Quantitative comparison of direct phase retrieval algorithms in in-line phase tomography," *Med. Phys.*, vol. 35, pp. 4556-66, Sep. 18, 2008.

[118] B. Sick, B. Hecht, and L. Novotny, "Orientational imaging of single molecules by annular illumination," *Phys. Rev. Lett.*, vol. 85, pp. 4482-4485, Nov. 20, 2000.

[119] M. E. Kandel, M. Fanous, C. Best-Popescu, and G. Popescu, "Real-time halo correction in phase contrast imaging," *Biomed. Opt. Express*, vol. 9, pp. 623-635, Feb. 2018.

[120] S. B. Ippolito and H. Terada, "Annular illumination and collection in solid immersion," in *ISTFA 2009*, San Jose, CA, 2009, pp. 60-64.

[121] Y. N. Sulai and A. Dubra, "Adaptive optics scanning ophthalmoscopy with annular pupils," *Biomed. Opt. Express*, vol. 3, pp. 1647-1661, Jul. 1, 2012.

[122] M. Enyama, K. Hamada, M. Fukuda, and H. Kazumi, "Method of improving image sharpness for annular-illumination scanning electron microscopes," *Jpn. J. Appl. Phys.*, vol. 55, p. 06GD02 (4 pp.), Jun. 2016.

[123] G. Terakado and H. Kano, "Localized surface plasmon microscope for simultaneous imaging of refractive index and fluorescence distributions: Fluorescence enhancement by annular pupil illumination," in *Biomedical Optics, BIOMED 2010*, Miami, FL 2010, p. BSuD62.

[124] S. Mehrabkhani, L. Wefelnberg, and T. Schneider, "Fourier-based solving approach for the transport-of-intensity equation with reduced restrictions," *Opt. Express,* vol. 26, pp. 11458-11470, Apr. 2018.

[125] J. Li, Q. Chen, J. Sun, J. Zhang, J. Ding, and C. Zuo, "Three-dimensional tomographic microscopy technique with multi-frequency combination with partially coherent illuminations," *Biomed. Opt. Express,* vol. 9, pp. 2526-2542, Jun. 1, 2018.

[126] K. A. Nugent and C. J. Bellair, "Emulated super-resolution using quantitative phase microscopy," *Micron,* vol. 34, pp. 333-338, Oct. 01, 2003.

[127] J. Li, Q. Chen, J. Zhang, Y. Zhang, L. Lu, and C. Zuo, "Efficient quantitative phase microscopy using programmable annular LED illumination," *Biomed. Opt. Express,* vol. 8, pp. 4687-4705, Oct. 1, 2017.

[128] J. S. Sun, C. Zuo, J. L. Zhang, Y. Fan, and Q. Chen, "High-speed Fourier ptychographic microscopy based on programmable annular illuminations," *Sci. Rep.,* vol. 8, pp. 7669-1--7669-12, May. 2018.

[129] C. Zuo, J. Sun, J. Li, J. Zhang, A. Asundi, and Q. Chen, "High-resolution transport-of-intensity quantitative phase microscopy with annular illumination," *Sci. Rep.,* vol. 7, p. 7654 (22 pp.), Aug. 9, 2017.

[130] L. Tian and L. Waller, "Quantitative differential phase contrast imaging in an LED array microscope," *Opt. Express,* vol. 23, pp. 11394-11403, May 4, 2015.

[131] Y. Suzuki, K. Kajitani, and H. Ohde, "Method for observing phase objects without halos or directional shadows," *Opt. Lett.,* vol. 40, pp. 812-815, Mar. 1, 2015.

[132] Y. Bao, G. C. Dong, and T. K. Gaylord, "Weighted-least-squares multi-filter phase imaging with partially coherent light: characteristics of annular illumination," *Appl. Opt.,* vol. 58, pp. 137-146, Jan. 1, 2019.

[133] S. J. Orfanidis, *Introduction to Signal Processing*: Prentice Hall, 1996.

[134] J. Luo, K. Ying, P. He, and J. Bai, "Properties of Savitzky–Golay digital differentiators," *Dig. Sig. Proc.*, vol. 15, pp. 122-136, Mar. 1, 2005.

[135] Z. Jingshan, R. A. Claus, J. Dauwels, L. Tian, and L. Waller, "Transport of intensity phase imaging by intensity spectrum fitting of exponentially spaced defocus planes," *Opt. Express,* vol. 22, pp. 10661-10674, May 5, 2014.

[136] K. Falaggis, T. Kozacki, and M. Kujawinska, "Optimum plane selection criteria for single-beam phase retrieval techniques based on the contrast transfer function," *Opt. Lett.*, vol. 39, pp. 30-33, Jan. 1, 2014.

[137] P. A. Gorry, "General least-squares smoothing and differentiation of nonuniformly spaced data by the convolution method," *Anal. Chem.*, vol. 63, pp. 534-536, Mar. 1991.

[138] Y. Bao and T. K. Gaylord, "Iterative optimization in tomographic deconvolution phase microscopy," *J. Opt. Soc. Am. A,* vol. 35, pp. 652-660, Apr. 1, 2018.

[139] F. Macias-Garza, K. R. Diller, and A. C. Bovik, "Missing cone of frequencies and low-pass distortion in three-dimensional microscopic images," *Opt. Eng.*, vol. 27, pp. 461-465, Jun. 1988.

[140] A. Kuś, W. Krauze, and M. Kujawińska, "Active limited-angle tomographic phase microscope," *J. Biomed. Opt.*, vol. 20, pp. 111216-1--111216-10, Nov. 2015.

[141] U. S. Kamilov, I. N. Papadopoulos, M. H. Shoreh, A. Goy, C. Vonesch, M. Unser, and D. Psaltis, "Optical tomographic image reconstruction based on beam propagation and sparse regularization," *IEEE Trans. Comput. Imaging*, vol. 2, pp. 59-70, 2016.

[142] L. Ma, H. Wang, L. Su, Y. Li, and H. Jin, "Digital holographic microtomography with few angle data-sets," *J. Mod. Opt.*, vol. 61, pp. 1140-1146, 2014.

[143] P. Charbonnier, L. Blanc-Feraud, G. Aubert, and M. Barlaud, "Deterministic edge-preserving regularization in computed imaging," *IEEE Trans. Image Process.*, vol. 6, pp. 298-311, Feb. 1997.

[144] M. Persson, D. Bone, and H. Elmqvist, "Total variation norm for three-dimensional iterative reconstruction in limited view angle tomography," *Phys. Med. Biol.,* vol. 46, pp. 853-866, 2001.

[145] K. T. Ladas and A. J. Devaney, "Generalized ART algorithm for diffraction tomography," *Inverse Probl.,* vol. 7, p. 109, 1991.

[146] L. Ma, H. Wang, Y. Li, and L. Su, "Three-dimensional refractive index measurement by digital holographic microscopy," 2013, pp. 87693H-1--87693H-7.

[147] J. Kostencka, T. Kozacki, and M. Józwik, "Holographic tomography with object rotation and two-directional off-axis illumination," *Opt. Express,* vol. 25, pp. 23920-23934, Oct. 2, 2017.

[148] J. Canning, "Fibre gratings and devices for sensors and lasers," *Laser & Photonics Rev.,* vol. 2, pp. 275-289, 2008.

[149] K. O. Hill and G. Meltz, "Fiber Bragg grating technology fundamentals and overview," *J. Lightwave Technol.,* vol. 15, pp. 1263-76, Aug. 1997.

[150] D. Mechin, P. Grosso, and D. Bosc, "Add-drop multiplexer with UV-written Bragg gratings and directional coupler in SiO_2-Si integrated waveguides," *J. Lightwave Technol.,* vol. 19, pp. 1282-1286, Sep. 2001.

[151] A. V. Tran, W. D. Zhong, R. S. Tucker, and K. Song, "Reconfigurable multichannel optical add-drop multiplexers incorporating eight-port optical circulators and fiber Bragg gratings," *IEEE Photonics Technol. Lett.,* vol. 13, pp. 1100-1102, Oct. 2001.

[152] S. Abad, M. Lopez-Amo, F. M. Araujo, L. A. Ferreira, and J. L. Santos, "Fiber Bragg grating-based self-referencing technique for wavelength-multiplexed intensity sensors," *Opt. Lett.,* vol. 27, pp. 222-4, Feb. 15, 2002.

[153] H. Kumazaki, Y. Yamada, H. Nakamura, S. Inaba, and K. Hane, "Tunable wavelength filter using a Bragg grating fiber thinned by plasma etching," *IEEE Photonics Technol. Lett.,* vol. 13, pp. 1206-1208, Nov. 2001.

[154] S.-L. Tsao and J. Wu, "Highly accurate temperature sensor using two fiber Bragg gratings," *IEEE J. Sel. Top. Quantum Electron.,* vol. 2, pp. 894-897, Dec. 1996.

[155] E. J. Friebele, "Fiber Bragg grating strain sensors: present and future applications in smart structures," *OPN Optics & Photonics News,* vol. 9, pp. 33-7, Aug. 1998.

[156] V. M. Murukeshan, P. Y. Chan, L. S. Ong, and A. Asundi, "Intracore fiber Bragg gratings for strain measurement in embedded composite structures," *Appl. Opt.,* vol. 40, pp. 145-149, Jan. 1, 2001.

[157] M. Froggatt and J. Moore, "Distributed measurement of static strain in an optical fiber with multiple Bragg gratings at nominally equal wavelengths," *Appl. Opt.,* vol. 37, pp. 1741-6, Apr. 1, 1998.

[158] S. E. Kanellopoulos, V. A. Handerek, and A. J. Rogers, "Simultaneous strain and temperature sensing with photogenerated in-fiber gratings," *Opt. Lett.,* vol. 20, pp. 333-335, Feb. 1, 1995.

[159] H. Z. Yang, X. G. Qiao, Y. P. Wang, M. M. Ali, M. H. Lai, K. S. Lim, and H. Ahmad, "In-fiber gratings for simultaneous monitoring temperature and strain in ultrahigh temperature," *IEEE Photonics Technol. Lett.,* vol. 27, pp. 58-61, Jan. 1, 2015.

[160] Y. Zhang, D. Feng, Z. Liu, Z. Guo, X. Dong, K. S. Chiang, and B. C. B. Chu, "High-sensitivity pressure sensor using a shielded polymer-coated fiber Bragg grating," *IEEE Photonics Technol. Lett.,* vol. 13, pp. 618-619, Jun. 2001.

[161] A. Rauf, J. Zhao, and B. Jiang, "High-sensitivity bend angle measurements using optical fiber gratings," *Appl. Opt.,* vol. 52, pp. 5072-5078, Jul. 20, 2013.

[162] S. C. Tjin, R. Suresh, and N. Q. Ngo, "Fiber Bragg grating based shear-force sensor: Modeling and testing," *J. Lightwave Technol.,* vol. 22, pp. 1728-1733, Jul. 2004.

[163] J. Hernandez-Cordero, V. A. Kozlov, A. L. G. Carter, and T. F. Morse, "Fiber laser polarization tuning using a Bragg grating in a Hi-Bi fiber," *IEEE Photonics Technol. Lett.,* vol. 10, pp. 941-3, Jul. 1998.

[164] A. Othonos, L. Xavier, and T. Din Ping, "Spectrally broadband Bragg grating mirror for an erbium-doped fiber laser," *Opt. Engr.,* vol. 35, pp. 1088-92, Apr. 1996.

[165] S. Li and C. Kam Tai, "A novel configuration for multiwavelength actively mode-locked fiber lasers using cascaded fiber Bragg gratings," *IEEE Photonics Technol. Lett.,* vol. 11, pp. 179-81, Feb. 1999.

[166] R. Kashyap, *Fiber Bragg Gratings*. San Diego: Academic Press, 1999.

[167] T. Erdogan, "Fiber grating spectra," *J. Lightwave Technol.,* vol. 15, pp. 1277-94, Aug. 1997.

[168] P. Petruzzi, C. Lowry, and P. Sivanesan, "Dispersion compensation using only fiber Bragg gratings," *IEEE J. Sel. Top. Quantum Electron.,* vol. 5, pp. 1339-1344, Sep./Oct. 1999.

[169] J. A. J. Fells, S. E. Kanellopoulos, P. J. Bennett, V. Baker, H. F. M. Priddle, W. S. Lee, A. J. Collar, C. B. Rogers, D. P. Goodchild, R. Feced, B. J. Pugh, S. J. Clements, and A. Hadjifotiou, "Twin fiber grating tunable dispersion compensator," *IEEE Photonics Technol. Lett.,* vol. 13, pp. 984-6, Sep. 2001.

[170] B. J. Eggleton, J. A. Rogers, P. S. Westbrook, and T. A. Strasser, "Electrically tunable power efficient dispersion compensating fiber Bragg grating," *IEEE Photonics Technol. Lett.,* vol. 11, pp. 854-6, Jul. 1999.

[171] N. M. Litchinitser and D. B. Patterson, "Analysis of fiber Bragg gratings for dispersion compensation in reflective and transmissive geometries," *J. Lightwave Technol.,* vol. 15, pp. 1323-1328, Aug. 1997.

[172] G. Lenz, B. J. Eggleton, and N. Litchinitser, "Pulse compression using fiber gratings as highly dispersive nonlinear elements," *J. Opt. Soc. Am. B,* vol. 15, pp. 715-21, Feb. 1998.

[173] T. Komukai, K. Tamura, and M. Nakazawa, "Efficient 0.04-nm apodized fiber Bragg grating and its application to narrow-band spectral filtering," *IEEE Photonics Technol. Lett.,* vol. 9, pp. 934-936, Jul. 1997.

[174] J. Canning, D. C. Psaila, Z. Brodzeli, A. Higley, and M. Janos, "Characterization of apodized fiber Bragg gratings for rejection filter applications," *Appl. Opt.,* vol. 36, pp. 9378-82, Dec. 20, 1997.

[175] K. Saitoh and S. Matsuo, "Multicore fibers for large capacity transmission," *Nanophotonics,* vol. 2, pp. 441-454, 2013.

[176] K. Saitoh and S. Matsuo, "Multicore fiber technology," *J. Lightwave Technol.,* vol. 34, pp. 55-66, Jan. 1, 2016.

[177] L. J. Cooper, A. S. Webb, A. Gillooly, M. Hill, T. Read, P. Maton, J. Hankey, and A. Bergonzo, "Design and performance of multicore fiber optimized towards communications and sensing applications," *Proc. SPIE,* vol. 9359, pp. 93590H-1--93590H-7, 2015.

[178] M. J. Gander, D. Macrae, E. A. C. Galliot, R. McBride, J. D. C. Jones, P. M. Blanchard, J. G. Burnett, A. H. Greenaway, and M. N. Inci, "Two-axis bend measurement using multicore optical fibre," *Opt. Commun.,* vol. 182, pp. 115-121, 2000.

[179] G. M. H. Flockhart, W. N. MacPherson, J. S. Barton, J. D. C. Jones, L. Zhang, and I. Bennion, "Two-axis bend measurement with Bragg gratings in multicore optical fiber," *Opt. Lett.,* vol. 28, pp. 387-389, 2003.

[180] D. Barrera, I. Gasulla, and S. Sales, "Multipoint two-dimensional curvature optical fiber sensor based on a nontwisted homogeneous four-core fiber," *J. Lightwave Technol.,* vol. 33, pp. 2445-2450, Jun. 15, 2015.

[181] R. G. Duncan, M. E. Froggatt, S. T. Kreger, R. J. Seeley, D. K. Gifford, A. K. Sang, and M. S. Wolfe, "High-accuracy fiber-optic shape sensing," *Proc. SPIE,* vol. 6530, pp. 65301S-1—65301S-11, 2007.

[182] R. G. Duncan and M. T. Raum, "Characterization of a fiber-optic shape and position sensor," *Proc. SPIE,* vol. 6167, pp. 616704-1—616704-11, 2006.

[183] C. Ledermann, H. Pauer, and H. Woern, "Fiber optical sensor system for shape and haptics for flexible instruments in minimally invasive surgery: overview and status quo," *Proc. SPIE,* vol. 9157, pp. 915766-1--915766-4, 2014.

[184] A. Gillooly, "Medical fiber-optic sensors offer haptics, 3D shape sensing, and pressure sensing," *Laser Focus World,* vol. 52, pp. 43-46, Aug. 2016.

[185] D. P. Tsai, Y. L. Chung, and A. Othonos, "Subwavelength imaging of an etched fiber with an intracore Bragg grating by apertured photon scanning tunneling microscope," *Proc. SPIE*, vol. 2384, pp. 191-197, 1995.

[186] J. D. Mills, C. W. J. Hillman, W. S. Brocklesby, and B. H. Blott, "Evanescent field imaging of an optical fiber Bragg grating," *Appl. Phys. Lett.*, vol. 75, pp. 4058-4060, Dec. 27, 1999.

[187] L. M. Baskin, M. Sumetsky, P. S. Westbrook, P. I. Reyes, and B. J. Eggleton, "Accurate characterization of fiber Bragg grating index modulation by side-diffraction technique," *IEEE Photonics Technol. Lett.*, vol. 15, pp. 449-51, Mar. 2003.

[188] P. A. Krug, R. Stolte, and R. Ulrich, "Measurement of index modulation along an optical fiber Bragg grating," *Opt. Lett.*, vol. 20, pp. 1767-9, Sep. 1, 1995.

[189] F. El-Diasty, A. Heaney, and T. Erdogan, "Analysis of fiber Bragg gratings by a side-diffraction interference technique," *Appl. Opt.*, vol. 40, pp. 890-896, Feb. 20, 2001.

[190] H. Kuei-Chu, S. Lih-Gen, H. Wei-Wei, and L. Yinchieh, "Methods of achieving linear index-change response for narrow-band fiber Bragg grating sequential writing," *Opt. Commun.*, vol. 277, pp. 310-14, Sep. 15, 2007.

[191] I. Petermann, S. Helmfrid, and A. T. Friberg, "Limitations of the interferometric side diffraction technique for fibre Bragg grating characterization," *Opt. Commun.*, vol. 201, pp. 301-308, Jan. 15, 2002.

[192] S. Loranger and R. Kashyap, "Are optical fibers really uniform? Measurement of refractive index on a centimeter scale," *Opt. Lett.*, vol. 42, pp. 1832-1835, May 1, 2017.

[193] R. J. Espejo, M. Svalgaard, and S. D. Dyer, "Characterizing fiber Bragg grating index profiles to improve the writing process," *IEEE Photonics Technol. Lett.*, vol. 18, pp. 2242-2244, Nov. 1, 2006.

[194] X. Chapeleau, D. Leduc, C. Lupi, F. López-Gejo, M. Douay, R. Le Ny, and C. Boisrobert, "Local characterization of fiber-Bragg gratings through combined use of low-coherence interferometry and a layer-peeling algorithm," *Appl. Opt.*, vol. 45, pp. 728-735, Feb. 1, 2006.

[195] D.-W. Huang and C.-C. Yang, "Reconstruction of fiber grating refractive-index profiles from complex Bragg reflection spectra," *Appl. Opt.*, vol. 38, pp. 4494-4499, Jul. 20, 1999.

[196] Z. Zhang, C. Tian, M. A. F. Roelens, M. R. Mokhtar, P. Petropoulos, D. J. Richardson, and M. Ibsen, "Direct characterization of the spatial effective refractive index profile in Bragg gratings," *IEEE Photonics Technol. Lett.*, vol. 17, pp. 2685-2687, Dec. 2005.

[197] G. A. Cranch and G. M. H. Flockhart, "Tools for synthesising and characterising Bragg grating structures in optical fibres and waveguides," *J. Mod. Opt.*, vol. 59, pp. 493-526, Mar. 20, 2012.

[198] A. Rosenthal and M. Horowitz, "Inverse scattering algorithm for reconstructing strongly reflecting fiber Bragg gratings," *IEEE J. Quantum Electron.*, vol. 39, pp. 1018-1026, Aug. 2003.

[199] S. Keren, A. Rosenthal, and M. Horowitz, "Measuring the structure of highly reflecting fiber Bragg gratings," *IEEE Photonics Technol. Lett.*, vol. 15, pp. 575-577, Apr. 2003.

[200] D. Leduc, X. Chapeleau, C. Lupi, F. Lopez Gejo, M. Douay, R. Le Ny, and C. Boisrobert, "Experimental synthesis of fibre Bragg gratings index profiles: comparison of two inverse scattering algorithms," *Meas. Sci. Technol.*, vol. 18, p. 12, Nov. 23, 2007.

[201] H.-C. Cheng and Y.-L. Lo, "The synthesis of multiple parameters of arbitrary FBGs via a genetic algorithm and two thermally modulated intensity spectra," *J. Lightwave Technol.*, vol. 23, p. 2158, Jun. 1, 2005.

[202] C. C. Cheng, Y. L. Lo, W. Y. Li, C. T. Kuo, and H. C. Cheng, "Estimations of fiber Bragg grating parameters and strain gauge factor using optical spectrum and strain distribution information," *Appl. Opt.*, vol. 46, pp. 4555-4562, Jul. 20, 2007.

[203] N. M. Dragomir, D. Garchev, G. W. Baxter, P. M. Farrell, and A. Roberts, "Nondestructive imaging and characterization of optical fiber Bragg gratings," in *Photonics, Devices, and Systems II*, Prague, Czech Republic, 2003, pp. 182-186.

[204] C. M. Rollinson, S. A. Wade, G. W. Baxter, and S. F. Collins, "Imaging of various optical fiber Bragg gratings using differential interference contrast microscopy: analysis and comparison," *Appl. Opt.,* vol. 55, pp. 783-790, Feb. 1, 2016.

[205] N. M. Dragomir, C. Rollinson, S. A. Wade, A. J. Stevenson, S. F. Collins, G. W. Baxter, P. M. Farrell, and A. Roberts, "Nondestructive imaging of a type I optical fiber Bragg grating," *Opt. Lett.,* vol. 28, pp. 789-791, May 15, 2003.

[206] C. Y. Wei, C. C. Ye, S. W. James, P. E. Irving, and R. P. Tatam, "AFM observation of surface topography of fibre Bragg gratings fabricated in germanium–boron codoped fibres and hydrogen-loaded fibres," *Opt. Mater.,* vol. 20, pp. 283-294, Nov./Dec. 2002.

[207] X. M. Goh, S. S. Kou, B. P. Kouskousis, N. M. Dragomir, S. F. Collins, G. W. Baxter, and A. Roberts, "Non-destructive three-dimensional optical imaging of a fiber Bragg grating," *IEEE Photonics J.,* vol. 6, pp. 6900207-1--6900207-7, Sep. 24, 2014.

[208] Y. Bao and T. K. Gaylord, "Characterization of fiber Bragg gratings in multicore fibers using quantitative phase imaging," in *Frontiers in Optics / Laser Science*, Washington, DC, 2018, p. JTu2A.74.

[209] C. Fournier, F. Jolivet, L. Denis, N. Verrier, E. Thiebaut, C. Allier, and T. Fournel, "Pixel super-resolution in digital holography by regularized reconstruction," *Appl. Opt.,* vol. 56, pp. 69-77, Jan. 1, 2017.

[210] R. S. Ruskin, Z. Yu, and N. Grigorieff, "Quantitative characterization of electron detectors for transmission electron microscopy," *J. Struct. Biol.,* vol. 184, pp. 385-393, Dec. 1, 2013.

[211] G. D. Boreman, *Modulation Transfer Function in Optical and Electro-optical Systems*. Bellingham, WA: SPIE, 2001.

[212] R. G. Lyons, *Understanding Digital Signal Processing* 2nd ed.: Prentice Hall PTR, 2004.

[213] R. G. Vaughan, N. L. Scott, and D. R. White, "The theory of bandpass sampling," *IEEE Trans. Signal Process.,* vol. 39, pp. 1973-1984, Sep. 1991.

[214] M. Feldman, *Hilbert Transform Applications in Mechanical Vibration*. Hoboken, N.J.: Wiley, 2011.

[215] Y. Bao, G. C. Dong, and T. K. Gaylord, "Weighted-least-squares multi-filter phase imaging with partially coherent light: Characteristics of annular illumination," *Appl. Opt.,* p. *submitted,* 2018.

[216] B. Bhaduri, C. Edwards, H. Pham, R. Zhou, T. H. Nguyen, L. L. Goddard, and G. Popescu, "Diffraction phase microscopy: principles and applications in materials and life sciences," *Adv. Opt. Photonics,* vol. 6, pp. 57-119, Mar. 31, 2014.

[217] L. Hongpu, L. Ming, S. Yunlong, and J. E. Rothenberg, "Advances in the design and fabrication of high-channel-count fiber Bragg gratings," *J. Lightwave Technol.,* vol. 25, pp. 2739-50, 2007.

[218] A. Arigiris, M. Konstantaki, A. Ikiades, D. Chronis, P. Florias, K. Kallimani, and G. Pagiatakis, "Fabrication of high-reflectivity superimposed multiple-fiber Bragg gratings with unequal wavelength spacing," *Opt. Lett.,* vol. 27, pp. 1306-1308, Aug. 1, 2002.

[219] M. Habaza, B. Gilboa, Y. Roichman, and N. T. Shaked, "Tomographic phase microscopy with 180 degrees rotation of live cells in suspension by holographic optical tweezers," *Opt. Lett.,* vol. 40, pp. 1881-1884, Apr. 15, 2015.

[220] A. Kus, M. Dudek, B. Kemper, M. Kujawinska, and A. Vollmer, "Tomographic phase microscopy of living three-dimensional cell cultures," *J. Biomed. Opt.,* vol. 19, pp. 046009-1--046009-7, Apr. 2014.

[221] J. Kostencka, T. Kozacki, A. Kuś, and M. Kujawińska, "Accurate approach to capillary-supported optical diffraction tomography," *Opt. Express,* vol. 23, pp. 7908-7923, Mar. 23, 2015.

[222] C. Trujillo, R. Castañeda, P. Piedrahita-Quintero, and J. Garcia-Sucerquia, "Automatic full compensation of quantitative phase imaging in off-axis digital holographic microscopy," *Appl. Opt.,* vol. 55, pp. 10299-10306, Dec. 20, 2016.

[223] K. Komuro and T. Nomura, "Quantitative phase imaging using transport of intensity equation with multiple bandpass filters," *Appl. Opt.,* vol. 55, pp. 5180-5186, Jul. 1, 2016.

[224] R. Zhou, C. Edwards, G. Popescu, and L. Goddard, "Semiconductor defect metrology using laser-based quantitative phase imaging," *Proc. SPIE,* vol. 9336, pp. 93361I-1--93361I-6, 2015.

[225] A. Nativ and N. T. Shaked, "Compact interferometric module for full-field interferometric phase microscopy with low spatial coherence illumination," *Opt. Lett.,* vol. 42, pp. 1492-1495, Apr. 15, 2017.

[226] T. Chakraborty and J. C. Petruccelli, "Source diversity for transport of intensity phase imaging," *Opt. Express,* vol. 25, pp. 9122-9137, Apr. 17, 2017.

[227] Q. Li, M. Chambonneau, M. Chanal, and D. Grojo, "Quantitative-phase microscopy of nanosecond laser-induced micro-modifications inside silicon," *Appl. Opt.,* vol. 55, pp. 9577-9583, Nov. 20, 2016.

[228] J. Sun, C. Zuo, and Q. Chen, "Iterative optimum frequency combination method for high efficiency phase imaging of absorptive objects based on phase transfer function," *Opt. Express,* vol. 23, pp. 28031-28049, Oct. 19, 2015.

[229] T. H. Nguyen, H. Majeed, C. A. Edwards, M. N. Do, L. L. Goddard, and G. Popescu, "Halo-free quantitative phase imaging with partially coherent light," *Proc. SPIE,* vol. 9336, pp. 93360N-1--93360N-5, 2015.

[230] J. M. Soto, J. A. Rodrigo, and T. Alieva, "Partially coherent illumination engineering for enhanced refractive index tomography," *Opt. Lett.,* vol. 43, pp. 4699-4702, Oct. 1, 2018.

[231] Y. Saad, *Iterative Methods for Sparse Linear Systems: Second Edition*: Society for Industrial and Applied Mathematics (SIAM, 3600 Market Street, Floor 6, Philadelphia, PA 19104), 2003.

[232] I. Nemoto and A. Takahashi, "Methods of improving the images in phase-contrast microscopy: theory and computer simulation," *J. Opt. Soc. Am. A,* vol. 8, pp. 511-519, Mar. 1, 1991.

[233] C. Preza, D. L. Snyder, and J.-A. Conchello, "Theoretical development and experimental evaluation of imaging models for differential-interference-contrast microscopy," *J. Opt. Soc. Am. A,* vol. 16, pp. 2185-2199, Sep. 1, 1999.

[234] M. D. Feit and J. A. Fleck, "Light-propagation in graded-index optical fibers," *Appl. Opt.,* vol. 17, pp. 3990-3998, Dec. 15, 1978.

[235] H. Sierra, C. A. DiMarzio, and D. H. Brooks, "Modeling phase microscopy of transparent three-dimensional objects: a product-of-convolutions approach," *J. Opt. Soc. Am. A,* vol. 26, pp. 1268-1276, May 1, 2009.

[236] B. R. Frieden, "Optical transfer of the three-dimensional object," *J. Opt. Soc. Am.,* vol. 57, pp. 56-66, Jan. 1, 1967.

[237] P. Bon, B. Wattellier, and S. Monneret, "Modeling quantitative phase image formation under tilted illuminations," *Opt. Lett.,* vol. 37, pp. 1718-1720, May 15, 2012.

[238] J. D. Jackson, *Classical Electrodynamics*. New York: Wiley, 1998.

[239] J. M. Cowley, *Diffraction Physics*, 3rd ed. Amsterdam, Netherlands: Elsevier Science, 1995.

[240] I. Nemoto, "Three-dimensional imaging in microscopy as an extension of the theory of two-dimensional imaging," *J. Opt. Soc. Am. A,* vol. 5, pp. 1848-1851, Nov. 1, 1988.

VITA

Yijun Bao is a PhD student in School of Electrical and Computer Engineering at the Georgia Institute of Technology. He was born in Linhai, Zhejiang, China. He received his BS in physics from Peking University in China in 2014. In his undergraduate, he received Outstanding Graduate Award from both Peking University and Beijing city. He also received National Scholarship of China in 2013 and Pacemaker to Merit Student of Peking University in 2012. After coming to Georgia Tech, he received Oscar P. Cleaver Award for obtaining highest score on Ph.D. Preliminary Exam. He is a student member of Optical Society of America and a reviewer of OSA publishing. He received Incubic/Milton Chang Student Travel Grant in Frontiers in Optics conference in 2017.